EXPERIMENTAL AND COMPUTATIONAL STUDY OF NON-TURBULENT FLOW REGIMES AND CAVERN FORMATION OF NON-NEWTONIAN FLUIDS IN A STIRRED TANK

by

Luke Wayne Adams

A thesis submitted to
The University of Birmingham
for the degree of

DOCTOR OF PHILOSOPHY

Chemical Engineering
School of Engineering
University of Birmingham
Edgbaston
Birmingham
B15 2TT
March 2009

UNIVERSITYOF
BIRMINGHAM

University of Birmingham Research Archive

e-theses repository

ABSTRACT

When non-Newtonian fluids are mixed in a stirred tank at low Reynolds numbers caverns can be formed around the impeller. If the fluid contains a yield stress the cavern has a fixed boundary where no flow occurs outside of it. When the fluid does not contain a yield stress a pseudo-cavern is formed, the cavern boundary is not fixed since flow can occur outside of it, but the majority of the flow is present in a region around the impeller. Mixing and cavern formation of a variety of non-Newtonian fluids are studied using experimental techniques and computational fluid dynamics (CFD). Cavern data extracted from both methods are compared with mechanistic cavern prediction models. An adapted planar laser induced fluorescence technique showed that mixing inside of a shear thinning Herschel-Bulkley fluid is very slow. Positron emission particle tracking obtained flow patterns and cavern sizes of three rheologically complex opaque fluids. CFD was able to predict the data obtained from both experimental techniques fairly well at low Reynolds numbers. A toroidal cavern model provided the best fit for single phase fluids but for the opaque fluids all models drastically over predicted the cavern size, with the cylindrical model only predicting cavern heights at high Reynolds numbers.

ACKNOWLEDGEMENTS

TABLE OF CONTENTS

LIST OF FIGURES

LIST OF TABLES

NOMENCLATURE

Upper case

B	Baffle width	m
C	Impeller off bottom clearance	m
D	Impeller diameter	m
D_c	Cavern diameter	m
D_{Hub}	Hub diameter	m
D_{Shaft}	Shaft diameter	m
F	Total force imparted by the impeller on the cavern boundary	$N\,m^{-2}$
F_a	Axial force imparted by the impeller	$N\,m^{-2}$
F_θ	Tangential force imparted by the impeller	$N\,m^{-2}$
H	Fluid height in vessel	m
H_c	Cavern height	m
M	Torque	N m
N	Impeller speed	s^{-1}
N_f	Axial force number	-
P	Power	W
P_o	Power number	-
P_r	Pressure	Pa
R	Impeller radius	m
Re	Reynolds number	-
T	Tank diameter	m
W	Hub height	m

Lower case

b	Radius of cavern surrounding torus with diameter equivalent to T	m
g	Acceleration due to gravity	$m\ s^{-2}$
k	Consistency factor	$Pa\ s^{n}$
k_s	Metzner and Otto constant	-
n	Flow behaviour index	-
r_c	Cavern radius ($D_c/2$ for sphere, D_c for toroid)	m
t	Time	s
t_c	Shear stress at cavern boundary	Pa
v	Velocity	$m\ s^{-1}$
v_a	Axial velocity	$m\ s^{-1}$
v_r	Radial velocity	$m\ s^{-1}$
v_θ	Tangential velocity	$m\ s^{-1}$
v_o	Fluid velocity at cavern boundary	$m\ s^{-1}$
v_{Tip}	Velocity at the impeller tip	$m\ s^{-1}$

Greek letters

$\dot{\gamma}$	Shear rate	s^{-1}
μ	Viscosity	Pa s
η	Apparent viscosity	Pa s
η_B	Plastic viscosity	Pa s
ρ	Density	$kg\ m^{-3}$
τ	Shear stress	Pa
τ_y	Yield stress	Pa

CHAPTER 1

INTRODUCTION

1.1. Motivation and Background

The mixing of fluids is an essential process that occurs throughout industry in many different apparatus and processes, whether in a mechanically agitated vessel or a static mixer within a pipe. Correct mixing is needed to achieve the homogeneity of materials in reactor vessels to ensure all reactive components can interact and create the desired product: poor mixing can lead to an inefficient reactor, thus requiring much longer residence times or higher energy input, both cases costing time and money. Heat transfer is also directly affected by the degree of homogeneity in a system; a well mixed system would remain at a constant temperature throughout the bulk liquid, and would respond quickly to changes. Poor mixing would lead to large temperature variations throughout the vessel, leading to differing reaction rates and thus poorer product yields.

Mixing in stirred tanks is achieved via the use of an impeller. Mixing vessels vary in shape and size, from cylindrical to square. There are also a large range of impellers that can be used: radial flow impellers such as the Rushton Turbine move the fluid out radially, axial flow impellers move the fluid out in an axial direction, and mixed flow impellers generate both radial and axial motion. These three types of impellers are generally much smaller than the tank and cause fluid motion by stirring at high speeds. Other types of impellers, such as helical screw, helical ribbon, and anchors, sweep the entire volume of the tank and so run at much slower speeds due to their size and power consumption. Impeller location is not always constant: the most common orientation is

with the impeller entering from the top in the centre of the vessel. Eccentric and non-vertical impeller positions have been used to generate motion within non baffled tanks that mimic, with some success, the flow patterns in baffled tanks. Side entering impellers are also used for highly viscous materials such as paper pulp. Baffles are used when mixing with the smaller impellers described above to help improve mixing when flow is seen throughout the entire vessel, and also to prevent solid body rotation. Correct choice of equipment is made dependant on the type of fluid to be mixed.

Many different types of fluids are mixed, with single phase liquids, solid-liquid suspensions, gas-liquid and three phase flow being the most common. The solid phase can be of various size and shape, whether granular, spherical beads, fibres or very small particles. The liquid itself can be of various types, but mainly classified in two separate categories: Newtonian or non-Newtonian. Newtonian fluids are described as having constant viscosity independent of shear and time whereas non-Newtonian fluids do not. There are many different types of non-Newtonian fluid behaviour, ranging from shear thinning materials where the viscosity decreases with shear rate and yield stress fluids that do not flow until a certain shear stress is reached. Both types of fluids can cause detrimental mixing conditions most notably creating caverns or pseudo-caverns.

Caverns are regions of intense flow around the impeller and are formed when mixing yield stress materials, such as paper pulp, polymers, and ceramic pastes; the remainder of the tank experiences no flow. The cavern boundary is assumed to be when the shear stress of the fluid is equal to the yield stress of the material: when shear stress is greater than yield stress, i.e. near the impeller, the fluid can flow. When shear stress is less than yield stress the material behaves as a solid and no flow can occur. Thus at the cavern

boundary the shear stress equals the yield stress, forcing flow to drop to zero and delineating the well mixed region from the stagnant regions.

Pseudo-caverns are very similar to normal caverns except they are created in fluids that do not have a yield stress but are shear thinning. These types of caverns are commonly present in the laminar and transitional regimes. Pseudo-caverns have no fixed boundary as velocities are still present throughout the entire mixing vessel. However, velocities outside the pseudo-cavern are usually orders of magnitude smaller than those found within. The shear thinning fluids generate these pseudo-caverns due to the increase in viscosity away from the impeller as the shear rate drops. The drop in viscosity accompanied with the drop in shear rate greatly slows down the fluid motion. Both factors generating a pseudo-cavern were the majority of fluid motion occurs inside of it, while only small velocities are present outside. The boundary of a pseudo-cavern is usually defined as the point at which the tangential velocity equals 1% of the tip speed (Amanullah *et al.,* 1998). Pseudo-caverns can also be formed in highly viscous Newtonian fluids due to the high viscosity rapidly reducing the fluid motion away from the impeller.

Caverns and pseudo-caverns are very detrimental to mixing, heat and mass transfer as very high impeller speed and high torque is required to cause motion in all regions of the tank. To avoid such high power requirements, whilst maintaining high-quality mixing, different impellers can be used that sweep the entire volume, such as helical ribbon impellers. However these impellers may cause motion throughout all regions of the tank they do not maintain it and causes caverns that move through each revolution. Increasing the impeller speed may remove this but since the swept volume for these

impellers is essentially the volume of the vessel, the power consumption will be inordinately high. Anchor impellers also sweep the entire volume but the fluid in-between the blades is not sheared at all causing larger dead zones. New methods for increasing the size of the cavern or removing them completely are needed.

A third, and much less common, type of non-Newtonian fluid is shear thickening: viscosity increases with shear rate. Due to current optical experimental techniques and the opaque nature of shear thickening fluids, it is not known if mixing results in the formation of caverns.

1.2. Objectives

The aim of this thesis is to understand the mixing and cavern formation of complex fluids in a vessel stirred with a 6 bladed pitch blade turbine in the laminar and low transitional flow regimes.

- To study the mixing inside of the cavern of a single phase non-Newtonian fluid by applying an adapted PLIF (Planar Laser Induced Fluorescence) technique and through the application of CFD (Computational Fluid Dynamics).
- To use PEPT (Positron Emission Particle tracking) to measure flow patterns and caverns generated when mixing two shear thinning cosmetic foundation cream slurries, a shear thickening china clay slurry and a paper pulp fibre suspension.
- To use CFD to simulate the mixing of two shear thinning cosmetic foundation cream slurries and a shear thickening china clay slurry to predict the experimental PEPT results.

- To test numerous cavern prediction models against all experimental and computational cavern data.

1.3. Layout of the Thesis

Chapter 2 is a critical literature review of the work undertaken to study the mixing of Newtonian and non-Newtonian fluids containing all experimental, computational and analytical techniques. Chapter 3 contains all the experimental methods used to obtain the results, the computational set-up for all the simulations and all the analytical cavern prediction models used. Chapters 4, 5, 6, and 7 are all results chapters. Chapter 4 deals with the caverns formed during the mixing of a Carbopol solution using an adapted PLIF technique in a small tank to delineate the cavern boundary. Simulations were also performed to mimic the experiments as well as a similar set of simulations based on a fictitious power law fluid. Theoretical cavern boundary models obtained from the literature were used to estimate the shape and size of the cavern for both the Carbopol and fictitious power law fluid results. Chapter 5 explores the mixing of two shear thinning cosmetic foundation creams in a small tank and the caverns formed within them using PEPT, CFD and the cavern boundary models. Chapter 6 and Chapter 7 use the same methods as Chapter 5 but with a shear thickening china clay suspension and a paper pulp fibre suspension, respectively. Chapter 7 describes further PEPT experiments on the paper pulp fibre suspension carried out using a larger tank. Finally Chapter 8 contains the major conclusions obtained from the results Chapters with ideas for future work to further the understanding of the mixing of these fluids.

CHAPTER 2

LITERATURE SURVEY

2.1. Rheology

Fluids can be prescribed with a rheological model that describes how the fluid deforms under an applied force. It is common for these models to provide a relationship between the shear rate ($\dot{\gamma}$) and the shear stress (τ). For a Newtonian fluid the relationship is linear and independent of time. The model is shown below in equation (2.1).

$$\tau = \mu\dot{\gamma} \tag{2.1}$$

The constant proportionality factor μ is the viscosity of the Newtonian fluid and is constant for all shear rates and shear stresses at constant temperature. This model also gives a definition for the viscosity of a fluid, the ratio of the shear stress to the shear rate. The Reynolds number for a Newtonian fluid in a stirred tank is defined below in equation (2.2).

$$Re = \frac{\rho N D^2}{\mu} \tag{2.2}$$

Where ρ is the fluid density, N is the impeller speed, D is the impeller diameter. Reynolds number is a ratio of the inertial forces to the viscous forces of the fluid, thus high values (Re > 10000) dictate turbulent flow where low values (Re < 10) mean laminar flow.

Non-Newtonian fluids do not have a constant viscosity, the most common being shear thinning materials, as the shear rate is increased the viscosity drops. The most common rheological model for these materials is the power law model shown below in equation (2.3)

$$\tau = k\dot{\gamma}^n \tag{2.3}$$

Where k is the consistency factor and n is the flow behaviour index. The consistency factor is a measure of how thick the fluid is, similar to the viscosity, whereas the flow behaviour index is a measure of how non-Newtonian the fluid is. A value of one means the fluid is Newtonian and for shear thinning fluids the value is between 0 and 1. Since the viscosity of these materials is not constant the Reynolds number shown above cannot be used. By applying the Metzner and Otto correlation to calculate the average shear rate the Reynolds number for a fluid described by the power law model is shown below in equation (2.4).

$$Re = \frac{\rho N^{2-n} D^2}{k k_s^{n-1}} \tag{2.4}$$

Where k_s is the Metzner and Otto constant and is dependent on the impeller type, for a pitched blade turbine the value is between 11 and 13, for this work 11 is used (Metzner and Otto, 1957). Another type of non-Newtonian behaviour can be described by the power law model and that is shear thickening. These materials behave in the opposite manner to shear thinning fluids, as the shear rate is increased the viscosity increases. The flow behaviour index for shear thickening materials is above unity.

Another common type of non-Newtonian fluid are viscoplastic materials, these are described by having an apparent yield stress. The shear stress of the material must be above the apparent yield stress for the fluid to flow, below the yield stress the material behaves much like a solid. There are two common rheological models that describe viscoplastic fluids, the simplest being the Bingham plastic model shown below in equation (2.5).

$$\tau = \tau_y + \eta_B \dot{\gamma} \quad for\ \tau > \tau_y$$
$$\dot{\gamma} = 0 \qquad for\ \tau < \tau_y$$

(2.5)

Where η_B is the plastic viscosity and τ_y is the yield stress of the fluid. The apparent viscosity of Bingham plastic materials decreases with an increase in shear rate similar to shear thinning fluids. There is some debate on whether the yield stress actually exists, as it is difficult to measure accurately the shear stress at very small shear rates. The yield stress is normally obtained by extrapolating the plot back to zero shear rate and hence why it is sometimes referred to as the apparent yield stress. The other common viscoplastic model is an amalgam of the power law and Bingham plastic model called the Herschel-Bulkley model presented below in equation (2.6)

$$\tau = \tau_y + k\dot{\gamma}^n \quad for\ \tau > \tau_y$$
$$\dot{\gamma} = 0 \qquad for\ \tau < \tau_y$$

(2.6)

This model is more encompassing than the Bingham model due to the inclusion of the0 flow behaviour index. As for power law fluids, the flow behaviour index is equal to 1 or less the viscosity drops with shear rate whereas if it is larger than 1 it increases with

shear rate. Thus this model can describe both shear thinning and shear thickening materials that have an apparent yield stress. Similar to the power law model the standard Reynolds number cannot be used, so by using the Metzner and Otto correlation the Reynolds number for a Bingham fluid is shown below in equation (2.7).

$$Re = \frac{\rho k_s N^2 D^2}{\tau_y + \eta_B k_s N} \tag{2.7}$$

And for a Herschel-Bulkley fluid the Reynolds number is shown below in equation (2.8).

$$Re = \frac{\rho k_s N^2 D^2}{\tau_y + k(k_s N)^n} \tag{2.8}$$

Some solid liquid suspensions such as paper pulp have been found to have a yield stress however the measurement of such is extremely difficult, due to the interaction between the two phases. Ayel *et al*. (2003) attempted to measure the yield stress of an ice slurry but found it to be quite difficult to obtain.

2.2. Experimental Techniques

2.2.1. Power Measurements

Power requirements of vessels are a commonly measured due to its simplicity and important relationship to mixing performance. Large power draw is avoided as this requires a lot of energy to mix and thus will cost more money, achieving the same level of mixing at lower power consumption is desirable. Numerous factors affect the power

draw such as fluid type, vessel geometry and choice of impeller. As fluid type and vessel geometry is generally fixed it is most common to change the impeller type. To measure the power requirement of a mixing vessel the torque M on the shaft of tank is measured and converted into power by equation (2.9).

$$P = 2\pi NM \tag{2.9}$$

It is more common to use Power numbers instead of power since they are dimensionless and thus can be compared between different vessel geometries. The Power number of a mixing vessel is shown below in equation (2.10).

$$P_0 = \frac{P}{\rho N^3 D^5} \tag{2.10}$$

Where ρ is the density of the fluid, N is the impeller speed and D is the impeller diameter. Power numbers are normally taken at a corresponding Reynolds number and for Newtonian fluids they are proportional to the Reynolds number in the laminar regime and are constant in the turbulent regime. The transitional regime separating these two is poorly understood and no simple relationship can be seen, but numerous empirical models have been proposed.

Extensive work has been done on the measurement of power numbers and power consumption of mixing apparatus for various Newtonian fluids. Rusthon *et al*., 1950, completed an in depth study of the mixing of various Newtonian fluids in a stirred tank. Different impellers were investigated and Power numbers were extracted over a large range of Reynolds numbers. This led to the Power number versus Reynolds number

plot showing that in the laminar regime on a log-log scale Power number decreases proportionally to an increase in Reynolds number. At high Reynolds numbers in the turbulent regime Power numbers are constant, the transitional regime between these two flow types shows a much more complex relationship. Other earlier work on power consumption and power numbers have been completed by Tay and Tatterson, 1985, Sano and Usui, 1985, Bujalski *et al.,* 1986 and 1987, Yianneskis *et al.,* 1987, Raghav Rao and Joshi, 1988, as a function of impeller and tank dimensions, impeller choice and pumping directions. Showing among other things that form drag is more dominant than skin drag, larger diameter impellers provide more efficient power draw. Power number is a function of disk thickness for a Rusthon turbine and blade thickness for a pitch blade turbine. Also larger diameter impellers affect the Power number whereas clearance does not and that down pumping pitch blade turbine is more efficient than up pumping.

Work on power numbers has also been completed on non-Newtonian fluids, some of the earlier work completed by Edwards *et al.,* 1976, considered a large range of rheologically different fluids and Metzner and Otto constants were calculated for various impellers. Nienow and Elson, 1988, also completed power measurements of yield stress and shear thickening materials. A much more recent work conducted by Ascanio *et al* 2004, used time periodic mixing of a shear thinning fluid to monitor power consumption, this technique stops and starts the motor periodically. At lower impeller speeds the use of intermittent mixing helped lower energy consumption of the impeller. Jomha *et al* 1990, completed power measurements of a shear thickening solid-liquid suspension and found that the values obtained can be predicted quite well with existing equations.

2.2.2. Mixing Times

Mixing time is defined as the time it takes for a volume of fluid to have the same concentration in all locations. Since this definition however would lead to large times, a percentage of complete mixing is used generally such as 95% or 99% mixedness. Numerous experimental techniques can be used to measure mixing times of stirred vessels such as acid based neutralisation (Norwood and Metzner, 1960; Bujalski *et al.,* 2002(b); Szalai *et al.,* 2004, Ascanio *et al* 2004) and decolourisation techniques (Nienow and Elson, 1998) where when the system is fully mixed the vessel becomes a single colour. Similarly injections of a tracer dye (Schofield, 1994; Mavros *et al.,* 2001; Kovács *et al* 2003) would yield similar results to the acid base test but without the need for a reaction to take place.

Multiple measuring probes can be placed in the vessel, (Procházka and Landau, 1961; Sano and Usui, 1985; Ruszkowski and Muskett, 1985; Rielly and Britter, 1985; Raghav Rao and Joshi, 1988; Yianneskis, 1991; Mahmoudi and Yianneskis, 1991; Mahouast, 1991; Schofield, 1994; Nienow, 1997; Zipp and Patterson, 1998; Osman and Varley, 1999; Jaworski *et al.,* 2000; Bujalski *et al.,* 2002(a); Guillard and Trägårdh, 2003; Montante and Magelli, 2004; Montante *et al.,* 2005) measuring anything from conductivity, fluorescence or pH, measuring the time it takes for the values to stabilise.

A much more complicated technique called liquid crystal thermography LCT (Lee and Yianneskis, 1994(a); Lee and Yianneskis, 1997) uses liquid crystals and laser sheets. The crystals reflect light at different colours depending on the temperature, thus a uniform temperature would yield a uniform colour scattered by the liquid crystals.

Electrical resistance tomography ERT (Holden *et al.,* 1998; Kovács *et al* 2003) works by using multiple probes to measure a resistance map of the vessel, an equal resistance would imply a well mixed system.

A much newer technique call Planar Laser Induced Fluorescence (PLIF) (Szalai *et al.,* 2004) uses a laser sheet passing through the vessel and a fluorescent tracer injected into the vessel. The tracer interacts with the laser sheet absorbing then fluorescing light which is capture by a CCD camera right angles to the laser sheet, complete mixing is obtained when the light fluoresced is even over the whole laser sheet.

The effect of tank geometry, fluorescent intensity, impeller geometry and impeller type on mixing time has been fully investigated for Newtonian fluids, however little work has been completed on non-Newtonian fluids. For Newtonian fluids it was found that mixing times are independent of the Reynolds number in the turbulent regime (Sano and Usui, 1985), impeller types of relative size are equally effective due to the Power number and energy dissipation being constant (Nienow, 1997) and for highly viscous materials even after hours of mixing homogeneity is not attained (Szalai *et al.,* 2004).

Kovács *et al* 2003, proved that mixing times were different for the same mixing geometry and power input for a shear thinning fluid compared with a Newtonian fluid, due to the rheology and polymeric structure of the non-Newtonian fluid. The mixing times for the shear thinning fluids are much larger than the Newtonian fluid mixing times at the same conditions (Montante *et al.,* 2005). Similarley for Newtonian fluids, time periodic mixing of a shear thinning fluid drastically reduces mixing times at low

impeller speeds, this technique stops and starts the motor periodically (Ascanio *et al* 2004).

2.2.3. Flow Patterns

The study of flow patterns is common practice, since flow patterns dictate how the system is mixed. The formation, shape and velocities of these flow patterns are of vital importance to understanding all manner of mixing configurations for all fluids. Most work has been done on Newtonian fluids since most non-Newtonian fluids are opaque and many of the flow pattern measurement techniques are optical and thus require transparent materials. In Addition non-Newtonian materials have complex rheologies making them very difficult to work with (Maingonnat *et al* 2005). Shear thickening materials have a had very little work completed on them compared to other non-Newtonian fluids. These fluids are very rare and extremely difficult to work with, however Grisky and Green, 1971, worked on them in the laminar regime but only measured friction coefficients in a conduit.

2.2.3.1. Flow Followers

One of the simplest techniques to understand flow patterns is by using a flow follower, a particle of neutral buoyancy is inserted into the flow and is followed either by eye or camera techniques. Sano and Usui, 1985, measured the discharge flow in a stirred tank for water using the flow follower technique, by measuring the number of times the particle passes through the impeller region for a given time. Yianneskis, 1991, used the technique much further to obtain flow patterns in a jet agitated vessel using many

acrylic particles with a light sheet used to illuminate the flow. Mahmoudi and Yianneskis, 1991, measured flow patterns in stirred tank using flow followers with a laser sheet used to select the plane to be studied. Three stable and 4 unstable flow patterns were measured for different impeller spacings of two Rusthon turbines. Solomon, *et al.,* 1981, used flow followers to measure flow inside a Carbopol solution using a vertical light beam. It was able to show that the flow inside of the cavern formed around the impeller was well agitated.

This technique can only be used on transparent materials since the camera needs to be able to see the particle, also the particle is moving in multiple dimensions so more than one camera is needed to get an idea of the full flow pattern. Due to the necessity of the particle to be seen, a fairly large size is used. This particle however is much too large to follow any of the small structures such as *Kolmogorov* scale of turbulence and the boundary layer flow near the cavern boundary. For this technique it will be impossible to follow a particle of the size needed for these structures but a good overall estimation of the flow pattern can be obtained.

2.2.3.2. Multiple Camera Techniques

Multiple camera techniques can be used to track the three dimensional motion of a particle by using three monochrome cameras. Two cameras are on each side of the tank with the third being at the bottom, thus aiming at all three axis of the tank. The particle is seeded in the vessel and all three cameras start recording, enabling the 3D motion of the particle to be derived and make it possible to determine the velocity distribution (Wittmer *et al.,* 1998; Barrue *et al.,* 1999). The technique requires a lot of data

manipulation to link all three images to provide the flow fields and also requires the fluid to be transparent.

2.2.3.3. Hot Wire Anemometry

Hot wire anemometry is a probe technique using two separate wires, as the flow passes these wires a voltage is recorded and this can be translated into a velocity. Gunkel and Weber, 1975 used this technique to measure the flow of air in a baffled tank and was able to measure the pumping capacity of the six bladed disc turbine quite reliably. Since this is a probe technique it is quite intrusive since the probe has to disrupt the flow to measure it and thus the readings are not entirely accurate. Also it only measures one direction of flow and one location at a time, so a full flow field using this technique would take a very long time.

2.2.3.4. Planar Laser Induced Fluorescence

Planar laser induced fluorescence (PLIF) is another optical technique for measuring flow patterns, this technique is explained above in the mixing time section 2.2.2. Concentration maps before the dye is fully mixed will show the flow patterns of the system, including dead zones (Kukura *et al.,* 2002). Bakker and van den Akker, 1996(a), used this technique to measure the yield of a reactor system in turbulent flow. Guillard *et al.,* 2000, studied the turbulent flow in a stirred tank with a Rusthon turbine and PLIF showed the presence of coherent mixing structures in the upper part of the tank and strong tangential flow in the impeller stream. Fountain *et al.,* 2000, used PLIF to measure the flow structure of a stirred tank with a disc impeller. Zalc *et al.,* 2002,

found that flow of a Rusthon turbine is partially chaotic and contained large areas of poor mixing in the laminar regime, increasing the Reynolds number did not yield more efficient mixing. Alvarez-Hernández *et al.,* 2002, and Szalai *et al.,* 2004, used PLIF to study the flow patterns in the laminar regime for a variety of impellers. Eccentric agitation in a small un-baffled tank was investigated using PLIF by Hall *et al.,* 2005. It was found that eccentric mixing in an un-baffled vessel provides improved mixing over a baffled system with centrally fixed impeller at this small scale.

PLIF is good at obtaining flow pattern data but is unable to measure velocities, also this technique can only be used on transparent fluids since it is an optical technique.

2.2.3.5. Laser Doppler Velocimetry/Anemometry

Laser Doppler Velocimetry (LDV) or Laser Doppler Anemometry (LDA) is an optical technique for measuring fluid velocity and flow patterns. It uses two argon-ion laser beams pinpointing on a location in the tank, the crossing of the laser forms a small volume. The fluid is seeded with small reflective particles of neutral buoyancy, these particles would pass through the small volume, and scatter the laser light. This scatter is detected and can then be used to calculate the velocity at that location. By measuring at multiple locations the overall flow field can be extracted.

Rushton *et al.,* 1950 and Yianneskis *et al.,* 1987, measured the flow fields generated in a stirred tank mixed by a 6 blade disk turbine. The inclination of the impeller stream was found to change when a lower impeller clearance was used. The impeller diameter was also found to affect this but not as prominently as the clearance. Nouri *et al.,* 1987,

found that the impeller diameter did not affect the normalised velocities near the impeller in a stirred tank. Weetman and Oldshue, 1988, studied the flow fields formed by different impellers. Wu and Patterson, 1989, found for a Rusthon turbine in a stirred tank that the normalised velocities were function of location and not impeller speed.

Ranade and Joshi 1989(a), found that the angle of the pitch blade turbine greatly affected the flow fields whereas blade width changes the flow slightly, also a larger diameter impeller produced more radial flow. Hutchings *et al.,* 1989, and Ranade *et al.,* 1991, measured flow fields in a stirred tank with various impellers. Yianneskis and Whitelaw, 1993, and Lee and Yianneskis, 1994(b), studied the trailing vorticies generated by the impeller blades. Harvey III *et al.,* 1995, and Xu and McGrath, 1996, measured flow fields induced by a pitch blade turbine. Rutherford *et al.,* 1996, found that thinner blade impellers produced higher mean velocities, power numbers and flow numbers for a Rusthon turbine. Armenante and Chou, 1996, showed that a second impeller changed the flow pattern completely, giving strong vertical circulation between the impellers.

Bakker and van den Akker, 1996, was able to investigate the yield of a reactor system in turbulent conditions. Bakker *et al.,* 1996, showed that a pitch blade turbine in the laminar regime pumps radially with the flow confined to the impeller with the tangential velocities dominating. Schäfer *et al.,* 1998, Naude *et al.,* 1998, and Sahu *et al.,* 1999, obtained flow field data for a variety of different impeller types. Bittorf and Kresta, 2000, found through LDV that the active volume during mixing with an axial impeller is not the whole tank but on two thirds of the tank height and the size of this volume is independent of impeller diameter, impeller speed and off bottom clearance. However

for a pitch blade turbine the location of this volume is dependent on the impeller off bottom clearance.

Bittorf and Kresta, 2001, showed that the flow at the wall generated by an axial impeller forms a 3D wall jet that agrees well with jet theory. Patwardhan, 2001, measured the residence time distribution of a down pumping pitch blade turbine. Montante *et al.,* 2001(a), noticed that when the impeller off bottom clearance was changed for a Rusthon turbine it changes the flow pattern from a double loop to a single loop. Mavros *et al.,* 2001, measure the flow patterns of a new impeller called Narcissus and was found to develop and original flow pattern unlike any other impeller.

Jones *et al.,* 2001, Nikiforaki *et al.,* 2003, Micheletti, 2004, and Hartmann *et al.,* 2004(b), also measured flow patterns for various tank configurations and impeller types. Galletti *et al.,* 2005, aimed to measure the instabilities of the flow seen in stirred vessels and found that they vary greatly from one region to another.

LDV is an accurate technique for measuring flow patterns and velocities however the data acquisition takes a long time since each location has to be done individually. Also since this is another optical technique only transparent materials can be used.

2.2.3.6. Particle Image Velocimetry

Particle Image Velocimetry (PIV) is another optical technique similar to LDV for measuring fluid velocity and flow patterns. The method uses a laser sheet projected into the vessel, a fast CCD camera at right angles to the laser sheet captures many images

over a period of time of small tracer particles (~60µm) in the mixing fluid passing through the laser sheet. From these interactions, 2D velocity fields can be obtained (Kukura *et al.,* 2002). La Fontaine and Shepherd, 1996, measured flow fields in a stirred tank and were able to identify stagnant flow regions, circulation loops and the turbulent flow. Bakker *et al.,* 1996, and Sheng *et al.,* 1998, measure the flow fields generated in a stirred tank with a pitch blade turbine and an axial impeller respectively.

Lamberto *et al.,* 1999, found that after 2 hours 15% of the tank was still not mixed due to segregated zones in an un-baffled tank with a radial impeller, changing the impeller speeds caused these segregated zones to move. Fountain *et al.,* 2000, measured the flow fields on a disc impeller, where Ranade *et al.,* 2001, looked at the trailing vortices formed with a Rusthon turbine. Bugay *et al.,* 2002, and Escudié and Liné, 2003, measured the flow patterns formed with a Lightnin A310 axial impeller and Rusthon turbine respectively. Yoon *et al.,* 2003, used a variant of PIV called stereoscopic PIV which enables the measurement of all three velocity components, with this they measured the velocity on a cylindrical surface surrounding the impeller swept volume.

Khopkar *et al.,* 2003, confirmed that trailing vortices are present for a down pumping pitch blade turbine in an aerated and non-aerated vessel. Escudié *et al.,* 2004, located the trailing vortices of a Rusthon turbine and was able to measure the size of them. Szalai *et al.,* 2004, and Micheletti, 2004, measured flow patterns and mixing performance of 4 Ekato Intermig® impellers and a Rusthon turbine respectively. Hall *et al.,* 2005, found that an eccentrically agitated un-baffled vessel provided better mixing than a baffled system with a centrally placed impeller in a small scale vessel, similar findings obtained above for PLIF.

Couerbe *et al.,* 2008, measured flow patterns of a non-Newtonian fluid exhibiting thixotropic shear thinning behaviour with a yield stress being mixed with an axial impeller. Outward pumping was seen at high impeller speeds but at lower speeds caverns were formed, thus dramatically reducing the pumping capacity of the impeller. The lower flow loop could not be measured due to that the tank had a conical bottom and thus parallaxing effects would make it impossible to measure in this region.

PIV is a good technique to obtain velocity instantaneous fields within a given measurement plane and in this sense is a more rapid technique than LDV, however the accuracy in the recorded velocitie values are not as good. PIV has the same difficulties that LDV has in that it is an optical technique so the fluid must be transparent.

2.2.3.7. 3D Phase-Doppler Anemometry

3D Phase-Doppler Anemometry (PDA) is a similar technique to LDV, instead it uses six lasers instead of two and so all three velocity components can be measured at once. Pettersson and Rasmuson, 1998, was able to use this technique and measure flow patterns and local fluid velocity vectors in a stirred tank. Due to the extra component of velocity the technique takes longer to compute than LDV, also again due to lasers being used the material studied has to be transparent.

2.2.3.8. Two Component Phase-Doppler Anemometry

Two component PDA is similar to LDV but uses two different size tracers instead of one. The technique can distinguish between the two particle sizes and so can be used to measure the flow field of two different phases at the same time (Lyungqvist and

Rasmuson, 2001), such as measuring the flow field of a solid-liquid suspension. A very small particle would be used to measure the fluid flow field while selecting a larger particle of similar size to the solid fraction to measure the solid fractions flow field. However as mentioned previously the smaller particle used to measure the fluid flow fields would not be small enough to measure kolmogorov eddies. This technique is again optical and so can only be used on transparent materials.

2.2.3.9. Ultrasonic Doppler Velocimetry

Ultrasonic Doppler velocimetry (UDV) is an unobtrusive probe technique to measure flow fields in opaque materials by using ultrasonic signals. A probe is used to transmit and receive ultrasonic signals that are being reflected back by the structure of the fluid. The difference in the transmitted and received signal can be used to determine the velocity, and by measuring in multiple locations it is possible to get an idea of the overall flow pattern of the system. Ein-Mozaffari *et al.,* 2007, measured the flow field at critical locations inside a rectangular tank for a paper pulp suspension, it is the fibres of this suspension that reflect the ultrasonic signals back to the probe. Dead zones were found in the corners of the rectangular tank and grew in size with the yield stress of the paper pulp suspension. Pakzad *et al.,* 2008, was also able to use this technique to measure the flow field in an opaque solution of Xanthum gum which is pseudoplastic and has an apparent yield stress.

This technique is good since it is able to measure the velocity of the flow inside of opaque materials, but due to the each location has to be recorded separately a full flow field for a stirred tank would take a very long time to obtain.

2.2.3.10. Computer Automated Radioactive Particle Tracking

Computer-automated radioactive particle tracking (CARPT) uses a radioactive tracer that is neutrally buoyant in the studied liquid. The tracer emits radiation via β-decay, this means an atom inside the tracer particle emits either an electron or a positron. This can cause a nearby nucleus to become excited, it reduces to its ground state via emitting one or more γ-rays. Also the emitted positrons immediately annihilate with any electron giving off back to back γ-rays (Chaouki *et al.,* 1997). These γ-rays are detected by many scintillation detectors placed all around the sides of the tank. The intensity of the radiation measured decreases with increased distance from the detector, this needs to be calibrated for each particle used. By measuring multiple detections along with the corresponding intensity at a short interval of time it is possible to determine the particles' 3D location. Doing this successively yields the trajectory of the particle and from this data it is possible to obtain velocity flow fields, dead zones and eyes of circulation (Rammohan *et al* 2001, Guha *et al*., 2008). This technique is much quicker at obtaining results than the laser based techniques, is non-invasive and can be used for opaque materials and equipment.

2.2.3.11. Positron Emission Particle Tracking

Positron emission particle tracking (PEPT) is a radioactive tracer technique similar to CARPT that can be used to measure flow fields unobtrusively in both transparent and opaque fluids and equipment (Barigou 2004), a full explanation of the technique is given in chapter 3 section 3.1.4. Fangary *et al* 2000, measured flow fields of both water and a shear thinning CMC solution in a stirred tank. Zones of effective fluid agitation

and zones of stagnation are well shown, also axial flow impellers become more axial the more viscous the fluid. Guida *et al.,* 2009, measured the flow fields of a solid liquid suspension of glass particles in water stirred by a pitch blade turbine. Both phases were measured by running two separate experiments, one with the tracer following the fluid while another with the tracer inserted into a glass particle, thus obtaining both the liquid and solid flow field for the suspension. This is still a fairly new technique so little work has been published on the mixing of opaque fluids using PEPT. Similarly with the CARPT, PEPT is able to get overall flow patterns much quicker than optical techniques, is non-invasive and can be used with opaque materials. However the tracer particles used in PEPT are much easier to make, as when making the particles for CARPT it is very difficult to maintain the physical properties of said particle (Link *et al.,* 2008). However PEPT does not need a calibration before the experiment for it to know where the particle is inside of the tank since it does not rely on radiation strength to locate it.

2.2.4. Turbulence Measurements

Turbulence occurs at high Reynolds numbers, for Newtonian fluids this is above 10000, and contains random flow structures compared to the simple stream lines of laminar flow. Velocity values are not constant and fluctuate around a mean value, the larger the fluctuations the more turbulent the system is. Since turbulence is extremely complex it is commonly described by certain parameters rather than the continually changing flow patterns. Turbulent kinetic energy and energy dissipation are the most common parameters used to describe turbulent mixing. Lots of work has been done on measuring the turbulence parameters of Newtonian fluids using such techniques as hot film anemometry (Anandha Rao and Brodkey, 1972; Nishikawa *et al.,* 1976), where a

probe is inserted into the flow and voltages are recorded. These voltages can be calibrated to specific velocities and the fluctuations of these velocities can give a measure of the turbulence.

Constant temperature anemometry CTA (Wernersson and Trägårdh, 1998) measures turbulent parameters with a probe that can measure velocities in two directions simultaneously at a single location. Numerous optical laser techniques have been used such as LDV (Ranade and Joshi 1989(a); Zhou and Kresta, 1996(a); Zhou and Kresta, 1996(b); Rutherford *et al.,* 1996; Michelet *et al.,* 1997; Mavros *et al.,* 1998; Nikiforaki *et al.,* 2003; Micheletti, 2004, Kilander and Rasmuson, 2005), PIV (Sheng *et al.,* 1998; Sheng *et al.,* 2000; Bugay *et al.,* 2002; Escudié and Liné, 2003; Escudié *et al.,* 2004; Micheletti, 2004, Kilander and Rasmuson, 2005, Escudié and Liné, 2006, Chung *et al.,* 2007, Liu *et al.,* 2008, Gabriele *et al*., 2009) and 3D phase -doppler anemometry (Pettersson and Rasmuson, 1998). This 3D method is similar to LDV and LDV but uses 6 lasers instead of two, so is able to measure all three velocity components. A much more simplistic method to observe turbulence structures are Photographic velocity measurements (Van 't Riet and Smith, 1975), this technique uses seeded particles in the flow with successive photographs taken to observe the particles motion.

Van 't Riet and Smith, 1975, found for Newtonian fluids that turbulence was present at Reynolds numbers as low as 300. Tank geometry, especially impeller clearance and diameter has a large effect on energy dissipation with the number of baffles having no real effect (Zhou and Kresta, 1996(a)). Also different flow impellers have very different dominant characteristics of energy dissipation (Zhou and Kresta, 1996(b)).

2.2.5. Cavern Data

Cavern data are the experimentally determined shape and size of caverns or pseudo-caverns formed when mixing yield stress or shear thinning materials. Little work has been done on obtaining pseudo-cavern data since the cavern boundary is not fixed so normal techniques to measure the shape and size do not work, so most cavern data are obtained from yield stress materials.

Solomon, *et al.,* 1981, used hot film anemometry to determine the cavern boundary of Xantham gum an opaque yield stress material. Since hot film anemometry can detect fluid motion the probe was inserted in the tank and the impeller speed was increased until a reading was measured. Thus meaning that the cavern boundary is at this location at the corresponding impeller speed, multiple locations at multiple speeds allows an idea of cavern shape and size at different Reynolds numbers. When measuring caverns sizes under aerated conditions proved quite difficult due to interaction of the gas with the probes causing false readings. Solomon, *et al.,* 1981, also used the flow follower measure the size and shape of caverns, and found that they grow in size with an increase in impeller speed with stagnant fluid seen outside.

Elson and Cheesman, 1986, used an X-ray technique to visualise caverns in opaque yields stress fluids. An X-ray opaque fluid such as a Barium solution was injected into the impeller region, this solution would fill the cavern and so when an X-ray is taken the cavern shape can be seen (Nienow and Elson, 1988). Elson, 1990, used a much simpler technique by monitoring the tank walls, bottom and free surface bye eye for motion and thus cavern boundary as the impeller speed was increased for an opaque xantham gum

solution. Observed values were very close to predictions from the Elson and Cheesman, 1986, model for when the cavern touched the tank wall. The presence of baffles was shown to have a negative effect on cavern growth, both vertically and horizontally, so higher impeller speeds are needed to obtain complete motion of the tank for baffled systems.

Amanullah *et al.,* 1997, measured caverns formed by a shear thinning Herschel-Bulkley Carbopol solution, stirred with a down pumping axial impeller measured using crystal violet injections near the impeller. At higher impeller clearance larger caverns were detected for the same power input and larger caverns were generated with the axial impeller compared with a Rusthon turbine. Cavern height to diameter ratio remained constant with increase in impeller speed until the cavern touched the tank wall. Wilkens *et al.,* 2005, used a novel technique to measure caverns formed in Heinz ketchup. Glitter was injected in the impeller region during mixing, the vessel was then frozen, freezing the ketchup solid. Dissecting the frozen ketchup yielded the cavern shape by the location of the glitter. Elliptical torus caverns were found for both impeller types, with the taller caverns formed when using a pitch blade turbine compared to a radial impeller. Pakzad *et al.,* 2008(b) used electrical resistance tomography to study the formation of caverns during the mixing of pseudoplastic fluids possessing yield stress (xantham gum). Significant cavern growth was seen during the transitional regime and gave good experimental agreement with Elson and Cheesman, 1986, cylindrical model when the cavern did not interacted with the tank walls.

Ein-Mozaffari *et al.,* 2007, and Hui *et al.,* 2009 used ultrasonic doppler velocimetry UDV to measure cavern sizes in a pulp suspension. UDV uses a single probe to

transmit and receive ultrasonic signals, these are reflected back by the fibres. From these reflections the velocity of the fibre can be determined and by measuring at different locations until a zero velocity is recored the cavern boundary can be found. Ein-Mozaffari *et al.,* 2007, cavern measurements agreed well with the spherical cavern model developed by Amanullah *et al.,* 1997.

Hui *et al.,* 2009, compared UDV to ERT and found the measurement accuracy to be much better but the processing time was also much longer. ERT also measured larger cavern volumes than UDV, with UDV under predicting the location of the cavern boundary. This was attributed to the image reconstruction technique for UDV, even so the differences in volumes were only 10%. Amanullah *et al.,* 1997, models produced the best agreement with the cavern data, even though the shape of cavern was somewhat cylindrical. Elson and Cheesman, 1986, cylindrical model under predicted the cavern volumes, this was attributed to the fact that this model does not contain an axial force component. The large discrepancy between the cavern prediction models and the experimental techniques was found to be due to the cavern interaction with the walls of the tank.

2.3. Computational Fluid Dynamics

Computational Fluid Dynamics (CFD) is a powerful tool for exploring mixing systems since almost anything can be simulated and little to no experimental work is required. Almost anything that can be obtained through experimental techniques can be extracted from a correctly simulated system (Mann *et al.,* 1995; Kukura *et al.,* 2002). Again most

CFD has been performed on Newtonian fluids since the viscosity of these fluids is constant and so the Navier Stokes equation can be more easily solved.

2.3.1. Newtonian Simulations

Ranade and Joshi, 1989(b), used a technique called FIAT (which uses SIMPLE, semi-implicit algorithm pressure linked equation) to simulate the flow patterns generated by a pitch blade turbine. This was the first time this code was used and was found to agree reasonably well with experimental data, but the axial velocities below impeller were over predicted. Hutchings *et al.,* 1989, used the commercial CFD software FLUENT model the flow fields of both a Rusthon turbine and axial impeller. The k-ε turbulence model was used to handle the turbulent flow structures and only a 2D model of the tank was simulated due to limited computer resources. Experimental data from LDV was used as boundary conditions for the impeller region, thus this region is not simulated. Using all these techniques yielded good comparison with the overall flow patterns obtained from the experimental data.

Ranade *et al.,* 1991, also used the k-ε turbulence model to measure the flow of a down pumping pitch blade turbine. The simulations showed good comparison with the experimental data. Bakker and van den Akker, 1994, was able to model the micro mixing of a Rusthon turbine to predict the yield of a chemical reactor, but all the micromixing models over predicted the yield. Bakker and Fasano, 1994, measured the mixing times and chemical distributions in a vessel stirred by a Rusthon turbine, both factors were well predicted. Schofield, 1994, used another CFD program called PHOENICS to simulate the transient tracer dye diffusion in a stirred tank with a

Rusthon turbine. By using the k-ε turbulence model the simulations agreed well with experimental visualisations.

Sahu and Joshi, 1995, used SIMPLE and the k-ε turbulence model to simulate an axial impeller in a stirred tank. Predicted values were in good qualitative agreement with the experiments and were able to predict most of the flow patterns. Harvey III *et al.,* 1995, used another technique called multiblock incompressible Navier-Stokes solver to measure the flow field induced by a pitch blade turbine. The radial and axial components were in good agreement at low Reynolds number (Re < 21) with the tangential velocities differing by 25% near the impeller. Ranade and Dommeti, 1996, used FLUENT to simulated the mixing of a pitch blade turbine without using any experimental data as boundary conditions near the impeller. Both a good qualitative and quantitative agreement with experimental data was achieved and showing for the first time the correctly simulated flow characteristics in the impeller swept volume.

Eggels, 1996, was the first use of large eddy simulations (LES) to study the turbulent flow generated by a Rusthon turbine. LES simulations provide much more detailed data than the standard CFD simulations that use Reynolds Averaged Navier Stokes (RANS) as they are computed on a much finer grid and are able to resolve turbulent flow structures and instantaneous flow characteristics but are much more computationally expensive. Both the mean flow and turbulence intensities were found to be in good agreement with known experimental data. Ciofalo *et al.,* 1996, used two turbulence models to measure the flow and free surface of an un-baffled tank with a radial impeller. Poor predictions were obtained with the k-ε turbulence model but the differential stress turbulence model agreed well with experiments. Xu and McGrath, 1996, showed that

there is little difference between simulations using experimental data in the impeller region and ones that use a prediction model to measure the flow of a pitched blade turbine. This allows simulations to be carried out without the need for experimental input, this does not mean that experiments should not be carried to confirm the simulations are correct just that a simulation can be run without any prior data.

Armenante and Chou, 1996, used FLUENT with experimental data in the impeller region and two different turbulence models to predict the flow of one and two pitch blade turbines. The algebraic stress model showed better agreement with experiments than the k-ε turbulence model. Bakker and van den Akker, 1996(a), used a new lagrangian CFD model to measure the yield of a reactor in turbulent conditions and found when the feed was simulated far away from the impeller the predictions of the yield were very good. Bakker *et al.,* 1996(b), used current CFM (computational fluid mixing) software to measure the flow patterns in the laminar and turbulent regimes using a pitch blade turbine. Laminar predictions were very good when correct velocities are used on the boundary conditions surrounding the impeller. The turbulent simulations however only predicted some of the flow structures, drastically under predicting the turbulence.

Ranade, 1997, used FLUENT to simulate the laminar and turbulent flow generated by a Rusthon turbine without using any experimental data as boundary conditions. The simulations showed good agreement with experimental data for a wide range of Reynolds numbers and the flow in the impeller region was also captured. Jaworski *et al.,* 1997, used a sliding grid to simulated the laminar flow of a rusthon turbine. A sliding grid is where the tank is split into two regions, one remains stationary while the

other rotates, mimicking the rotation of the impeller. Flow patterns and power numbers obtained showed good agreement with experimental data without the need for experimental data input. Hobbs and Muzzio, 1997, used FLUENT to measure the flow at low Reynolds through a kenics static mixer, particle tracking was also completed obtain a prediction of the residence time distribution. The mixing characteristics simulated showed good agreement with reported experimental data.

Revstedt *et al.,* 1998, also used LES to simulate flow fields generated by a Rusthon turbine and found good agreement with experimental data. There are some discrepancies however in the impeller region caused by an inadequate description of the impeller. Brucato *et al.,* 1998, used three modelling approaches to simulate the flow field of a single and dual Rusthon turbine and an axial impeller. Impeller boundary conditions gave satisfactory results if reliable empirical data are known. The inner-outer method gave quite good results for flow and turbulence, being more accurate than the impeller boundary conditions technique but more computationally demanding. The inner-outer method uses two overlapping regions in the simulations, one containing the impeller and the other containing the tank wall and baffles. One region is solved first, the overlapping data are then used to solve the other region, and the data are passed back and forth until no difference is obtained. The sliding grid however gave the best agreement concerning flow patterns but under predicted the turbulence. This method however is the most computationally demanding but can be used to obtain transient simulations.

Zipp and Patterson, 1998, simulated the conversion rate of a chemical reaction with a Rusthon turbine, the results agreed well with the experimental data. Sheng *et al.,* 1998,

used RANS to simulate the flow of an axial impeller using two turbulence models, using experimental boundary conditions on the impeller. Flow fields were very similar for both the k-ε RNG and the Reynolds stress model, however the turbulence values widely different. Naude *et al.,* 1998, used the multiple frames of reference technique (MFR) with an unstructured mesh to simulate the flow of a complex impeller type in turbulent flow. MFR uses the sliding grid technique but the rotating grid does not move, instead each element has a tangential velocity, allowing fast steady state simulations. Pumping and power numbers obtained agreed well with experimental data.

Wechsler *et al.,* 1999, used RANS with the k-ε turbulence model to complete steady and unsteady simulations of a pitch blade turbine. There was good agreement between the steady and unsteady simulations, even though the steady state simulations only require a fraction of the time and computational expense. Ducoste and Clark, 1999, used a new CFD technique called FIDAP (fluid dynamics International, Evanston, IL) to simulate flocculator fluid mechanics with a Rusthon turbine and an A310 foil impellers. Reasonable agreement was found with experimental data for both impellers. Derksen and van den Akker, 1999, used LES to simulate the flow of a Rusthon turbine, the turbulent kinetic energy was well predicted but the impeller outflow was not.

Osman and Varley, 1999, used fluent in conjunction with a pre-processing software MIXIM to perform a finite volume simulation of the flow generated by a Rusthon turbine and found that the mixing times were twice that of the experimental data, but the tracer movement was well simulated. Barrue *et al.,* 1999, used FLUENT to simulated the particle trajectory in a stirred tank with a Rusthon turbine in turbulent flow. The particles lagrangian trajectory match well with experimental results. Sahu *et al.,* 1999,

simulated five different axial impellers used a technique called zonal modelling, turbulence was modelled using the k-ε turbulence model. Lamberto *et al.,* 1999, used FLUENT to simulate the laminar flow in an un-baffled tank with a radial impeller, the computational results where validated with experimental data.

Aubin *et al* 2000, also used FLUENT software in conjunction with SIMPLE to simulate the laminar flow of viscous glucose stirred by a helical screw with and without a draft tube, the use of the draft tube showed more efficient circulation. Verzicco *et al.,* 2000, used direct numerical simulations (DNS) to measure the flow induced by an 8 bladed paddle impeller. DNS is the most computationally demanding CFD technique since an extremely fine grid has to be used to complete the simulations, but it does give much better data than both LES and RANS. As the name implies, DNS directly solves the Navier Stokes equations by using an extremely fine grid. However DNS can only be used to simulate fairly small Reynolds numbers due to computational expense. Unsteady flow patterns were obtained despite a low Reynolds number of 1636, but the results obtained matched well with some LES simulations, RANS however does not detect these unsteady flow patterns as a steady state solution is forced. The DNS simulations do not match the experimental data due to only 1/8th of geometry was simulated and thus has a forced symmetry. DNS would require over 40 revolutions to obtain the overall averaged flow field and thus would take a long time to simulate, however RANS directly obtains it.

Harvey III *et al.,* 2000, simulated the mixing times and isolated mixing regions by allowing 10^4 passive particles allowed to move through one period of flow. This technique gave very accurate results when compared with direct particle integration at a

fraction of the computational cost. Brucato *et al.,* 2000, simulated a mixing sensitive parallel reaction in stirred tank with a Rusthon turbine. Good comparison with experimental results at low impeller speeds and the selectivity of the reaction process was also well predicted. Revstedt *et al.,* 2000, used LES to measure the flow generated by dual radial impellers of two different types. Data was similar for both types of impellers at the same power input, but at equal impeller speed the Rusthon turbine gave higher velocities and volumetric flow.

Jaworski *et al.,* 2000, used FLUENT to understand the degree of homogenisation for a dual Rusthon turbine stirred tank. The sliding grid technique was used along with two different turbulence models. The k-ε turbulence model gave the most accurate simulations but the predicted mixing times were two to three times longer than experimental values. Fountain *et al.,* 2000, simulated the flow fields in a stirred tank caused by a disc turbine using FLUENT. Nere *et al* 2001, used the impeller boundary condition approach in the turbulent regime to simulate the flow fields generated by multiple impellers. A new model for predicting the eddy viscosity was developed that gave much better predictions for all three velocity components, turbulent kinetic energy, energy dissipation and power numbers.

Montante *et al.,* 2001(a) and Montante *et al.,* 2001(b), simulated the flow generated by a rusthon turbine using both the sliding grid technique and the inner-outer method. Flow patterns are predicted well, especially at high impeller clearances, at low clearances the flow in the upper part of the tank agrees well with experiments. The change of flow pattern when the clearance is changed happens at the same locations as the experiments. The simulations predicts most poorly in the impeller region, also there was little

difference between the sliding grid and inner-outer methods. Lamberto *et al.,* 2001, used FLUENT to simulate lagrangian particle tracking in an un-baffled tank with a radial flow impeller. The particle showed the poorly mixed regions seen in experiments and once the particle entered one of these zones it remained there indefinitely. A complex internal structure of these poorly mixed regions was extracted. The mean velocities were well predicted but were less accurate when only a single loop was present, also the discharge angle was over predicted for these cases.

Jayanti, 2001, simulated jet mixing in cylindrical vessel and found that having a conical bottom reduces and removes some of the dead zones, and thus reducing the mixing time. Derksen, 2001, performed LES with a pitch blade turbine in the turbulent regime and found that a mesh of size 360^3 agreed the best with the experimental data. Ranade *et al.,* 2001, used FLUENT to measure the trailing vortices of a Rusthon turbine using two different turbulence models. A satisfactory agreement was found when compared with experimental data, with the k-ε turbulence model predicting the turbulence much better than k-ε RNG turbulence model.

Patwardhan, 2001, found that the simulated residence time distribution of a down pumping pitch blade turbine matched well with experimental results. Mavros *et al.,* 2001, simulated a new agitator called Narcissus using the MFR approach and an unstructured mesh. An original flow pattern was obtained and was validated by experimental results. Lyungqvist and Rasmuson, 2001, used another commercial CFD package called CFX4 to model the two-phase flow fields in an axially stirred vessel. Good agreement was found with the axial slip velocities and turbulent kinetic energy difference between each phase. However the radial and tangential velocities were

greatly under predicted, but the overall flow fields showed good comparison with experimental data.

Jones *et al.,* 2001, tested six different two-equation turbulence models on flow in an un-baffled tank with paddle impeller. The radial velocities in the impeller discharge stream were over predicted by all models while tangential velocities were predicted well by all models expect near the shaft. The low Reynolds k-ε turbulence model was the only one to predict the kinetic energy well in the discharge stream, but all models were able to qualitatively predict the circulation patterns well. Sun *et al.,* 2002, simulated the flow created by a Rusthon turbine using the inner-outer technique with the anisotropic algebraic stress model to handle the turbulence. This new turbulence model gave better predictions than the standard k-ε turbulence model, showing good turbulent flow field comparisons with experimental data. Revstedt and Fuchs, 2002, used LES to simulate the flow in a stirred tank using single and multiple impellers of various types. Good agreement was obtained with experimental data and other simulations.

Murthy Shekhar and Jayanti, 2002, simulated the flow field of an 8 bladed paddle impeller in the laminar, transitional and turbulent flow regimes using the sliding mesh approach. The k-ε turbulence model predicted flow and turbulence near the impeller well but the low Reynolds k-ε turbulence model gave better predictions away from the impeller, meaning that the flow in the vessel is not fully turbulent. Power numbers measured in the laminar regime matched well with experimental data but the mixing times did not. Overall the low Reynolds k-ε turbulence model provided the better comparison with experimental results.

Bartels *et al.,* 2002, compared DNS simulations and RANS simulations of flow in a stirred vessel using a Rusthon turbine, the RANS use the k-ε turbulence model. DNS gave much closer results to experiments but the computational power and time were extremely large. Whereas the RANS simulations still gave relatively accurate predictions despite the much simpler and less time consuming model. Bhattacharya and Kresta, 2002, used the MFR technique alongside the k-ε turbulence model to simulate the flow at the wall when using a pitch blade turbine. Circulation patterns and velocity profiles of the jets matched well with experimental results. Zalc *et al.,* 2002, simulated the flow patterns generated by the three Rusthon turbines and found good agreement with experimental data when using particle tracking methods. The flow present is partially chaotic and contains large areas of poor mixing, increasing the Reynolds number does not yield more efficient mixing. Alvarez-Hernández *et al.,* 2002, also simulated the flow of three Rusthon turbines.

Bujalski *et al.,* 2002(a), used FLUENT to simulate the flow of a dual Rusthon turbine in the turbulent regime. The sliding grid method along with MFR was used and two turbulence models were tested. The power number predictions were improved compared to earlier attempts. Bujalski *et al.,* 2002(b), used FLUENT to measure the mixing times of a Rusthon turbine. The sliding grid was used along with the k-ε RANS turbulence model. Position of feed point of tracer is of high importance for simulations, related to its proximity to the sliding mesh boundary. Some of the simulations were able to almost predict the mixing times obtained from experiments. Kovács *et al* 2003, used FLUENT to simulate the mixing of a viscous Newtonian fluid in a Lightnin 45 static mixer. Particle tracking simulations were preformed to measure the degree of mixing.

Campolo *et al.,* 2003, used the RANS approach with the k-ε turbulence model to simulate the flow of a Rusthon turbine in a stirred tank by simulating a dispersion of fluid particles. Satisfactory agreement was achieved with experimental data concerning the flow fields. The fluid particles showed that mixing proceeds differently in the lower and upper parts of the tank. Khopkar *et al.,* 2003, aimed to simulate with FLUENT 4.5 the gas-liquid flow in a stirred vessel with a down pumping pitch blade turbine with the k-ε turbulence model.   Simulations accurately predicted flow patterns shown in experiments and the decrease in pumping efficiency with aeration, however the axial velocities and turbulent kinetic energy are over predicted near the impeller.

Yeoh *et al.,* 2004(a), used both LES and RANS to simulate the flow of a Rusthon turbine in turbulent flow using a sliding deforming mesh. This uses a similar approach to the sliding gird, except the mesh at the interface deforms during rotation, once deformation is too great the mesh is reset and then deforms again.   Very good quantitative and qualitative agreement was shown between LES and experimental data. LES is substantially better at predicting mean velocities and turbulence values than RANS but takes substantially longer to compute. Hartmann *et al.,* 2004(a), also used LES to study the flow in a stirred tank caused by a Rusthon turbine, concerning the frequency of the mean flow variations.

Bakker and Oshinowo, 2004, used LES to predict the large-scale chaotic structures in stirred tanks generated by multiple impeller configurations.   Pitch blade turbine simulations agreed well with PIV experimental data from earlier papers and the Rusthon turbine simulation compared well with earlier LES simulations. LES is able to predict rich structures of turbulent flow however it is 1 to 2 orders or magnitude more time

consuming that RANS. Yeoh *et al.,* 2004(b), did some further LES work on Rusthon turbines using a sliding deforming mesh and found that it was able to accurately simulate the complex 3D turbulent flow structures. Szalai *et al.,* 2004, simulated the mixing performance of 4 Ekato Intermig® impellers in laminar flow. The computational flow patterns matched well with the experimental data.

Montante and Magelli, 2004, completed some RANS simulations of the homogenisation of a multiple Rusthon turbine tank at various different spacings. Good prediction of the time evolution of the tracer dispersion, mixing times and flow patterns was achieved at all the different impeller spacings. Micheletti, 2004, simulated the flow of a Rusthon turbine to obtain the energy dissipation rates in the vessel. Hartmann *et al.,* 2004(b), compared LES and RANS simulations of a stirred tank with a Rusthon turbine and found that LES gave much better results than RANS. Phase averaged flows were in good agreement with experimental data but all simulations over predicted the velocities at the impeller tip. LES can provide more turbulent data than RANS due to the fact that the flow is not averaged. Yeoh *et al.,* 2005, used LES with the sliding mesh to simulate the mixing of an inert scalar in a stirred vessel with a rusthon turbine. It was found that this technique can characterise the mixing state in a stirred vessel and the detailed evolution of a concentration field. Substantial amount of tracer is trapped between two baffles at the height of the impeller but still good agreement of mixing times with predictive equations was obtained.

2.3.2. Shear Thinning Simulations

Some CFD has been performed on shear thinning non-Newtonian fluids, these are fluids that decrease in viscosity with increase in shear rate. Aubin *et al* 2000, used the FLUENT software and SIMPLE to study the laminar flow of two shear thinning fluids, Carbopol and natrosol, stirred by a helical screw impeller with and without a draft tube. The draft tube provided better circulation and the axial velocities were less significant for these shear thinning fluids when compared to the mixing of a Newtonian fluid. Kelly and Gigas, 2003, also used FLUENT in the laminar regime to model the mixing a shear thinning Carbopol solution stirred by an axial impeller. Power numbers were predicted with 5% of experimental values and were found to be a function of Reynolds number and flow behaviour index. The discharge angle from the impeller was also well predicted when compared with experimental flow patterns.

Kovács *et al* 2003, used FLUENT to study the mixing of a shear thinning fluid flowing through a Lightnin 45 type static mixer. Particle tracking was also simulated to measure the degree of mixedness of the static mixer. No difference was seen after 4 elements of the static mixer when compared with Newtonian fluid data for Reynolds below 10. However at a Reynolds of 100 the shear thinning fluid generated secondary motion creating better mixing. Montante *et al.,* 2005, simulated the mixing of a shear thinning fluid with multiple pitch blade turbines. A passive tracer was used to estimate mixing times and the values obtained matched well with experimental results.

2.3.3. Yield Stress Simulations

Some CFD has been performed on yield stress non-Newtonian fluids, these are fluids only flow once the shear stress of the fluid is above the yield stress of the material. Balhoff and Thompson, 2004, simulated the flow of a yield stress fluid in a packed bed using a network model. Comparison with experimental data showed good agreement with Bingham Plastic Fluids but not Herschel-Bulkley materials. Couerbe *et al.,* 2008, simulated the mixing of a thixotropic shear thinning fluid with a yield stress in a tank stirred with an axial impeller by using the commercial CFD code CFX 10. The viscosity used in the simulations used two shear dependent laws, on for high shear rates and one for low shear rates. Good quantitative comparison was achieved when comparing against experimental results, however near the impeller at low speeds the prediction became quite poor. This was attributed to the experimental data obtained from PIV that is unable to measure slow speeds very accurately.

Pakzad *et al.,* 2008(a), simulated the xanthum gum mixed by a Scaba 6SRGT impeller in the laminar regime using FLUENT and MFR. The velocity profiles agreed well with UDV experimental data also the simulated power numbers were predicted well. The simulated cavern data also agreed well with Elson and Cheesman, 1986, cylindrical cavern model. Pakzad *et al.,* 2008(b), studied the cavern formation of a shear thinning fluid possessing a yield stress for a radial flow scaba 6srgt impeller using FLUENT. Simulations agreed well with experimental data and theory and that significant cavern growth was seen in the transitional regime. Also the simulations seem to suggest for this material the laminar model can be used for Reynolds numbers up to 200.

2.4. Mechanistic Cavern Models

Models have been developed to try and predict the size and shape of caverns developed during the mixing of yield stress materials at low Reynolds numbers. Solomon, *et al.,* 1981, developed a spherical cavern model by equating the torque on the shaft to the torque on a sphere. The model agreed well with experimental data obtained and was found to be able to predict the apparent yield stress of materials if they are highly pseudoplastic. Elson and Cheesman, 1986, then developed a right angular cylinder using the same approach as the Solomon spherical model. Good agreement was found with the experimental results and that cavern height increased with impeller speed at high Reynolds numbers. For low Reynolds numbers the cavern height to diameter ratio is approximately constant around a value of 0.4.

Amanullah *et al.,* 1998, improved on the earlier spherical cavern model of Solomon by basing the model on axial force as well as the tangential force. The new spherical model gave much better fits in both size and shape compared to the earlier models but was found to be highly sensitive to the yield stress. Dye injection experiments performed proved the existence of axial flows within the cavern, giving weight to the new approach of incorporating the axial force.

Wilkens *et al.,* 2005, developed a brand new toroidal model by equating the torque, similar approach to the much earlier Solomon model, predictions of cavern height and diameter were well within experimental uncertainty. However at higher Reynolds numbers the model under predicted for axial impellers since axial forces were becoming more dominant. Hui *et al.,* 2009, developed a model to incorporate tank wall

interactions and a side entering impeller. New model predicted better than earlier models but was found to be very sensitive to the yield stress.

Since shear thinning fluids can generate pseudo caverns, Amanullah *et al.,* 1998, developed both spherical and toroidal pseudo cavern models based on the idea of estimating the velocity at the cavern boundary. The toroidal model predicted well above Reynolds numbers of 20, agreeing within 10% when the torus shape was well developed. The value of the velocity of the cavern boundary was found to be only slightly sensitive, with a value of 0.001ms^{-1} used. The experiments performed however were on a yield stress material force fitted to the power law model, thus not a proper comparison of pseudo cavern data

CHAPTER 3

EXPERIMENTAL AND THEORETICAL METHODS

3.1. Experimental

3.1.1. Mixing Rigs

Two rigs were used for the whole of the experiments conducted in this study; a small glass stirred tank was used for the PLIF experiments and the PEPT experiments of all fluids and a larger Perspex stirred tank was used for another set of PEPT experiments for the fibre suspension. Figure 3.1 shows the common dimensions used to describe a stirred tank and Table 3.1 shows the values of these dimensions for both tanks. Where T is the tank diameter, H the liquid or suspension height, D the impeller diameter, C the impeller off-bottom clearance and B the baffle width. The tanks are cylindrical and have four evenly spaced baffles, and are stirred by a centrally fitted 6 bladed 45 degree pitched blade turbine (PBT).
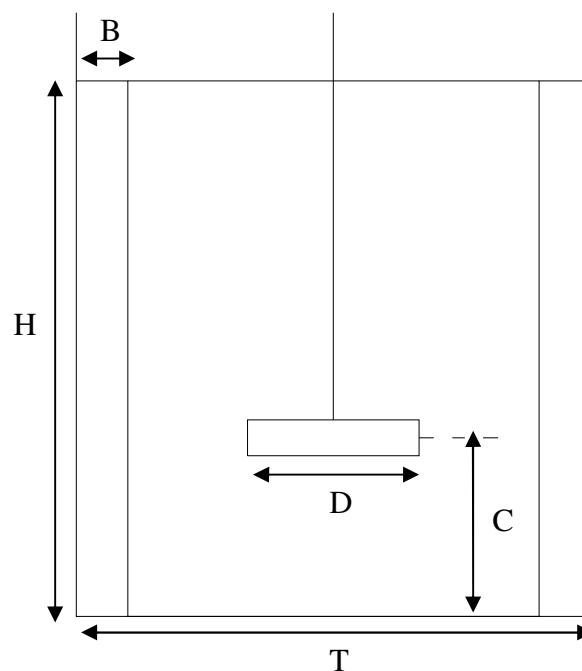
Figure 3.1 Representation of tank with common dimension symbols

Table 3.1 Dimensions of the two sizes of tanks used for experiments

Tank	T	H	D	C	B
Small	148mm	148mm	50mm	50mm	14.8mm
		T	0.34T	0.34T	0.1T
Large	287mm	287mm	144mm	95mm	28.7mm
		T	0.5T	0.33T	0.1T

Three different impellers were used for the experiments, two for the small tank and one for the large tank. One of the small tank impellers was used for the Carbopol PLIF experiments only, with the second small impeller used for all the small tank PEPT experiments. The dimensions of the three different diameter impellers are described below in Figure 3.2 and the values are given in Table 3.2. Where D_{Hub} is the hub diameter, D_{Shaft} is the shaft diameter and W is the hub height.
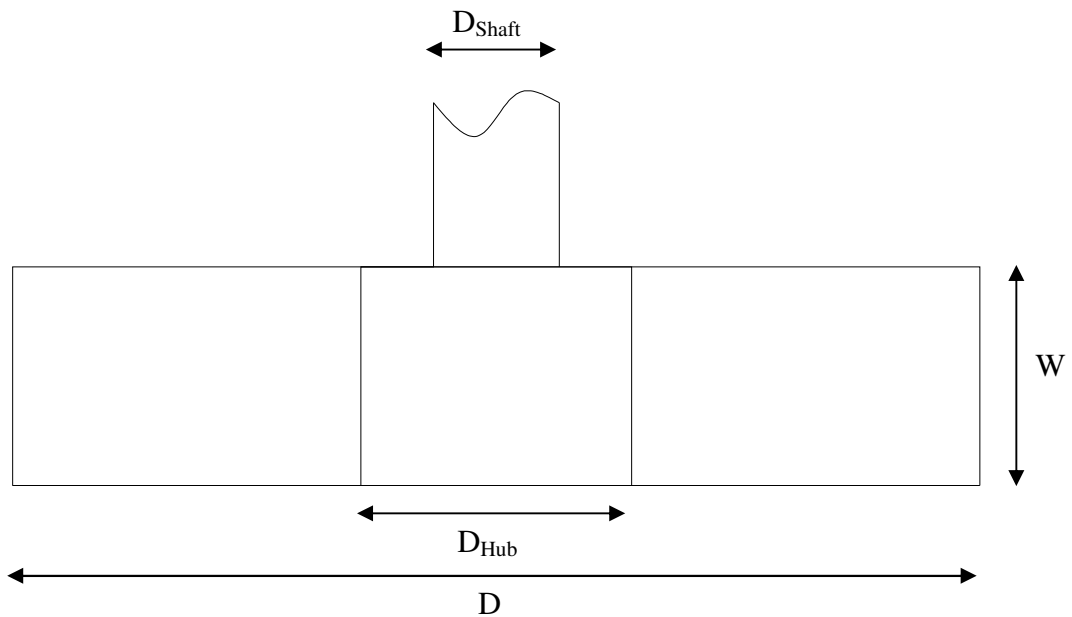
Figure 3.2 Representation of impeller with common dimension symbols

The small impeller used for the Carbopol experiments hub was spherical while the hub for the other small impeller and the large impeller was hexagonal with a blade projecting from each of the hexagons sides. Thus the hub diameter for the hexagonal

hub impellers is the perpendicular distance between two of the parallel sides shown in Figure 3.3.
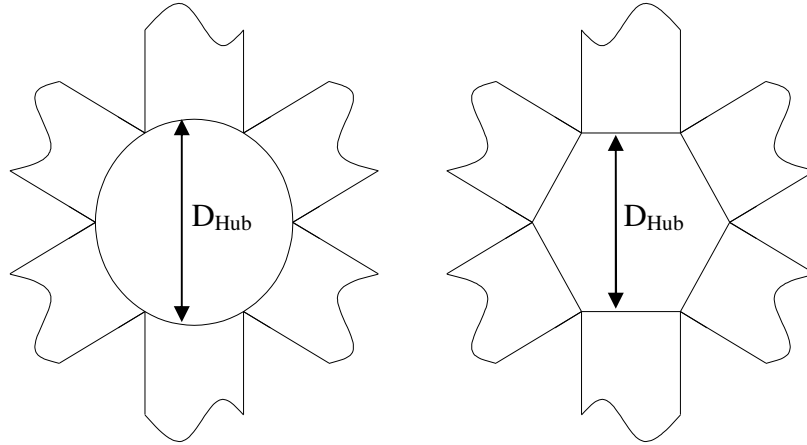
Figure 3.3 Spherical and Hexagonal hubs showing diameter definition and blade array

Table 3.2 Dimensions of the two sizes of impellers used for experiments

Impeller	D	D_{Hub}	D_{Shaft}	W	Blade Thickness
pbtC	50mm	14mm	6.5mm	10mm	1mm
		0.28D	0.13D	0.2D	0.02D
pbtS	50mm	21mm	8mm	10mm	1mm
		0.42D	0.16D	0.2D	0.02D
pbtL	144mm	37mm	19mm	28mm	2.5mm
		0.26D	0.13D	0.2D	0.017D

3.1.2. Materials and characterisation

3.1.2.1. Carbopol

3.1.2.1.1. Description

Carbopol is a white powder polymer material and can be added to water to create a transparent shear thinning material with a yield stress, in this work a 0.1 wt% aqueous solution of Carbopol 940 was used. To prepare the solution the Carbopol is slowly added to the continually agitated water, once all material has been added the solution is left to mix until fully dissolved. At this point the solution is slightly opaque and has

little non-Newtonian behaviour. Only when the pH has been altered to 4.6 by the addition of sodium hydroxide the solution then becomes a fairly transparent Herschel-Bulkley material. Different pH values around 4.6 will lead to different non-Newtonian rheology but if it is made much more acidic the fluid becomes thinner, losing most of its non-Newtonian behaviour. Due to the yield stress of this material the pH is only altered once the solution is transferred into the tank. This avoids the entrapment of air bubbles when moving from the preparation container to the mixing container. The sodium hydroxide is added slowly to the eye of the vortex in the mixing tank to allow thorough dissipation. If added to a stagnant surface, only the surface of the Carbopol solution would be altered and become too thick to alter the rest.

3.1.2.1.2. Rheology

Since each experiment used a fresh aliquot and was pH altered separately the rheology for each run was slightly different. A sample was taken at the end of each run from the impeller region for rheological characterisation. The results from the rotational viscometry are shown in Table 3.3, Reynolds numbers shown are the values of the sample when run in the mixing equipment.

Table 3.3 Rheological data for Carbopol experiments

Re	τ_y (Pa)	k (Pa.s^n)	n
7.3	2.63	0.54	0.56
20.4	1.41	0.37	0.57
70.3	1.29	0.35	0.57
86.6	1.56	0.45	0.55
163.2	1.97	0.37	0.58

3.1.2.2. Cosmetic Foundation Cream: Sample 1 and 2

3.1.2.2.1. Description

The foundation cream used was supplied by Proctor and Gamble. Two samples were used in this work, with slightly different rheological characteristics as described below in the next section. They are a cosmetic material and are used on the skin, and thus they are an opaque highly concentrated suspension of very fine particles. They exhibit a shear thinning behaviour with a yield stress and the average density of both samples was 1100 kgm^{-3}.

3.1.2.2.2. Rheology

From some early testing of the rheology of both foundation creams, they were found to have a viscosity that reduces with time. This was proven through repetition of the rheological characterisation of the same sample and a constant shear rate test. As shown in Figure 3.4 the viscosity dropped with time for both materials, and thus a method is needed to estimate the rheology of the material.
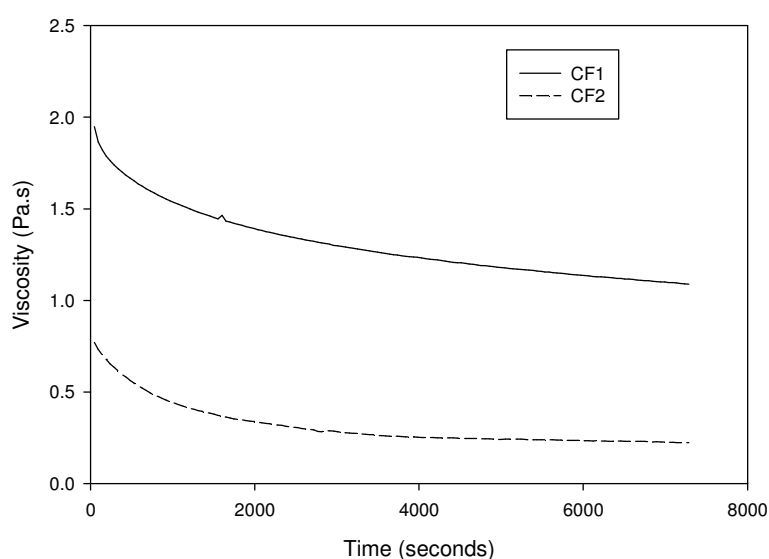
Figure 3.4 Constant shear rate over time of foundation cream

It was decided to take a sample of the cream from the impeller region before each experiment whose rheology was immediately measured. Since the material also degraded with time without shear the rheological measurements was conducted at the same time as the experiment was carried out. Each sample was shear stress ramped up and down six times; the data used for every experiment was the fourth up ramp of stress as this reading would be taken halfway through the PEPT experiment and thus would result in the average rheology of the experiment. Each ramp was done in sixty seconds to try and measure the instantaneous rheology rather than its steady state rheology. An example of one of the ramps is shown below in Figure 3.5 for both samples, showing the direction of the ramping. This again shows the drop in viscosity over time of this material as the down ramp is below the up ramp. Another observation of note is the difference in the two materials; sample two is much thinner than sample one.
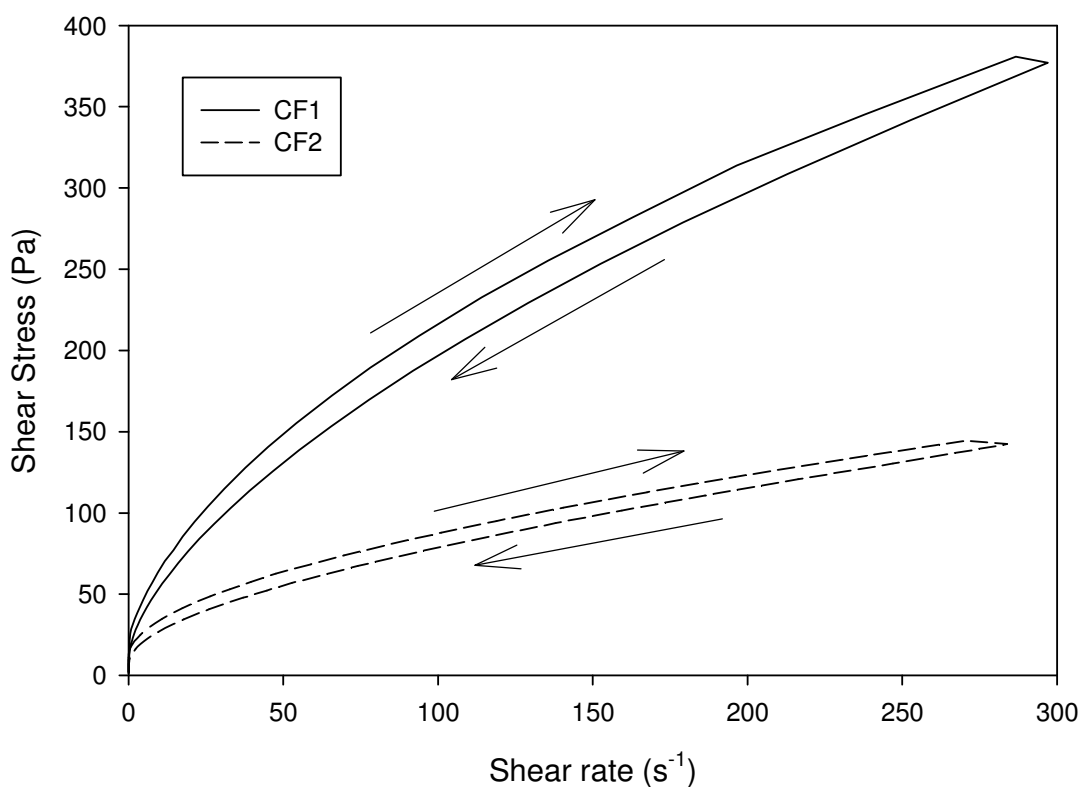
Figure 3.5 A single shear rate ramp for foundation cream

To further illustrate the time dependency of the material, Figure 3.6 shows a complete rheological experiment including all six ramps. As the experiment progressed the ramps moved further to the right, indicating a drop in viscosity between each ramp. For each successive run the rheological plots for both materials moved further to the right, thus becoming thinner and thinner. One particular thing to note is that sample one by the end of the experiments started to stabilise in its results pointing towards a complete breakdown of any time sensitive structure. Sample two however continued to degrade right to the last experiment; this may lead to the conclusion that sample two has a much more complex and robust structure requiring further shearing to remove any time dependant rheology.
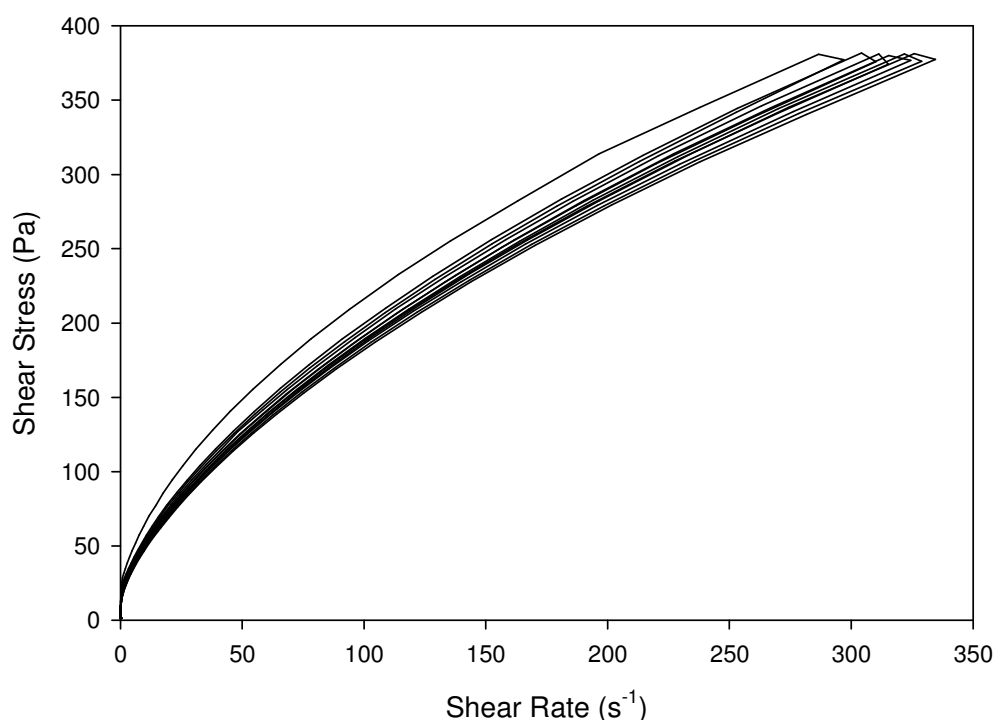
Figure 3.6 Full shear ramp experiment of CF1

From these curves both foundation creams were fitted to the Herschel Bulkley model and the parameters are shown in Table 3.4 and Table 3.5 at its impeller speed, Reynolds

number and direction of pumping. The fourth up ramp for each experiment was used to obtain these values, this was done as this ramp is in the middle of the rheological measurement and it is assumed that the sample is stable. Sample 1 as noted before is much thicker and so has a higher yield stress and consistency factor, however the flow behaviour index is comparable for the two. As the experiments proceed in the order presented the yield stress and consistency index drop while the flow behaviour index remains roughly the same for both samples.

Table 3.4 Rheological data for Cosmetic sample 1 (CF1)

Impeller Speed	Re	Pumping Direction of PBT	τ_y (Pa)	k (Pa.s^n)	n
100	1.16	PBTD	4.72	11.61	0.604
	1.14	PBTU	5.06	11.9	0.602
400	8.29	PBTD	5.29	11.59	0.607
	8.27	PBTU	5.35	11.49	0.609
650	16.35	PBTD	5.26	11.19	0.615
	16.67	PBTU	4.9	11.38	0.608
800	22.49	PBTD	4.52	10.8	0.617
	23.85	PBTU	4.68	10.36	0.613

Table 3.5 Rheological data for Cosmetic sample 2 (CF2)

Impeller Speed	Re	Pumping Direction of PBT	τ_y (Pa)	k (Pa.s^n)	n
60	1.31	PBTD	3.48[*]	4.93[*]	0.576[*]
	1.31	PBTU	3.48	4.93	0.576
250	10.86	PBTD	3.56	4.91	0.578
	12.30	PBTU	3.01	3.84	0.611
380	22.30	PBTD	2.85	3.94	0.606
	24.51	PBTU	2.45	3.37	0.622
460	33.46	PBTD	2.28	3.19	0.624
	35.19	PBTU	2.13	2.87	0.637

* Values used are same as for up pumping as rheological experiment failed

3.1.2.3. China Clay

3.1.2.3.1. Description

China clay is a white powder and when mixed with water can exhibit non-Newtonian behaviour; in this work the recipe used generated an opaque shear thickening material. The recipe consisted of 38.3%wt water, 61.3%wt PSD China Clay and 0.4%wt Dispex N40 (a dispersant) adjusted to a pH of seven using a sodium carbonate solution. The suspension was created by first adding the water to the Dispex to make sure the thick material was fully dissolved. The china clay was first passed through a blender to reduce the size of the lumps and aid in dissolving into the water. This fine china clay was then slowly added to the water a small amount at a time, mixing by hand until all was dispersed. Once all material was added a very strong sodium carbonate was slowly added to alter the pH to seven. Care was taken when measuring the pH as due to the nature of the material ion flow is restricted. Once the pH was correct the suspension was mixed with a helical ribbon impeller to keep the suspension stable. If left to rest the china clay settles to the bottom, therefore care must be taken in using the suspension as soon as it is made. The overall density of the material ended around $1400 \, \text{kgm}^{-3}$.

3.1.2.3.2. Rheology

Similar to the cosmetic suspension an early test on the china clay indicated that its viscosity reduced with time at a constant shear rate, this is shown in Figure 3.7, after around 1500 seconds (25 minutes) the viscosity seems to stabilize. The initial drop in viscosity could be contributed to the phase separation of the china clay material observed at the end of the rheometry. In the early stages a thin layer of liquid would form on the surface of the sample and thus give rise to reduced measured viscosity. As

the phase separation proceeded the layer of liquid would become thicker and continue to reduce the viscosity until the material is fully settled achieving a constant viscosity. Due to the long time frame however this could not be the only effect, constant shearing by the rheometer geometry would also cause a breakdown in the structure of the china clay sample. This structure would be the cause of the non-Newtonian and time dependant behaviour, so destroying this would also reduce the viscosity over time. This structure would slow down the phase separation of the material leading to a prolonged time for the viscosity to stabilise.
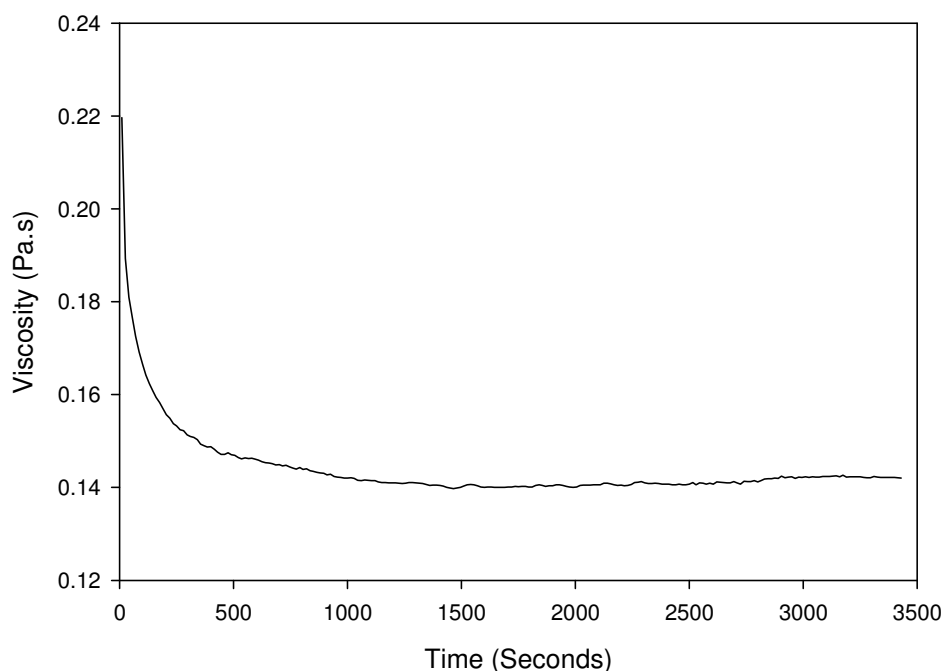
Figure 3.7 Constant shear rate over time of China Clay

In the initial part of the rheometry the viscosity drops drastically, so the same method of obtaining the rheological characteristics for the cosmetic suspension was used. Six ramps of shear stress, up and down, each sixty seconds to try and eliminate the time dependency were used. The sample was taken before each experiment from the impeller region and measured immediately. Figure 3.8 shows one such ramp of the

china clay, the time dependant behaviour is still present due to the down ramp being below the up ramp. Even so the curves of both ramps exponentially increase indicating a shear thickening rheology, i.e. the viscosity increases with shear rate.
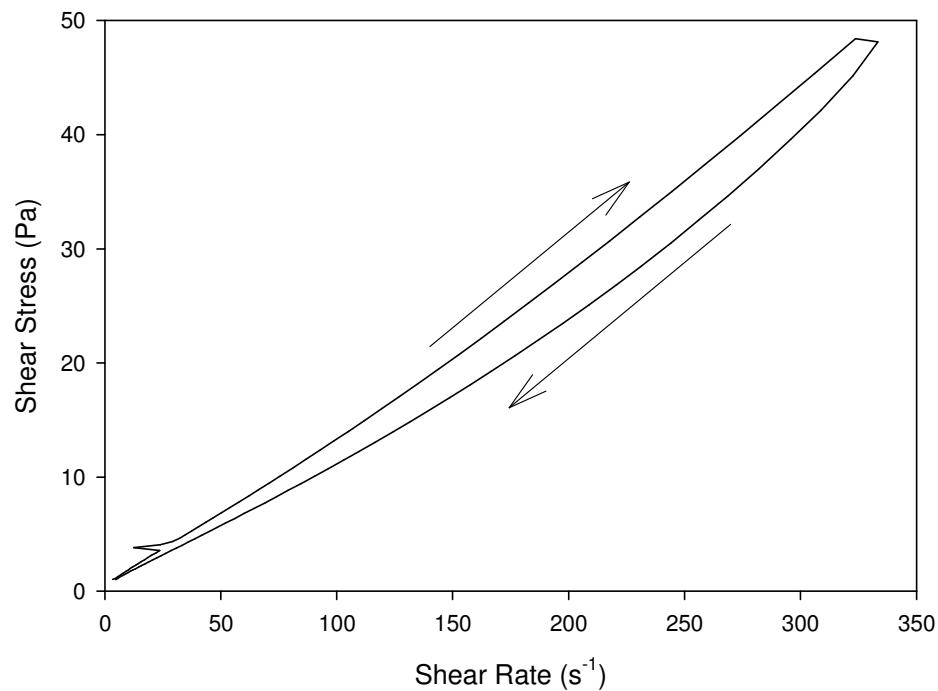
Figure 3.8 A single shear rate ramp for China Clay

Figure 3.9 shows a complete set of flow curves for one sample of the china clay, each progressive ramp moves further to the right, another indication of the thinning with time effect. The area of hysteresis however does not change very much after each ramp, indicating that even though the material is settling and the structure is being destroyed there is still a similar drop in viscosity after each ramp. Again similar to the cosmetic suspension the fourth ramp up was used to extract the rheological parameters for fitting to the Herschel Bulkley model.
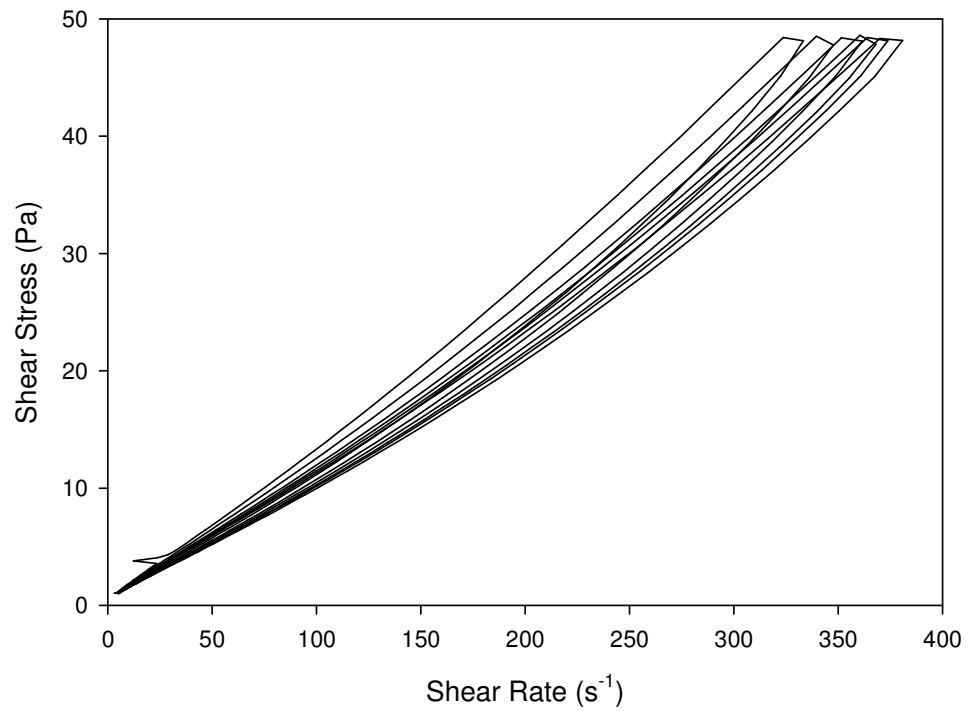
Figure 3.9 Full shear ramp experiment of China Clay
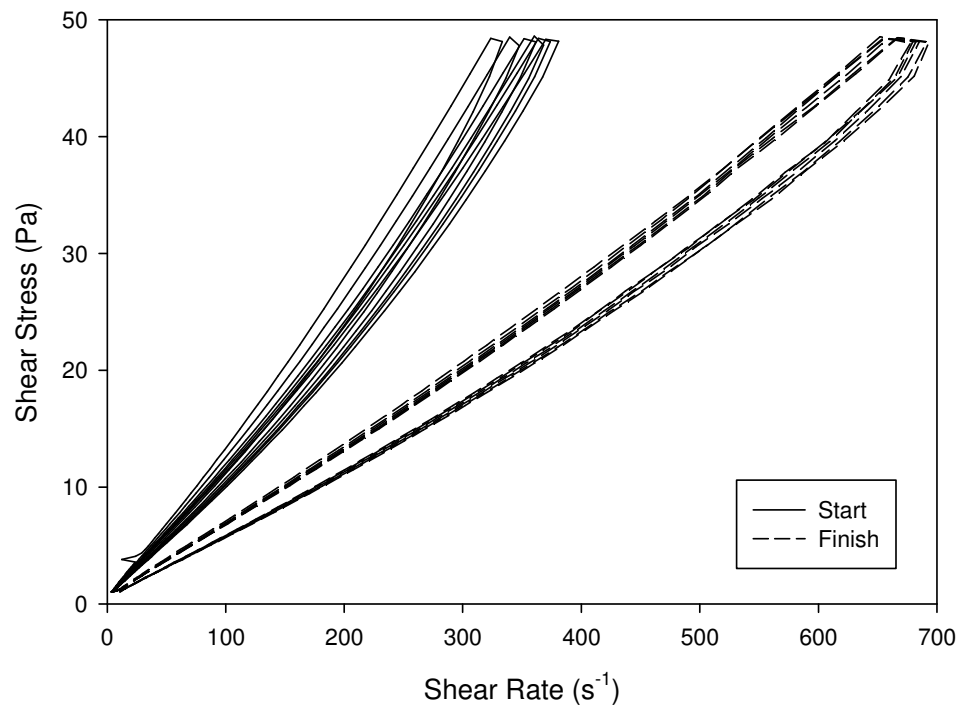
Figure 3.10 Two full shear ramp experiments for China Clay

Figure 3.10 depicts the flow map of the sample taken before the first and after the last experiment. By the last experiment the china clay had become much thinner but still retained its shear thickening behaviour. The six ramps now overlap each other, indicating that the irreversible shear thinning behaviour seen at the start of the experiments has mostly been removed due to the mixing incurred from all of the experiments.

Table 3.6 shows all the rheological data for the china clay, described by the Herschel-Bulkley model. The flow behaviour index remained roughly the same throughout the set of experiments while the yield stress and consistency factor dropped by a significant degree.

Table 3.6 Rheological data for China Clay

Impeller Speed	Re	Pumping Direction	τ_y (Pa)	k (Pa.s^n)	n
80	29.99	Down	1.24	0.045	1.18
	28.09	Up	1.22	0.0546	1.16
150	70.91	Down	1.2	0.0481	1.16
	69.20	Up	1.2	0.0495	1.16
400	237.75	Down	1.16	0.0421	1.16
	215.23	Up	1.18	0.0503	1.14
850	633.49	Down	1.06	0.0353	1.14
	767.93	Up	1.08	0.0293	1.14

3.1.2.4. Paper Pulp

The fibre suspension investigated in this work was paper pulp. The paper pulp was prepared by soaking sheets of roughly pressed paper in water. Once the paper was fully wetted it was shredded by hand into small strips and placed into a container full of

water of known volume a few sheets at a time. The concentration of paper pulp in this container was lower than needed around 1% w/w solids; this was done to help the fibres in the paper to disperse much easier. In order to destroy more of the structure a hand blender was introduced into this low concentration suspension. After a few minutes of blending the resultant paper pulp was sieved out and placed into a larger container. This was repeated until all of the sheets of paper needed were shredded. This damp mass of paper pulp was then made to a 3% w/w solids concentration and left to mix over night with a helical ribbon impeller. This final step helps give the suspension a good structure and overall homogeneity. The density of the suspension was 983 kgm^{-3}. No rheology data could be obtained due to the clumpy structure of the paper pulp. Any attempt at placing a sample of the suspension in a rheometer caused the water to be squeezed out once the geometry was lowered.

3.1.3. Rotational viscometry

Rotational viscometry is a technique that enables the measurement of the rheology of a fluid sample by the shearing it between rotating surfaces. For this work two types of geometries were used to measure the rheology of the fluids, a cone and plate geometry and parallel plate geometry shown in Figure 3.11.
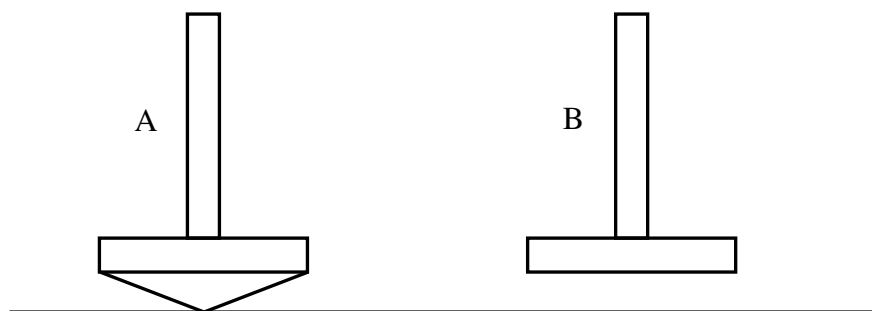
Figure 3.11 Types of rotational viscometer geometries; A - Cone and Plate and B – Parallel Plate

Both work by placing a small sample of fluid on a temperature controlled stationary surface, lowering the geometry to the required distance making sure that the fluid completely fills the gap with no overlap. The cone and plate geometry does not in fact touch the bottom as this would cause friction and therefore has a small gap around 100 microns. Cone and plate geometry is used for fluids that are completely homogenous or containing no particles larger than a tenth of the gap used. Parallel plate is used for more complex fluids containing particulates, setting the gap to at least ten times the largest particle size. For this work the cone and plate was used for the Carbopol solution and the parallel plate for both the shear thinning and shear thickening slurries. For the Carbopol rheometry the geometry was covered with a fine sandpaper to avoid slip at high angular velocities, this was not necessary for the parallel plate rheometry as the samples were viscous enough to prevent slip.

3.1.4. Positron Emission Particle Tracking (PEPT)

Positron emission particle tracking or PEPT is a technique that is able to track the position over time of a positron emitting particle, accurately and non-invasively, inside an opaque vessel or material such as in a high solid fraction solid-liquid pipe flow (Fairhurst *et al.*, 2001) and a non-Newtonian fluid in a stirred tank (Fangary *et al.*, 2000). This technique was used in this work to measure flow patterns and velocities during the mixing of the two shear thinning cosmetic foundation cream slurries, a shear thickening china clay slurry and a paper pulp suspension.

PEPT takes advantage of a positron emitting tracer; these positrons annihilate with a nearby electron releasing energy in the form of back-to-back 511 keV gamma-rays. By

detecting multiple emissions it is possible to triangulate the position of the tracer and its trajectory over time. Manipulation of this trajectory yields flow patterns and velocities within the flow being studied, this was done by a Matlab routine developed by Antonio Guida. The tracers are normally labelled with the radionuclide's ^{18}F, ^{61}Cu and ^{66}Ga with a radioactivity in the range of 300-1000µCi (Parker and Fan, 2008). The radioactivity has to be large enough to enable smooth tracking of the tracer at high velocities, if not high enough there would be few events over a large area and thus tracer motion is poorly detected.

This work used a tracer labelled with ^{18}F as it only emits gamma-rays with 511 keV so producing higher accuracy of detected locations. ^{18}F is made via the bombardment of purified deionised water with a 33MeV ^{3}He beam from a cyclotron, this radioactive water is then used to make the tracer via ion exchange with a resin particle (Fan *et al.*, 2006(a), Fan *et al.,*2006(b)). In ion exchange the ^{18}F exchanges with the counter ions in the resin beads causing them to have a radioactive level in the range of 350 to 1000 µCi with a half life of around 110 minutes. The tracer particle is then painted to ensure no radioactive material leaches out of the tracer when used in the experiments.

The PEPT experiments used two gamma-ray detectors each having an area of 51X38 cm^2, these detectors are set at opposite ends to one another with equipment to be studied in between as shown in Figure 3.12. The detectors are able to collect up to 10^5 events a second able to give a location to within 0.5 mm every 2 ms at speeds up to 2 ms^{-1} with reasonable tracking up to 10 ms^{-1} (Barigou., 2004). Gamma-rays are only recorded if both detectors collect them within 12ns of each other (Fairhurst *et al.*, 2001); a lot of

gamma-rays are lost due to the size and location of the detectors. Since gamma-rays are emitted in all directions two rectangular detectors either side of the equipment would only be able to capture a small portion of them. A detector that encompasses the entire equipment would provide more data, however would lead to difficulties with the running of the experiment, i.e. getting the equipment inside the detectors and having detectors big enough to encompass the equipment. Even with the limited detector coverage enough data are captured as well as giving easy access for large pieces of equipment to be investigated. Since the tracer is radioactive, fewer and fewer positrons are emitted as time goes by, so it is common practice to run the faster speed experiments when the tracer is young as this would enable the measurement of faster velocities much easier.

The painted tracer particles described above aim to match the flow of the fluid and thus need to be as neutrally buoyant as possible by changing the density of the fluid to match the tracer. For some cases it is impossible to do so without drastically changing the structure of the fluid. This neutrally buoyant tracer is also larger than most Kolmogorov eddy sizes but it is difficult to make a tracer at that scale and still have enough radioactivity to run an experiment. The tracer particle relaxation time was calculated for both the cosmetic foundation cream and china clay and was found to be 2 orders of magnitude smaller than the acquisition time. This means even though the liquid and particle densities do not match, the inertia of the particle is so small that it is already following the flow by the time the PEPT is measuring the motion. For this equation the viscosity was calculated through the Metzner and Otto correlation, however since there

is no rheology data for the paper pulp fibre suspension the relaxation times for those sets of experiments could not be measured.
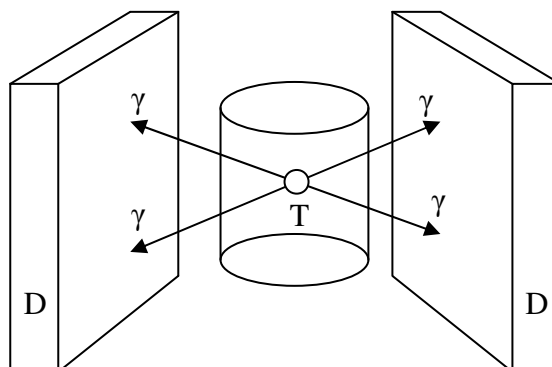
Figure 3.12 Simplified diagram of PEPT set-up; D – detectors, T – tracer and γ - gamma-rays

The tracer used for all experiments was the 600 μm painted tracer, this was used as it was radioactive enough for a full days experiment even with a half life of just under two hours. Neither material was density altered so as not to affect the structure of the fluid and the size of the tracer was not deemed too large as it is assumed that all materials were viscous enough as not to generate very small eddies that the tracer could not be able to follow. Also contrary to what was stated above each experiment was run from the slowest speed to the highest. This was thought necessary to ensure that the tracer particle would not get trapped outside of the well mixed region where little to no flow would occur, i.e. outside of the cavern. Higher speeds would generate more flow in further parts of the tank, generating a larger cavern, thus giving more space for the particle to move. If done from highest speed to lowest, the area of flow (Cavern) would shrink with impeller speed, increasing the risk of the tracer becoming trapped.

The tank and motor were placed centrally between the two detectors, the detectors were then brought as close as possible to the equipment so as to capture as many gamma-rays as possible. Since the mixing of the fluids would generate caverns around the impeller combined with how thick the materials were it was not possible to place the tracer on the surface of a filled tank. Instead the tank was filled up to the impeller where the tracer was carefully placed near one of the blades. The tank was then filled up slowly so as to try and keep the tracer in the impeller region and not move it to the bottom of the tank where little flow would occur.

At the start of each run a sample of fluid was extracted from the impeller region using a glass tube by applying a negative pressure on the other end. Only a small volume of fluid was extracted, enough for the rheometer, so as not to alter the overall volume of material. The sample was always taken from the same region near the impeller as this was where most of the fluid was being mixed; also the sample was checked with a Geiger counter to make sure that the tracer was not removed. This was only done for the shear thinning and shear thickening material as it was impossible to measure the rheology of the paper pulp and thus no sample was needed.

The impeller was then turned on to the required speed and the detectors were turned on to start recording gamma-rays. Each experiment was run for half an hour to ensure enough locations were recorded, as well as giving enough time for all the experiments to be performed with the same tracer. It would be better to run each experiment for longer than thirty minutes as this would capture more data points and allow the tracer to visit more regions of the tank. Thus yielding better quality results but would require the

experiments to run over numerous days and thus would have decidedly different rheologies if the material was time dependant. As the experiment was being run the sample of fluid from the impeller region was tested in the rheometer to obtain its rheology. The order of experiments was run from down pumping lowest speed to up pumping lowest speed then to the next higher speed for down pumping and so on. If the particle became stuck during the experiment for a prolonged period of time either caused by the baffles or the stagnant region of non-mixing, the detectors would be turned off and the fluid was manually mixed to move the tracer into a region of motion.

3.1.5. Power measurement

Two different rigs were used for the measurement of power; the small rig was used for the power measurements of both shear thinning slurries and the shear thickening one, whereas the large rig was used to measure the power for the fibre suspension. The latter was done due to considerable fluctuations of the torque when using the fibre suspension in the small tank. Power measurements on the small tank were achieved by the measurement of torque on the shaft. Starting at rest the impeller speed was ramped up to 800 rpm then back to rest, recording torque values at regular intervals when a steady state had been achieved. The larger tank was mounted on an air bearing so that the torque could be measured on the tank and the baffles. Starting at rest the impeller speed was ramped up to 400 rpm for both down pumping and up pumping configurations, again recording values at regular intervals when a steady state had been achieved. Torque values and impeller speeds could then be converted into Power numbers and Reynolds numbers with the aid of some physical data of the equipment and rheological data of the fluid shown in Chapter 2.

3.2. CFD Simulations

CFD stands for computational fluid dynamics; it enables the user to simulate the flow of a fluid through a given geometry. The software used for this work was Ansys CFX version 5.7 to version 11 (Ansys Europe Ltd, 2005).

3.2.1. Theory

CFD aims to solve the Navier Stokes equation of motion by applying it to a known geometry and making certain simplifying assumptions. The vector form of the Navier Stokes is given below in equation (3.1),

$$\rho \frac{Dv}{Dt} = \mu \nabla^2 v - \nabla P_r + \rho g \qquad (3.1)$$

The term on the left hand side of the equals sign is the combined accumulation and convection term. The first term on the right hand side is the viscous forces, and then follows the pressure forces and finally the gravity forces. To obtain the solution of a specific fluid or material, the rheology must be known and is inserted into the above equation within the viscous forces term.

Turbulent viscosity can be added into the above equation, but due to the fluctuations of turbulent flows the equations becomes increasingly difficult to evaluate, even for the simplest cases of a Newtonian fluid. Numerous turbulence models are used to circumvent this, but these are all approximations to the above equation and thus do not provide exact solutions.

3.2.2. Geometry

Two different geometries were simulated: one is an exact replica of the small tank used for the Carbopol and PEPT experiments with dimensions as shown in Table 3.1. A second smaller tank was simulated only for the fictitious power law fluid shown below in Table 3.7. To save computational power and time only half of the geometry is used as there is a rotational order of symmetry of two for a steady state simulation.

Table 3.7 Simulated geometry dimensions for the power law fluid only

Tank	T	H	D	C	B
Power	0.1m	0.1m	0.333m	0.333m	0.01m
law		T	~T/3	~T/3	T/10

The geometry of any system has to be split up into domains; these domains are a physical representation of where flow can occur, not the geometry itself. Two types of domains are used in these simulations, stationary and rotating. A stationary domain does not mean there is no flow within it but that the domain itself is stationary where a rotating domain rotates on an axis. Since for a mixing tank there are moving parts such as the impeller and stationary parts such as the tank and the baffles a single simple domain cannot be used. There are four methods that can be used to solve this problem, they are;

- Impeller boundary conditions
- Inner-outer
- Moving deforming mesh
- Sliding grid method

For this work the sliding grid method was used as it provides much clearer representation of the flow field than the others at only a slight additional computational

expense. A full comparison of the impeller boundary conditions, inner-outer and sliding grid method can be seen in Brucato *et al.,*1998. The sliding grid (SG) method works by having two domains, one rotating and one stationary as described above. The rotating domain contains the impeller and shaft, while the stationary domain contains the tank walls, baffles and floor. The domains do not overlap but touch, transferring flow across the boundary. However for steady state simulations some of the results at low Reynolds numbers may be affected when taking different planes since the impeller and baffles are in relative positions. There are three possible different arrangements for the sliding method as shown in Figure 3.13.

Top to bottom	Impeller	Top only
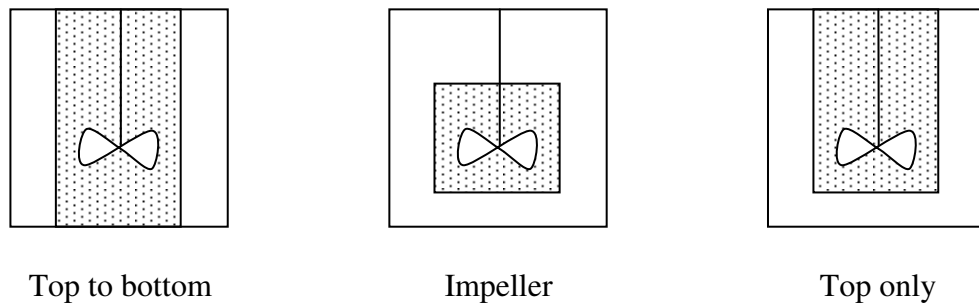
Figure 3.13 Different arrangements for sliding grid method, dotted region – rotating domain

The first arrangement has the rotating domain extending from the surface of the tank to the tank floor, the problem with this method is that part of the tank floor is in the rotating domain and so needs to be corrected. The second arrangement encapsulates the impeller and only part of the shaft, thus part of the shaft is in the stationary domain and again needs to be corrected. The third and final arrangement removes the problems of the previous two by having the rotating domain containing nothing but rotating parts and vice versa for the stationary domain. This arrangement was used for all of the simulations and the distances of the domain split for both geometries are given below in Table 3.8.

Table 3.8 Distances of domain split

	Power Law	Carbopol and PEPT
Radius of domain split	35mm	51.8mm
Distance from bottom of tank	10mm	14.8mm

There are also two different methods of running this domain type; one is to let the rotating domain spin with respect to the other. This is the most obvious and common sense method but requires a lot of computational power as it requires a transient simulation. For steady state simulations it is possible to use a technique called multiple frames of reference, with this both domains remain stationary but the rotating domain is given an angular velocity in each of its elements. This method is much quicker and simpler than the rotating mesh method but cannot yield transient results. Since all of the simulations needed for this work are steady state the multiple frame of reference model is used.

3.2.3. Meshing

The geometry then needs to be divided into many small cells, this is done by a process called meshing. There are four valid mesh elements, hexahedral, tetrahedral, wedge and pyramid. The geometry has to be divided into these elements as it is within each of these that the calculations are performed, and thus the smaller the element and a higher number of them generates better results. Conversely the more elements there are the more computational demanding the simulation is and so a compromise has to be made. CFX first generates a surface mesh by setting constraints for the mesh at every face of the geometry, from this surface mesh the volume mesh is generated. The settings of the mesh for both simulations are presented below in Table 3.9. Default body spacing is

maximum length any element can be, default face spacing is the maximum length on any face. Face spacing can be described in multiple ways, three ways are used in these meshes. Volume meshing uses the same as the default body spacing, constant length overrides the default body spacing and angular resolution is based on the angle between elements. The radius of influence affects how far these settings affect any other face around them and the expansion factor effects how the face settings affect into the volume mesh. Bottom interface, side interface, shaft and blades are the face settings for these surfaces.

Inflation layers are special elements used on surfaces that have a rapid change in velocities. These layers are comprised of prismatic element layers inflated off the triangular surface elements. These are used on the tank wall, tank floor, shaft and impeller blades; they were not put on the baffles or the hub so as not to over complicate the mesh. Periodicity was used between the interfaces between the rotating and stationary domain so that they have identical meshes and thus easier to simulate. Periodicity was also used for the cut surfaces due to the use of only half of a domain, thus both halves of the stationary and rotating domains match. Table 3.10 shows the total number of elements generated by the settings in Table 3.9 with the breakdown of each type of element. The settings present below were obtained from increasing the mesh quality until the simulated data obtained achieved no discernable difference. The mean value of the cell equiangle skew for both meshes was below 0.4 showing a high quality mesh (Ferziger and Peric, 1997).

Table 3.9 Settings used to generate the two meshes

	Power Law	Carbopol and PEPT
Default body spacing	5mm	7.4mm
Default face spacing		
Angular resolution	18 degrees	30 degrees
Minimum edge length	1mm	1.48mm
Maximum edge length	5mm	7.4mm
Bottom Interface		
Volume spacing		
Radius of influence	0	0
Expansion factor	1.2	1.2
Side Interface		
Angular resolution	18 degrees	18 degrees
Minimum edge length	1mm	1.48mm
Maximum edge length	2mm	2.5mm
Radius of influence	0	0
Expansion factor	1.2	1.2
Shaft		
Angular resolution	18 degrees	18 degrees
Minimum edge length	1mm	1.48mm
Maximum edge length	5mm	7.4mm
Radius of influence	0	0
Expansion factor	1.2	1.2
Blades		
Constant length	1mm	1mm
Radius of influence	0	0
Expansion factor	1.2	1.2
Inflation		
Number of layers	5	5
Expansion factor	1.2	1.2
Total thickness model with max thickness	5mm	7.77mm

Table 3.10 Number of elements and their type in each mesh

	Power Law Fluid	Carbopol and PEPT
Total number of elements	383451	434197
Tetrahedrons	336976	391018
Prisms	45259	41786
Pyramids	1216	1393

3.2.4. Boundary Conditions and Settings

Boundary conditions are used in the simulation to define what happens at any surface in the simulation, such as in pipe flow, what is an outlet and inlet and what are the

velocities at these openings. Since these simulations are on a mixing tank there is no inlets or outlets, only the free surface. Firstly the whole domain was set to have the viscosity function of the desired fluid used with the corresponding rheological values and density. The surface of the fluid was set up as a free surface, thus the fluid would flow over with no friction. However in the simulation this free surface had a fixed level surface contrary to the experimentally undulating observed surface, but to simulate a moving surface would generate a very complex system and hence would take much longer to solve. The complications would arise from simulating a multiphase system (the material being mixed and the air above the surface) and the constantly changing surface of the fluid domain. The likely error in doing this simplification would only occur when flow is present in the upper region of the vessel, as most of these simulations deal with low Reynolds numbers the majority of flow is around the impeller so the error is limited. Every other solid surface in the tank was set as zero slip and so no flow would occur on them, these surfaces are the tank wall, tank floor, baffles, impeller and shaft.

Since the geometry is in two domains and only half of it being simulated (due to rotational symmetry), domain interfaces are used to allow transfer of flow between them properly. Two domain interfaces are used to transfer flow from the rotating to the stationary domain, one for the side and one for the bottom interfaces. Two further domain interfaces are used to fix the problem of only half of the geometry being used, one transfers flow from one half of the stationary domain to the other and the other does the same for the rotating domain.

To account for the different rheological models simulated, a viscosity function and density value was required. Density values were assumed to be constant and thus a single value was added for each simulation. Since all simulations were performed on non-Newtonian fluids the viscosity was not constant so a function was needed to describe how it changed. Since viscosity is the ratio of shear stress to shear rate, so for the power law fluid simulations the viscosity function is shown below in equation (3.2)

$$\eta = k\dot{\gamma}^{n-1} \tag{3.2}$$

The rest of the fluids simulated were all described by the Herschel-Bulkley model, the viscosity equation as a function of shear rate could not be used directly as CFD cannot directly cope when the shear stress drops below the yield stress (i.e. when shear rate drops to zero). To avoid this a minimum limit of shear rate was imposed so that shear stress in every part of the tank always exceeded the yield stress, if the shear rate dropped below 10^{-4} s^{-1} then that value was taken. This equation is provided in the CFX tutorials for handling materials that have a yield stress, the standard minimum shear rate is 10^{-3} s^{-1} but for this work a smaller value was taken to provide more accurate results. The viscosity function for the Herschel-Bulkley model is shown below in equation (3.3) with this slight condition imposed.

$$\eta = \frac{\tau_y + k\dot{\gamma}^n}{\dot{\gamma}} \tag{3.3}$$

This way of simulating a fluid with a yield stress causes some slight errors in the simulation. The shear stress will drop to the yield stress as it approaches the cavern boundary, but at the cavern boundary it is still slightly greater than the yield stress. The shear stress then reduces to the yield stress the closer it gets too the wall, only equalling

the yield stress at the wall caused by the non-slip condition. This causes small velocities to occur outside of the cavern boundary, where in reality they do not exist. These velocities are very small and so contribute only slightly to the simulations, as is shown later in the results.

This approach simplifies the complexity of both the china clay suspension and cosmetic foundation cream to a single rheology. This assumes that if the rheology of the sample is known there is no need to simulate the particle interactions of these two suspensions. If the particles of these slurry suspensions are flowing at the same velocity as the bulk material (i.e. no particle slip) it can be construed that it is behaving as a single homogenous fluid. Fishwick *et al.,* 2003 found for particle sizes of 200 µm that slip velocities were only high (around 1%) in the high shear regions, however at least half of the tank had shear rates below 20% of the maximum. It can be construed that for the much smaller particles in both suspensions (nano metres rather micro metres) that the slip velocities would be much smaller. Also since all experiments were run at low Reynolds numbers the degree of high shear needed to cause slip velocities would be very minimal and only close to the impeller blade. Thus the simplification of a complex rheology to a single rheology can be used for these systems.

3.2.5. Solving Scheme

All simulations were run at steady state until the differences between each iteration dropped below 10^{-5}, the four parameters monitored were mass, and velocity in the X,Y and Z directions. Even though some of the Reynolds numbers were in the transitional regime all simulations were run using the laminar model. This was deemed the best

method as the turbulence models usually only work well for high transitional Reynolds numbers, however no turbulence characteristics will be calculated for the simulations in the transitional regime. Also using the laminar model for each simulation made them much simpler to solve since all the fluids have non-constant viscosities.

3.3. Theoretical Cavern Models

Cavern models are used to estimate the size and shape of the cavern formed by a fluid within a tank around the impeller. Each model uses physical dimensions of the mixing apparatus as well as rheological data of the fluid. As these models are described by equations only simple shapes have been investigated, three such shapes used in this work are shown in Figure 3.14. These three shapes are all centred on the impeller, i.e. the centre of these shapes are positioned on the impeller shaft at the off bottom clearance. The first shape is a cylinder of diameter D_c and height H_c, the second being a sphere with diameter D_c with $2r_c = D_c$ and finally a toroid with diameter D_c with $4r_c = D_c$. However real caverns are much more complicated than these perfect shapes described by these models so they can only give an assumption of cavern shape and size.

(a)   (b)   (c)
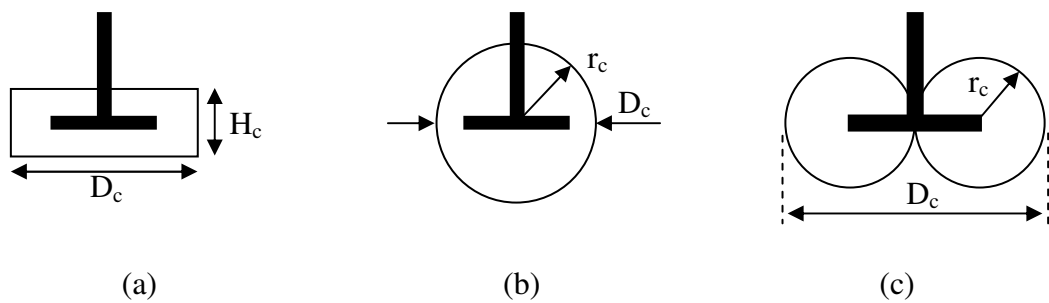
Figure 3.14 Cavern model shapes; a – Cylindrical, b – Spherical and c - Toroidal

Two sets of models were used in this work, the first based on power law fluids with no yield stress and the second on fluids with a yield stress. Regardless of the fluid the spherical and toroidal models developed all use the idea of total force F imparted by the impeller in the axial and tangential directions as shown below in equation (3.4) (Amanullah *et al.,*1997).

$$F = \sqrt{F_a^2 + F_\theta^2} \qquad (3.4)$$

Where the tangential force is described in equation (3.5).

$$F_\theta = \frac{4M}{3R} = \frac{4\rho N^2 D^5 P_0}{6\pi R} = \frac{4\rho N^2 D^4 P_0}{3\pi} \qquad (3.5)$$

And the axial force in equation (3.6).

$$F_a = N_f \pi N^2 D^4 \qquad (3.6)$$

Where N_f is a dimensionless axial force number and for this work the value was taken to be 0.4 for all materials and Reynolds numbers. The value does however change with Reynolds number, around 0.15 to 0.5, a constant value was taken as the axial force could not be measured. A value 0.1 was used as the axial force number to test its sensitivity, very small difference were recorded. At the lower speeds the predictions differed by around 1mm while at the highest speed they differed around 8mm. Compared to the size of the caverns studied these differences were deemed to be negligible, the small differences can be attributed to the fluid that all the caverns studied

were tangentially dominant.   Substituting both into the total force equation and rearranging gives equation (3.7).

$$F = \rho N^2 D^4 \sqrt{N_f^2 + \left(\frac{4P_0}{3\pi}\right)^2}$$

(3.7)

So in the models describe below for both power law and yield stress fluids the F term is equation (3.7) above. The cylindrical model for yield stress fluids was developed much earlier and is derived on the torque rather than with this force.

3.3.1. Power law models

The following set of equations is used for power law fluids with no yield stress but due to its shear thinning behaviour it is capable of generating pseudo caverns at low impeller speeds. The main down fall with these models is the requirement of a velocity at the cavern boundary, due to the absence of a yield stress the velocity will not drop to zero at the cavern boundary. 1% of the tip speed is used in this work, as this value is used when working out the thickness of the boundary layer for flow over a stationary plate (Amanullah *et al.,*1997). These models were only used for the fictitious power law fluid. Both models begin with working out the shear stress at the cavern boundary by manipulating the power law equation shown below in equation (3.8).

$$\tau = k\dot{\gamma}^n$$

(3.8)

Setting the shear stress to that of the cavern and the shear rate to the velocity gradient at the cavern boundary equation (3.8) becomes equation (3.9) below.

$$\tau_c = -k\left(\frac{dv}{dr_c}\right)^n \tag{3.9}$$

The shear stress can be related to the total force over the surface area of the cavern, the following sections incorporate this equation with equation (3.9) above to obtain the cavern prediction models.

3.3.1.1. Spherical

The shear stress over the surface area of a spherical cavern can be described as shown in equation (3.10)

$$\tau_c = \frac{F}{4\pi r_c^2} \tag{3.10}$$

By equating equations (3.9) and (3.10) and rearranging gives equation (3.11)

$$\frac{dv}{dr_c} = -\left(\frac{F}{4\pi k}\right)^{1/n}\left(r_c^{-2/n}\right) \tag{3.11}$$

Integrating the above equation from radius b (the radius of a cavern that touches the tank wall and the fluid velocity is zero, thus b =T/2) and rearranging gives equation (3.12) below (Amanullah *et al.,*1997).

$$r_c^{(1-(2/n))} = v_0\left[\left(\frac{2}{n}-1\right)\left(\frac{4\pi k}{F}\right)^{1/n}\right] + b^{(1-(2/n))} \tag{3.12}$$

Thus if the rheology, tank dimensions and total force are known it is possible to get a spherical cavern radius.

3.3.1.2. Toroidal

Similarly for the spherical cavern the shear stress over the surface area of a toroidal cavern can be described as shown in equation (3.13)

$$\tau_c = \frac{F}{4\pi^2 r_c^2} \tag{3.13}$$

Since the only difference with equation (3.10) is a factor of Pi the equation for a toroidal cavern is given below in equation (3.14), this time b=T/4 (Amanullah *et al.,*1997).

$$r_c^{(1-(2/n))} = v_0 \left[\left(\frac{2}{n} - 1\right) \left(\frac{4\pi^2 k}{F}\right)^{1/n} \right] + b^{(1-(2/n))} \tag{3.14}$$

Again if the rheology, tank dimensions and total force are known it is possible to get a toroidal cavern radius, not forgetting that the definition of cavern radius is different for toroidal than it is for spherical as shown in Figure 3.14.

3.3.2. Yield stress models

The following sets of equations are for fluids that have a yield stress and thus the cavern boundary is described as when the shear stress in the fluid equals the yield stress. The following equations where used for the Carbopol, both shear thinning slurries and the shear thickening slurry. It was assumed that even though these fluids where not purely

yield stress fluids that the yield stress was the dominating factor in determining the cavern boundary.

3.3.2.1. Spherical

Setting the shear stress at the cavern boundary to the yield stress of the fluid in equation (3.10) and replacing r_c to D_c by $D_c=2r_c$ gives equation (3.15).

$$F = \tau_y \pi D_c^2 \qquad (3.15)$$

Combining the total force equation (3.7) with equation (3.15) above gives equation (3.16) below (Amanullah *et al.*, 1997).

$$\left(\frac{D_c}{D}\right)^2 = \frac{1}{\pi}\left(\frac{\rho N^2 D^2}{\tau_y}\right)\sqrt{N_f^2 + \left(\frac{4P_0}{3\pi}\right)^2} \qquad (3.16)$$

If the yield stress, tank dimensions and Power number are known it is possible to get a spherical cavern diameter.

3.3.2.2. Toroidal

Similarly to the spherical model setting the shear stress at the cavern boundary to the yield stress of the fluid in equation (3.13) and replacing r_c to D_c by $D_c=4r_c$ gives equation (3.17).

$$F = \frac{\tau_y \pi^2 D_c^2}{4} \qquad (3.17)$$

Since the force term is only different from the spherical yield stress model by a factor of $\pi/4$ the toroidal model is shown below in equation (3.18) (Adams and Barigou, 2007).

$$\left(\frac{D_c}{D}\right)^2 = \frac{4}{\pi^2}\left(\frac{\rho N^2 D^2}{\tau_y}\right)\sqrt{N_f^2 + \left(\frac{4P_0}{3\pi}\right)^2} \tag{3.18}$$

Again if the yield stress, tank dimensions and Power number are known it is possible to get a toroidal cavern diameter.

3.3.2.3. Cylindrical

The cylindrical model is a much earlier equation based on equating torque, the power required to obtain the torque on the shaft is shown below in equation (3.19).

$$P = 2\pi NM \tag{3.19}$$

Also since power can be written in terms of power number, rearranging equation (2.10) from Chapter 2 gives equation (3.20).

$$P = P_0 \rho N^3 D^5 \tag{3.20}$$

Also the total torque on the shaft due to the surface of a cylindrical cavern is shown below in equation (3.21).

$$M = \frac{\pi}{2}\tau_y H_c D_c^2 + \frac{\pi}{6}\tau_y D_c^3 \tag{3.21}$$

The first part of the above equation is the torque on the curved side of the cavern and the second part is the torque on the two circular surfaces. Combining all three equations to gives equation (3.22) (Elson and Cheesman, 1986).

$$\left(\frac{D_c}{D}\right)^3 = \frac{P_0}{\left((H_c/D_c) + 1/3\right)\pi^2}\left(\frac{\rho N^2 D^2}{\tau_y}\right) \qquad (3.22)$$

An estimation of the cavern height to diameter ratio is needed for this equation, usually a value 0.4 is used. So knowing the yield stress, tank dimensions and Power number it is possible to get a cylindrical cavern diameter and height. Even though this model is developed slightly differently to the spherical and toroidal models they do share a similar dimensionless term containing the yield stress. This is known as the yield stress Reynolds number.

CHAPTER 4

MIXING OF SINGLE PHASE

NON-NEWTONIAN FLUIDS

4.1. Introduction

Single phase non-Newtonian fluids are extremely common through industry as they are pretty much all liquids processed besides water and hydrocarbons. They do not have the complication of other phases so the processing of these materials is only hampered by their rheology and since they are a single phase the rheology is a product of the structure of the fluid. These materials can have varying rheologies such as containing a yield stress or being shear thinning or shear thickening. The limitations to mixing of these rheologies are most notable in the laminar and transitional regimes where caverns or pseudo-caverns are formed around the impeller. These caverns are detrimental to any mass and heat transfer and so should be investigated to understand how they are formed. Also the size and shape of such caverns and also what type of flow is occurring inside of them should be determined.

4.2 Summary

This Chapter studies the caverns and pseudo-caverns developed during the mixing of a Herschel-Bulkley fluid and a shear thinning power-law fluid respectively, in the down pumping configuration of the PBT. The Herschel-Bulkley fluid was studied in the T = 148 mm tank and the power-law fluid in the T = 100 mm tank. The Herschel-Bulkley fluid used is a 0.1 wt% aqueous solution of Carbopol 940, the description and rheology

are described in Chapter 3 section 3.1.2.1. The shear thinning power-law fluid is a fictitious fluid with rheology as follows, $\tau = k\dot{\gamma}^n$ with k = 10 Pas^n and n = 0.2 used in the CFD simulations. A technique adapted from Planar Laser Induced Fluorescence (PLIF) was used to understand the mixing time and cavern size and shape for the Herschel-Bulkley fluid. Simulations were then performed to mimic the PLIF experiments for the Herschel-Bulkley fluid. The power-law fluid was also simulated to see the differences in cavern size and shape due to different rheology. Finally the cavern prediction models were used to estimate the cavern size for both fluids. Thus a full comparison of experimental, simulation and model could be obtained to test the accuracy of both simulations and models.

4.3. Fluorescent Dye Technique/PLIF of Carbopol

Planar Laser Induced Fluorescence (PLIF) technique was adapted to measure the size and shape of caverns developed during the mixing of transparent fluids. The adapted technique can also be used to get an idea of the effectiveness of the mixing inside the cavern. PLIF uses the same equipment as 2-D particle image velocimetry (PIV) and can be used to determine mixing times and localised intensity of mixing of stirred tanks. It works by firing a laser sheet at a vessel containing the fluid under investigation with a single fast 1000X1016 pixel CCD camera set at right angles to the laser sheet as shown in Figure 4.1.

The vessel and fluid both have to be transparent, and if a cylindrical tank is being investigated it must be placed in a square tank with the gap between both tanks filled with water. The second step is performed so as to reduce any parallaxing caused by the

curved surface of the tank. The laser sheet can be directed anywhere in the tank when using the square tank, but the most common location is vertical, directly on the impeller. A fluorescent dye is then injected into the mixing fluid while at the same time the camera starts taking pictures at a defined interval of time. The fluorescent dye spreads throughout the tank and is illuminated on the laser sheet, through analysis of the images taken by the CCD camera it is able to measure mixing time by calculating how long it takes for the illuminated plane to become a homogenous colour. Also local areas of high or low mixing can be observed via fast or slow dissipation of dye (Hall *et al*., 2005).
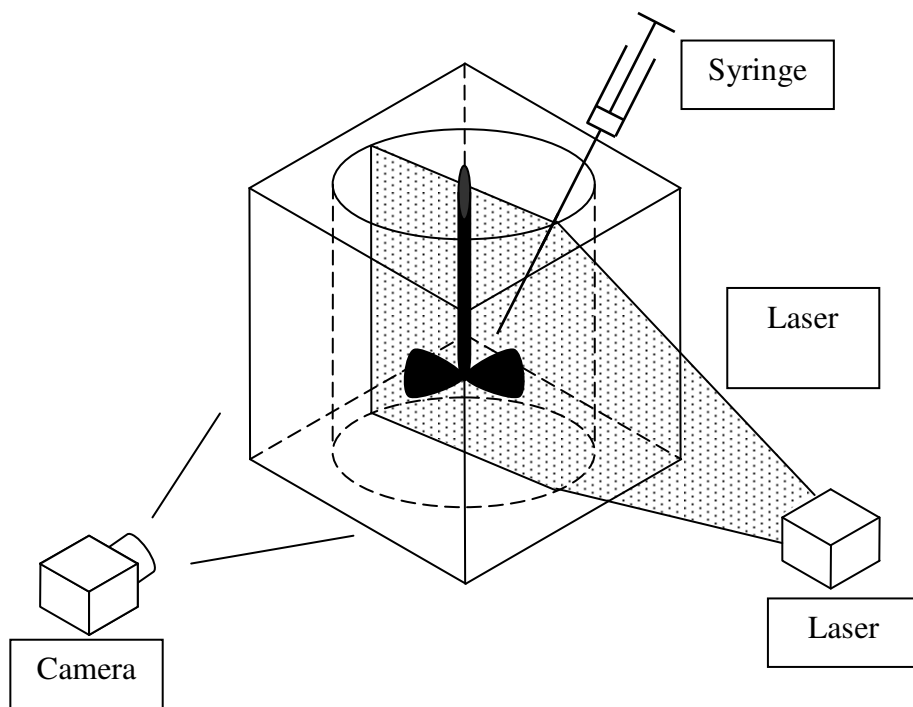
Figure 4.1 Adapted PLIF technique

For our purposes the dye was injected using a syringe just above one of the impeller blades (Figure 4.1), ensuring that the dye would start off inside the cavern with the laser sheet aimed directly at the impeller halfway between two baffles. The impeller speed was then turned on to the required value and the laser sheet and camera was then

started. One frame per second was recorded until the dye stopped propagating throughout the fluid. The visualised vertical cross-sectional area of the caverns was subsequently measured using image analysis software. This enables us to measure the effective degree of mixing occurring inside the cavern. This technique is different to ordinary PLIF since the dye does not move throughout out the entire fluid and is only confined to the inside the cavern.

Cavern growth is thought to be very fast and almost instantaneous but after turning on the impeller the dye slowly fills up the cavern volume. This increase of area of dye over time gives an indication of mixing inside the cavern. Finally after a length of time the dye stops propagating and thus can be used to define the edge of the cavern. This adapted PLIF experiment was only performed on the Herschel-Bulkley fluid in the T = 148 mm tank as direct experimental visualisation and validation of the pseudo-caverns developed by the power-law fluid was too difficult. In this case, the tracer dye tends to diffuse fairly quickly into the bulk of a fluid due to the lack of an apparent yield stress.

Pure PIV was tried on the small tank for the Carbopol solution using a vertical laser sheet. Due to the flow regimes studied very little flow was recorded as the predominant velocities are tangential. Horizontal PIV was undertaken on the impeller to measure these tangential velocities; however no results were able to be obtained within the limited time scale. Further PIV work on the mixing of Carbopol using horizontal planes at different heights to obtain flow patterns within the cavern is recommended in the future.

4.3.1. Size of cavern

Figure 4.2 shows a series of PLIF images for the Herschel-Bulkley fluid for various Reynolds numbers at the time at which the dye has stopped expanding throughout the cavern and thus depicts the cavern boundary. At lower Reynolds numbers the cavern is a simple sphere like object just surrounding the impeller. As the impeller speed is increased so does the size of the cavern, increasing approximately linearly with Re as shown in Figure 4.3. As the size increases, the cavern shape complexity also increases, becoming less like a sphere and more kidney shaped. At high Re the cavern starts to be confined by the tank walls and floor and is only permitted to grow in the upper part of the vessel. At the highest Reynolds number of 163.2 the cavern has almost filled the entire vessel.

(a) Re = 7.43   (b) Re = 20.4   (c) Re = 70.3   (d) Re = 86.6   (e) Re = 163.2
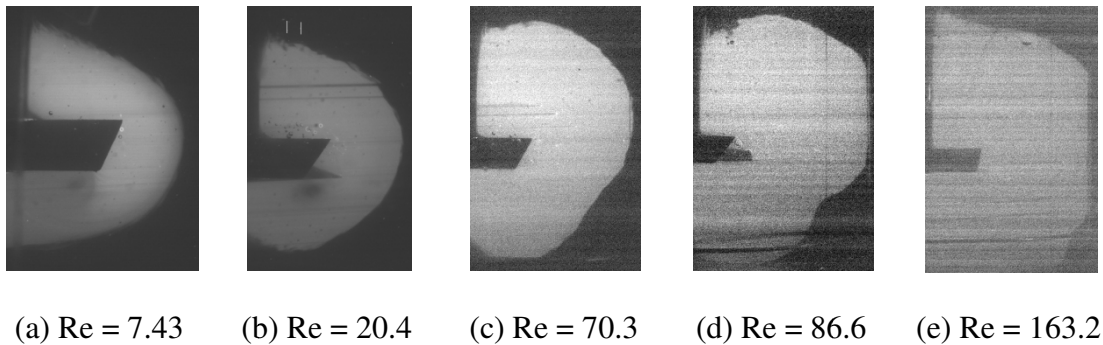
Figure 4.2 PLIF Images captured of caverns in Herschel-Bulkley fluid at various Reynolds numbers
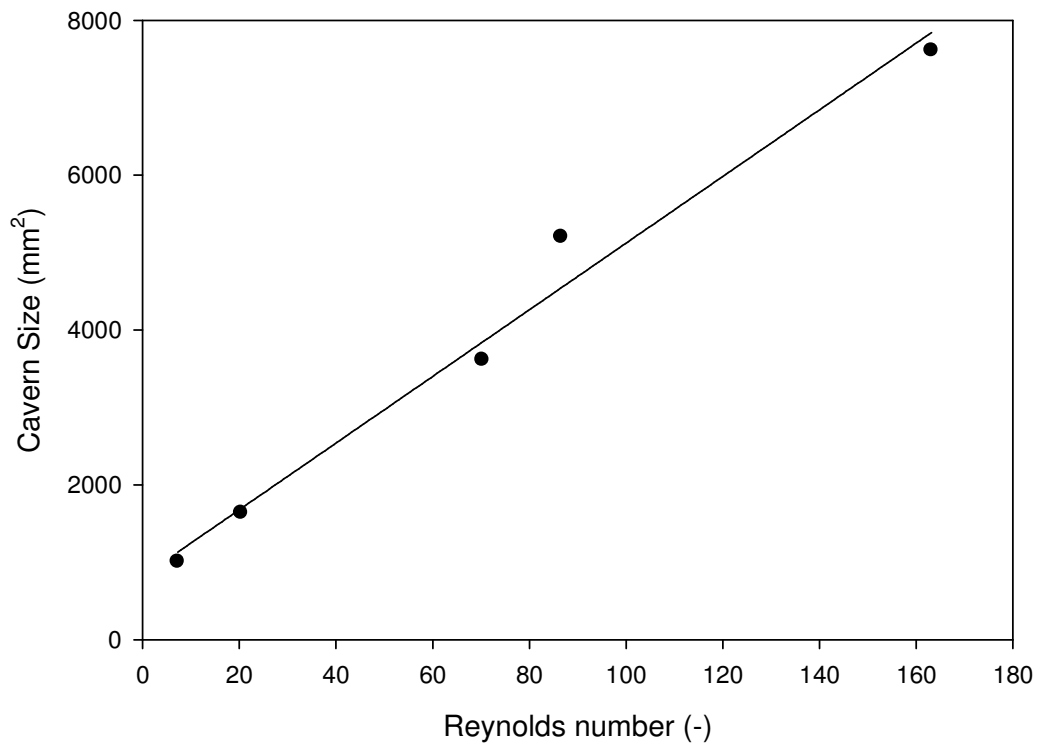
Figure 4.3 Final cavern size versus Reynolds number

4.3.2. Mixing time

Figure 4.4 gives an indication of cavern mixing time as a function of Reynolds number for the Herschel-Bulkley fluid. However it does not take into account a small localised region below the impeller of low energy dissipation that may ultimately only mix by molecular diffusion. The degree of cavern mixing was estimated from the ratio of the vertical cross-sectional area of the dyed fluid to that of the cavern. The fluid mixing inside the cavern is relatively fast signified by the sharp gradient in the degree of mixing, higher speeds generate faster mixing and larger areas in a shorter time. The degree of mixing then dramatically slows down, due to the poor mixing near the cavern boundary. However despite the impeller speed each cavern reaches its final size at roughly the same time, meaning the flow field at the cavern boundary are the same

independent of Re. This is understandable due to the velocity at the cavern boundary for yield stress fluids is fixed at zero for any system and thus for the same material the velocity gradient at the boundary would also be the same. The initial rise of the curve can be approximated by an exponential relationship of the form $\alpha(1-e^{-\beta\theta})$, where θ is time, and α and β are constants. The values of the constants can be seen in Table 4.1 below.
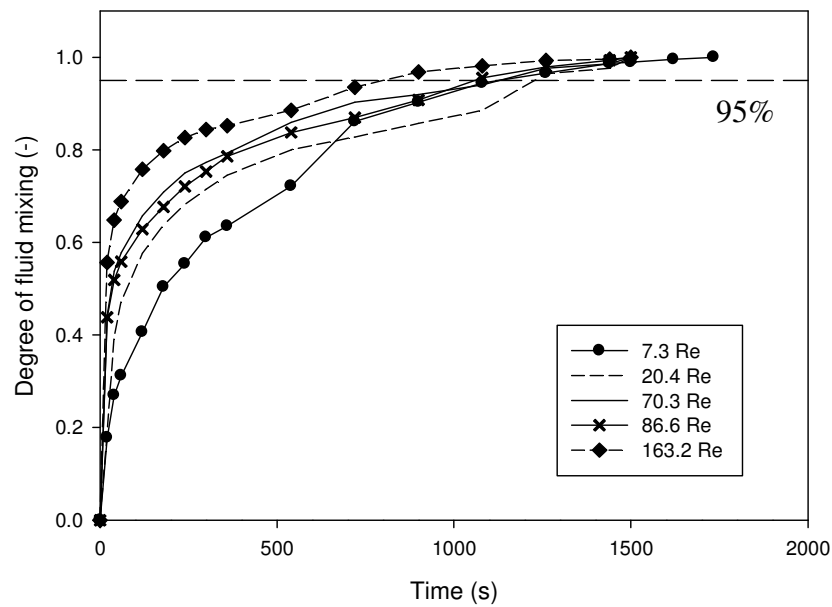
Figure 4.4 Mixing of Herschel-Bulkley fluid within cavern as a function of time and Reynolds number

Table 4.1 Values of constants in exponential equation fitting the data in Figure 4.4

Re	α	β
7.3	0.9637	0.00366
20.4	0.8723	0.00895
70.3	0.8707	0.02072
86.6	0.8626	0.01834
163.2	0.9023	0.03311

4.4. Simulations of Power-Law and Herschel-Bulkley fluids

Simulations of both fluids were performed based on the apparent viscosity function given by the Power-Law and Herschel-Bulkley model respectively. Three speeds where selected to simulate the shear thinning fluid to give an understanding of the mixing in the laminar to low transitional regime in the T = 100 mm tank. The simulations for the Herschel-Bulkley fluid were run to mimic the impeller speeds and rheology of the PLIF experiments performed.

4.4.1. Power-Law fluids

Figure 4.5 shows the normalised velocity flow field taken directly between two of the baffles of the fictitious power-law fluid at three Reynolds numbers, 10, 20 and 50 in the T = 100 mm tank. The arrows denote the 3D velocity vectors on a 2D plane, thus the component coming out of the plot cannot be seen. The grey scale contour plots depict the magnitude of the velocity vector normalised by the impeller tip speed as calculated below in equation 4.1.

$$Normalised\ Total\ Velocity = \frac{\sqrt{V_a^2 + V_\theta^2 + V_r^2}}{\pi ND} \tag{4.1}$$

At the lowest speed the flow is mainly situated around the impeller region with a single loop of motion. This is not unexpected as a Reynolds number of 10 is the maximum limit of the laminar regime for stirred tanks. It may be worth noting however that the guidelines for laminar, transitional and turbulent limits are devised mainly for Newtonian fluids, and thus it is not entirely clear which regime we are in. However

from the results it can be concluded that the estimation is acceptable as little flow is occurring in the tank.

Increasing the speed it can be noticed that a secondary lower loop of motion is generated below the impeller, even though only slightly in the Re 20 case, but is much larger and better developed at Reynolds equal to 50. In both instances this secondary loop is much smaller than the primary one. However the flow is still only encompassing a small portion of the tank even at the highest Re, indicating that this flow is either still in the laminar regime or has entered the low transitional regime. Maximum velocities measured only reach around 0.6 U_{Tip} for each speed, being slightly higher at the highest speed. The discharge angle also seems to increase with impeller speed, becoming more and more axial.

Re 10   Re 20   Re 50
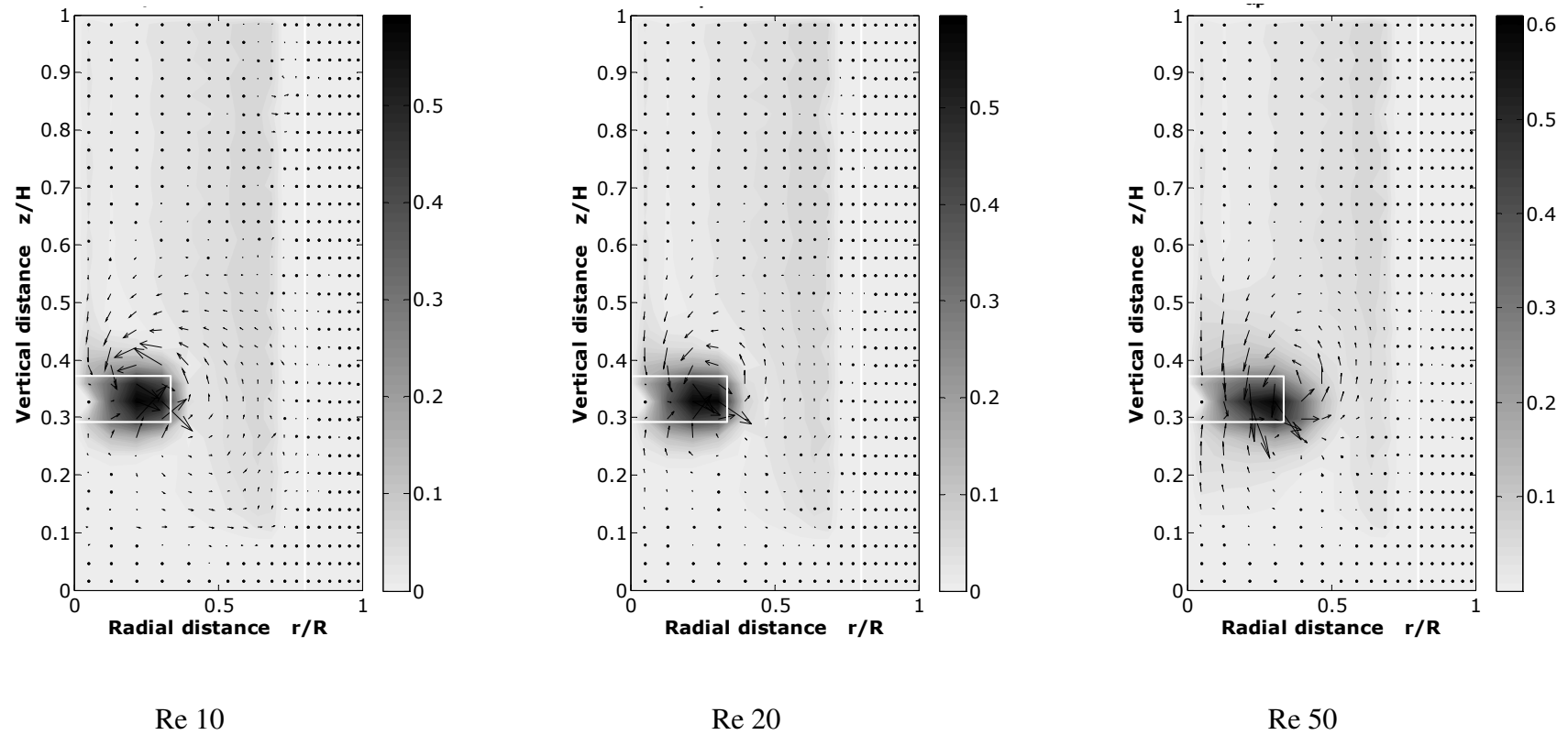
Figure 4.5 CFD normalised velocity flow fields of fictitious power-law fluid at different speeds

4.4.2. Herschel-Bulkley fluids

Figure 4.6 shows the normalised velocity flow field taken directly between two of the baffles of the Herschel-Bulkley fluid at the five impeller speeds in the T = 148 mm tank. Each simulation was run with its own specific rheology, the rheological values were slightly different due to the nature of the preparation as explained in Chapter 3. The lowest Reynolds number case is very similar to the lowest Reynolds number power-law fluid simulations in that it is one single loop of flow centred on the impeller with little to no flow encompassing the rest of the tank. Due to a Reynolds of 7.3, the small flow structures present and simplicity of the flow it can be estimated that we are in the laminar regime.

As the impeller is increased a secondary smaller lower loop is formed beneath the impeller, again posing a similarity with the power-law simulations. This is expected as this is known to happen when mixing a Newtonian fluid using a pitched blade turbine. Increasing impeller speed both loops increase in size with the secondary loop becoming more prominent but always smaller than the primary one. At the highest Reynolds number the dominating upper loop has become rather large and including the lower loop mixing has encompassed a fairly big portion of the bottom of the tank, to almost a half. Still however most of the tank is near motionless and with a Reynolds number of 163.1 it would still be in the transitional regime. In contrast to the power-law fluid plots in Figure 4.5 the maximum velocities obtained decrease with impeller speed starting with around 0.6 and degrading to just under 0.55 of the tip speed. Again however the change in discharge angles do agree, starting with near radial at the lowest speeds approaching axial at the highest speeds.

Re 7.3   Re 20.4   Re 70.3   Re 86.6   Re 163.1
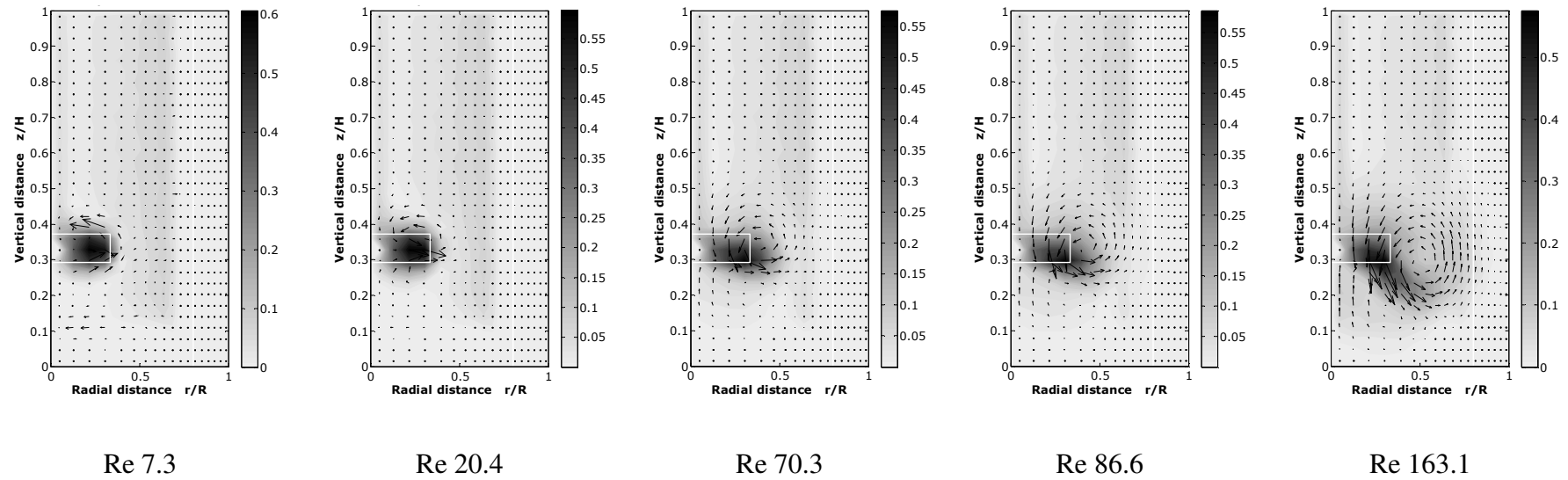
Figure 4.6 CFD normalised velocity flow fields of Carbopol solution at different speeds

4.5. Comparison of experiments, CFD and theoretical models

4.5.1. Power-Law fluids

As the power-law model does not have an apparent yield stress the concept of a fixed cavern boundary does not apply due to the fact there will be motion throughout the entire vessel, however small. However, the apparent shear viscosity of the fluid, if high enough, can lead to a well mixed region around the impeller, i.e. a pseudo-cavern, where most of the flow occurs with small flow velocities occurring outside it. This is especially a problem in the laminar and transitional regimes. Figure 4.7 shows the cavern boundary data for both simulations and cavern prediction models. There are two simulated cavern data represented, one based on tangential velocities by plotting a contour line when the tangential velocity is equal to 1% of the tip speed, and the other on radial-axial velocities by plotting a contour line when the combined radial and axial velocities are equal to 1% of the tip speed as shown below in equation (4.1) and (4.2).

$$0.01V_{Tip} = V_\theta \qquad (4.1)$$

$$0.01V_{Tip} = \sqrt{V_a^2 + V_r^2} \qquad (4.2)$$

The cavern prediction models are shown by a half circle for the spherical model and a full circle for the toroidal model. Comparison between the two CFD methods of cavern boundaries shows a large difference in both size and shape. The tangential plots seem to stick to a small volume around the impeller, increasing in size with increased impeller speed, yet the shape remains pretty much the same for all cases showing none of the complexity of the flow patterns above. The radial-axial plots however show a

much more complex shape at all Reynolds numbers yielding a much more realistic idea of what a cavern looks like since it fits with known flow pattern behaviour, seeming to show the boundaries of the circulation loops. Due to this the radial-axial CFD cavern approach is assumed a more accurate representation of the cavern boundary, this approach is confirmed by PEPT results of the various fluids later on in the thesis. Cavern growth is much more prominent compared to the tangential approach showing a much larger cavern size than the tangential at Re = 50.

In comparison with the cavern prediction models, both spherical and toroidal fail to achieve the shape described by both CFD caverns. This is to be expected as these are perfect shapes and in reality the system is not that simple. However at the two lowest speeds the toroidal model seems to give the best fit for both descriptions of the CFD caverns due to the pseudo-cavern being confined to a small region around the impeller. At the highest speed however both models fall short on size for the radial-axial CFD cavern size and over predict for the tangential approach. Overall the toroidal model fits best at all Reynolds numbers with the radial-axial CFD data with both size and shape taken into account. Amanullah *et al.* 1997, also reported that the toroidal model described the cavern shape better than the spherical approach, although in their work the fluid was a yield stress material described by the power-law model.
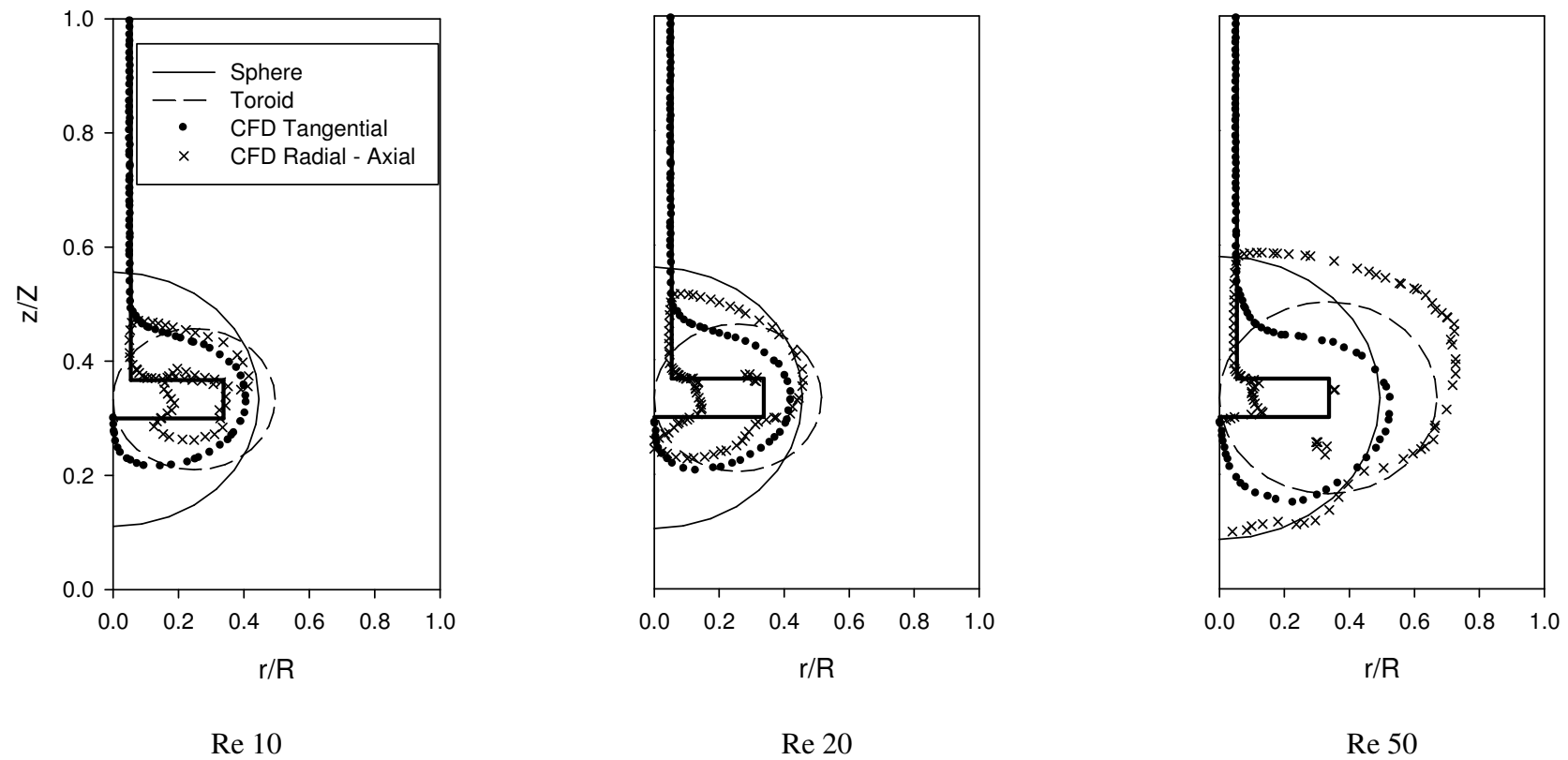
Figure 4.7 Cavern boundary plots for fictitious power-law fluid showing CFD and cavern prediction models

4.5.2. Herschel-Bulkley fluids

Unlike a power-law fluid, a Herschel-Bulkley fluid contains a yield stress and thus has a fixed cavern boundary since fluid will stop flowing where the shear stress of the material is less than the yield stress of the material. Figure 4.8 shows the experimentally determined cavern boundary obtained from the adapted PLIF technique compared with those predicted via CFD.

The tangential and radial-axial CFD caverns are obtained in the same way as for the power-law fluid. The tangential CFD cavern prediction is very similar to the power-law fluid tangential caverns, situating itself around the impeller region at low speeds with a very simple shape. As impeller speed is increased the tangential cavern becomes larger yet retaining a similar shape until at Re 163.1 the tangential cavern almost reaches the tank wall and floor. The tangential cavern only matches the experimental data at the lowest Reynolds number when the flow is concentrated on the impeller and no secondary loops have been formed.

The radial-axial interpretation however provides a much more complex and realistic shape, seeming to encompass the two flow loops produced at the higher Reynolds numbers. At the lowest speed the radial-axial cavern greatly underestimates the size of the cavern but once the impeller speed is increased, both size and shape is a very good fit, matching perfectly at Re 70.3. Although at the two highest speeds the radial-axial cavern under predicts the size of the experimental cavern but the shape is a good fit and much better than the tangential CFD data. Thus the radial-axial CFD representation can

be used as a good approximation of caverns formed in Herschel-Bulkley fluids in laminar and low transitional flow regimes.

Figure 4.9 shows the experimentally determined cavern boundary obtained from the adapted PLIF technique compared with the cavern prediction models. The cavern prediction models are shown the same as for the power-law fluid plots with the addition of the cylindrical model shown by a rectangle. Again all models fail to predict the shape of the experimentally obtained cavern, but the cylindrical and toroidal models give a reasonable approximation of the size of the cavern at the two lowest Reynolds numbers while the spherical model greatly over predicts. As the impeller speed is increased the cylindrical model starts to under predict the cavern size while the toroidal model still provides a reasonable approximation if a little over predicting at the Re 70.3 case. At the two highest Reynolds number cases, the spherical model also gives a good estimation of the cavern size if a little over predicting, this is caused by the experimental cavern having hit the tank wall and floor.

Re 7.3   Re 20.4   Re 70.3   Re 86.6   Re 163.1
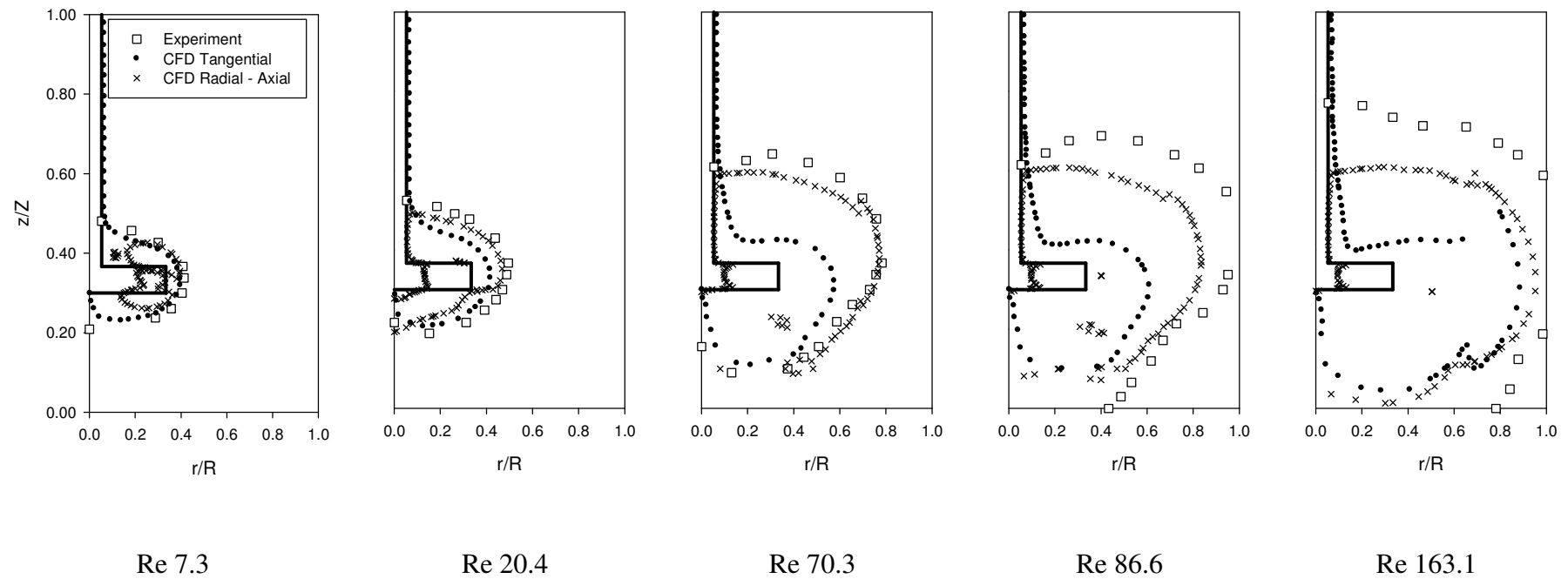
Figure 4.8 Cavern boundary plots for Carbopol solution showing CFD and experimental data

Re 7.3   Re 20.4   Re 70.3   Re 86.6   Re 163.1
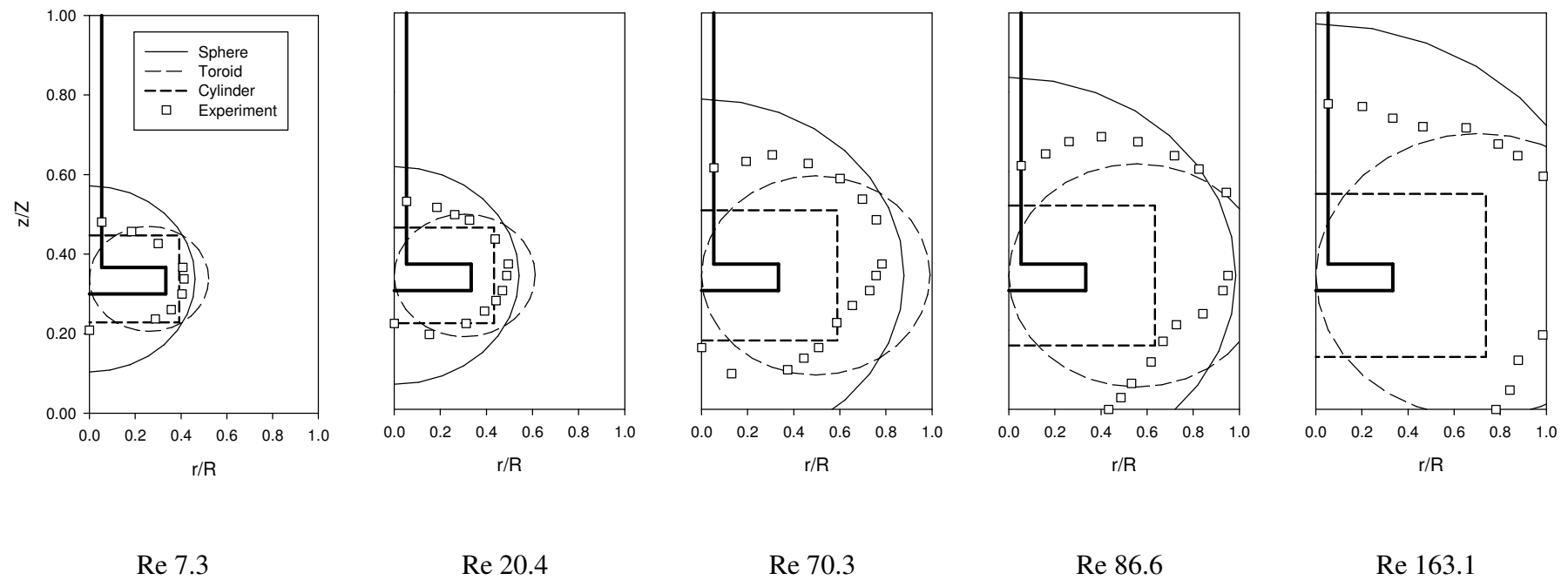
Figure 4.9 Cavern boundary plots for Carbopol solution showing experimental data and cavern prediction models

4.6. Conclusions

Numerical CFD simulations were performed to determine the cavern shape and size for a yield-stress Herschel-Bulkley type fluid over a range of Reynolds numbers in the laminar and transitional regimes. Such caverns were also visualised using a PLIF technique. Fluid mixing inside caverns was shown to be relatively fast near the centre where high velocities and shear rates occur but is very slow near the boundary where the velocities drop to zero.

For both power-law fluid and Herschel-Bulkley fluid simulations it was found that when the cavern boundary was defined using the radial-axial velocity scheme it gave a more realistic shape than the tangential approach. The radial-axial representation also gave a very good fit in both size and shape when compared with the experimental cavern data obtained through the adaptive PLIF technique for the Herschel-Bulkley fluid.

CFD was able to accurately predict the cavern size and shape at low Reynolds numbers, at the two highest impeller speeds cavern shape was still fairly well represented but the size was under predicted. This enables the use of CFD to obtain cavern size and shape predictions of Herschel-Bulkley fluids in the laminar and low transitional regimes. For higher Reynolds numbers CFD can be used to get a general idea of cavern shape but not cavern size.

Since the power law simulations were much simpler than the Herschel-Bulkley simulations it can be postulated that CFD can be used to predict pseudo-caverns at low Reynolds numbers. All cavern prediction models for both fluids failed to predict the shape of the cavern at all speeds but the size was reasonably predicted by the toroidal model. Predicting very well a low speeds for both fluids due to the flow mainly concentrated around the impeller. Once the secondary loop became more dominant and the shape of the cavern became more complex the toroidal model started to under predict the cavern size, but still proved to be the better model when compared with the cylindrical and spherical models.

CHAPTER 5

MIXING OF A SHEAR THINNING SLURRY

5.1. Introduction

Shear thinning slurries are complex materials made up of many components and are normally fine particulate solid liquid suspensions. Many slurries handled in industry are shear thinning with a yield stress, meaning they require a minimum force to flow and once they flow they become less viscous with increase in shear. Also due to the presence of an apparent yield stress, caverns can be formed if the mixing vessel is run in the laminar or low transitional regimes. As mentioned previously these caverns are detrimental to the quality of mixing and therefore should be thoroughly understood concerning how they are formed. Also the size and shape of such caverns and also what type of flow is occurring inside of them. Since all of these slurries are opaque little to no data has been extracted on how they mix since optical techniques cannot be used to measure the flow patterns and velocities.

5.2. Summary

This Chapter deals with the flow patterns and caverns formed when mixing two shear thinning cosmetic foundation cream slurries labelled CF1 and CF2 using both experimental PEPT measurements and CFD simulations at different speeds in both down and up pumping configurations. Full rheological data of both slurries is presented earlier in section 3.1.2.2, both slurries have been fitted to the Herschel Bulkley model but they also have a thinning time dependency. Thus both slurries have a yield stress and flow behaviour index less than one, with CF1 exhibiting slightly thicker rheology

than CF2, i.e. a higher yield stress and consistency factor. Experiments were carried out in the small tank (described in section 3.1.1.) and an exact replica was used in the simulations with the corresponding rheology for each run. A single rheology was used for each simulation and thus does not represent the time dependency that both slurries exhibit, to model the time dependency would be computationally expensive. Due to the difference in rheologies of both suspensions impeller speeds were chosen to obtain roughly the same Reynolds numbers for each run to aid the comparison between the two fluids. Flow patterns, cavern size and cavern shape data are compared between fluids and their associated simulations. Cavern prediction models were compared with the cavern data produced from both experiments and simulations.

5.3. Power Measurements

Power measurements were taken for both slurries, the range of impeller speeds for these measurements were wide enough to cover the Reynolds numbers of the experiments undertaken. Measurements were carried out in the down pumping configuration as it is assumed that pumping direction would not affect the power draw of the impeller. The rheology of the power measurements was slightly different than the experimental results but this was unavoidable due to the time dependent nature of the material, since it is the same fluid and the rheology was only slightly different the following power curves should still apply. Figure 5.1 shows the Power number versus Reynolds number plot, displaying both slurries with their up and down ramp of impeller speed. Both were started at rest, and then ramped up to 800 rpm then back again. The down ramp of impeller speed falls beneath the up ramp for both slurries, showing the shear thinning time dependency. CF2 is moved further to the right due to its thinner rheology than

CF2, thus at the same rpm CF2 would have a higher Reynolds number. The figure also shows that CF1 has higher Power numbers at a given Reynolds than CF2. Both curves exhibit a large linear region up to a maximum Reynolds number of around 30, indicating that below this number we are in the laminar mixing region of these two fluids. Also the curves start to flatten off but do not reach a constant value of Power number, thus this section is in the transitional regime.
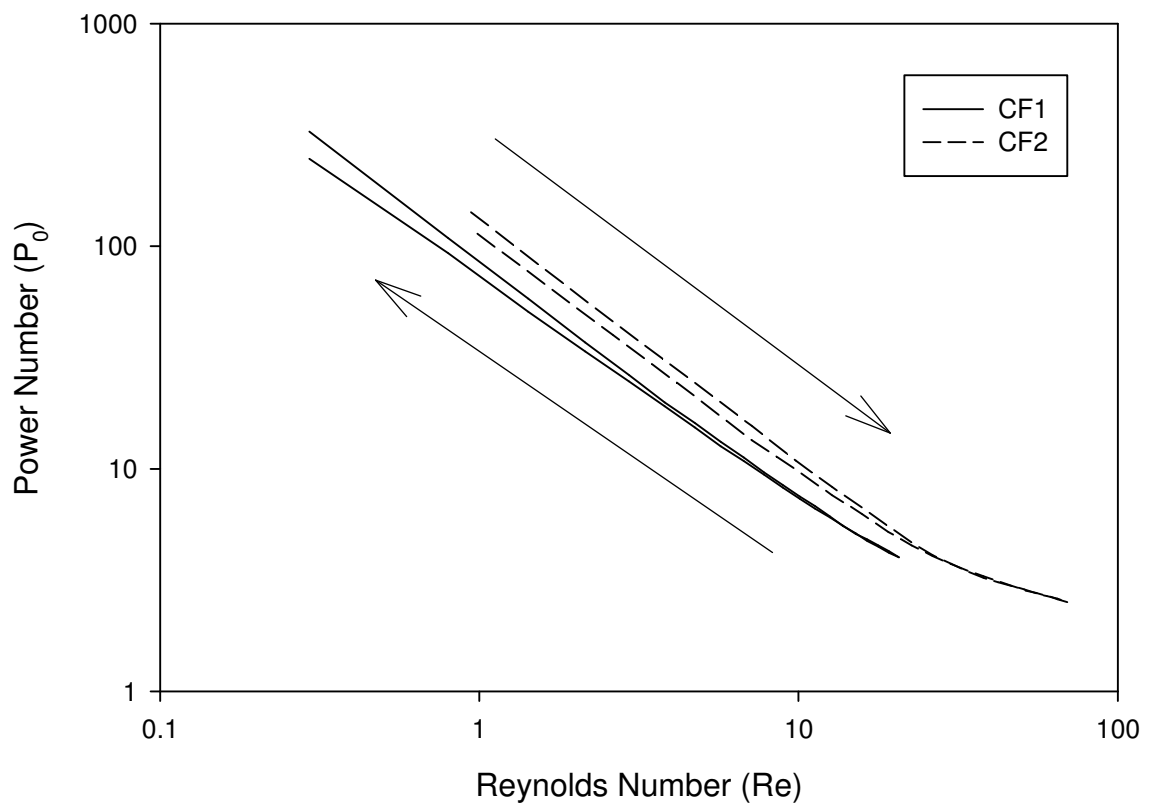
Figure 5.2 Power number versus Reynolds number plot for both cosmetic foundation creams including both up and down ramps for the PBTD

5.4. PEPT analysis of slurries

Figure 5.2 and Figure 5.3 show the flow patterns obtained through PEPT for the mixing of CF1 and CF2 respectively in the small tank (described in section 3.1.1.) for both up and down pumping configurations at different Reynolds numbers. The arrows denote the 3D velocity vectors on a 2D plane, thus the component coming out of the plot cannot be seen. The grey scale contour plots depict the magnitude of the velocity vector normalised by the impeller tip speed as calculated below in equation (5.1).

$$Normalised\ Total\ Velocity = \frac{\sqrt{V_a^2 + V_\theta^2 + V_r^2}}{\pi ND} \tag{5.1}$$

PEPT plots produced throughout the thesis are the entire flow field azimuthally averaged on a single plane, so they do not take into account locations of baffles or the impeller. According to the power measurements all experiments are run in the laminar regime except for the highest speeds being on the cusp of the transitional regime. During some of the experiments the tracer became stuck and so manual mixing was required to enable tracer motion once again, the PEPT cameras were turned off during these manual mixing periods.
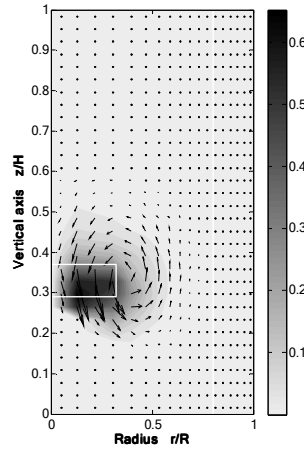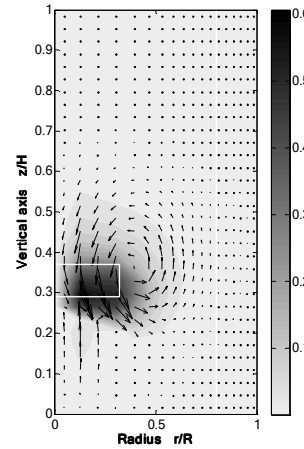
Down

Re 8.3

Re 16.4

Up
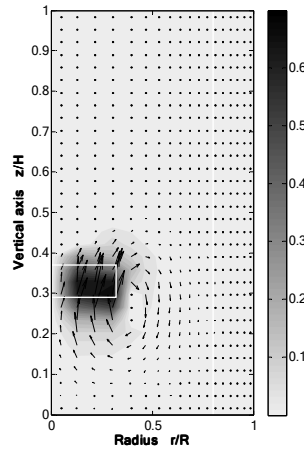
Re 8.3
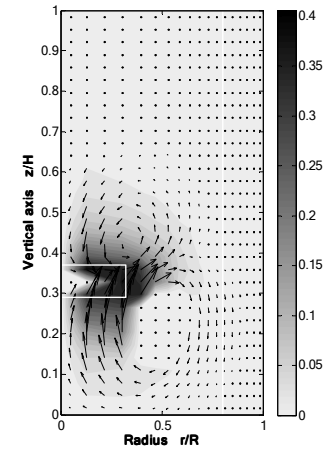
Re 23.9

Figure 5.3 PEPT normalised velocity flow fields of Cosmetic sample 1 at different Reynolds numbers in down and up pumping configurations

Down

Re 1.3   Re 10.9   Re 22.3   Re 33.5

Up

Re 1.3   Re 24.5   Re 35.2

Figure 5.4 PEPT normalised velocity flow fields of Cosmetic sample 2 at different Reynolds numbers in down and up pumping configurations

Chapter 5 – Mixing of a Shear Thinning Slurry

Not all PEPT experiments were successful, with some not recording enough data for a full flow analysis to be performed, so only the successful experiments are shown. More experiments were successful for CF2; this may be due to the slightly thinner rheology and thus easier tracer movement through the slurry. Due to CF1 and CF2 being similar fluids the missing experimental data can be extrapolated from each other as flow structures generated would be the same or similar but differing in size due to their different rheologies. Some of the discounted data showed the particle being stuck in a location for a long period of time, proving that outside of the cavern no motion was detected.

Both mixing configurations exhibit a single loop of mixing at the lower speeds while at higher speeds a secondary smaller loop is generated, a lower loop for the down pumping and an upper loop for the up pumping. The shape of the upper and lower flow loops in these slurries is consistent with previous published work for simple Newtonian fluids, where mixed-flow impellers generate double flow loops. Therefore, for better mixing it could be suggested that for an up-pumping slurry mixing system the clearance of the impeller should perhaps be set higher than $T/2$, and lower than $T/2$ for down pumping. Also there is no motion detected outside of these flow loops inferring these regions are completely stagnant, showing the adverse factors of mixing fluids that generate caverns.

Figure 5.2 shows the flow loops increase with speed, as expected, to cover at least the lowest half of the tank for the highest speed for up pumping. For the up pumping case the flow is constrained by the bottom of the tank so by setting the clearance to half of the tank height would be more preferable to enable larger flow coverage of the tank. CF2's flow patterns in Figure 5.3 show very similar flow development to CF1. Flow

loops grow in size with an increase in impeller speed, again covering around half the tank at the highest speeds, with the up pumping being constrained by the bottom of the tank. However given that the experiments were run at similar Reynolds numbers the CF2 flow loops are much smaller than CF1. This is contrary to the rheology as you would expect a thinner material at the same Reynolds number would generate more flow, since at the same shear rate the viscosity would be smaller and thus less resistance to flow. This could be attributed to the PEPT tracer not venturing into the furthest most regions of the cavern for CF2, instead following the faster streamlines away from the cavern boundary yielding smaller flow loops. Also at the lowest impeller speeds for CF2 the cavern seems to shrink towards the swept volume of the impeller. Impeller tip speed normalised maximum velocities for CF1 as shown in Table 5.1 were mainly between 60% and 70% of the tip speed, however at the highest speed for up pumping the value dropped drastically to 40%. This could be attributed to the PEPT cameras inability to measure the high speeds in the impeller region. CF2's impeller tip speed normalised maximum velocities as shown in Table 5.2 float around 60% to 70% dropping to around 57% at the highest speeds, again more than likely attributed to the limitations of the PEPT cameras.

Table 5.1 Velocity maxima and minima normalised to the impeller tip speed for CF1 PEPT data

Pumping	Re	V_r		V_θ		V_a		V		$\sqrt{(V_r^2 + V_a^2)}$	
		Max	Min	Max	Min	Max	Min	Max	Min	Max	Min
Down	8.3	0.0351	-0.0211	0.6516	0	0.0181	-0.0513	0.6532	0	0.0604	0
	16.4	0.0586	-0.0277	0.6036	0	0.0430	-0.0732	0.6070	0	0.0807	0
Up	8.3	0.0345	-0.0182	0	-0.6969	0.0616	-0.0148	0.6999	0	0.0647	0
	23.9	0.0629	-0.0258	0	-0.4028	0.0707	-0.0366	0.4057	0	0.0813	0

Table 5.2 Velocity maxima and minima normalised to the impeller tip speed for CF2 PEPT data

Pumping	Re	V_r		V_θ		V_a		V		$\sqrt{(V_r^2 + V_a^2)}$	
		Max	Min	Max	Min	Max	Min	Max	Min	Max	Min
Down	1.3	0.0171	-0.0270	0.6442	0	0.0269	-0.0321	0.6449	0	0.0325	0
	10.9	0.0476	-0.0319	0.7339	0	0.0261	-0.0708	0.7378	0	0.077	0
	22.3	0.0792	-0.0400	0.6334	0	0.0348	-0.0776	0.6358	0	0.1026	0
	33.5	0.1027	-0.0492	0.5677	0	0.0619	-0.1012	0.5721	0	0.1179	0
Up	1.3	0.0226	-0.056	0	-0.6577	0.042	-0.0104	0.6589	0	0.0561	0
	24.5	0.0802	-0.0436	0	-0.6148	0.0792	-0.0454	0.6189	0	0.1006	0
	35.2	0.1072	-0.0554	0	-0.5614	0.0931	-0.072	0.5669	0	0.1214	0

Further examination of these tables reveals that the flow within the cavern, at the Reynolds numbers investigated, is predominantly tangential, with the radial and axial velocity components being several folds smaller as shown in Figure 5.4. Hence the overall velocity is dominated by this component. On average the radial and axial component magnitudes do increase with Reynolds numbers for both fluids and both pumping configurations.

| Radial velocity | Tangential Velocity | Axial Velocity |
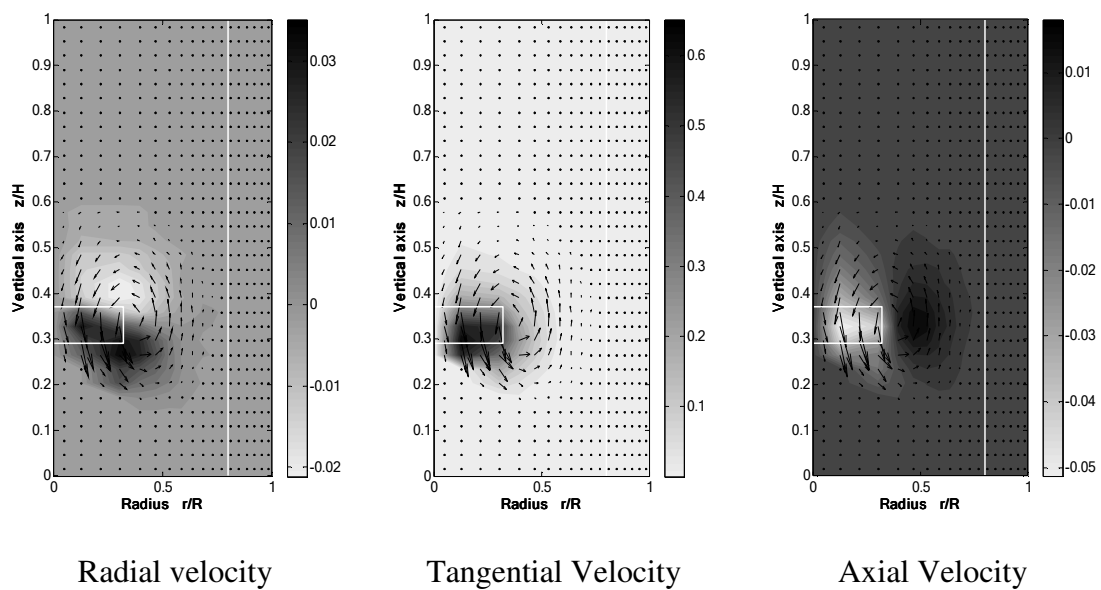
Figure 5.4 Example of PEPT normalised velocity flow fields showing the three velocity components

PEPT allows the spatial tracer occupancy distribution to be determined, which offers an additional tool for characterising fluid flow behaviour within the vessel. Occupancy is obtained by dividing the vessel volume into small cells, and calculating the fraction of time spent by the particle in each cell during the experiment. Occupancy can be defined as the ratio of time that the tracer spends inside the cell to the time that the tracer would spend in any cell if the system were ergodic; an ergodic system has the tracer spending equal time in all cells. Figure 5.5 shows the occupancy plots obtained for the PBTD and PBTU configurations for slurry CF2 at Reynolds numbers.
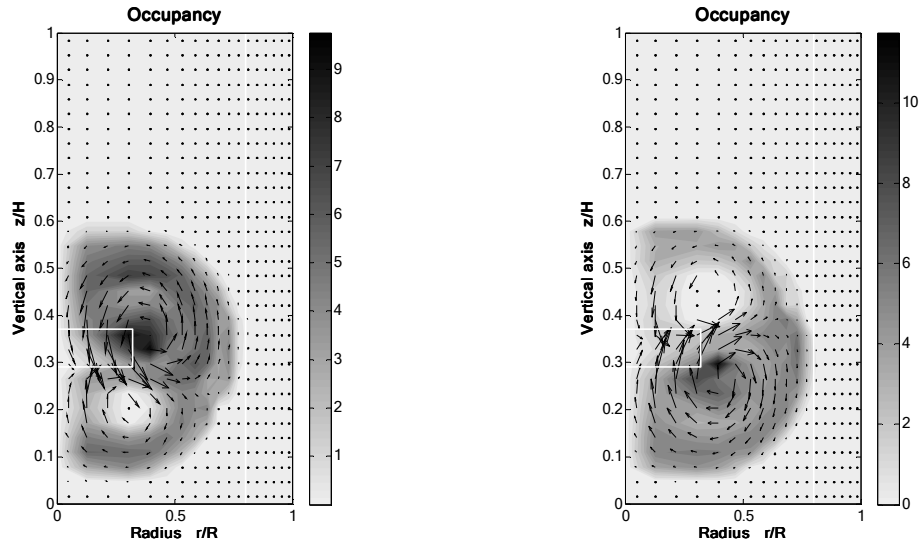
Re 33.5 Down pumping   Re 35.2 Up pumping

Figure 5.5 PEPT occupancy data for CF2

Within each cavern there are toroidal zones of intensive tracer motion depicted by a high density of detected locations or high level of occupancy, and blank areas which the PEPT tracer did not visit at all. It could be inferred that no fluid motion occurs in these regions or that the tracer does not enter those regions. It is more likely that the tracer did not enter these regions and that they are zones of high toroidal fluid motion, as in some other experiments the tracer would enter these regions and remain there for long lengths of time. This data is contrary to what was expected, the original understanding of the flow inside of caverns was that it was completely chaotic and homogenous. However as shown in Figure 5.5 the mixing is completely heterogeneous with very little chaotic behaviour.

Figure 5.6 and Figure 5.7 show how velocity and radial-axial velocity both normalised by the tip speed change with radius for all PEPT experiments carried out for CF1 and CF2 respectively. Normalised velocity is described above in equation (5.1) and the normalised radial-axial velocity is defined below in equation (5.2.)

$$Normalised\ Radial-Axial\ Velocity = \frac{\sqrt{V_a^2 + V_r^2}}{\pi ND} \qquad (5.2)$$

Down pumping data was taken at a fixed height just below the impeller blade (z/H = 0.297) while up pumping was taken at a fixed height just above the impeller blade (z/H = 0.372). These positions were taken as they are the discharge paths of the two pumping configurations. In Figure 5.6 as the impeller speed is increased normalised total velocities drop near the impeller but are maintained at higher values further into the tank for up pumping. The two down pumping cases however are very similar to each other, but do share the drop in normalised total velocity near the impeller. The radial-axial plots in Figure 5.6 do follow similar patterns for both pumping directions, increasing in value with impeller speed and increasing to a peak then dropping off with increased radius. The Re 8.3 down pumping case however does not increase to a peak but instead flattens out then drops off. The location of these peaks seem to move further into the tank at higher impeller speeds, signifying more flow throughout the tank.

In Figure 5.7 again as the impeller speed is increased normalised total velocities drop near the impeller for both pumping configurations, signifying less momentum being wasted in the impeller region. Both Re 1.3 experiments have a very different shape to the rest, probably due to these are at low Reynolds numbers and therefore have very slow flow structures, where the rest are higher and have more developed flows or that at these slow speeds the cavern volume shrinks to the impeller swept volume. The radial-axial plots in Figure 5.7 show very similar patterns to the ones for CF1, with the same peak shifting. The three lowest speeds also do not have the peaks as for the CF1 data.

	Down pumping	Up pumping

Total Velocity

$$\left(\sqrt{V_a^2 + V_\theta^2 + V_r^2}\right)$$

Radial-Axial Velocity

$$\left(\sqrt{V_a^2 + V_r^2}\right)$$
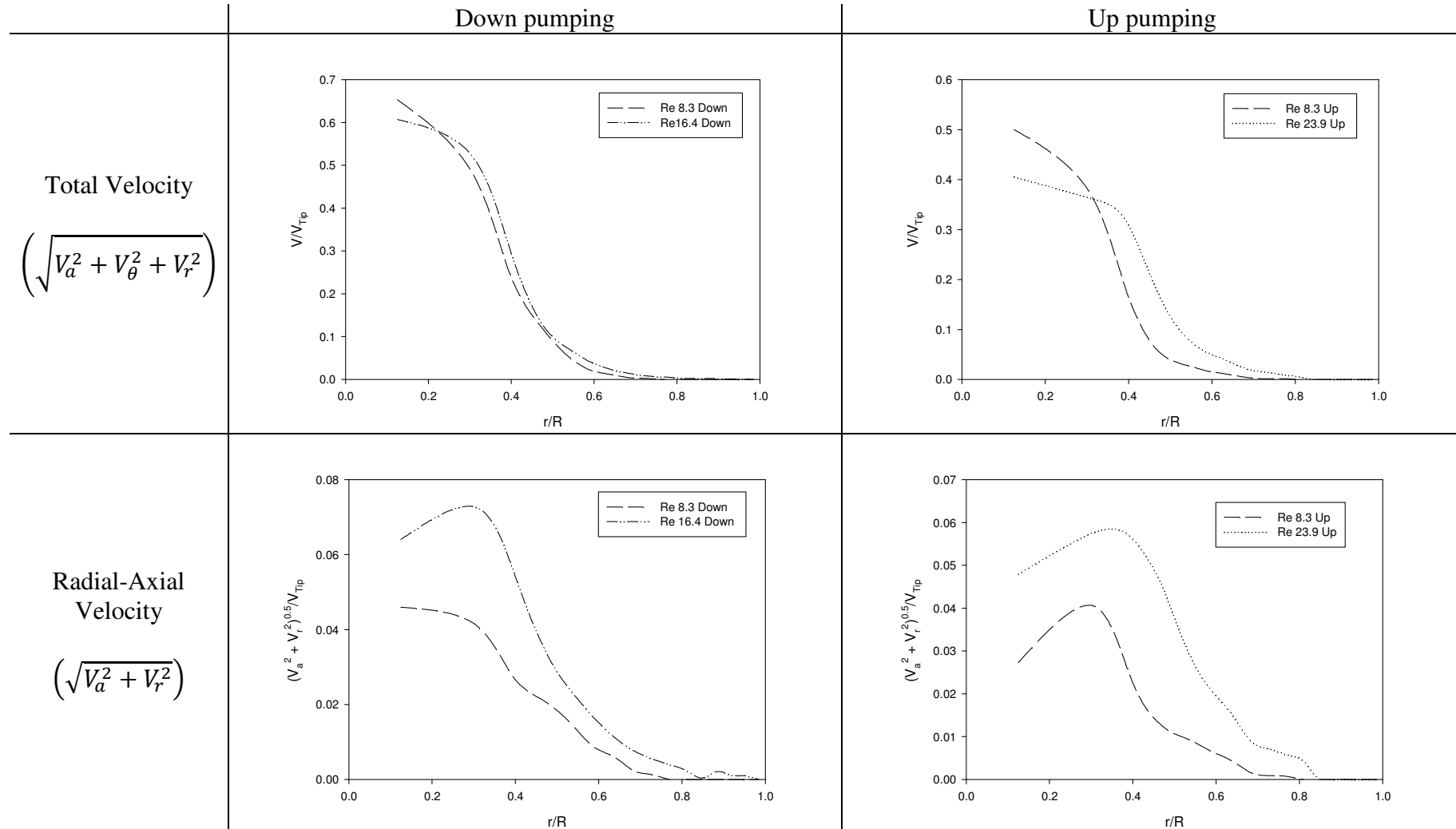
Figure 5.6 Radial plots of CF1 PEPT data total and radial-axial velocity for up (just above impeller, z/H = 0.372) and down (just below impeller, z/H = 0.297) pumping configurations

| Down pumping | Up pumping |

Total Velocity

$$\left(\sqrt{V_a^2 + V_\theta^2 + V_r^2}\right)$$

Radial-Axial Velocity

$$\left(\sqrt{V_a^2 + V_r^2}\right)$$
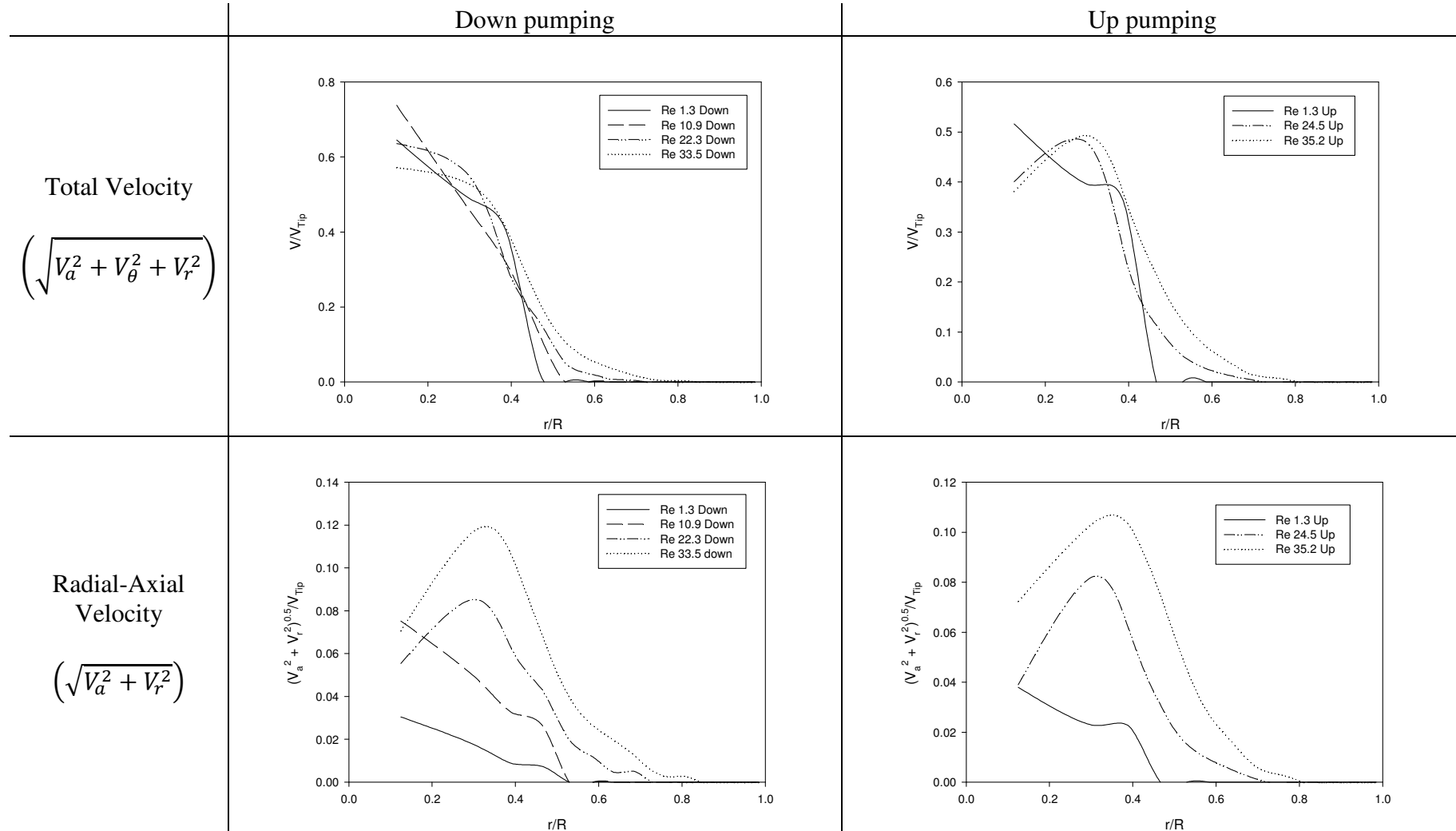
Figure 5.7 Radial plots of CF2 PEPT data total and radial-axial velocity for up (just above impeller, z/H = 0.372) and down (just below impeller, z/H = 0.297) pumping configurations

5.5. CFD simulations

CFD simulations where performed to mimic all the PEPT experiments performed using a single rheology that was obtained at the start at each experiment. Thus each simulation approximates the slurries as a homogenous fluid with a single rheology, ignoring any structural changes leading to time dependency. All CFD plots produced throughout the thesis are a slice of the entire flow field taken directly between two of the baffles, not azimuthally averaged. There is no simple way to produce an azimuthally averaged data within the CFD software and would require extensive post analysis to obtain. Figure 5.8 and Figure 5.11 show the data obtained through the simulations and it is presented in the same manner as for the PEPT experiments. The CFD data has been recalculated on the same grid as the PEPT experiments to enable a better comparison rather than use the original data that is calculated on an unstructured mesh.

The main difference to be noted is that there is small flow outside of the main flow loops whereas in the PEPT there was none at all. This could be attributed to two factors: firstly CFD does not require a tracer to calculate the flow, so the no flow in PEPT could just be down to the fact that the tracer never went into these regions thus also CFD would be able to calculate much smaller velocities at higher spatial resolution. The more likely second reason is the CFD's inability to handle the yield stress value properly in the viscosity function, as in reality for Herschel-Bulkley materials when the shear stress drops below the yield stress no flow occurs and the material behaves like a solid. This solid-like behaviour gives rise to an infinite viscosity. In CFD, to avoid this infinity as the shear rate drops a limit has to be put in. So instead of having a sharp drop to the yield stress at the cavern boundary the shear stress approaches the yield stress at

the boundary then slowly approaches asymptotically. The shear stress does eventually equal the yield stress but only at the tank wall. This approach gets around the problem of a fluid becoming a solid, which modern CFD programs cannot handle.

Figure 5.2 and Figure 5.8 which deal with CF1 are compared. Since half of the PEPT experiments failed only a limited comparison can be achieved. However if similarities do arise it could then be assumed that the CFD for the missing experiments may be used as a reasonable estimate. Very similar flow patterns are present showing large mixing loops above the impeller for down pumping and vice versa for up pumping. However for the highest Reynolds up pumping the discharge angle is much more radial in the PEPT with the CFD being more axial. Also the secondary loop present in the PEPT experiment is much less predominant in the CFD simulation. Even though the flow patterns are similar only the down pumping simulation at Re = 16.35 matches the experimental maximum and minimum values of the total velocity. However for the two slowest speeds for down and up pumping the total velocities are under predicted and for the highest speed up pumping the total velocities are over predicted as shown in Table 5.3.

Table 5.3 CFD normalised velocity maxima and minima for CF1 as a percentage of PEPT values

Pumping	Re	V_r		V_θ		V_a		V		$\sqrt{(V_r^2 + V_a^2)}$	
		Max	Min	Max	Min	Max	Min	Max	Min	Max	Min
Down	8.3	-6.6%	-8.5%	-10.7%	-	-8.8%	+27.3%	-10.3%	-	+21.0%	-
	16.4	+45.4%	+6.8%	-2.4%	-	+81.2%	+106%	+0.8%	-	+106%	-
Up	8.3	+3.8%	+0.5%	-	-16.6%	+9.4%	+10.1%	-16.3%	-	+17.9%	-
	23.9	+110%	+43.4%	-	42.5%	+313%	+273%	+58.0%	-	+272%	-

Breaking down the successful comparison at Re = 16.35 we notice that it is only accurately calculating the tangential velocities, severely over predicting radial and axial components. However due to their relative magnitude to the tangential velocity all of these errors sum to only 0.8% of the total velocity. It is also apparent that the higher the

Reynolds number the larger the deviation from the real velocities, with the axial portion deviating the most. This is probably contributed to the difference in discharge angle noted earlier.

Figure 5.9 and 5.10 show how the velocity and radial-axial velocity both normalised by the tip speed change with radius for both CFD and PEPT for CF1 down and up pumping respectively. The PEPT data are the same as in Figure 5.6 above. The CFD data was taken in the same manner but at two different locations: one between the two baffles and on the same plane as Figure 5.2 and Figure 5.8, while the other was taken on a plane directly on a baffle. This was done to see if there was any difference between the two planes as this cannot be done in the PEPT. Since PEPT is averaged data it should fall between the two CFD data if they modelled the experiment correctly.

Concerning the comparison between the CFD planes it can be seen that total velocities for both pumping directions vary very little only deviating slightly with the peak values, indicating that whatever plane taken from CFD does not affect the results a great deal, especially when flow does not extend that far into the tank. Thus the flow field comparison between the averaged flow field to a single plane is valid as long as the cavern does not interact with the baffles, i.e. behaving like an un-baffled vessel. However at the lowest speeds there are large deviations between the two CFD plane data for the radial axial velocity. As the impeller speed is increased they do become more similar but they are still not able to match their peaks, from this it must be inferred that if you are measuring the radial and axial components it can be quite crucial what plane you take at low speeds. These errors could be attributed to an artefact of the sliding mesh, the peaks do match as depending on what plane is taken the impeller and

baffles are in relative positions, this is described in more detail in Chapter 3 Section 3.2.2..

For the down pumping case (Figure 5.9) the radial-axial plots for both CFD planes are very erratic compared with how smooth they are for the up-pumping case, but their overall shape are similar to each other. This erratic behaviour can be contributed to the flow interacting with the domain boundary separating the stationary and rotating domains; it does not affect the up pumping case as the domain split is below the impeller. When compared with the PEPT data the fit is very good with the total velocity data, only struggling to predict nearer the impeller. This is more of a problem with the PEPT data as it is difficult to measure accurately in that region as well as the poorer spatial resolution. Comparison is very good with the radial-axial data for the down pumping case and the lowest speed up pumping but over predicts for the highest speed.
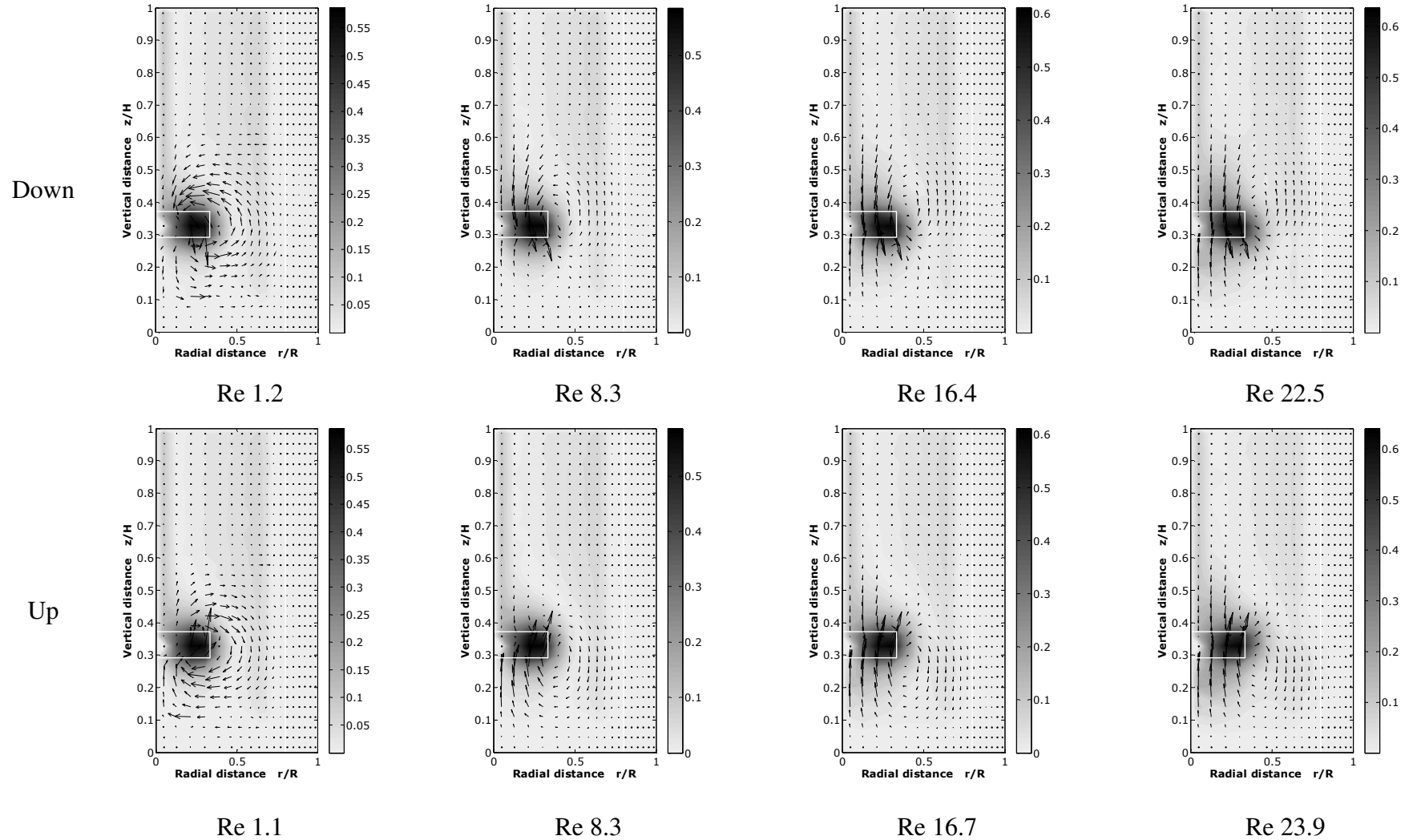
Figure 5.8 CFD normalised velocity flow fields of Cosmetic sample 1 at different Reynolds numbers in down and up pumping configurations

	Total Velocity $\left(\sqrt{V_a^2 + V_\theta^2 + V_r^2}\right)$	Radial-Axial Velocity $\left(\sqrt{V_a^2 + V_r^2}\right)$
Re 1.2		
Re 8.3		
Re 16.4		
Re 22.5		

Figure 5.9 Radial plots of total and radial-axial velocity for CF1 down pumping configuration (taken just below the impeller, z/H = 0.297) showing PEPT and CFD data

	Total Velocity $\left(\sqrt{V_a^2 + V_\theta^2 + V_r^2}\right)$	Radial-Axial Velocity $\left(\sqrt{V_a^2 + V_r^2}\right)$
Re 1.1		
Re 8.3		
Re 16.7		
Re 23.9		

Figure 5.10 Radial plots of total and radial-axial velocity for CF1 up pumping configuration (taken just above the impeller, z/H = 0.372) showing PEPT and CFD data

Comparing Figure 5.3 and Figure 5.11 which deal with CF2, only one of the PEPT experiments failed for this set so a full comparison is much more achievable. Again fairly similar flow patterns are present, exhibiting the known mixing loops above and below the impeller. However due to the nature of the CFD having a fix for the infinite viscosity the flow loops tend to be larger than the PEPT experiments especially notable at the lowest Reynolds numbers. Again CFD seems to predict a much more axial discharge angle than the PEPT experiments, and showing less predominant secondary loops.

From Table 5.4 it can be seen that again CFD can only predict the overall and tangential velocity minimum and maxima but only in most cases, with only the down pumping at Re = 10.86 falling above the 10 percent margin. It is of no coincidence that if it matches the tangential it matches the overall as all these flows are dominant. Radial velocities are under predicted at low Re and then over predicted at high Re, this trend is much more notable for the axial velocities, this again could be contributed to the difference in discharge angle seen from the simulations. Even with all of the drastically over or under predicted radial and axial velocities they do not affect the overall velocity a great deal similar with CF1.
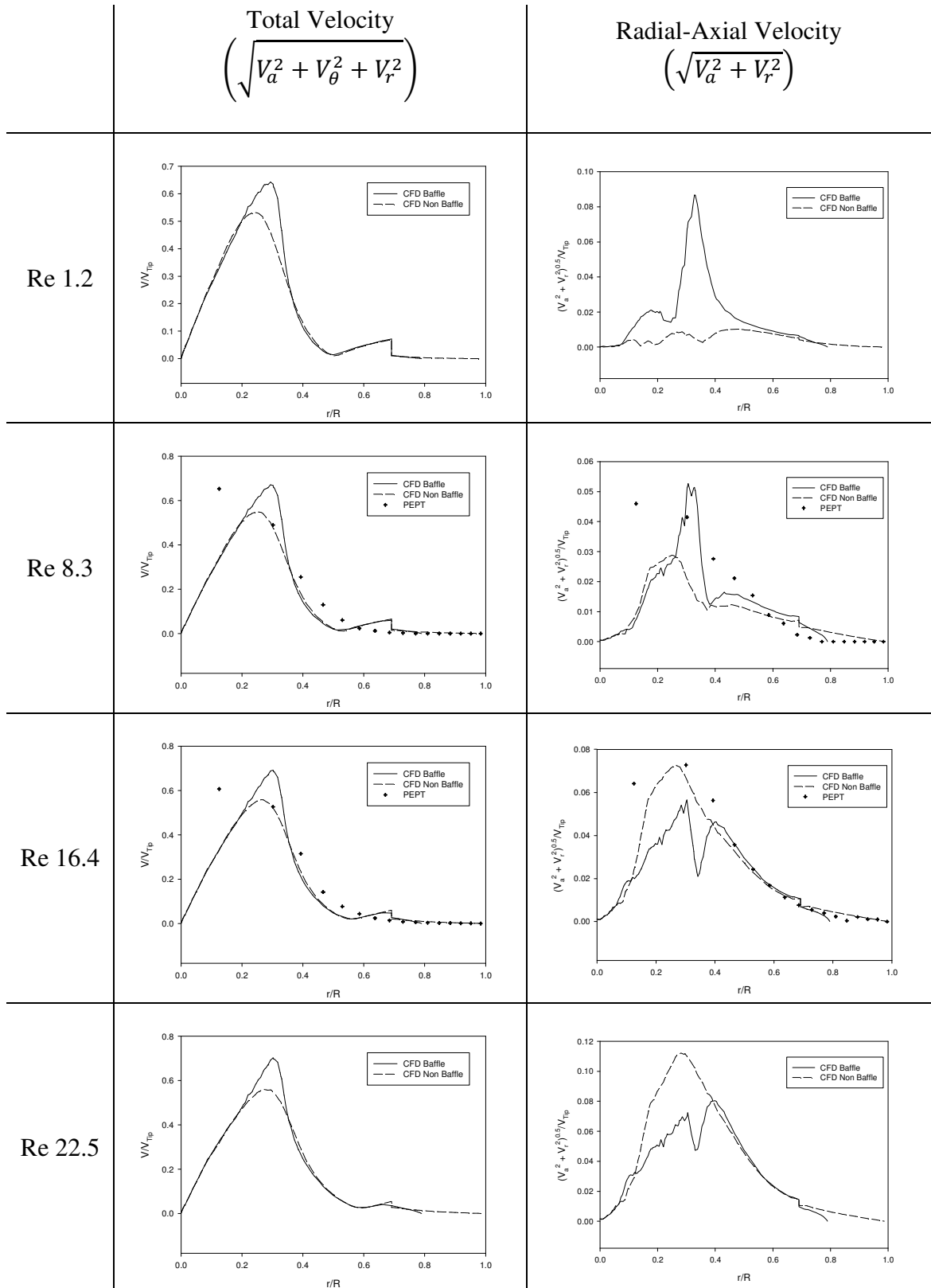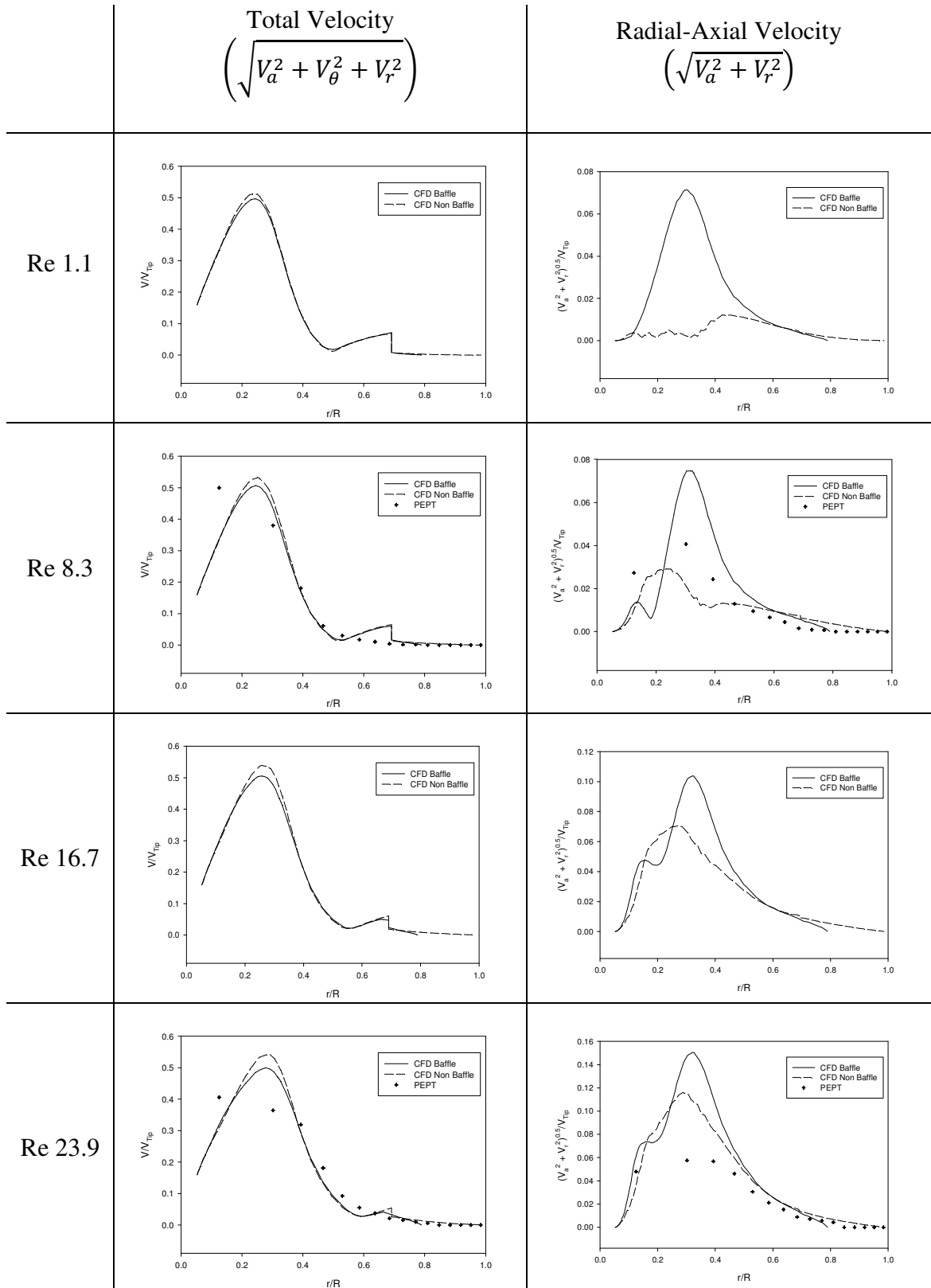
Table 5.4 CFD normalised velocity maxima and minima for CF2 as a percentage of PEPT values

Pumping	Re	V_r		V_θ		V_a		V		$\sqrt{(V_r^2 + V_a^2)}$	
		Max	Min	Max	Min	Max	Min	Max	Min	Max	Min
Down	1.3	-45.0%	-51.5%	-7.9%	-	-92.2%	-81.9%	-8.0%	-	-59.1%	-
	10.9	+15.5%	-18.8%	-20.4%	-	-45.6%	-46.6%	-20.5%	-	-27.6%	-
	22.3	+88.1%	-3.0%	-7.6%	-	+66.6%	+84.9%	-4.9%	-	+47.0%	-
	33.5	+72.2%	+7.7%	-4.4%	-	+70.8%	+120%	+4.2%	-	+109%	-
Up	1.3	-50.0%	-80.5%	-	-9.9%	-86.2%	-76.9%	-10.0%	-	-79.4%	-
	24.5	+64.3%	-11.5%	-	-6.4%	+72.7%	+38.8%	-2.7%	-	+75.0%	-
	35.2	+75.4%	-4.7%	-	-5.6%	+152%	+39.3%	+4.3	-	+122%	-

The large errors in both slurry simulations of the minimum values of both axial and radial velocities could be contributed to the infinite viscosity fix. As these small

velocities would be concentrated on the cavern boundary, in the experiments the velocities drop off sharply where as in the simulations they drop off slowly and thus would not be the same. The maximum velocities for both radial and axial appear more in the impeller region and it may be possible that the PEPT experiments are not picking these up. This is due to the fact that it is a region of high flow and is only recording the tangential component as it is dominant, therefore detecting the slight radial and axial component of velocities in this region is difficult. It is to be seen in the next section whether these large differences allow the CFD to accurately predict the cavern size and shape.

Figure 5.12 and Figure 5.13 show how the velocity and radial-axial velocity both normalised by the tip speed change with radius for both CFD and PEPT for CF2 down and up pumping respectively. These figures are presented in the same manner as Figure 5.9 and Figure 5.10. As with the CF1 CFD data, the total velocities data for both pumping directions are very similar, with the peak deviations as before. So again it makes little difference when choosing what plane you need when dealing with total velocities. Also the radial-axial velocity plots have similarly large deviations at low Reynolds numbers, decreasing with impeller speed, again an artefact of the sliding mesh. The erratic behaviour seen in the CF1 simulations is again evident here for the down pumping case along with the smooth data of the up pumping, again due to the domain interface. Comparing with the PEPT data the fit again is very good in all cases with total velocity data, only under predicting in the impeller region. Comparison is also very good for the two highest speeds for both up and down pumping configurations. At the two lower speeds the fit is only adequate, failing again to capture near the impeller.

Down

Re 1.3   Re 10.9   Re 22.3   Re 33.5

Up

Re 1.3   Re 12.3   Re 24.5   Re 35.2
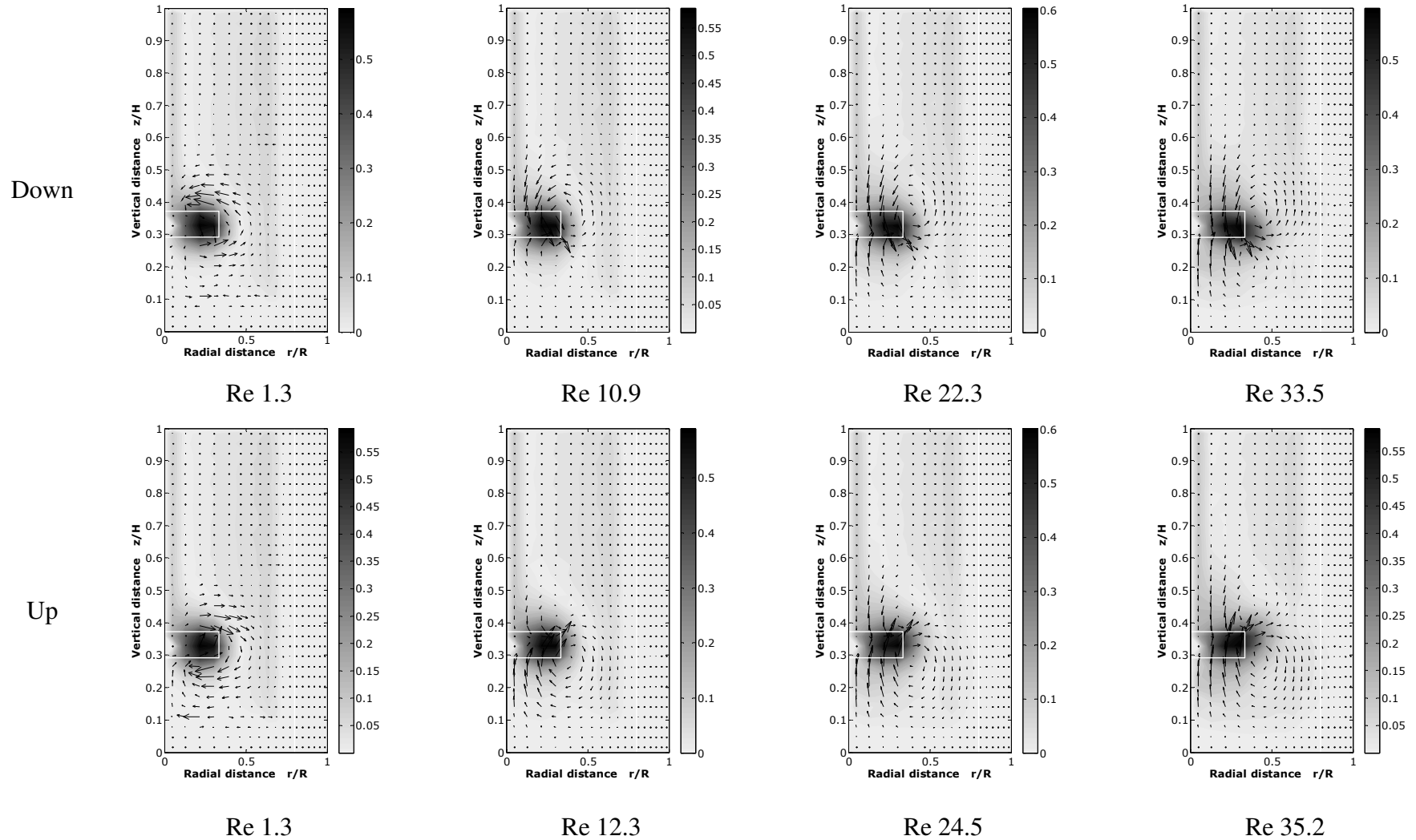
Figure 5.11 CFD normalised velocity flow fields of Cosmetic sample 2 at different Reynolds numbers in down and up pumping configurations
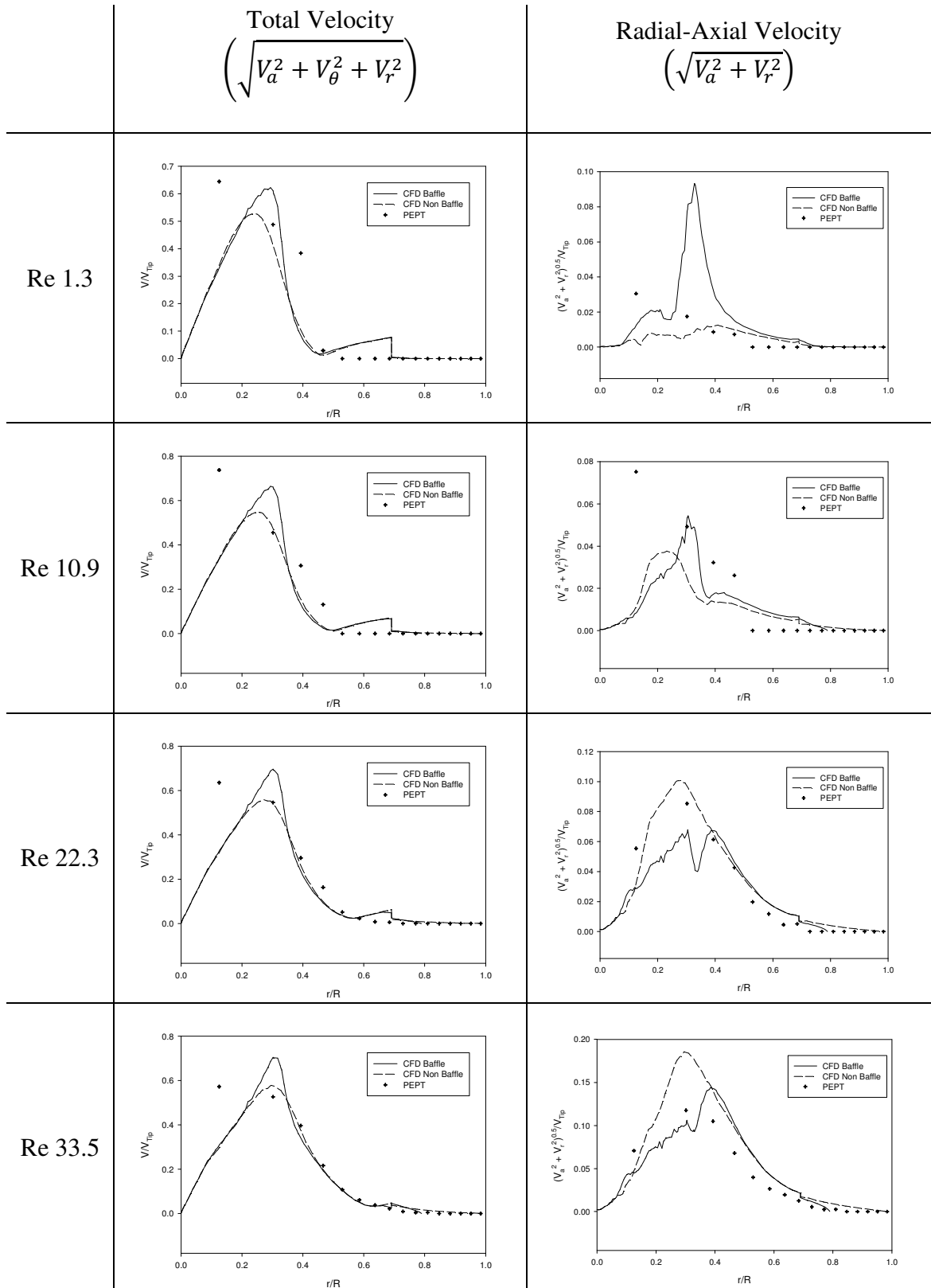
Figure 5.12 Radial plots of total and radial-axial velocity for CF2 down pumping configuration (taken just below the impeller, z/H = 0.297) showing PEPT and CFD data

	Total Velocity $\left(\sqrt{V_a^2 + V_\theta^2 + V_r^2}\right)$	Radial-Axial Velocity $\left(\sqrt{V_a^2 + V_r^2}\right)$
Re 1.3		
Re 12.3		
Re 24.5		
Re 35.2		

Figure 5.13 Radial plots of total and radial-axial velocity for CF2 up pumping configuration (taken just above the impeller, z/H = 0.372) showing PEPT and CFD data

5.6. Comparison of theoretical models, CFD and experimental caverns

Figure 5.14 to Figure 5.25 depict the cavern boundary estimates from experimental PEPT measurements, CFD simulations and mechanistic cavern prediction models for both slurries down and up pumping. Two cavern description methods are used for both the PEPT and CFD results. The first is plotting a contour line when the tangential velocity is equal to 1% of the tip speed, whereas the second is a contour line when the resultant of the radial and axial velocities is equal to 1% of the tip speed as shown below equations (5.3) and (5.4) respectively.

$$0.01V_{Tip} = V_\theta \tag{5.3}$$

$$0.01V_{Tip} = \sqrt{V_a^2 + V_r^2} \tag{5.4}$$

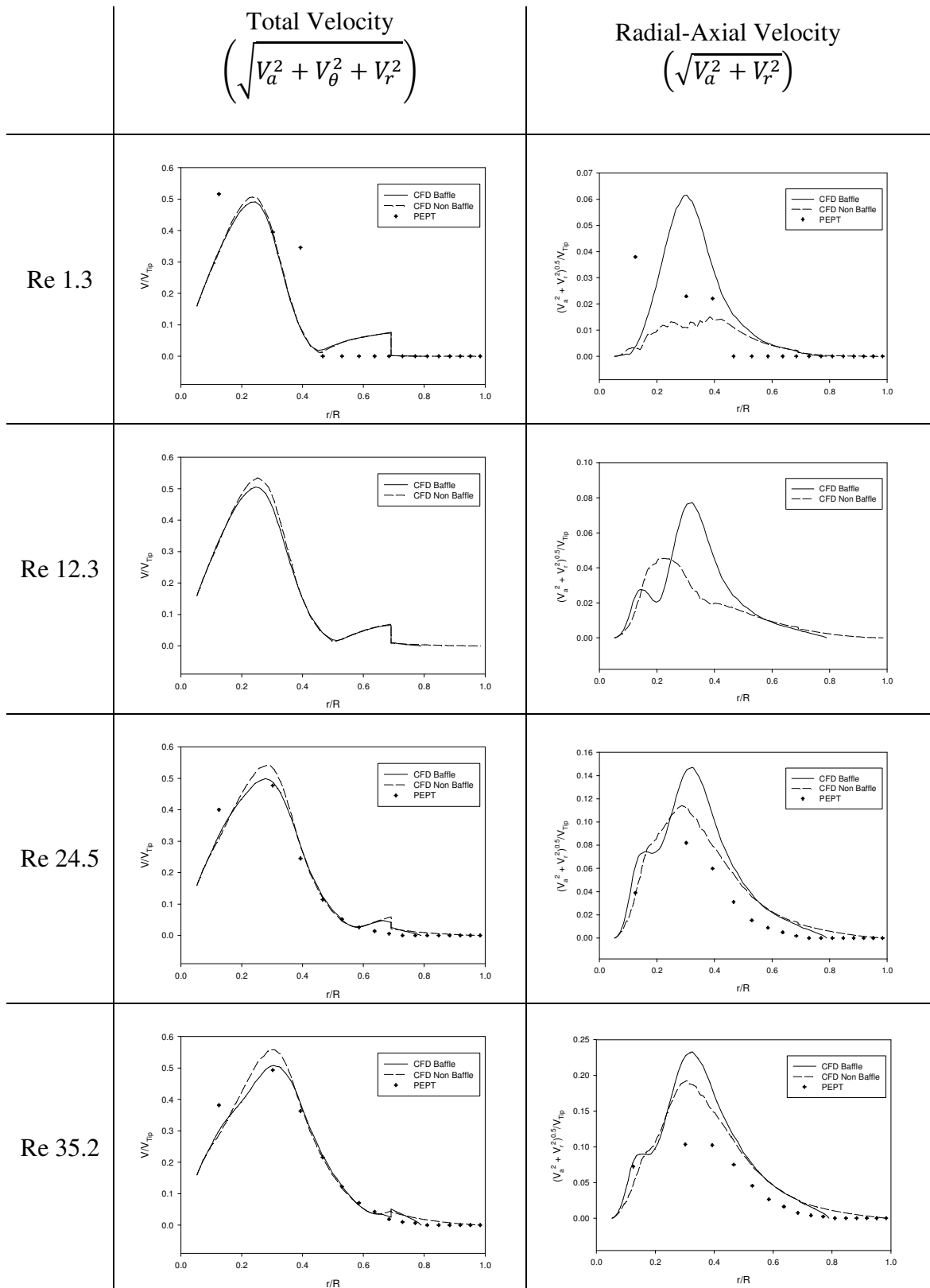Three mechanistic models are used all centred on the impeller, first being a sphere (equation (3.16)) depicted by a semi circle, secondly a toroid (equation (3.18)) depicted by a circle and a cylinder (equation (3.22)) depicted by a rectangle. Firstly for both slurries and pumping directions the spherical and toroidal models severely over predict the cavern size given by both experimental and simulation. The cylindrical model still over predicts for all models especially at low Reynolds for all cases, shown in Figure 5.15, Figure 5.18, Figure 5.21 and Figure 5.24. However at high Reynolds numbers for CF2 in Figure 5.22 and Figure 5.25 the cylindrical cavern model is able to predict the height of the cavern quite well with the radial-axial representation given by CFD, yet the cavern diameter is greatly over predicted.

A major difference notable in all figures is between the two CFD interpretations of the cavern. The tangential model (black dots) centres on the impeller in a toroidal fashion extending along the shaft to the top of the tank, with the down pumping configuration producing a much larger area below the impeller and the up pumping vice versa shown in Figure 5.16, Figure 5.19, Figure 5.22 and Figure 5.25. Cavern area increases with impeller speed but the overall shape remains unchanged. Whereas the radial-axial plot (small cross) produces a much more varied and complex shape even showing eyes of mixing. The shape seems to envelop flow loops rather than the impeller and thus gives a much more realistic shape of a cavern. The size of cavern still increases with impeller speed, encompassing secondary flow loops when formed.

Moving onto the experimental data there is very little difference between the tangential (squares) and the radial-axial (circles) representation shown most clearly in Figure 5.15, Figure 5.18, Figure 5.21 and Figure 5.24. The tangential model on average is larger than the radial-axial plot and the eyes of mixing of both are comparable. However on some of the plots, mainly the CF2 ones, it can be noticed that the radial-axial caverns seem to denote the discharge angle with a slight indent, this small artefact is a real characteristic of cavern shape shown in the two highest Reynolds number cases in Figure 5.21. This, and the fact that the CFD cavern predictions show that the radial-axial approach is better, leads us to believe that the radial-axial interpretation is also the best approach for the PEPT data.

Comparing the radial-axial CFD data with the PEPT data for CF1 show they match the shape and size very well almost capturing the same location of the eyes of mixing shown in Figure 5.14, Figure 5.17, Figure 5.20 and Figure 5.23. For CF2 all CFD

caverns slightly over predict the size of the cavern but their shape is well predicted, even some of the eyes of mixing overlap. The over prediction of the CFD cavern could be more of an under prediction from the PEPT cavern, as the PEPT results are obtained from a tracer path. It is possible that tracer was unable to get close to cavern wall as the velocities drop off to zero and would prefer to just follow the high velocity stream lines. For both cases this is surprising due to the major differences in the maximum and minimum values of the radial and axial velocities, implying that these do not affect the values used to plot the cavern, as well as the simplification of a time dependant slurry as a homogenous fluid with a single rheology. Since the minimum values would fall near the tank walls and the maximum values appear on the impeller tip, it is not surprising that even though they are not accurately predicted they have little bearing on the size of the cavern.

Also the methods used to determine the cavern boundary for simulation and experiments are slightly different because of how the data is obtained. For the PEPT data, the flow pattern velocities used to draw these caverns is restricted to where the particle has visited, there are no velocities present in the data outside of this and thus there is a definite zone of no flow where the cavern boundary just sits inside. For the CFD simulations however there is flow present throughout the entire tank due to the infinite viscosity fix. Due to this there is also no definite boundary where the cavern just fits inside. There is however a sharp drop in velocities to a point where the viscosity reaches the minimum value it is inside of this imaginary boundary that the cavern fits. Again despite this large difference the CFD is able to predict the cavern boundaries fairly well.
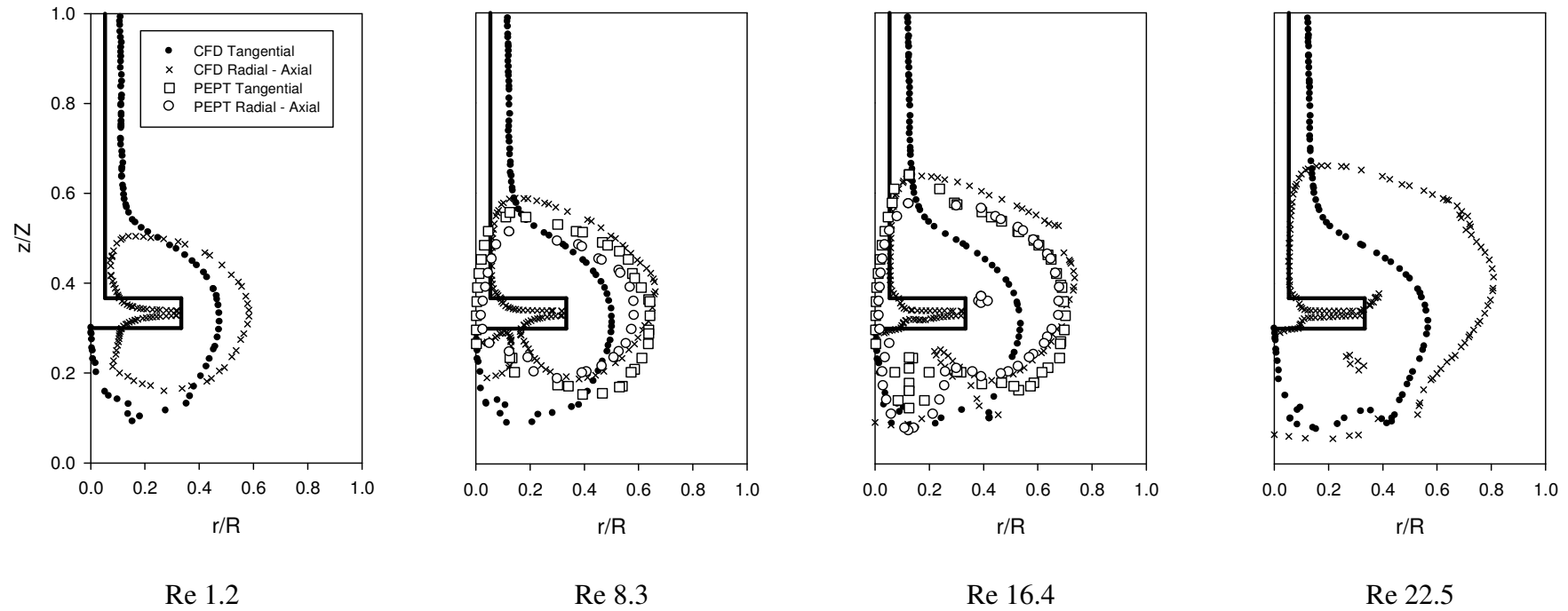
Figure 5.14 Cavern boundary plots for Cosmetic sample 1 (CF1) down pumping showing CFD and PEPT data

Figure 5.15 Cavern boundary plots for Cosmetic sample 1 (CF1) down pumping showing PEPT data and cavern prediction models
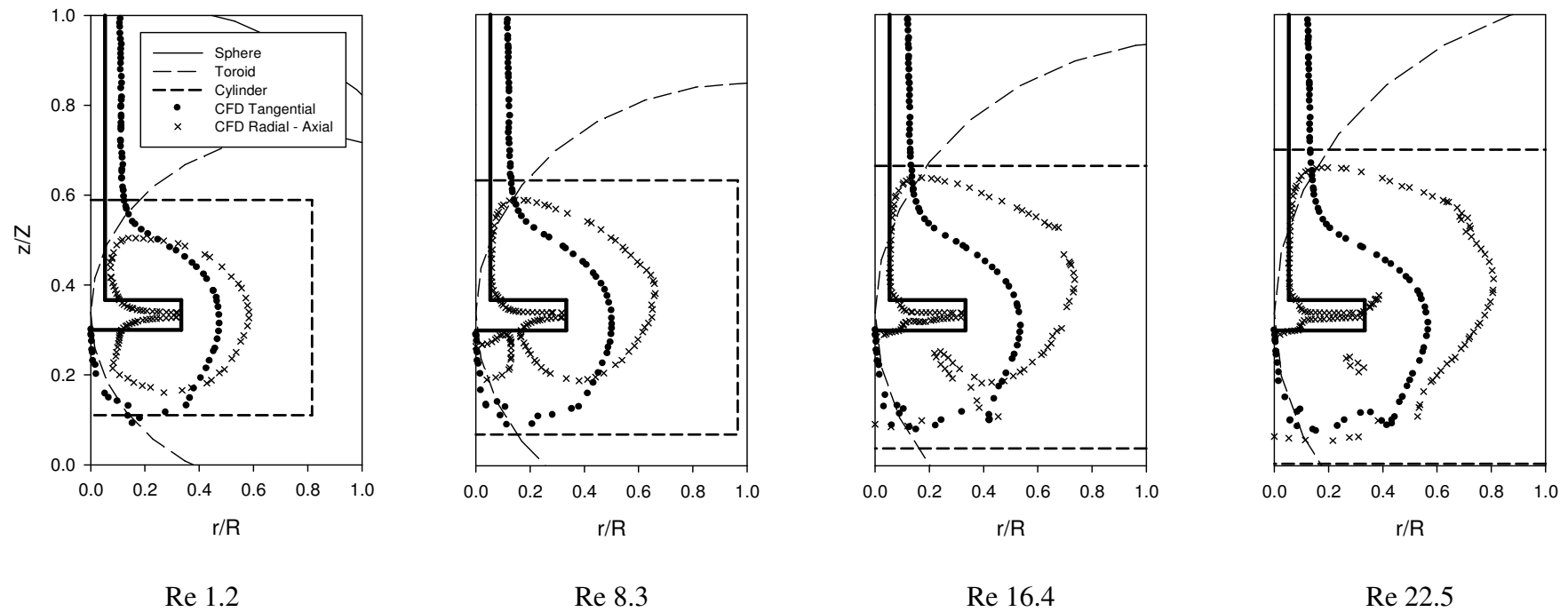
Figure 5.16 Cavern boundary plots for Cosmetic sample 1 (CF1) down pumping showing CFD and cavern prediction models
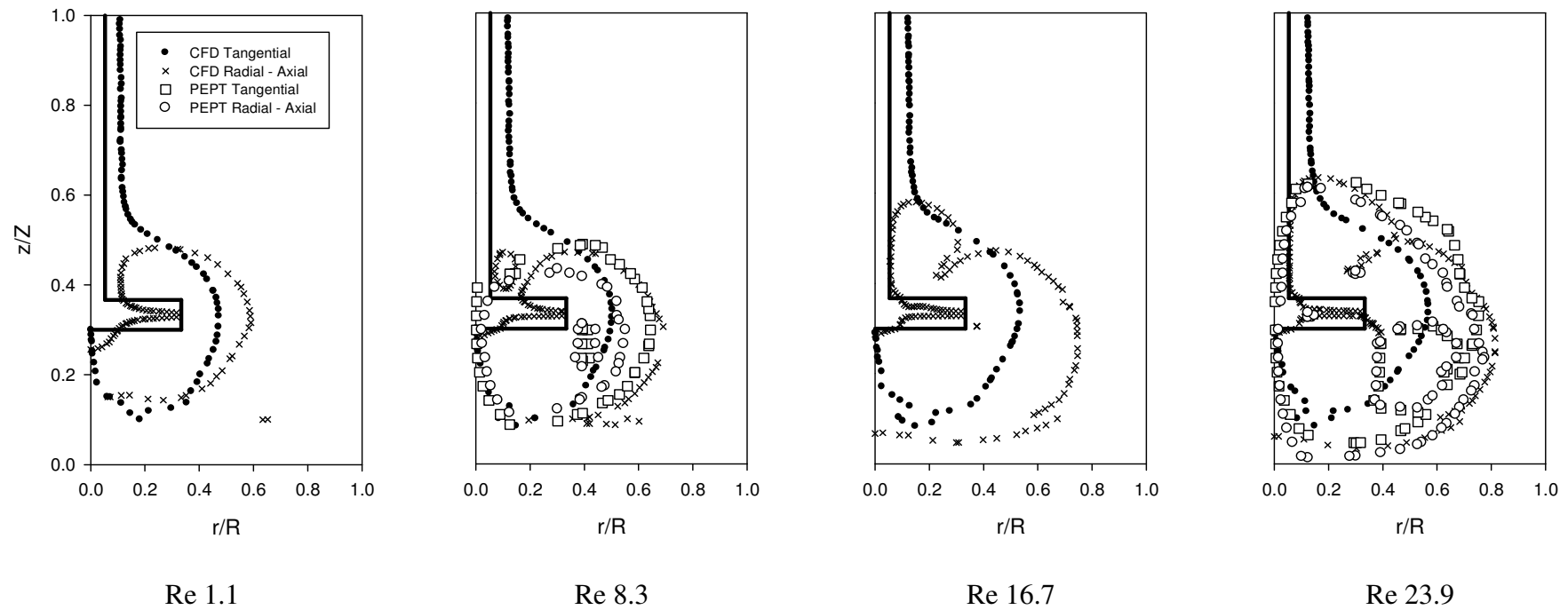
Figure 5.17 Cavern boundary plots for Cosmetic sample 1 (CF1) up pumping showing CFD and PEPT data
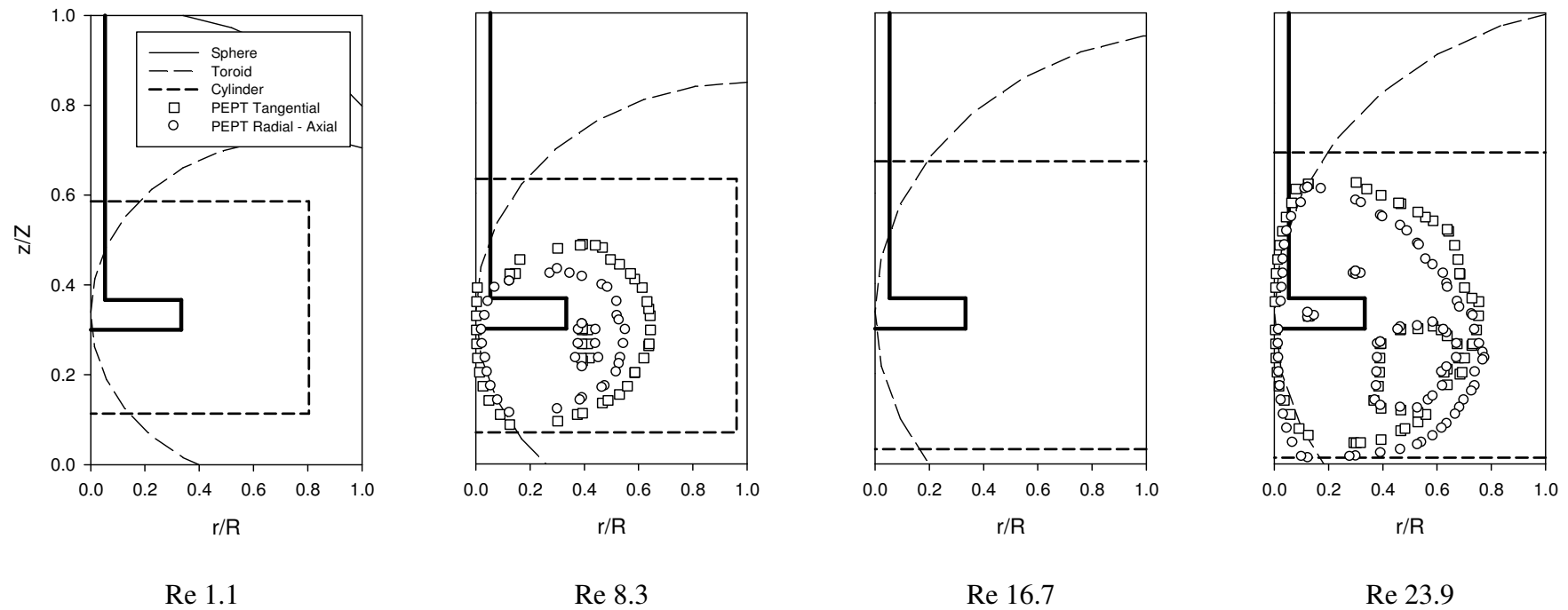
Figure 5.18 Cavern boundary plots for Cosmetic sample 1 (CF1) up pumping showing PEPT data and cavern prediction models
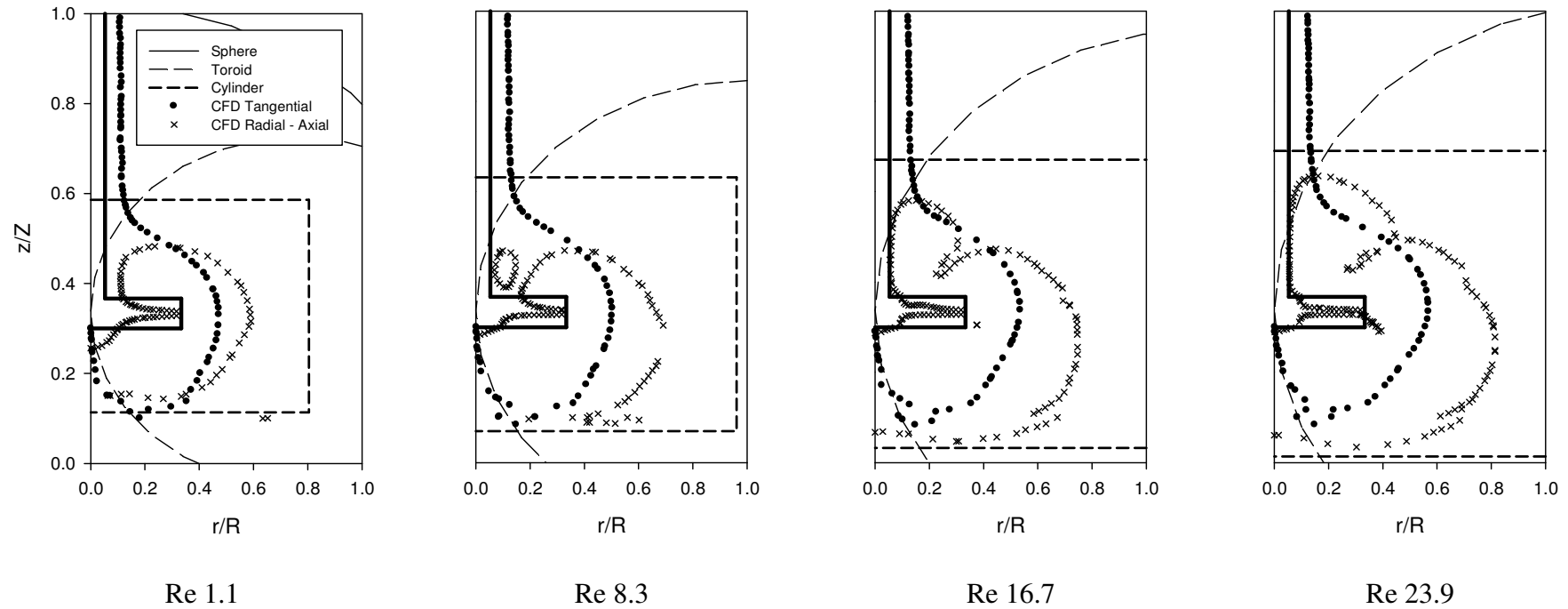
Figure 5.19 Cavern boundary plots for Cosmetic sample 1 (CF1) up pumping showing CFD and cavern prediction models
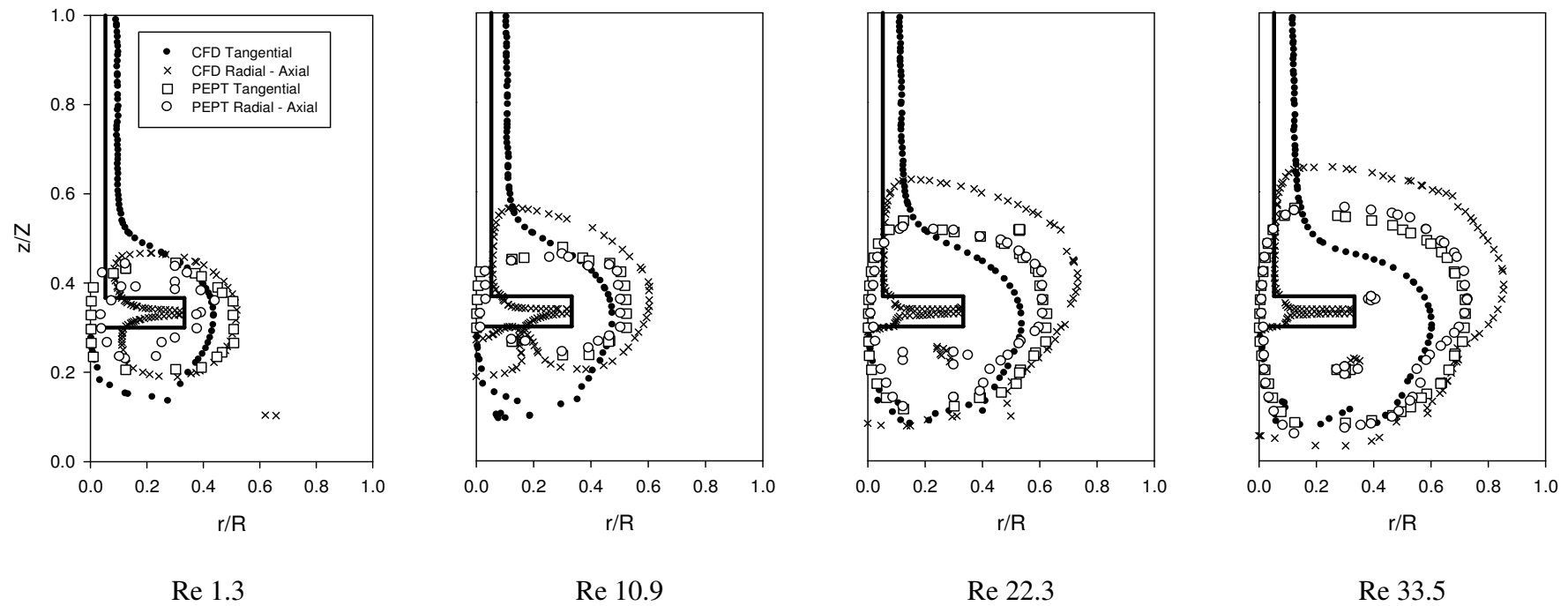
Figure 5.20 Cavern boundary plots for Cosmetic sample 2 (CF2) down pumping showing CFD and PEPT data
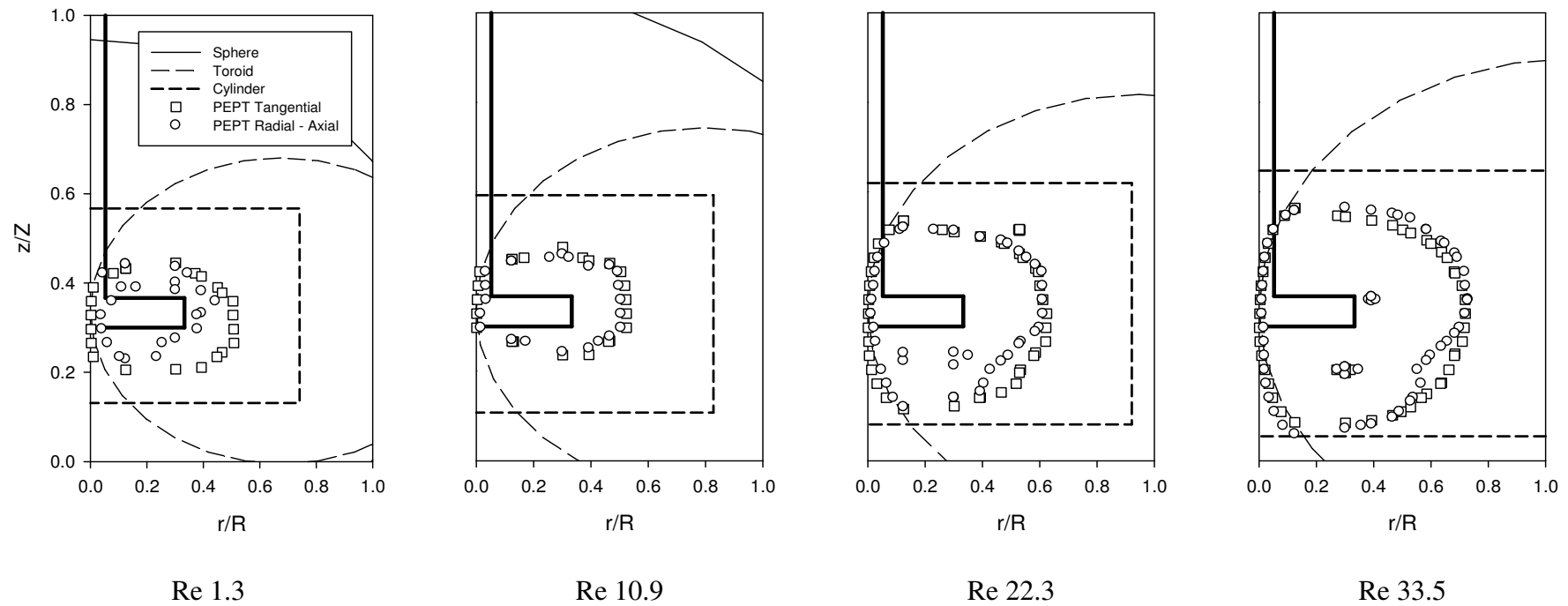
Figure 5.21 Cavern boundary plots for Cosmetic sample 2 (CF2) down pumping showing PEPT data and cavern prediction models

Re 1.3　　　　　　　Re 10.9　　　　　　　Re 22.3　　　　　　　Re 33.5
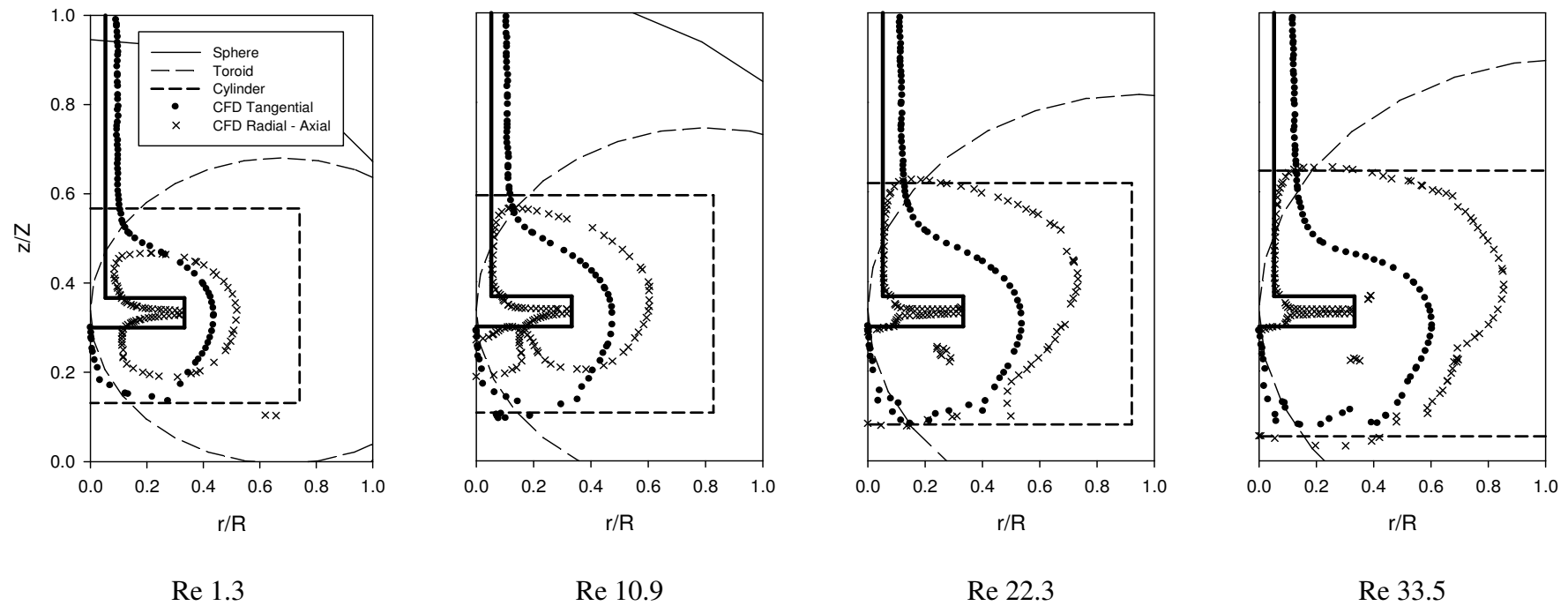
Figure 5.22 Cavern boundary plots for Cosmetic sample 2 (CF2) down pumping showing CFD and cavern prediction models
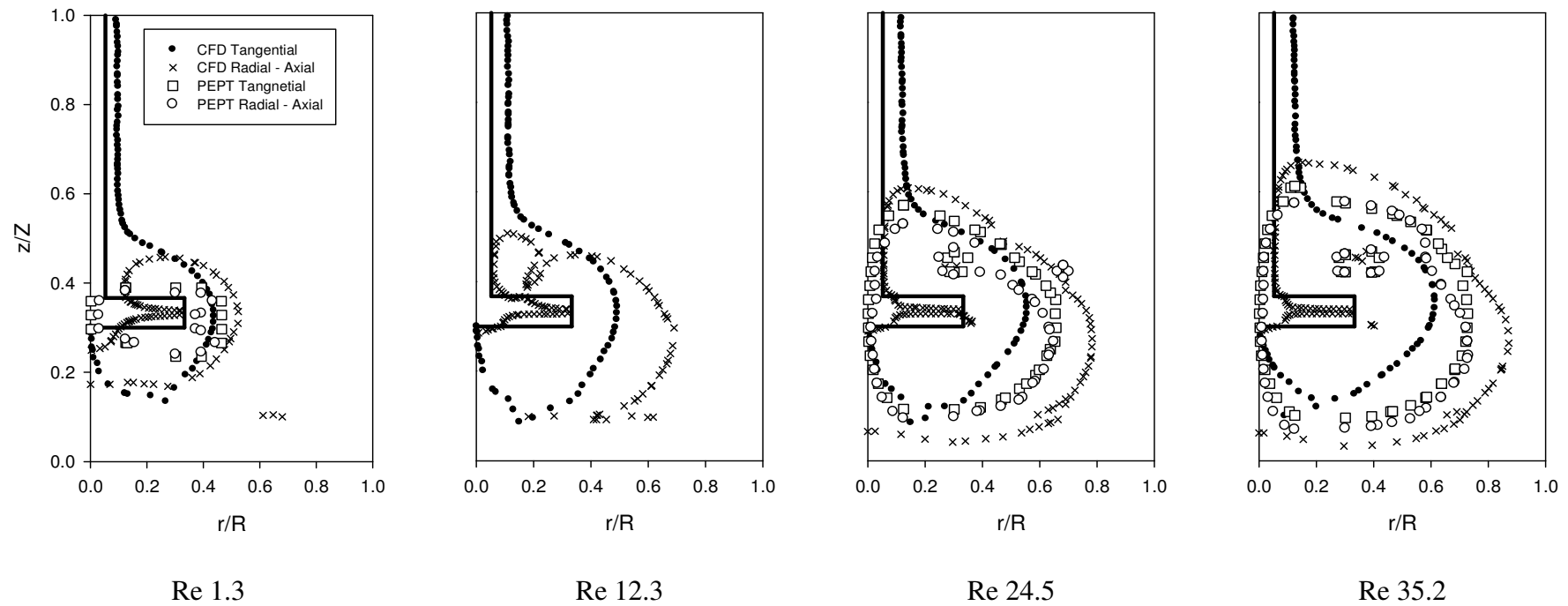
Figure 5.23 Cavern boundary plots for Cosmetic sample 2 (CF2) up pumping showing CFD and PEPT data
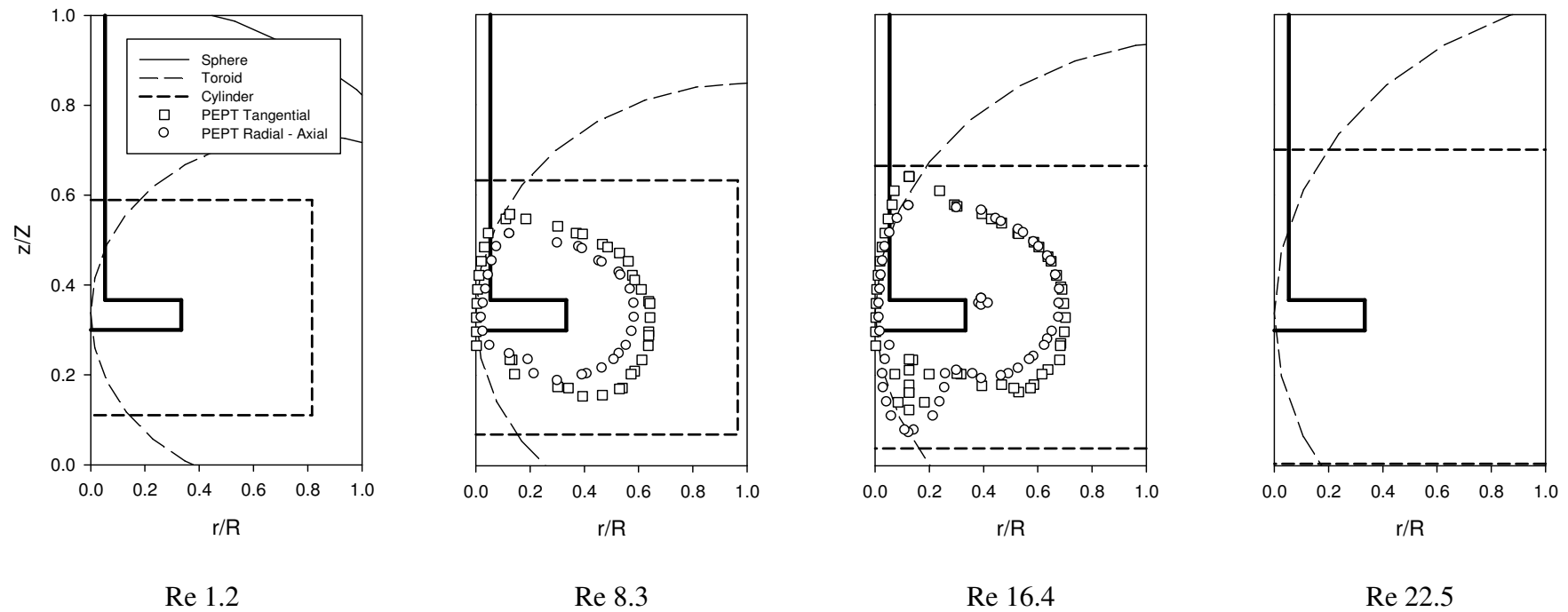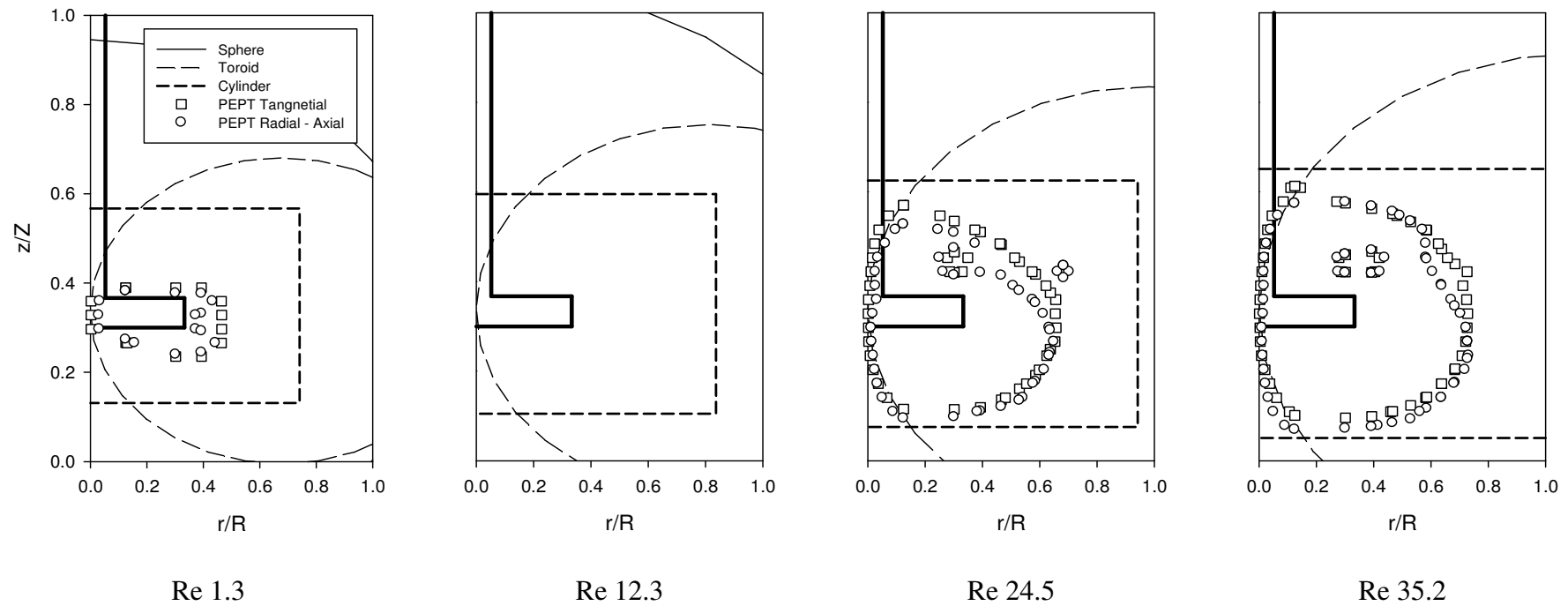
Figure 5.24 Cavern boundary plots for Cosmetic sample 2 (CF2) up pumping showing PEPT data and cavern prediction models
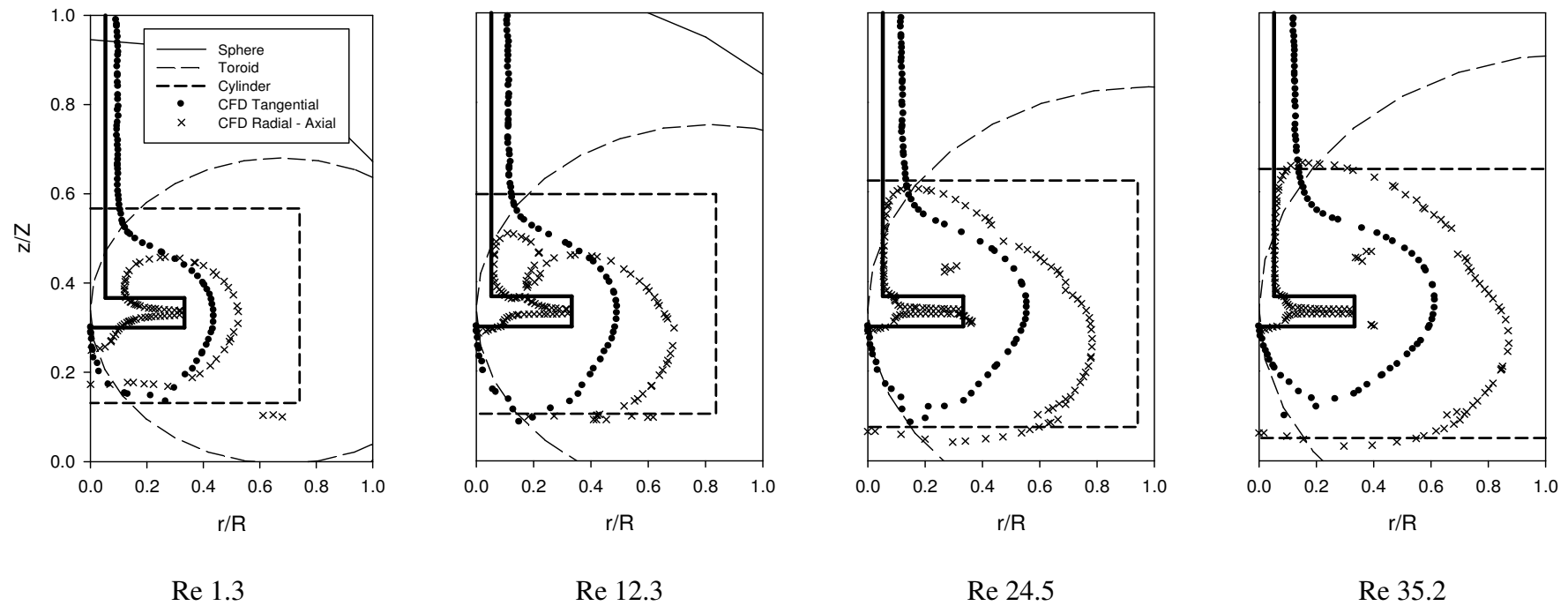
Figure 5.25 Cavern boundary plots for Cosmetic sample 2 (CF2) up pumping showing CFD and cavern prediction models

5.7. Conclusions

The PEPT technique was successful in enabling flow pattern data of two complex opaque shear thinning slurry systems to be analysed. This type of data are unique since it enables the measurement of overall flow patterns in opaque systems similar to the optical techniques for transparent fluids. CARPT can provide similar data obtained through PEPT, but to the authors knowledge this has not been done yet on these types of fluids on the same scale of experiments completed in this chapter.

CFD was able to predict flow patterns obtained by the PEPT technique however they differed slightly on the discharge angle with CFD being more axial at high impeller speeds. Overall velocities where predicted rather well on a whole with only a few giving predictions of over 10% of the maximum value. However the radial and axial components maximum and minimum values are poorly predicted. Radial velocity plots of both CFD and PEPT matched very well for total velocities, while CFD over predicted the radial-axial velocities. Comparison between the two CFD plane data proved that at high velocities when the flow loops do not interfere with the baffles or tank wall that it does not matter which plane is taken.

All cavern prediction models were grossly over predicting the cavern size of all experiments with the cylindrical model giving the best fit for cavern height at high Reynolds numbers. A cavern model that would incorporate more rheological data should improve accuracy as well as more accurate cavern shape such as a kidney or pear. The problem with latter is that both these shapes are quite difficult to describe

through a single equation. Radial-axial interpretation of cavern boundary was seen to be a more realistic shape for cavern prediction in the simulations. Comparison of both PEPT and CFD radial-axial caverns showed reasonable agreement with both size and shape for CF1 however for CF2 the size of the caverns were slightly over predicted. These fits are very good despite the simulations simplification of a time dependent slurry to a homogenous fluid with a single rheology, meaning that the time dependency had little effect on determining the cavern boundary. Thus enabling the use of CFD to predict cavern shapes and a reasonable approximation of cavern size for shear thinning slurries at low Reynolds numbers.

CHAPTER 6

MIXING OF A SHEAR THICKENING SLURRY

6.1. Introduction

Shear thickening materials are fairly rare in industry, but are present and need to be understood. Most shear thickening materials are complex slurry systems containing many different particulate phases and chemical components; it is the interaction between these many types of structures that lead to the slurry becoming more viscous with increase in shear. Since these shear thickening slurries contain high proportions of solid material they also have an apparent yield stress and thus when mixed at low Reynolds numbers can generate caverns, which as mentioned previously is very detrimental to mixing. It is unknown what the effect of the shear thickening rheology has on the generation of caverns, their shape and size and the mixing that goes on inside them since all of these types of slurries are opaque and thus no optical techniques can be used to study them.

6.2. Summary

This Chapter deals with the flow patterns and caverns formed when mixing a shear thickening slurry using both experimental PEPT measurements and CFD simulations at different speeds in both down and up pumping configurations. The shear thickening slurry used is based on china clay and the full rheological data are presented earlier in section 3.1.2.3. The slurry fits to a Herschel Bulkley model with yield stress and flow behaviour index greater than one, also it is shear thinning with time. Experiments were carried out in the small tank (described in section 3.1.1.) and an exact replica was used

in the simulations with the corresponding rheology for each run.. A single rheology was used for each simulation and thus does not represent the time dependency that the slurry exhibits. Flow patterns and cavern size and shape data are compared with the shear thinning foundation cream results and with their corresponding simulations. Cavern prediction models were compared with the cavern data produced from both experiments and simulations.

6.3. Power measurements

Power measurements were taken of the china clay slurry, the range of impeller speeds for these measurements were wide enough to cover the Reynolds numbers of the experiments undertaken. Measurements were undertaken in the down pumping configuration as it was assumed that pumping direction is inconsequential, as in the next chapter there is very little difference between power readings for paper pulp. The rheology of the power measurements were slightly different than the experimental results but this was unavoidable due to the time dependant nature of the material, since its the same fluid and the rheology was only slightly different the following power curves should still apply. Figure 6.1 shows the Power number versus Reynolds number plot for the china clay material, displaying up and down ramp of impeller speed. The measurements were started at rest then ramped up to 800 rpm and then back down again to rest. The ramp down of impeller speed falls beneath the ramp up showing the reduction in viscosity with time of the shear thickening china clay. Both ramps start in a linear region and start to flatten off at higher Reynolds numbers indicating that the first two speeds studied are in the laminar region with the latter two in the low to mid transitional regime. In comparison with Newtonian and shear thinning Power number

plots the shear thickening data shows a remarkable resemblance in the shape of the curves, if a little bit erratic.
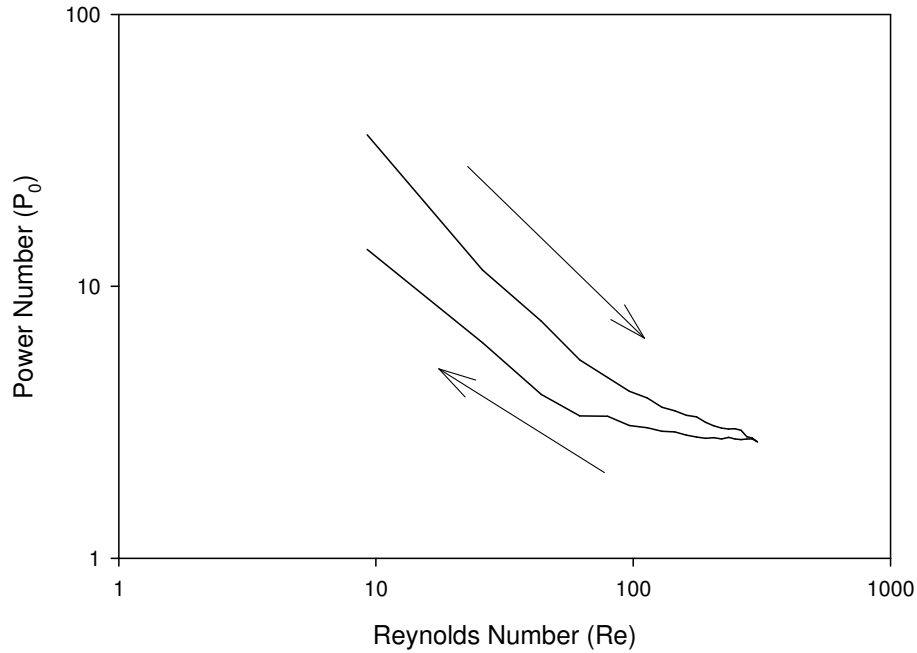
Figure 6.5 Power number versus Reynolds number plot for china clay including both up and down ramps for the PBTD

6.4. PEPT analysis of slurry

Figure 6.2 shows the flow patterns obtained through PEPT for the mixing of china clay in the small tank (described in section 3.1.1) for both up and down pumping configurations at different Reynolds numbers. The arrows denote the 3D velocity vectors on a 2D plane, thus the component coming out of the plot cannot be seen. The grey scale contour plots depict the magnitude of the velocity vector normalised by the impeller tip speed as calculated below in equation (6.1).

$$Normalised\ Total\ Velocity = \frac{\sqrt{V_a^2 + V_\theta^2 + V_r^2}}{\pi ND} \qquad (6.1)$$

Re 30.0   Re 237.8

Re 69.2   Re 215.2   Re 767.9
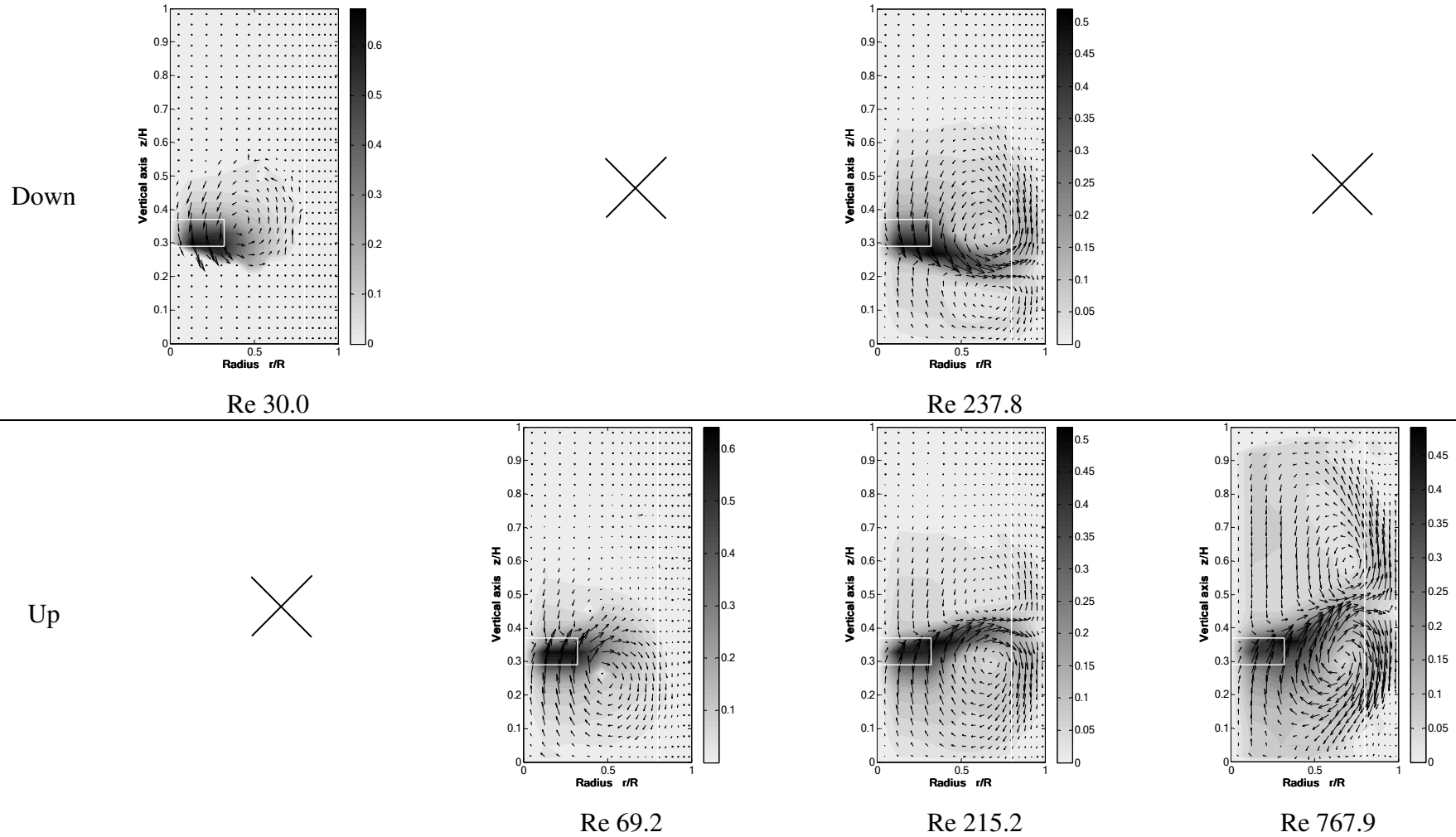
Figure 6.6 PEPT normalised velocity flow fields of china clay slurry at different Reynolds numbers in down and up pumping configurations

PEPT plots produced throughout the thesis are the entire flow field azimuthally averaged on a single plane, so they do not take into account locations of baffles or the impeller. The shear thickening material experiments required the least amount of manual mixing to move a trapped tracer from a stagnant zone into flow, when it did occur the PEPT cameras were turned off during this period. This is due to material being the thinnest used for PEPT experiments, despite its shear thickening behaviour. Not all PEPT experiments were successful; where not enough data were recorded for a full flow analysis to be performed, therefore only the successful experiments are shown. Some of these unsuccessful experiments showed the tracer sitting outside of the flow region for large periods of time, proving that there is not flow outside of the cavern boundary.

The flow loops recorded are a lot different compared to the shear thinning foundation cream slurry experiments presented earlier in Chapter 5. However there are some similarities, such as a large flow loops generated above the impeller for down pumping and vice versa for up pumping at low Reynolds numbers. Once the Reynolds numbers enter the transitional regime differences appear, namely a jet of flow extends from the impeller to the tank wall, maintaining an almost constant velocity. For the up pumping experiment at $Re = 215$ this jet moves from just above the impeller and then radially to the tank wall, once the impeller speed is increased to give a $Re = 767$ this jet becomes almost 45 degrees to the impeller all the way to the tank wall. Similar jets can be seen for the down pumping case at $Re = 237$ but pumping in the opposite direction. The jet for the down pumping $Re = 633$ is assumed to be similar to the up pumping case but with a slightly less angle than 45 degrees due to possible effects of the tank floor. If the clearance were set to a half, mirror images are highly probable, as this would reduce the

influence of the tank floor. This constant velocity jet produced at transitional Reynolds could be explained by the shear thickening behaviour of the slurry. Since the flow behaviour index is above one (section 3.1.2.3) the apparent viscosity would increase with shear rate and thus impeller speed. For any mixing experiment the shear rate would drop the further away you are from the impeller, as the impeller is the device that imparts shear into the fluid and shear is dissipated by the fluid. Thus if the shear rate is dropping with distance from the impeller the viscosity would also drop. This drop in viscosity would enable fluid to flow more easily and enable velocities to be maintained despite the drop in shear rate; a conservation of momentum.

Further distinguishing features are presented by the moving eyes of mixing, as for the shear thinning slurry the eyes of mixing remained close to the impeller. For this shear thickening slurry the eyes of mixing move with jets of constant velocity towards the walls of the tank, appearing above and below where the jet slows down and starts to rush up the walls of the tank. Again though this is only present in the cases when the Reynolds numbers are in the transitional regime, the laminar cases appear very similar to shear thinning cases. Outside of the flow loops the material behaves as a stagnant region of non-mixing inferring the detrimental implications of mixing with caverns. It does seem however that the mixing inside shear thickening material caverns is much better than shear thinning ones due to the presence of these constant velocity jets enabling more flow in the tank. However the torque required to get the mixing shown in the highest Reynolds number case for up pumping would be too impractical so better mixing configurations should be used to achieve the same effect.

Impeller tip speed normalised maximum velocities recorded for the shear thickening china clay slurry shown in Table 6.1 decreased with Reynolds number for both pumping configurations. Starting at 65% decreasing to 49% of the tip speed for up pumping, this is due to the shear thickening behaviour of the slurry as the higher impeller speed would create higher viscosities and thus a much lower maximum velocity.

Table 6.1 Velocity maxima and minima normalised to the impeller tip speed for China clay PEPT data

Pumping	Re	V_r		V_θ		V_z		V		$\sqrt{(V_r^2 + V_z^2)}$	
		Max	Min	Max	Min	Max	Min	Max	Min	Max	Min
Down	30.0	0.1005	-0.0423	0.6603	0	0.0519	-0.1252	0.6758	0	0.1440	0
	237.8	0.2650	-0.0629	0.4787	0	0.1253	-0.1696	0.5204	0	0.2687	0
Up	69.2	0.1444	-0.0512	0	-0.6162	0.1440	-0.0534	0.6416	0	0.1786	0
	215.2	0.2697	-0.0665	0	-0.4739	0.1667	-0.1340	0.5198	0	0.2744	0
	767.9	0.1371	-0.0964	0	-0.4738	0.1195	-0.1352	0.4917	0	0.1693	0

The velocity is mainly tangential, as for the shear thinning slurry. However the radial and axial component has a much larger contribution to overall velocity than the shear thinning slurry as shown in Figure 6.3; this is easily attributed to the constant velocity jets. Radial and axial velocities do increase with impeller speed for both pumping configurations, except for the highest Reynolds number case for up pumping. This is probably attributed to the 45 degree constant velocity jet.

| Radial velocity | Tangential Velocity | Axial Velocity |
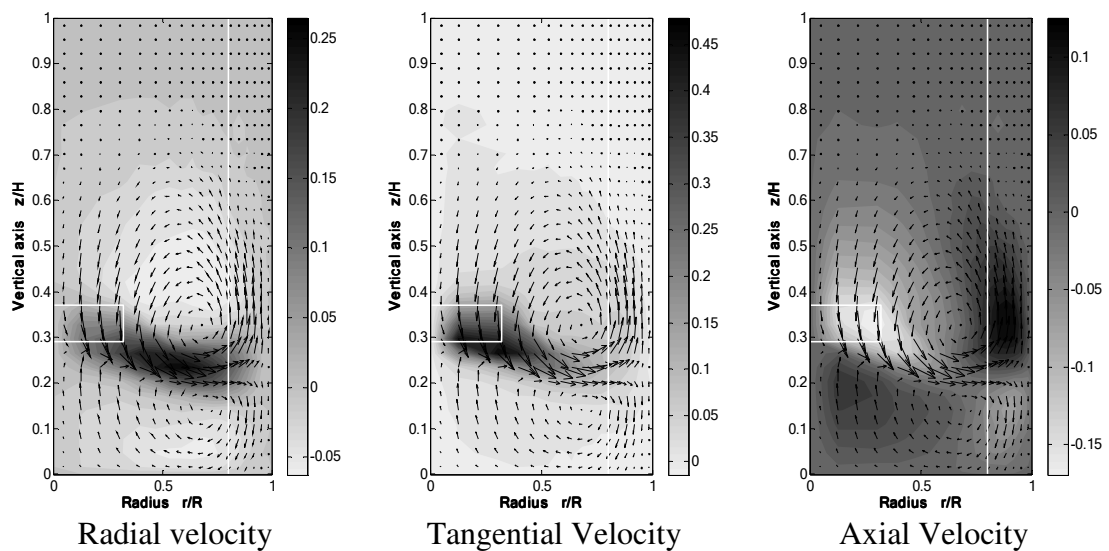
Figure 6.3 Example of PEPT normalised velocity flow fields showing the three velocity components

Chapter 6 – Mixing of a Shear Thickening Slurry

PEPT allows the spatial tracer occupancy distribution to be determined, which offers an additional tool for characterising fluid flow behaviour within the vessel, this is further explained in Chapter 5 Section 5.4. An occupancy plot of two experiments at similar Reynolds numbers is presented below in Figure 6.4. Both plots are very similar, the highest value of over 6 is only seen in the down pumping case in the upper part of the tank near the baffle, this is probably due to a trapped tracer. Overall the tracer spends equal time in each volume of the tank except for the stagnant region at the top of the tank, almost matching flow areas. Occupancy in the constant velocity jet is lower as this is the highest velocity region and thus the tracer would spend less time there.
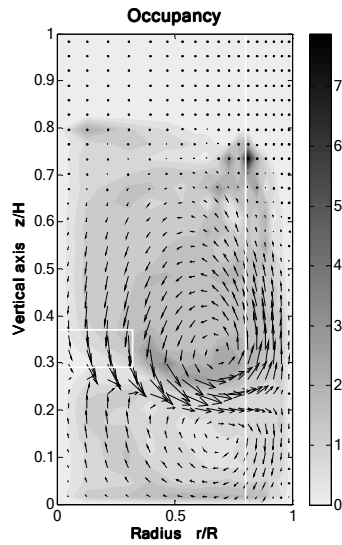
Re 237.8 Down pumping   Re 215.2 Up pumping
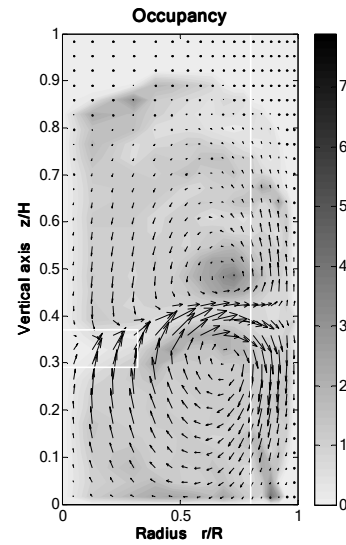
Figure 6.4 PEPT occupancy data for China clay down and up pumping

Figure 6.5 shows how velocity and radial-axial velocity both normalised by the tip speed change with radius for all PEPT experiments carried out for the china clay. Normalised velocity is described above in equation (6.1) and the normalised radial-axial velocity is defined below in equation (6.2).

$$Normalised\ Radial - Axial\ Velocity = \frac{\sqrt{V_a^2 + V_r^2}}{\pi ND} \qquad (6.2)$$

Down pumping data was taken at a fixed height just below the impeller blade (z/H = 0.297) while up pumping was taken at a fixed height just above the impeller blade (z/H = 0.372). These positions were taken as they are the discharge paths of the two pumping configurations. The most striking difference here with the normalised total velocity plots compared with the shear thinning material is the gradient of the drop off after the peak. The gradient presented here, more notably for the up pumping case, means velocities are maintained at higher values further into the tank. This is consistent with the constant velocity jet seen in the flow loop plots presented above.

For down pumping as the impeller speed is increased normalised total velocities drop near the impeller, this is similar with the shear thinning plots (Figure 5.6 and 5.7) however for the up pumping plots the reverse is presented. The radial-axial plots for the up pumping case increase in value with increase in impeller speed, maintaining similar patterns. The down pumping however only has a similar pattern at Re 237.8, the Re 30 flow pattern does not match due to that it has the lowest Reynolds number and a much smaller and single flow loop. The gradient of decline of the normalised radial-axial velocity is also much less sharp than the shear thinning case, emphasising once again the constant jet idea, as this jet is mainly radial.

Down pumping

Up pumping

Total Velocity

$$\left(\sqrt{V_a^2 + V_\theta^2 + V_r^2} \right)$$

Radial-Axial Velocity

$$\left(\sqrt{V_a^2 + V_r^2} \right)$$
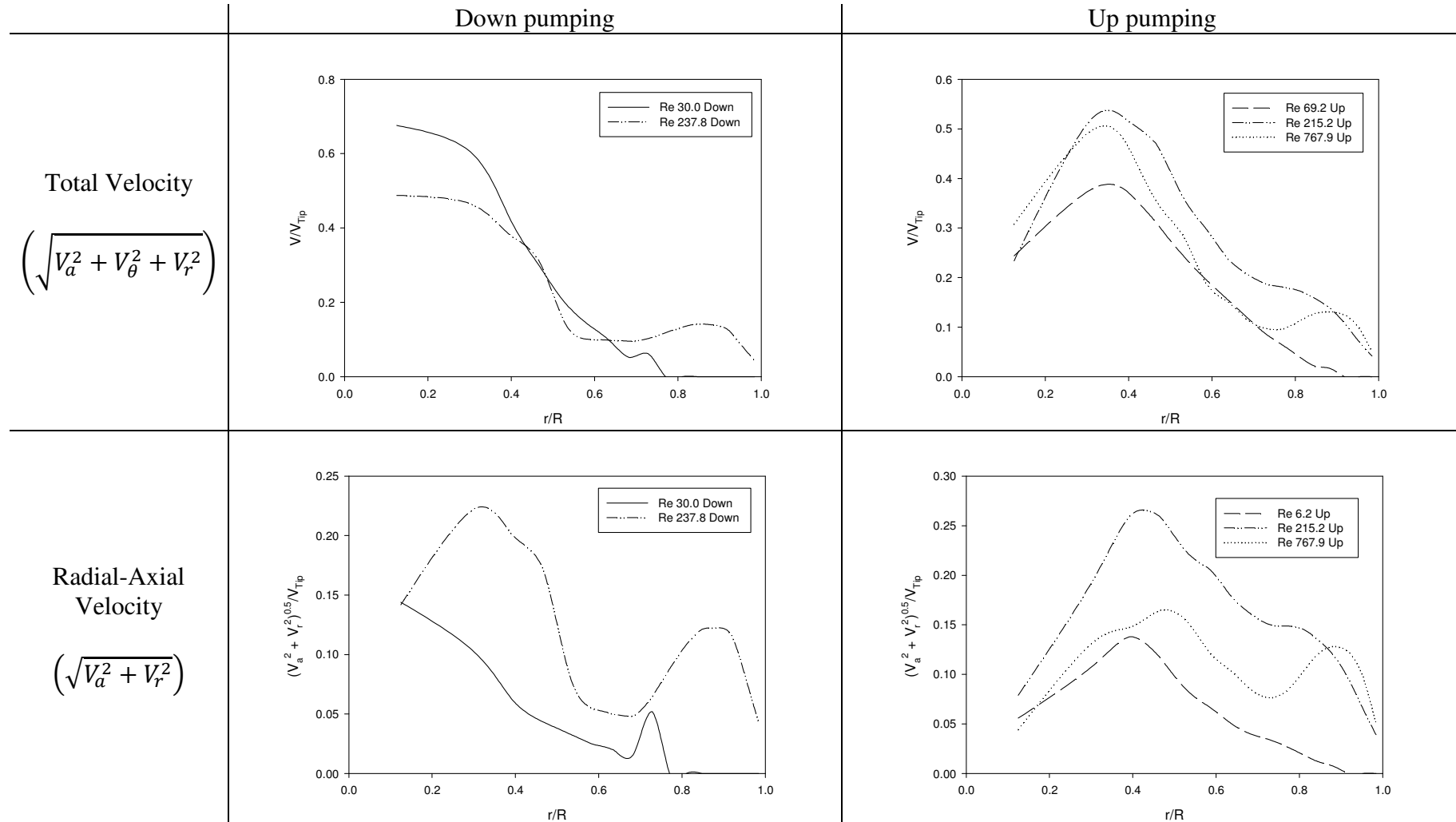
Figure 6.5 Radial plots of China clay PEPT data total and radial-axial velocity for up (just above impeller, z/H = 0.372) and down (just below impeller, z/H = 0.297) pumping configurations

6.5. CFD simulations

CFD simulations were performed to mimic all the PEPT experiments using a single rheology that was obtained at the start of each experiment. Thus each simulation estimates the slurry to be a completely homogenous fluid with a single rheology ignoring its structure and time dependency. All CFD plots produced throughout the thesis are a slice of the entire flow field taken directly between two of the baffles, not azimuthally averaged.

Figure 6.6 shows the data obtained through the simulations and is presented in the same manner as for the PEPT experiments. The CFD data has been recalculated on the same grid as the PEPT experiments to enable a better comparison rather than use the original data that is calculated on an unstructured mesh. As with the shear thinning slurry the main difference is that there is small flow outside of the main flow loops where in the PEPT (Figure 6.2) there was none at all. The two reasons could be that CFD does not require a tracer to calculate flow and can calculate smaller velocities at higher spatial resolution with the second reason being CFD's inability to handle yield stress correctly. This was explained in detail in chapter 5 and is assumed that the main problem is the yield stress. Again due to some of the PEPT not obtaining enough points to obtain a flow field only a limited comparison can be achieved, yet if the CFD matches the results it could be used to estimate the missing ones.

Comparing the down pumping cases first there are major differences apparent in the flow loops. In the simulations for the lowest speed the flow loop is very small and wholly located around the impeller where the experiments produced a much larger loop

almost touching the baffles. Also the discharge angle is much more radial in the simulations and more axial in the experiments. As for the higher Reynolds number case the constant velocity jet is present and the area the flow loops encompass is roughly the same. However the angle of discharge the jet takes is much less radial than the experiments seem to suggest, this causes the eye of mixing above the jet to be slightly lower in the simulations and the jet is much less intense than seen in the experiments. Also the secondary lower loop and lower eye of mixing is much less defined maybe due to the proximity of the jet to the bottom of the tank.

Moving onto the up pumping configuration similar differences are seen that were found in the down pumping case. Much smaller flow loops at the lowest Reynolds number case in the simulations with a predominantly more radial discharge angle. Moving into the transitional regime experiments where the constant velocity jet appears CFD predicts a much more axial discharge angle which the jet follows. Even though the jet is predicted it is less concentrated than the PEPT experiments seem to suggest. The lower eyes of mixing for both of these simulations are however very similar to the PEPT experiments despite the difference in discharge angle. The secondary loop and eye above the jet are again less predominant in the simulations but both seem to give similar areas of coverage within the tank.

Table 6.2 shows the differences in the maximum and minimum values of the simulations compared to the experiments. Tangential velocity predictions by CFD match the PEPT results quite well with only the lowest Reynolds number case for up pumping going over 10% error. However the radial and axial components are either grossly over predicted or under predicted, causing the overall velocity predictions to be

over predicted at high Reynolds numbers. Thus, for the simulations the tangential component becomes less dominant with increased impeller speed. Radial velocities fluctuate from 100% to 4% in no discernable pattern however they always over estimate the experimental values. The axial velocities maximum and minimum values are underestimated at low Reynolds numbers then grossly over estimates at higher Reynolds numbers. Thus the flow is becoming much more axial which can be seen from the discharge angles.

Table 6.2 CFD normalised velocity maxima and minima for China clay as a percentage of PEPT values

Pumping	Re	V_r		V_θ		V_z		V		$\sqrt{(V_r^2 + V_z^2)}$	
		Max	Min	Max	Min	Max	Min	Max	Min	Max	Min
Down	30.0	+17.5%	+41.4%	-6.38%	-	-79.6%	-84.4%	-6.86%	-	-17.6%	-
	237.8	+4.42%	+80.7%	+6.23%	-	+24.6%	+142%	+22.7%	-	+54.3%	-
Up	69.2	+93.3%	+87.3%	-	-14.2%	-20.1%	-38.2%	-6.53%	-	+58.4%	-
	215.2	+4.12%	+43.5%	-	+8.27%	+140%	+7.39%	+22.5%	-	+49.1%	-
	767.9	+103%	+62.6%	-	-6.99%	+631%	+230%	+86.6%	-	+416%	-

The large errors in the simulations of the minimum values of both axial and radial velocities could be contributed to the infinite viscosity fix. As these small velocities would be concentrated on the cavern boundary, in the experiments the velocities drop off sharply where as in the simulations they drop off slowly and thus would not be the same. The maximum velocities for both radial and axial appear more in the impeller region and it may be possible that the PEPT experiments are not picking these up due to the fact that it is a region of high flow and is only recording the tangential component as it is dominant. So detecting the comparatively small radial and axial components of velocity in this region is difficult.

The simulated discharge angle starts radially at low Reynolds numbers then switches to axial at high Reynolds numbers conversely to the experiments. It is to be seen in the

next section whether these large differences allow the CFD to accurately predict the cavern size and shape.

Figure 6.7 and Figure 6.8 show how the velocity and radial-axial velocity both normalised by the tip speed change with radius for both CFD and PEPT for China clay down and up pumping respectively. The PEPT data are the same as in Figure 6.5 above. The CFD data was taken in the same manner but at two different locations. One was between the two baffles and so the same plane as Figure 6.6, while the other was taken on a plane directly on a baffle. This was done to see if there was any difference between the two planes as this cannot be done in the PEPT. Since PEPT is averaged data it should fall between the two CFD data if experiments were modelled correctly.

Comparing the two CFD plane total velocity data it can be seen that they are very similar for both pumping configurations. The down pumping configuration peaks at higher impeller speeds and becomes sharper for the baffle plane while more rounded for the non baffle plane. Whereas for the up pumping case the shape remains much the same for all Reynolds numbers with the non baffle case having slightly smaller peaks. This was also seen for the shear thinning data as well. It is most notable that the lowest speed for both pumping directions is much more different than the others, due to the sliding mesh artefact described in Chapter 3 Section 3.2.2.. . The radial-axial CFD data also match fairly well, especially with the up pumping configuration. The down pumping baffle data does however fail to mimic the peak of the non baffle case for all Reynolds numbers, but the rest of data match fairly well. The erratic behaviour for the down pumping data is also present here, similarly to the cosmetic foundation cream simulations, again due to the domain interface. Overall the different plane data are

fairly the same, meaning the choice of plane extracted from CFD for this type of material doesn't matter under these operating conditions.

Comparing with the PEPT data the fit is sometimes good as in the down pumping case Re 237.8 and the up pumping case Re 69.2. However at other times the CFD under predicts and over predicts. The major difference notable in most cases is that the CFD was incapable of capturing the slow sloping gradient of the PEPT data. This is most likely due to the CFDs prediction of slightly different discharge angles. Still the overall shapes are fairly similar except near the impeller.

Re 30.0	Re 70.9	Re 237.8	Re 633.5
Re 28.1	Re 69.2	Re 215.2	Re 767.9
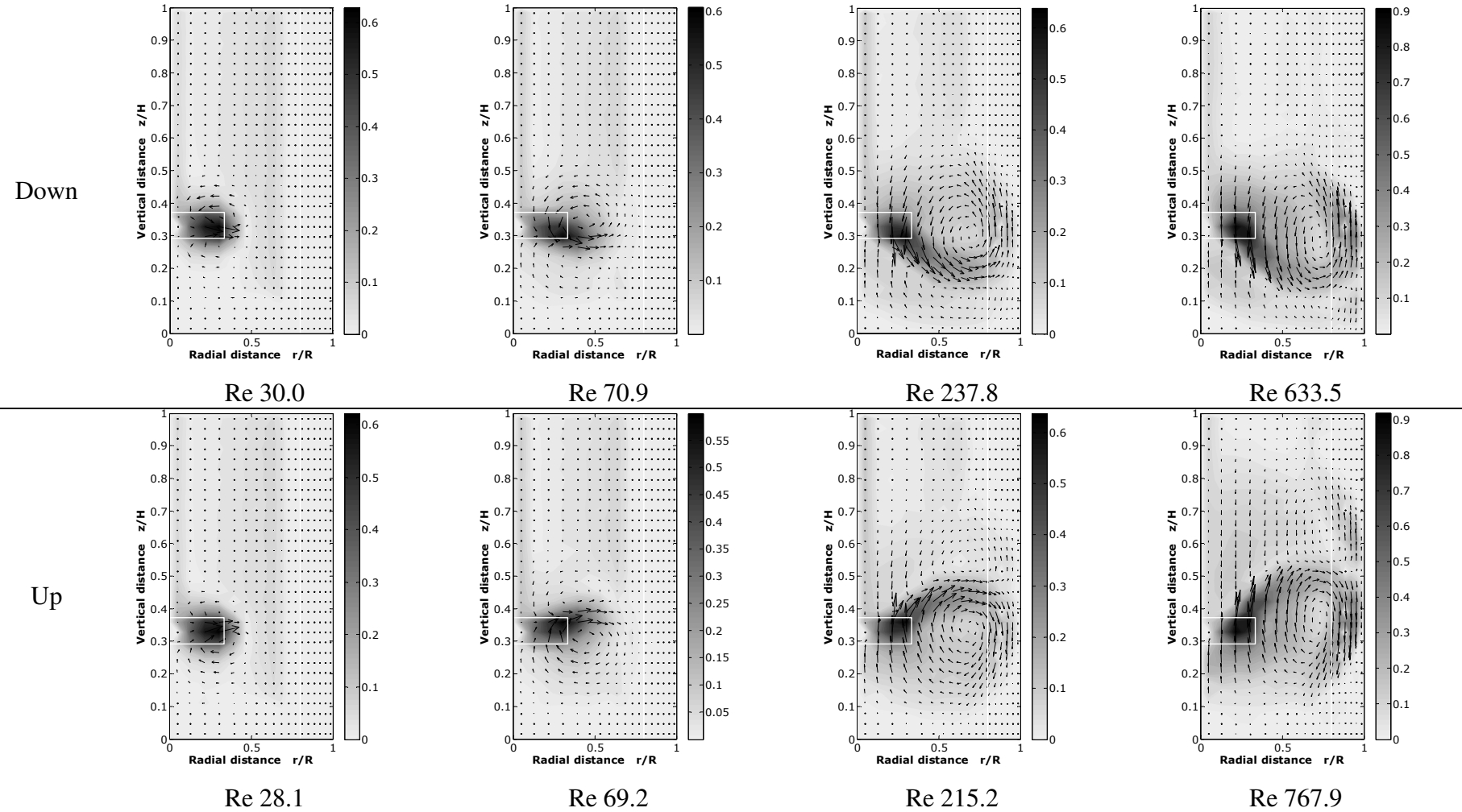
Figure 6.6 CFD normalised velocity flow fields of china clay slurry at different Reynolds numbers in down and up pumping configurations

	Total Velocity $\left(\sqrt{V_a^2 + V_\theta^2 + V_r^2}\right)$	Radial-Axial Velocity $\left(\sqrt{V_a^2 + V_r^2}\right)$
Re 30.0		
Re 70.9		
Re 237.8		
Re 633.5		

Figure 6.7 Radial plots of total and radial-axial velocity for China Clay down pumping configuration (taken just below the impeller, z/H = 0.297) showing PEPT and CFD data

	Total Velocity $\left(\sqrt{V_a^2 + V_\theta^2 + V_r^2}\right)$	Radial-Axial Velocity $\left(\sqrt{V_a^2 + V_r^2}\right)$
Re 28.1		
Re 69.2		
Re 215.2		
Re 767.9		

Figure 6.8 Radial plots of total and radial-axial velocity for China Clay up pumping configuration (taken just above the impeller, z/H = 0.372) showing PEPT and CFD data

6.6. Comparison of theoretical models, CFD and experiments caverns

Figure 6.9 to Figure 6.14 depict the cavern boundary estimates from experimental PEPT measurements, CFD simulations and mechanistic cavern prediction models for both slurries down and up pumping. Two cavern description methods are used for both the PEPT and CFD results. The process used to plot these figures is present in Chapter 5 Section 5.6., the equations are presented below first for 1% tangential (6.3) and the other for 1% radial-axial velocities (6.4).

$$0.01V_{Tip} = V_\theta \tag{6.3}$$
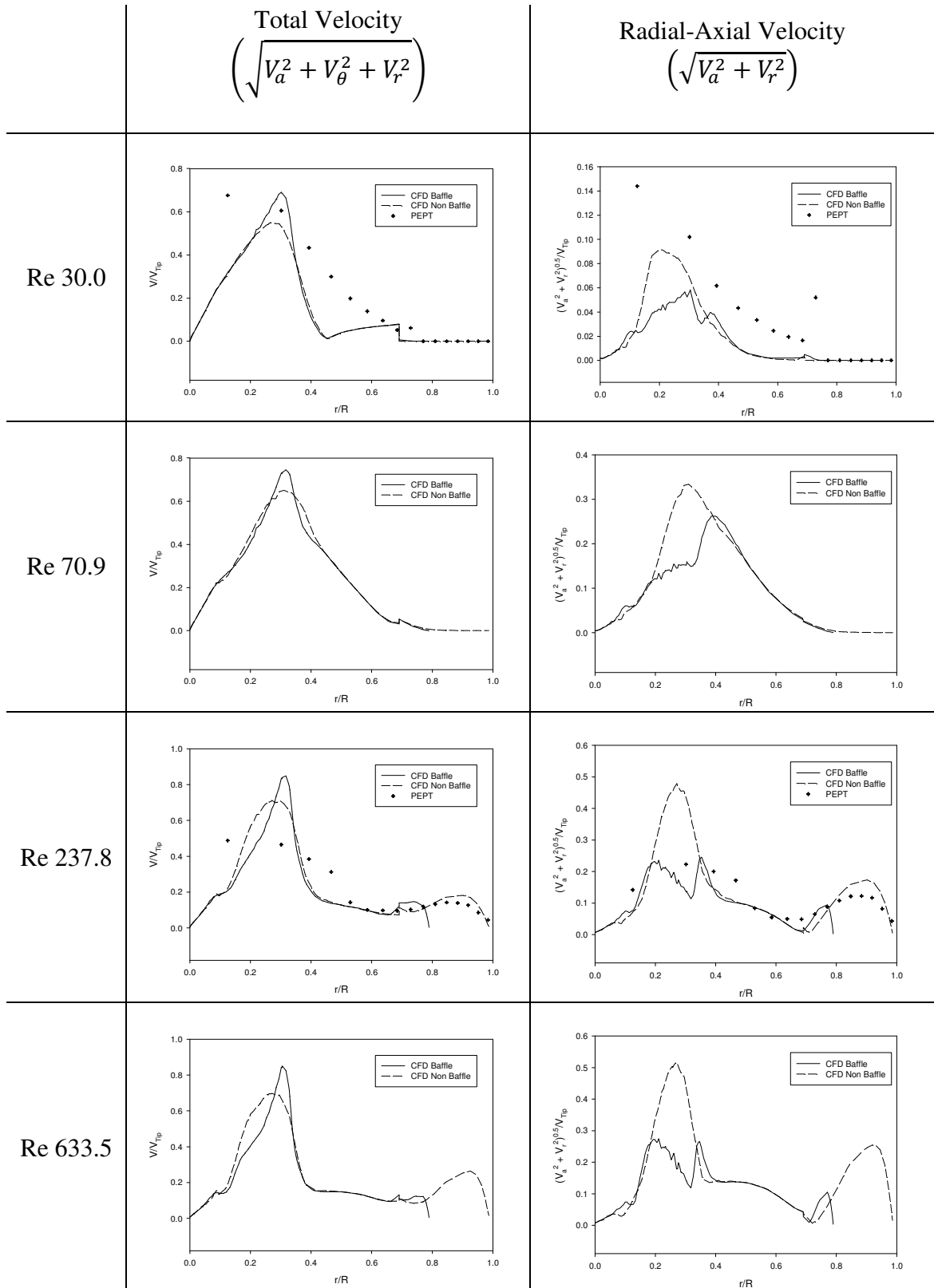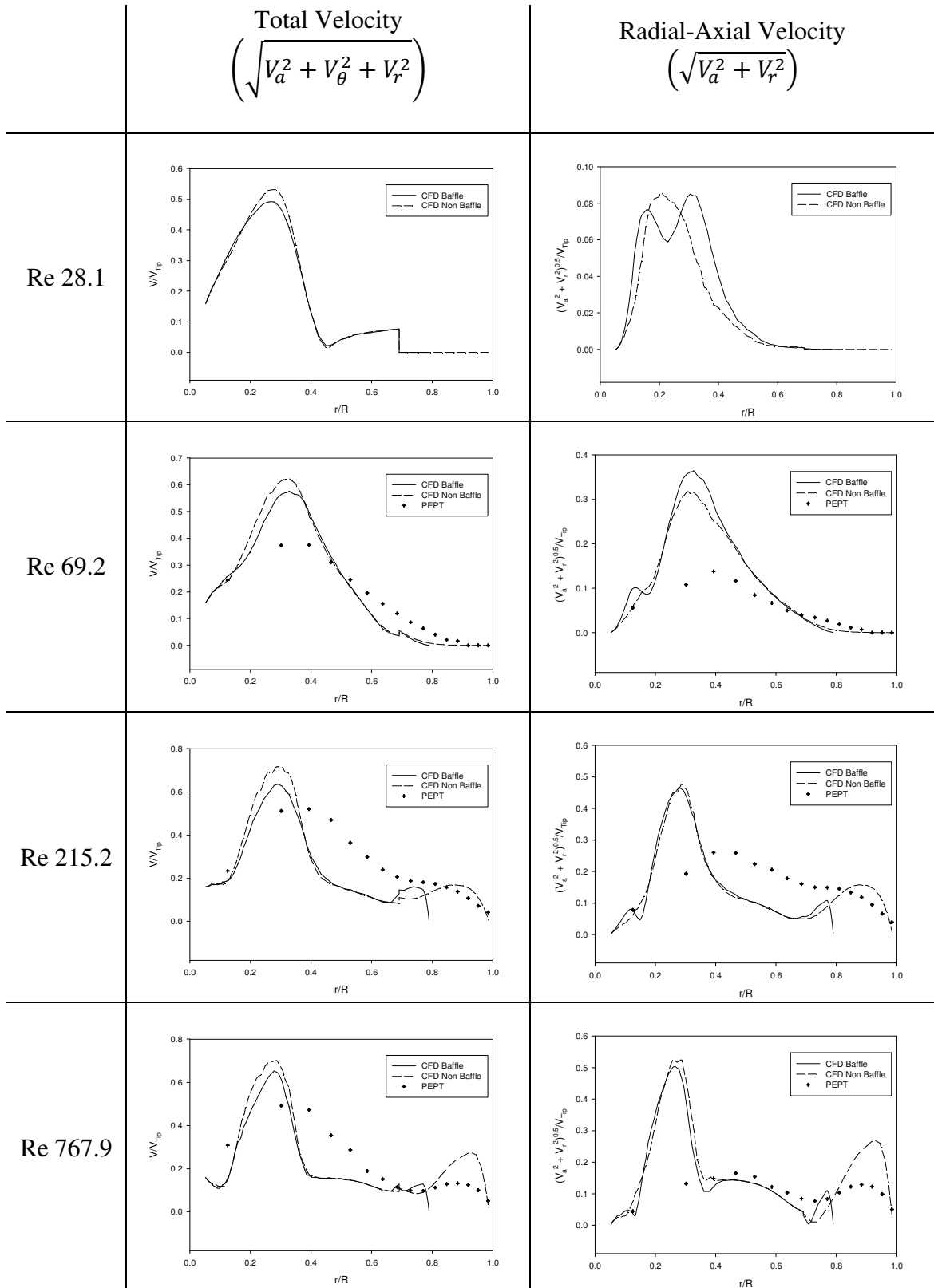
$$0.01V_{Tip} = \sqrt{V_a^2 + V_r^2} \tag{6.4}$$

Three mechanistic models are used all centred on the impeller, first being a sphere (equation (3.16)) depicted by a semi circle, secondly a toroid (equation (3.18)) depicted by a circle and a cylinder (equation (3.22)) depicted by a rectangle. The spherical model greatly over predicts the size of the cavern given by both experiment and simulation for all speeds and pumping configurations. The toroidal model also over predicts all simulated results and most of the experiments except only slightly over predicts for the lowest speeds for down and up pumping. The cylindrical model gives the best size predictions of all the models, matching cavern height with some of the experimental data and radial-axial simulated data. Especially notable for the down pumping Re = 70.91 and up pumping Re = 69.2 the cylindrical cavern matches almost exactly with the simulation data using the radial-axial interpretation. Once the cavern

data from both simulation and experiments touch the cavern wall so does the cylindrical model, thus predicting the cavern diameter well. It could be said for the highest Reynolds number case for up pumping where the cavern consumes the whole of the tank that all models predict the cavern well as they also consume the entire tank, but since this is now a fully mixed system the definition of a cavern does not hold.

Concerning the two different caverns from the simulations there are a few differences, the tangential cavern (black dots) for all results hugs the impeller shaft all the way to the top of the tank where as the radial-axial cavern (small cross) never does. At the lowest speeds for both configurations the tangential cavern hugs around the impeller in a toroidal fashion, as impeller speed is increased strange cavern shapes are created again in both configurations. The radial-axial caverns however gave the appearance of a more realistic cavern shape that seems to best resemble the flow loops presented earlier. At the highest speed for down pumping both CFD caverns appear to be very similar suggesting that this strange cavern shape is correct. Due to the more realistic nature of the radial-axial cavern this will be the one used to compare with the experimental data.

The two experimental cavern descriptions are very similar in all cases except for the up pumping case at Re = 215.23 where the radial-axial model (circles) takes much more of the tank volume. Since the radial-axial interpretation from the simulations gave the much more realistic fit we shall use the same approach for the experiments since there is little to distinguish between them. The experimental radial-axial cavern at the lowest speed down pumping is much larger that the simulated radial-axial cavern, however at the higher Reynolds number down pumping case the match is almost exact with the experimental cavern only being slightly larger at the top. For the up pumping

configuration the experimental cavern is slightly larger than the CFD at the lowest speed, but as speed is increased the match becomes almost exact. Therefore CFD is able to predict the cavern shape and size fairly well in the transitional regime but under predicts in the laminar regime.

However the cavern size and shape given by CFD is remarkable due to the major differences in the maximum and minimum values of the radial and axial velocities, implying that these values do not affect the values used to plot the cavern, as well as the simplification of a time dependant slurry as a homogenous fluid with a single rheology. Since the minimum values would fall near the tank walls and the maximum values appear on the impeller tip, it is not surprising that even though they are not accurately predicted they have little bearing on the size of the cavern. All these findings were seen for the shear thinning data, however for the shear thickening simulated cavern size and shape data is not as well predicted over the range of Reynolds numbers studied. The difference mentioned previously in Chapter 5 Section 5.6. about how the cavern data is differently obtained dependant on method could be the reason for these simulations poorer performance. Because of the shear thickening element of the Rheology this could have caused the infinite viscosity fix to be incorrect for these types of materials.

| | Re 30.0 | Re 70.9 | Re 237.8 | Re 633.5 |
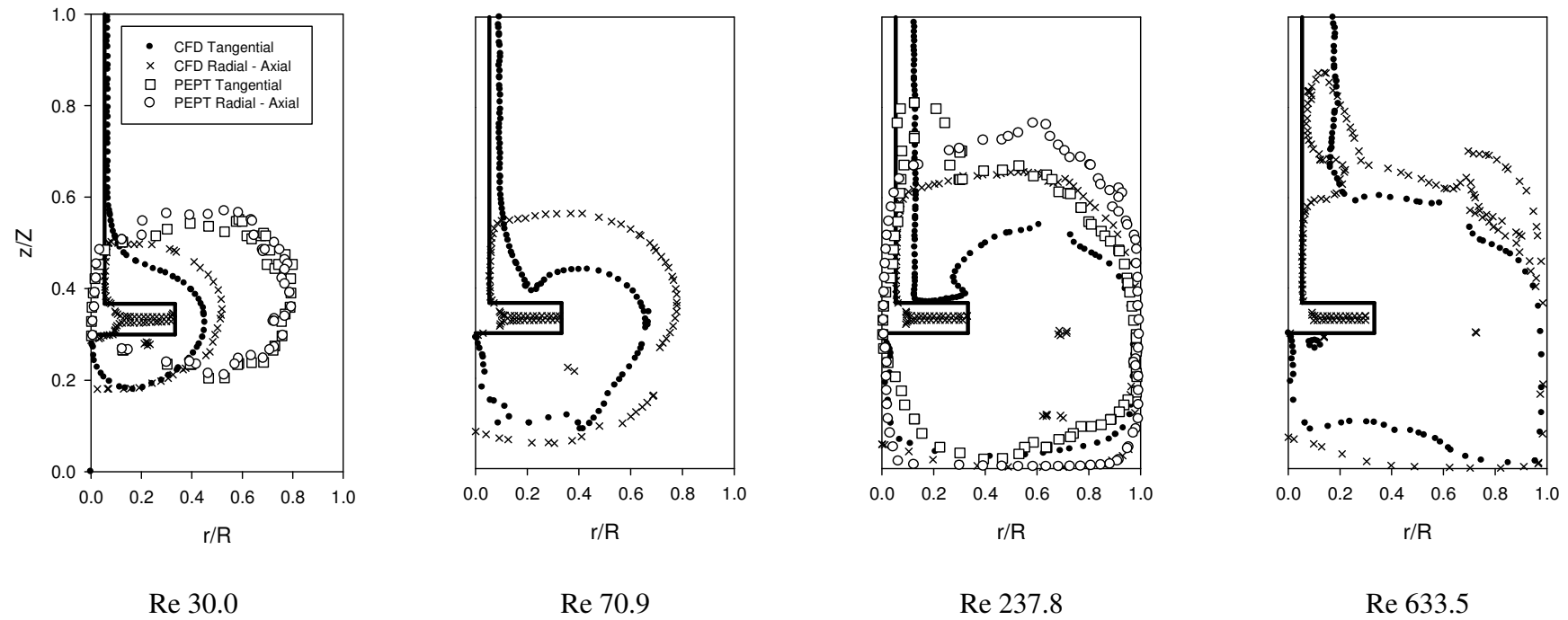
Figure 6.9 Cavern boundary plots for China clay down pumping showing CFD and PEPT data
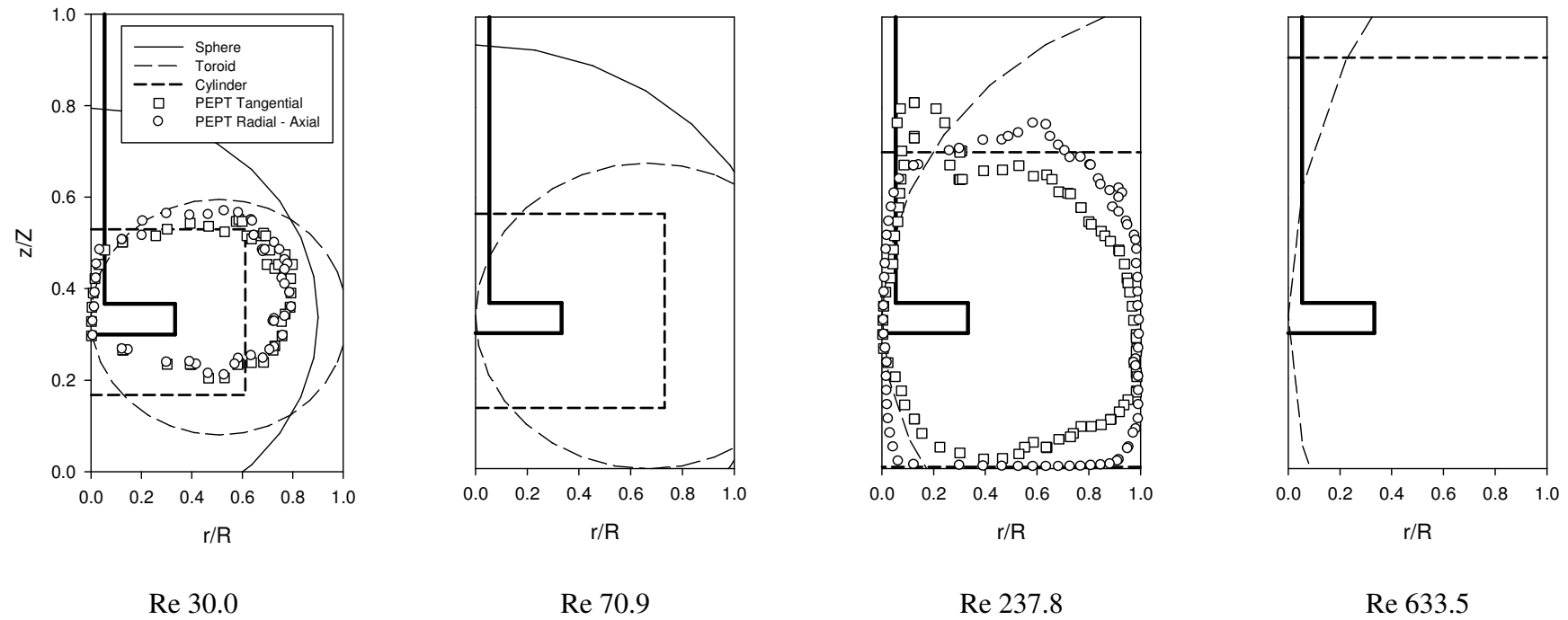
Figure 6.10 Cavern boundary plots for China clay down pumping showing PEPT data and cavern prediction models
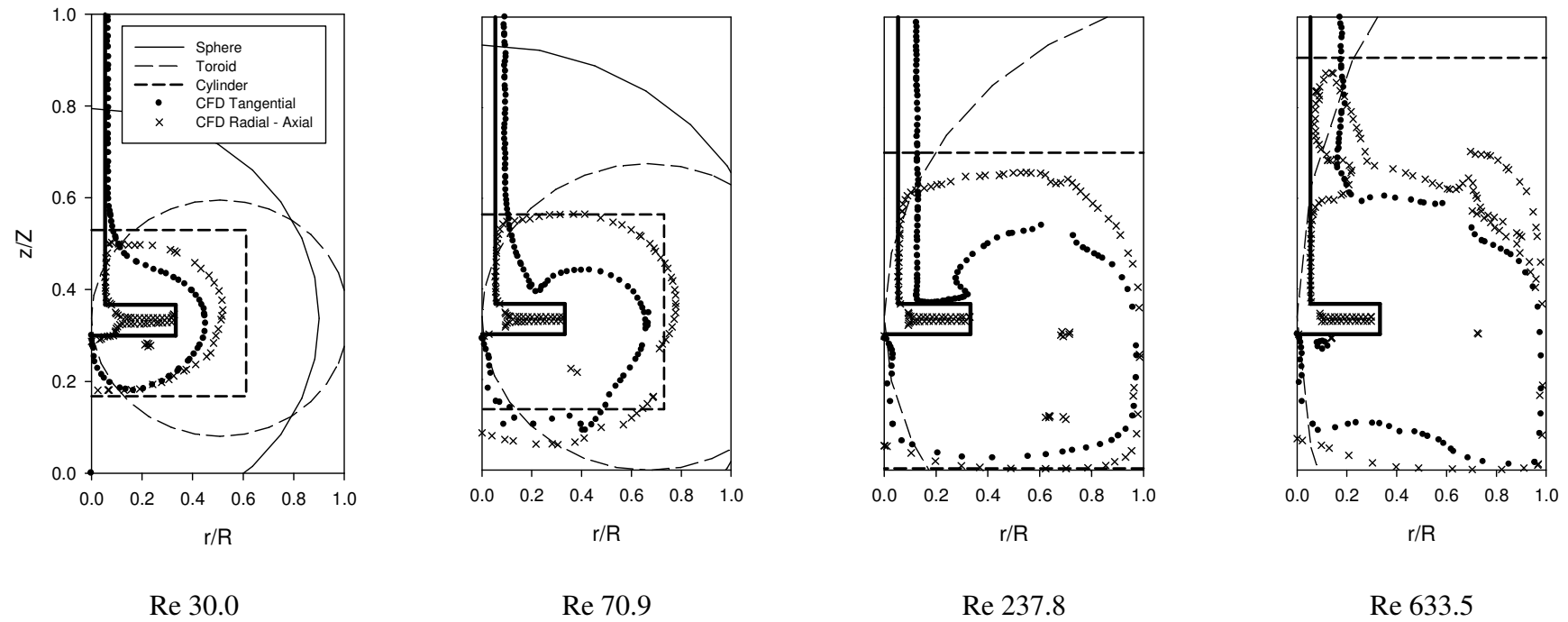
Figure 6.11 Cavern boundary plots for China clay down pumping showing CFD and cavern prediction models

Re 28.1   Re 69.2   Re 215.2   Re 767.9
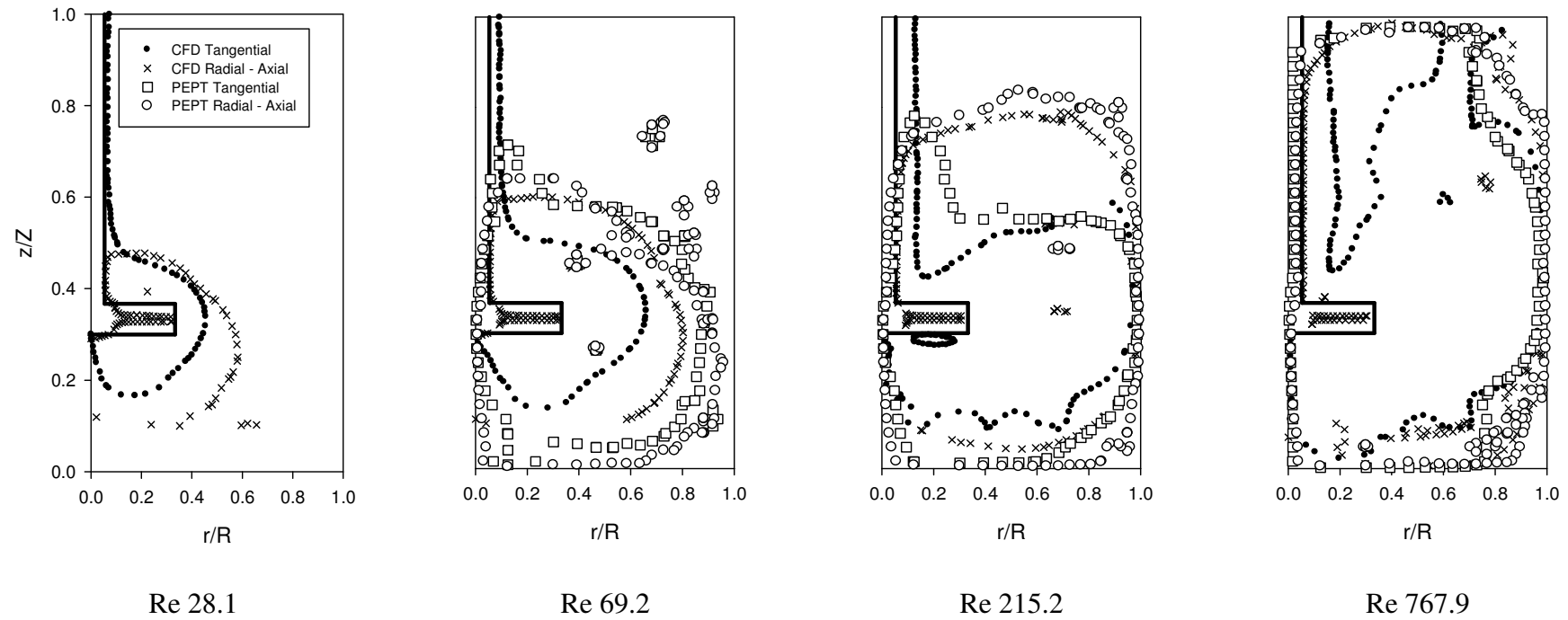
Figure 6.12 Cavern boundary plots for China clay up pumping showing CFD and PEPT data
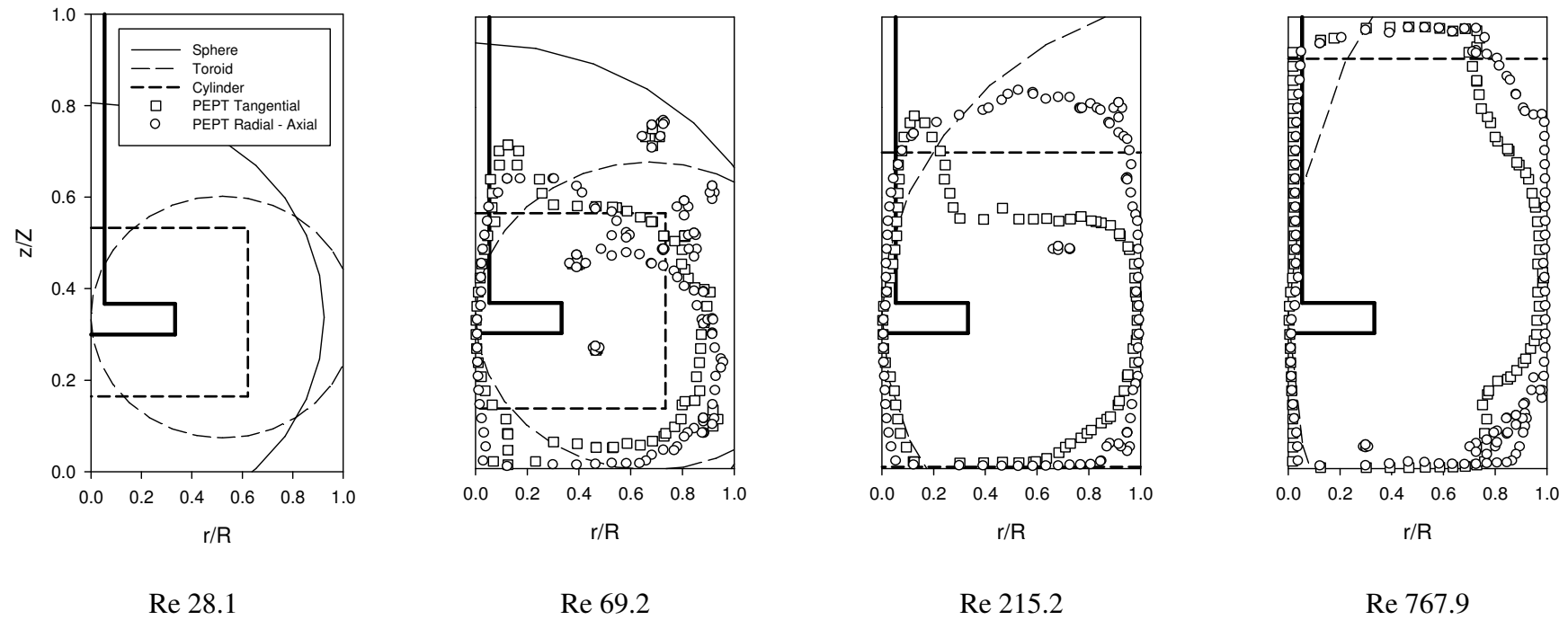
Figure 6.13 Cavern boundary plots for China clay up pumping showing PEPT data and cavern prediction models

Re 28.1   Re 69.2   Re 215.2   Re 767.9
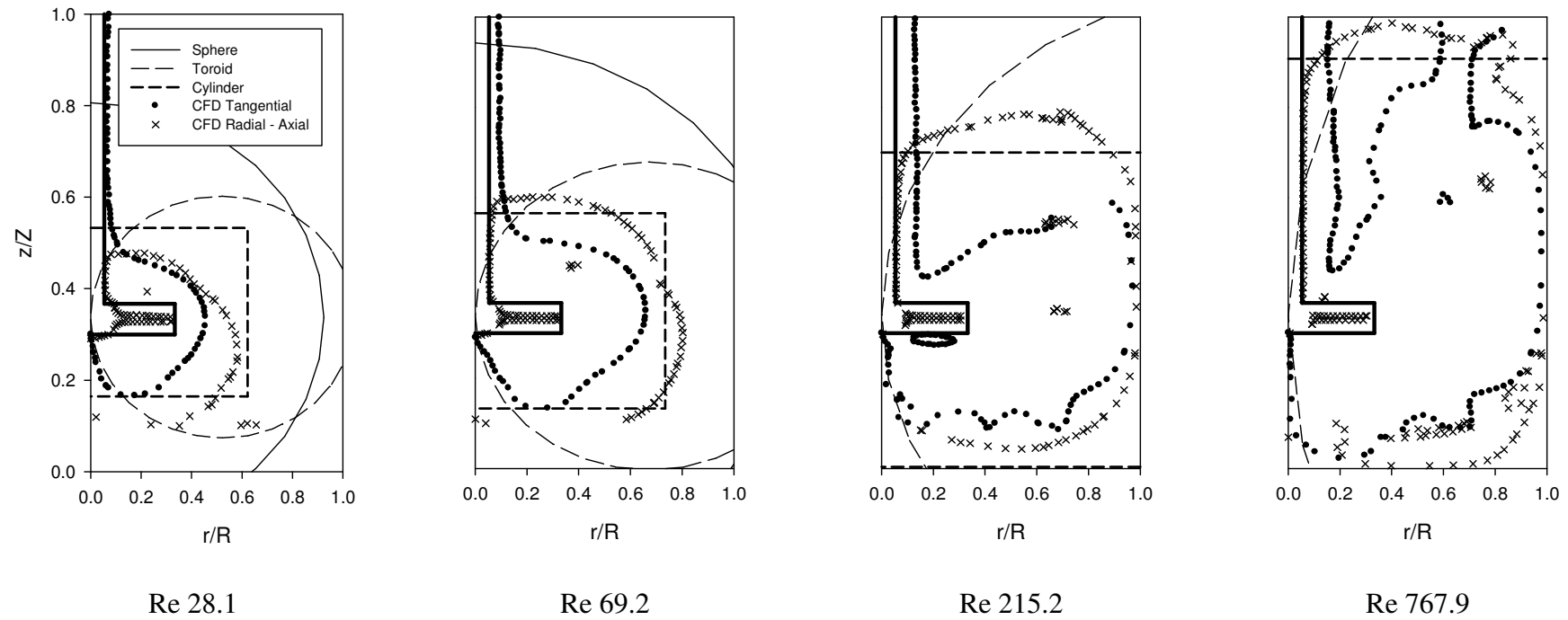
Figure 6.14 Cavern boundary plots for China clay up pumping showing CFD and cavern prediction models

6.7. Conclusions

Similar to the Cosmetic foundation cream the PEPT technique was able to obtain flow pattern data of an opaque shear thickening slurry system to be obtained. This data is a lot more unique than the shear thinning slurry data presented in the previous chapter. Since there are quite a few transparent shear thinning materials there has been some optical flow data obtained for them. However shear thickening materials are too my knowledge very rarely transparent and thus very little or no data has been obtained for them. Thus making this technique very valuable for understanding the mixing of shear thickening fluids, CARPT could be used to obtain similar data but to the authors knowledge this has not yet been done.

CFD predicted similar flow loops at high Reynolds numbers but under predicted their size at low Reynolds numbers. Discharge angles were more radial at low Reynolds numbers and more axial at high Reynolds numbers, contrary to the experiments. The constant velocity jets were seen in both experiments and simulations, being more dominant in the former. Tangential velocity predictions by CFD were very good, however the higher the Reynolds number the more the radial and axial velocities tended to differ, causing the simulations to be more axially dominant.

All cavern prediction models grossly over predicted the cavern size of all experiments with the cylindrical model giving the best fit. Radial-axial interpretation of cavern boundary was seen to be a more realistic shape for cavern prediction in the simulations. CFD was able to predict cavern shape and size very well at high Reynolds numbers

however under predicting at lower Reynolds numbers, at the lowest Reynolds number the prediction completely breaks down. These fits are good despite the simulations simplification of a time dependent slurry to a homogenous fluid with a single rheology, meaning that the time dependency had little effect on determining the cavern boundary, thus enabling the use of CFD to predict cavern shape and size for a shear thickening slurry at Reynolds numbers above 70 up until the cavern fills the whole tank.

CHAPTER 7

MIXING OF A FIBRE SUSPENSION

7.1. Introduction

The most common fibre suspension is paper pulp. The interaction of the many tiny fibres present in the paper pulp can cause the suspension to exhibit non-Newtonian behaviour. Since these fibres can create structures within the material they can cause the suspension to have an apparent yield stress or a shear thinning type of rheology. The shear thinning rheology is easy to visualise since at low shear, more of the fibres will be undisturbed, providing a more rigid structure and thus a high viscosity. As the speed is increased the fibres will become disturbed, destroying the structure and thus lowering the viscosity. Both an apparent yield stress and shear thinning rheologies can create cavern like behaviour when mixed at low Reynolds numbers which as mentioned previously is very detrimental to mixing. Due to the opaque nature of paper pulp fibre suspensions little to no data has been extracted on how they mix and what type of caverns are formed since optical techniques cannot be used to measure the flow patterns and velocities.

7.2. Summary

This Chapter describes the mixing and cavern formation of a 3% wt/wt paper pulp fibre suspension in two different sized stirred tanks via the application of PEPT; section 3.1.2.4 gives the complete make-up of the suspension. Due to the clumpy solid-liquid structure of the paper pulp suspension no rheological data could be extracted and thus no simulations could be performed to compare with the PEPT data, this is further

explained in section 3.1.2.4. Two sets of experiments were carried out, the first in the standard small tank (described in section 3.1.1) used for all of the previous experiments and the second in a larger tank used only for the paper pulp. The larger tank (described in section 3.1.1) was used to get accurate power measurements from the paper pulp in both down and up pumping configurations due to the erratic power consumption when mixing the paper pulp in the small tank. Through analysis of the PEPT data obtained from both tanks, flow patterns and cavern size and shape have been extracted. In an attempt at estimating the rheology of the paper pulp, the three different shape yield stress cavern prediction models have been used by taking the cavern diameters inferred from the PEPT data and working backwards.

7.3. Power measurements

The large tank (described in section 3.1.1) was used to extract the power measurements for the paper pulp. This was deemed necessary due to the measurements in the small tank (described in section 3.1.1) for the paper pulp being too erratic to get any sensible answers. This is because of the motor on the small tank could not provide enough torque to keep the speed constant when mixing the extremely clumpy paper pulp. The larger tank had a much higher torque motor and more sensitive torque meter, thus giving more stable and sensitive results. As no rheological data could be obtained the standard Reynolds number versus Power number plot cannot be obtained. Figures 7.1 – 7.3 depict the data that was obtained for both the down and up pumping configurations at varying impeller speeds.

Figure 7.1 shows the raw data of the torque meter, torque versus impeller speed. Both up and down pumping configurations follow pretty much the same path indicating that the power dissipation is independent of pumping direction. Torque increases with impeller speed and similarly so does the power as shown in Figure 7.2. The increase in curvature of the power plot is contributed to power having a component of torque multiplied by the impeller speed.

Figure 7.3 is similar to the classic Power number vs Reynolds number plot, but since the rheology is not known, Re cannot be calculated. However plotting power number versus impeller speed on a log-log plot shows a large linear region possibly indicating laminar behaviour. The visual inspection of the experiment supports this fact; little to no movement could be seen at the lower speeds. However at the higher speeds material at the sides and surface was beginning to move, especially notable in the impeller region. This could correspond to the slight flattening out of the power number at the high impeller speeds in Figure 7.9 indicating movement into the transitional regime.
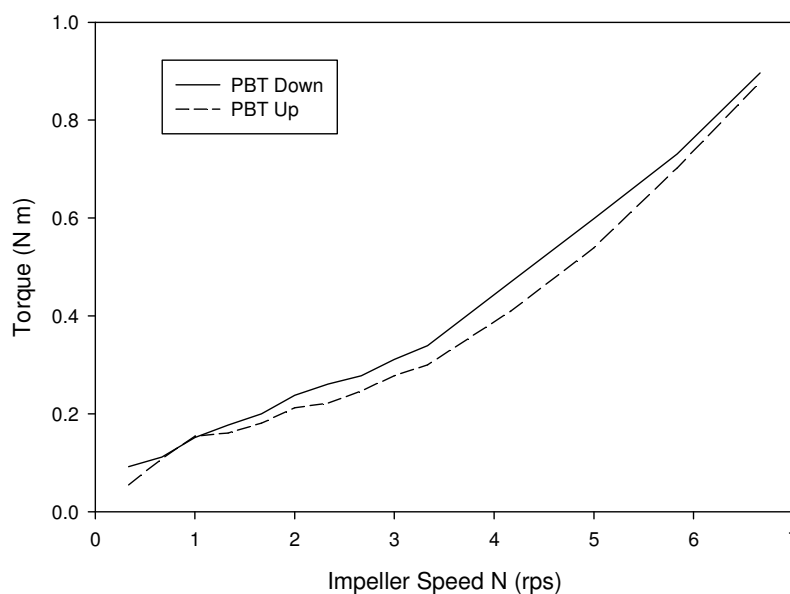

Figure 7.7 Torque versus impeller speed for paper pulp
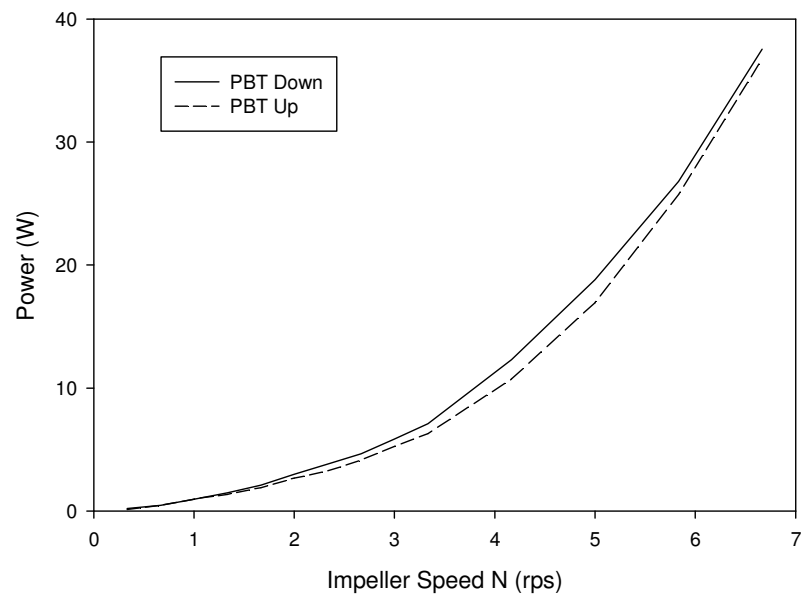
Figure 7.8 Power versus impeller speed for paper pulp
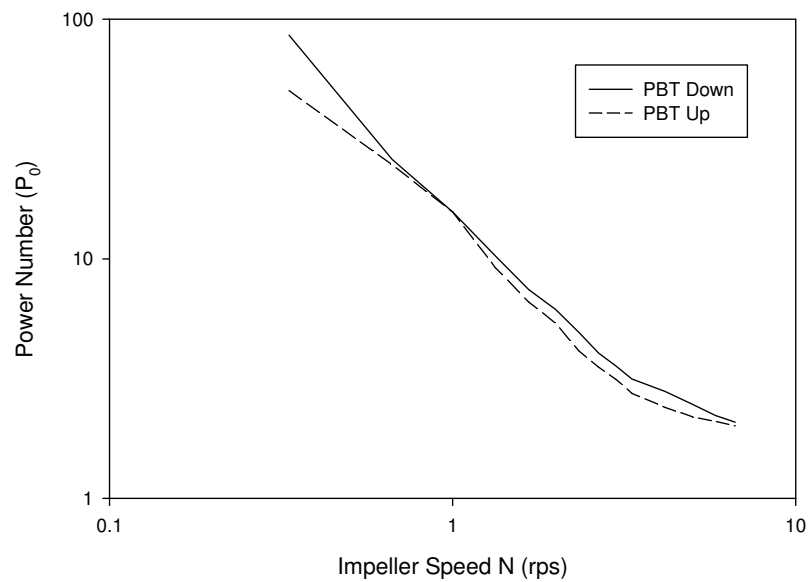
Figure 7.9 Power number versus impeller speed for paper pulp

7.4. PEPT analysis of fibre suspension

7.4.1. Small Tank

7.4.1.1. Flow Patterns

Figure 7.4 shows the flow patterns obtained through PEPT for the mixing of paper pulp in the small tank (described in section 3.1.1) for both up and down pumping configurations at 400, 600, 700 and 800 rpm. The arrows denote the 3D velocity vectors on a 2D plane, thus the component coming out of the plot cannot be seen. The grey scale contour plot shows the magnitude of the velocity vector normalised by the impeller tip speed as calculated below in equation (7.1).

$$\boldsymbol{Normalised\ Total\ Velocity} = \frac{\sqrt{V_a^2 + V_\theta^2 + V_r^2}}{\pi ND} \tag{7.1}$$

Experiments were also conducted at 100 and 200 rpm, but due to the apparent yield stress of the paper pulp as well as the slow speeds little to no motion was captured. Continuous particle motion started to be observed at 400 rpm and thus this was the slowest speed used. Even at this speed, the tracer would still stop moving at regular intervals, caused by the particle being thrown out of the high mixed area into the stagnant region (i.e. outside of the cavern). Manual mixing was required to move the tracer back into the impeller region, the PEPT camera was stopped and restarted for this procedure to ensure the manual mixing was not recorded. This was required less at the higher speeds due to the increase of area of high flow as shown in the figure, where as for the 700 and 800 rpm down pumping cases velocities are apparent in over two thirds of the tank volume.

With the impeller off-bottom clearance set to T/3 the same cannot however be said for the up pumping case where movement is apparent only in the lower half of the vessel. If for the up pumping configuration the impeller off-bottom clearance were set to 2T/3 the flow patterns obtained would be an inverted mirror image of the down pumping configuration at T/3, eliminating the effects of the tank floor. Maximum velocities were just over 60% of the tip speed for both up and down pumping at 400 rpm. As the impeller speed was increased the maximum velocities measured dropped to around 50% of the tip speed for both up and down pumping rather than increasing. This is probably due to the PEPT cameras being unable to capture the higher velocities caused by the increase in impeller speed or due to the nature of the fluid itself at these speeds with the more axial discharge angles.

Both mixing configurations exhibit a single loop of mixing at the lowest speed while at higher speeds a secondary much smaller loop is also generated, for the down pumping case the primary loop is below the impeller with secondary loop above and vice versa for the up pumping configuration.
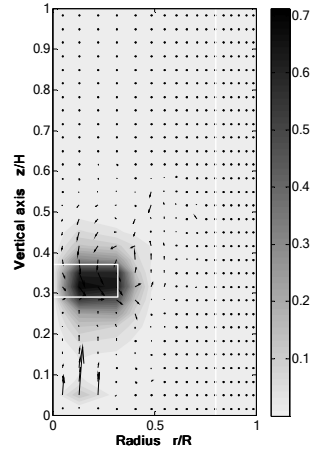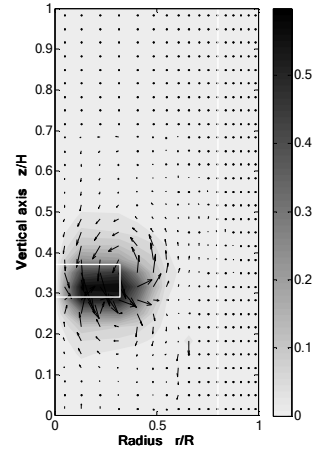
400 rpm Down Pumping   600 rpm Down Pumping   700 rpm Down Pumping   800 rpm Down Pumping
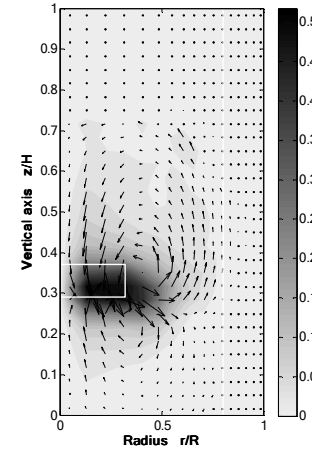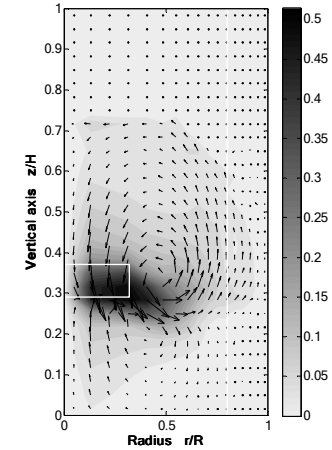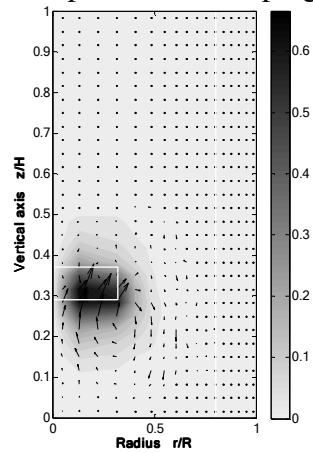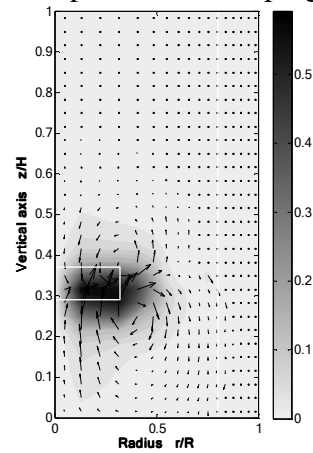
400 rpm Up Pumping   600 rpm Up Pumping   700 rpm Up Pumping   800 rpm Up Pumping
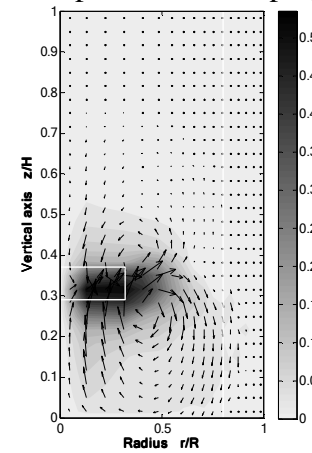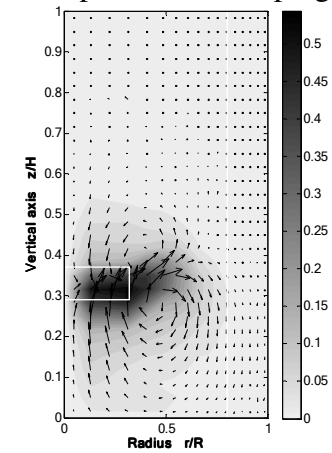
Figure 7.10 Normalised velocity flow fields for paper pulp mixed in the small tank

Figure 7.5 shows how total velocity and radial-axial velocity both normalised by the tip speed change with radius for all PEPT experiments carried out in the small tank. Normalised velocity is described above in equation (7.1) and the normalised radial-axial velocity is defined below in equation (7.2).

$$Normalised\ Radial - Axial\ Velocity = \frac{\sqrt{V_a^2 + V_r^2}}{\pi ND} \qquad (7.2)$$

Down pumping data was taken at a fixed height just below the impeller blade (z/H = 0.297) while up pumping was taken at a fixed height just above the impeller blade (z/H = 0.372). These positions were taken as they are in the discharge paths of the two pumping configurations. As impeller speed is increased normalised total velocities drop near the impeller but are maintained at higher values further into the tank for both up and down pumping. The higher the impeller speed, more momentum is transferred into the rest of the tank. Also the normalised total velocity drops off more gradually at higher impeller speeds, most notable for the down pumping case. The shape of the normalised radial-axial plots for both pumping configurations are similar, except at the two highest speeds the peak for the up pumping case is more acute. In all cases the radial-axial velocities increase to a peak and then drop off, the location and prominence of this peak moves further into the tank at higher impeller speeds. The drop off for the three highest speeds follows a similar gradient, indicating degradation towards the cavern boundary is the same for all impeller speeds. The 400rpm case in both pumping configurations starts at a different value at r/R=0 to the other speeds and is much less prominent than the other speeds, probably due to the flow field being not fully developed as this was the slowest speed where continuous motion of the tracer was achieved.

	Down pumping	Up pumping

Total Velocity

$$\left(\sqrt{V_a^2 + V_\theta^2 + V_r^2}\right)$$

Radial-Axial Velocity

$$\left(\sqrt{V_a^2 + V_r^2}\right)$$
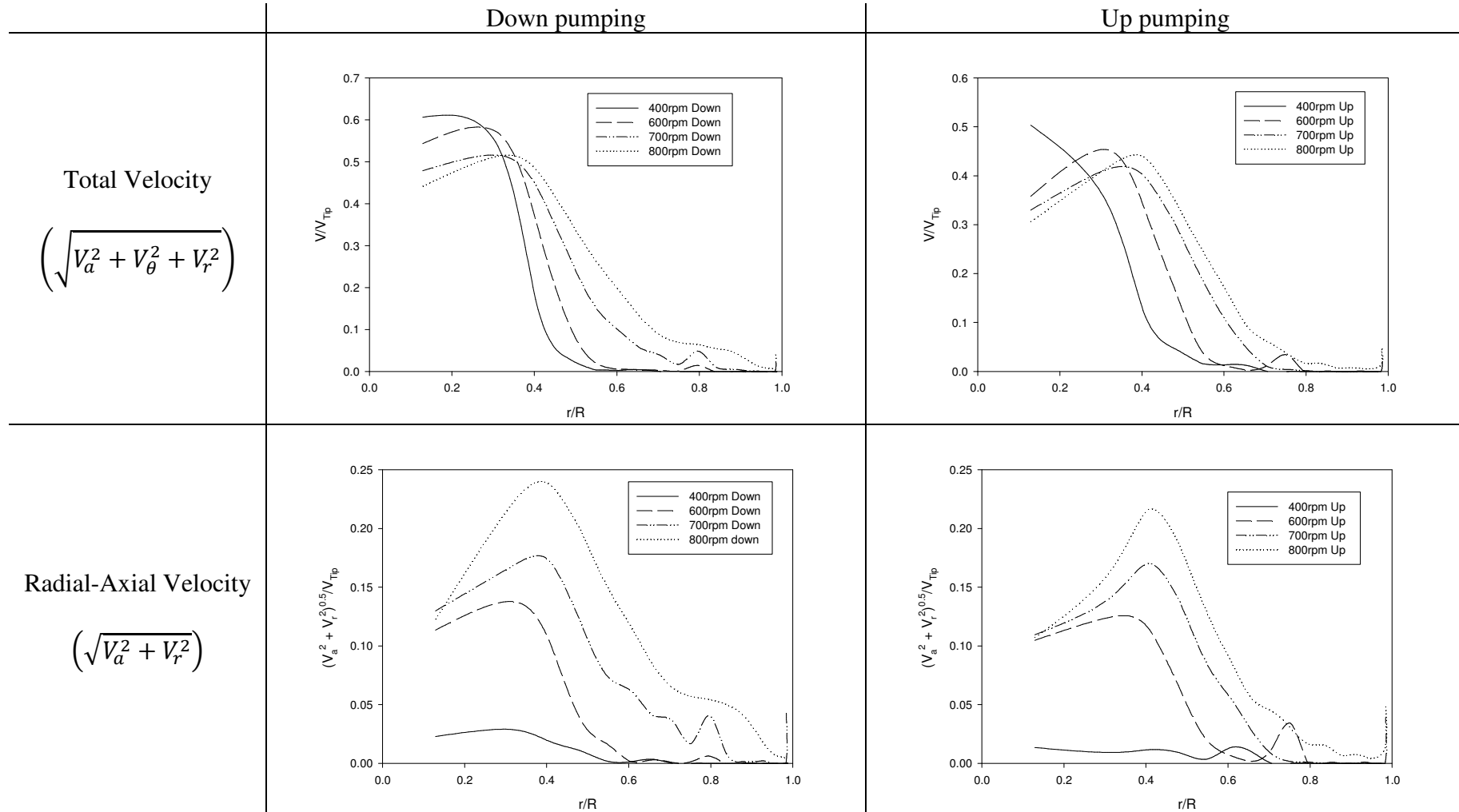
Figure 7.11 Radial plots of Paper pulp PEPT data total and radial-axial velocity for up (just above impeller, z/H = 0.372) and down (just below impeller, z/H = 0.297) pumping configurations in the small tank

Chapter 7 – Mixing of a Fibre Suspension

7.4.1.2. Cavern Description and Size

Figure 7.6 depicts the cavern boundary estimates for paper pulp mixed in the small tank based on two methods. The process used to plot these figures is present in Chapter 5 Section 5.6., the equations are presented below first for 1% tangential (7.3) and the other for 1% radial-axial velocities (7.4).

$$0.01V_{Tip} = V_\theta \tag{7.3}$$

$$0.01V_{Tip} = \sqrt{V_a^2 + V_r^2} \tag{7.4}$$

Thus the contour plots depict either the tangential or radial-axial values normalised by the tip speed, with the arrows showing the same as before. The up pumping tangential contour plots are an inverse colour scheme as the direction of pumping is going in the opposite direction. There is a major contrast between the two methods, the tangential line centres more around the impeller in a toroidal fashion, increasing in size with increase in impeller speed for both up and down pumping. The radial-axial is much more varied, even showing locations of eyes of mixing. Rather than forming a toroid around the impeller, the boundary encapsulates both the upper and lower loops, giving a much more realistic shape of the cavern. These boundaries also increase in size with increase in impeller speed, with the up pumping enveloping the lower half of the tank at the highest impeller speed.

rpm	Down Pumping		Up Pumping	
	Tangential V_θ	Radial-Axial $\sqrt{V_r^2 + V_a^2}$	Tangential V_θ	Radial-Axial $\sqrt{V_r^2 + V_a^2}$
400				
600				
700				
800				
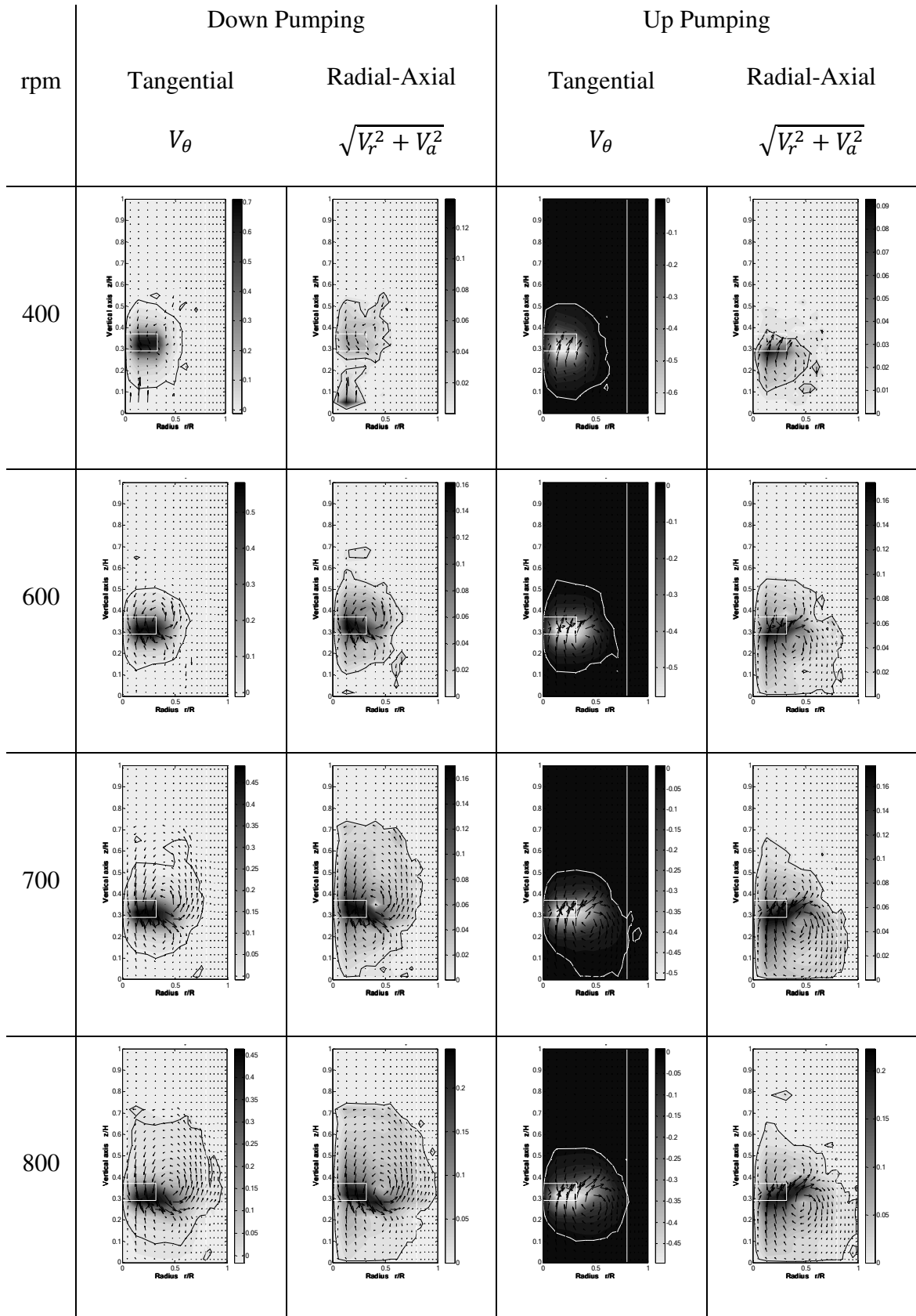
Figure 7.12 Cavern boundaries for paper pulp in the small tank

7.4.2. Large Tank

7.4.2.1. Flow Patterns

Figure 7.7 shows the flow patterns obtained through PEPT for the mixing of paper pulp in the large tank (described in section 3.1.1) for both up and down pumping configurations at 80, 100, 120 and 150 rpm. The data are presented in the same manner as in Figure 7.4, this tank does have a slightly larger impeller diameter to tank diameter than the small tank (a half instead of a third) but the rest of the ratios are very similar.

The speeds used were supposed to imitate similar Reynolds numbers using similitude, assuming the density and viscosity were the same and altering the diameter ratio. This was found unreasonable as the speeds needed could not be achieved easily with the large rig, the impeller speeds were too low forcing no particle movement to be obtained. Thus higher speeds were used to just achieve the PEPT tracer particle to move and three slightly higher speeds for further mixing. Similar problems were experienced with the particle becoming trapped in the stagnant region as for the small tank and thus manual mixing was needed to fix the issue.

Large areas of motion can be seen at the two highest speeds for the down pumping configuration extending to three quarters of the tank, whereas the up pumping case only seems to show motion in the lower half of the tank. Again a mirror image of the down pumping flow field could be achieved if the up pumping clearance were set to two thirds removing the influence of the tank floor. No secondary loops seem to be formed in both up and down pumping configurations; this is unexpected as we know this to occur as it was shown in the small tank in Figure 7.4. This could be attributed to the

difference in impeller diameter ratio, a much larger impeller may thus not produce secondary loops in paper pulp suspensions. What is considered more likely is that the tracer did not visit these secondary loops and thus led to no data being obtained.

The maximum normalised velocities for both configurations remain almost the same for each impeller speed, around 65%. This is due to the fact that even though they were at different Reynolds numbers the tip speeds were very close due to the increase of diameter of the impeller for these set of experiments. Thus confirming that PEPT is measuring the same magnitude of velocities for both tanks and thus having the same error in readings. Since the impeller speed is decreased with an increase in impeller diameter, the large tank experiments are run at close to equal power consumption when compared with the small tank experiments.
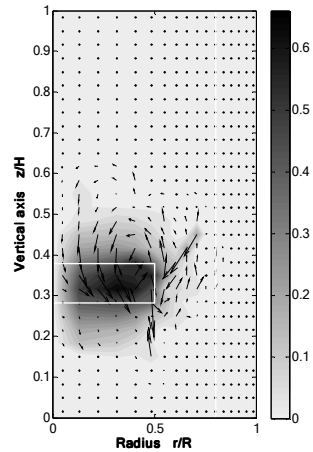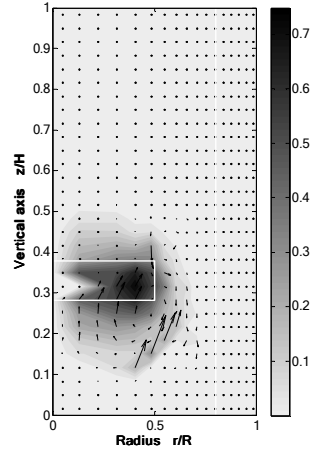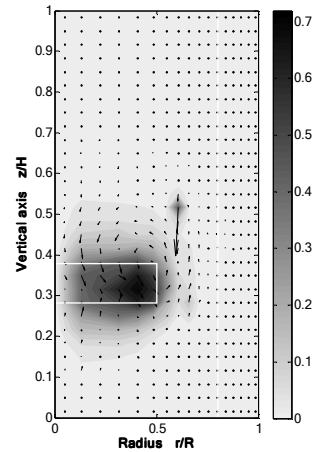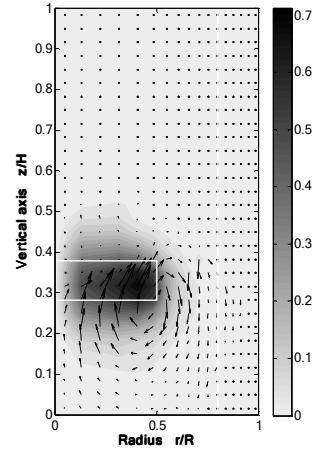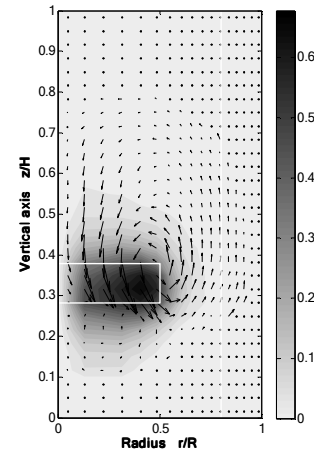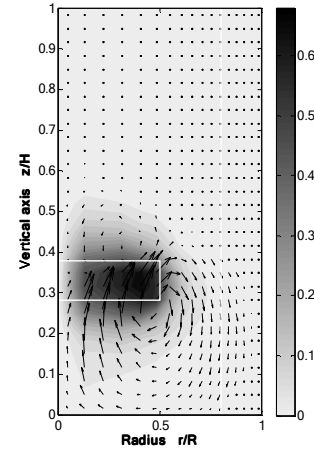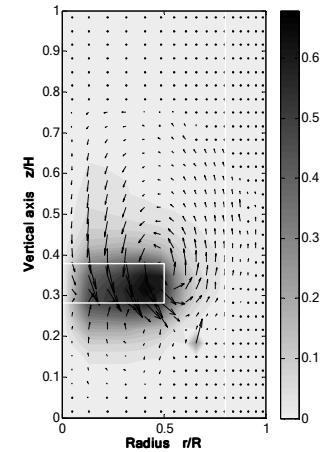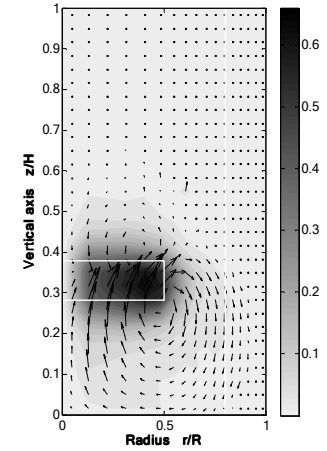
Figure 7.13 Normalised velocity flow fields for paper pulp mixed in the large tank

Figure 7.8 displays velocity and radial-axial velocity both normalised by the tip speed change with radius for all PEPT experiments in the large tank, data are presented in the same manner as Figure 7.5. The normalised total velocity plots for both pumping configurations vary very little with impeller speed. The exception is for the slowest speed for down pumping which is missing its peak. This peak however captured for the up pumping case at the same impeller speed implying maybe that it should be there but was not recorded by the tracer. The similarity with plots is probably due to the small differences in impeller speeds, 20 or 30 rpm, as where for the small tank the difference between impeller speeds was either 100 or 200rpm. Similar patterns with the small tank can be seen with the up pumping plot with the higher plots being a little bit more to the right at a normalised radius of 0.6, meaning more flow further into the tank at higher speeds. The gradient however does not change much at all compared with the small tank experiments, again due to the small difference in impeller speeds.

The shape of the normalised radial axial plots for both pumping configurations are very similar with the small tank data except for the 120rpm down pumping experiment that appears to have three peaks. These extra two peaks are presumed erroneous as the other experiments do not contain them. The up and down pumping at the highest Reynolds numbers are very similar, even having peaks at the same radial distance and normalised value, insinuating that the flow through the discharge plane at these speeds is independent of pumping direction. The drop off for the two highest speeds follows a similar gradient the same for the small tank, again indicating degradation towards the cavern boundary is the same above these impeller speeds

| Down pumping | Up pumping |

Total Velocity

$$\left(\sqrt{V_a^2 + V_\theta^2 + V_r^2}\right)$$

Radial-Axial Velocity

$$\left(\sqrt{V_a^2 + V_r^2}\right)$$
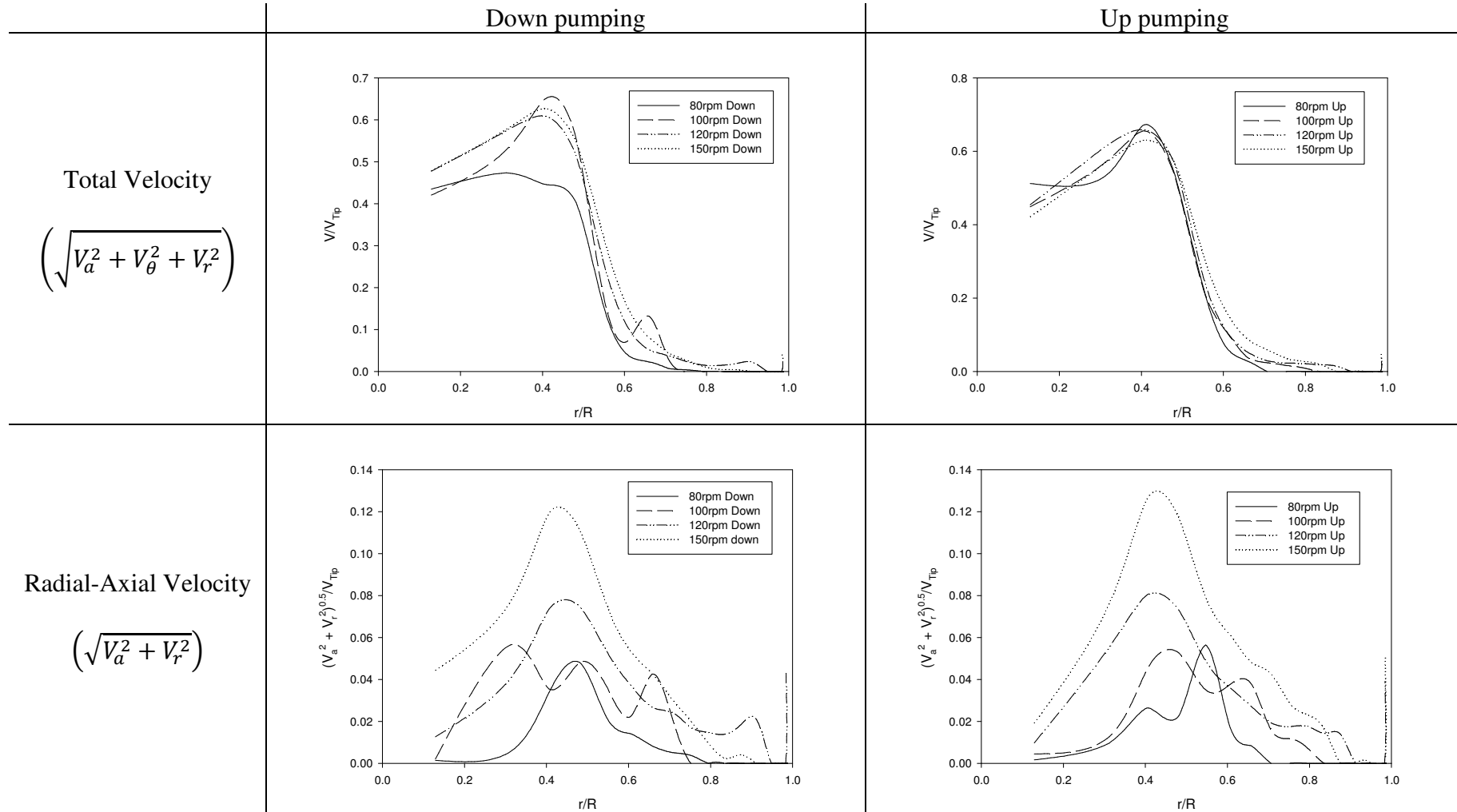
Figure 7.14 Radial plots of Paper pulp PEPT data total and radial-axial velocity for up (just above impeller, z/H = 0.372) and down (just below impeller, z/H = 0.297) pumping configurations in the large tank

7.4.2.2. Cavern Description and Size

Figure 7.9 depicts the cavern boundary estimates for paper pulp mixed in the large tank based on two methods, tangential and radial-axial, the data are represented in the same way as Figure 7.6. In contrast to the small tank the tangential and axial-radial plots give similar size and shape. This could be caused by the lack of a secondary loop captured during the experiments.

For down pumping both cavern descriptions increase with size encapsulating at least two thirds of the tank volume, neither of them covering the bottom of the tank, presumably if a secondary loop were captured they probably would have done. Whereas for up pumping at the highest impeller speed the axial-radial cavern only covers the lower third of the tank while the tangential extends slightly further. It appears in this case that the tangential lines seem to predict where the secondary loop could be a lot better than the radial-axial description. However no eyes of mixing have been captured in any of the tangential caverns, whereas for the radial-axial plot for the highest speed down pumping does.

rpm	Down Pumping		Up Pumping	
	Tangential V_θ	Radial-Axial $\sqrt{V_r^2 + V_a^2}$	Tangential V_θ	Radial-Axial $\sqrt{V_r^2 + V_a^2}$
80				
100				
120				
150				
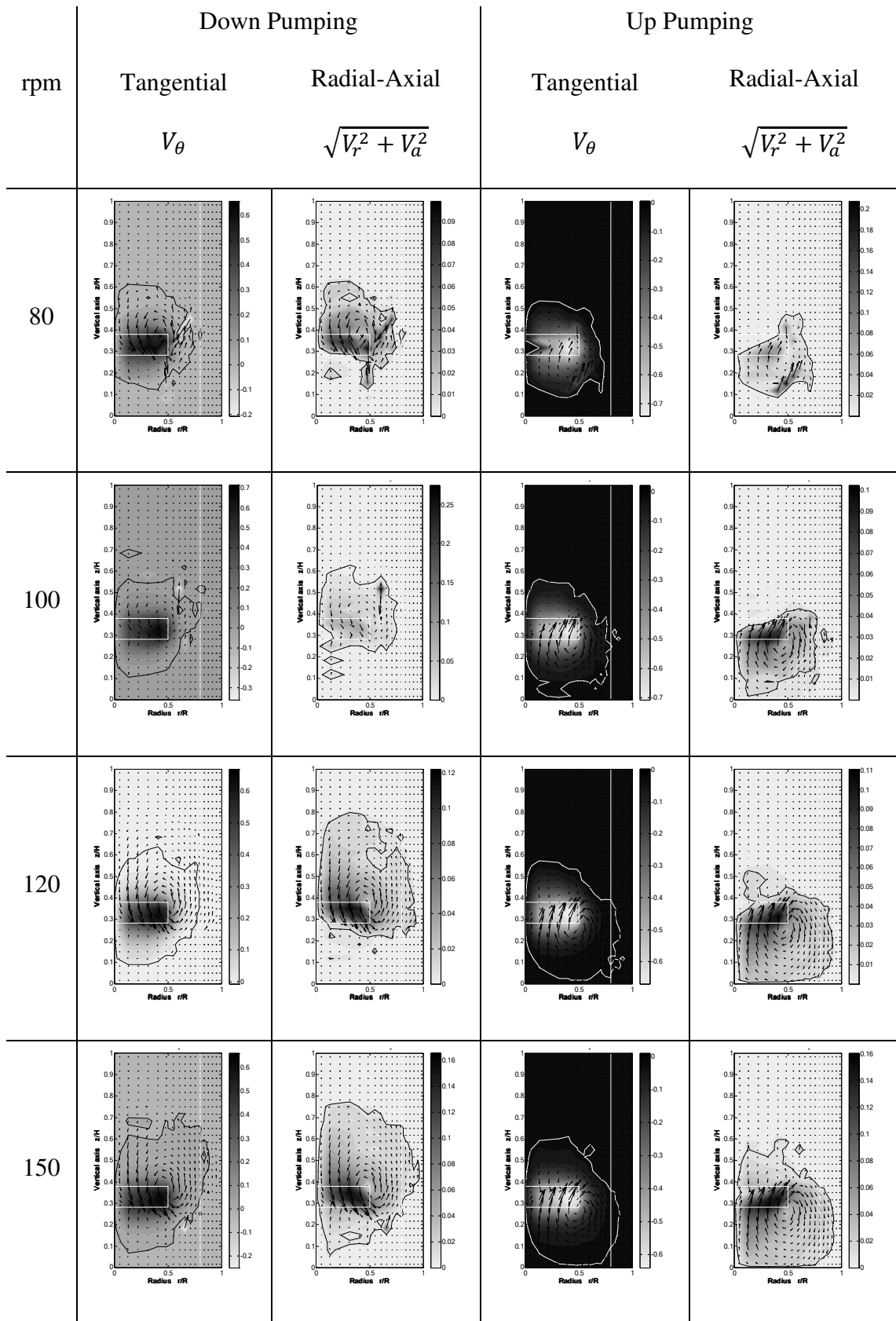
Figure 7.15 Cavern boundaries for paper pulp in the large tank

7.5. *Estimation of rheology through application of theoretical models to cavern size data*

Using the cavern prediction models it is possible to get some estimates for the yield stress of the paper pulp by rearranging the equations and inputting all the data including some cavern diameters from experimental results. Only the large tank data will be used as this is the only data with power measurements. The data cannot be converted to the small tank because of the lack of rheology data and the different impeller ratio. Estimation can be obtained for all three yield stress models; firstly cylindrical cavern model equation (7.5) can be rearranged as below into equation (7.6).

$$\left(\frac{D_c}{D}\right)^3 = \frac{P_0}{((H_c/D_c) + 1/3)\pi^2}\left(\frac{\rho N^2 D^2}{\tau_y}\right) \tag{7.5}$$

$$\therefore \quad \tau_y = \frac{\rho N^2 D^2 P_0}{((H_c/D_c) + 1/3)\pi^2}\left(\frac{D_c}{D}\right)^{-3} \tag{7.6}$$

And similarly for the spherical model as shown below in equation (7.7)

$$\tau_y = \left(\frac{\rho N^2 D^2}{\pi}\right)\left(\frac{D_c}{D}\right)^{-2}\sqrt{N_f^2 + \left(\frac{4P_0}{3\pi}\right)^2} \tag{7.7}$$

And the toroidal model as shown below in equation (7.8)

$$\tau_y = \left(\frac{4\rho N^2 D^2}{\pi^2}\right)\left(\frac{D_c}{D}\right)^{-2}\sqrt{N_f^2 + \left(\frac{4P_0}{3\pi}\right)^2} \tag{7.8}$$

To aid in consistency all cavern size measurements were taken based on the radial-axial velocity composite data. Spherical diameter was taken as twice the distance from the centre line of the impeller to the cavern edge. According to the definition of the toroidal cavern the diameter used would be the same as the spherical one, thus the only difference between the spherical and toroidal yield stress would be a factor of 4/Pi. Again based on the definition of the cylindrical model the diameter would be the same value, the height was taken as double the distance from the centre line to the top of the cavern for down pumping and the bottom of the cavern for up pumping. This is displayed more clearly below in Figure 7.10.

Below in Table 7.5 all estimated values are presented with a corresponding average for each. The spherical and toroidal values are much higher than the cylindrical model estimations, with the toroidal model values being slightly higher than the spherical. Based on the way these results were obtained it could be construed that any of the values could be the correct value since no model could completely cover the cavern volume without encompassing a large area of no flow. The spherical and cylindrical models were consistently larger than the cavern, with the toroidal always being smaller, this can be seen for the example in Figure 7.10. As a rough estimate of the yield stress, which under normal circumstances is difficult to obtain accurately, is at least a worthwhile guess. It would be best to use the model that fits the data better, thus producing a more reasonable estimation of the yield stress, but this would be time consuming as it would involve drawing each cavern for each data set.
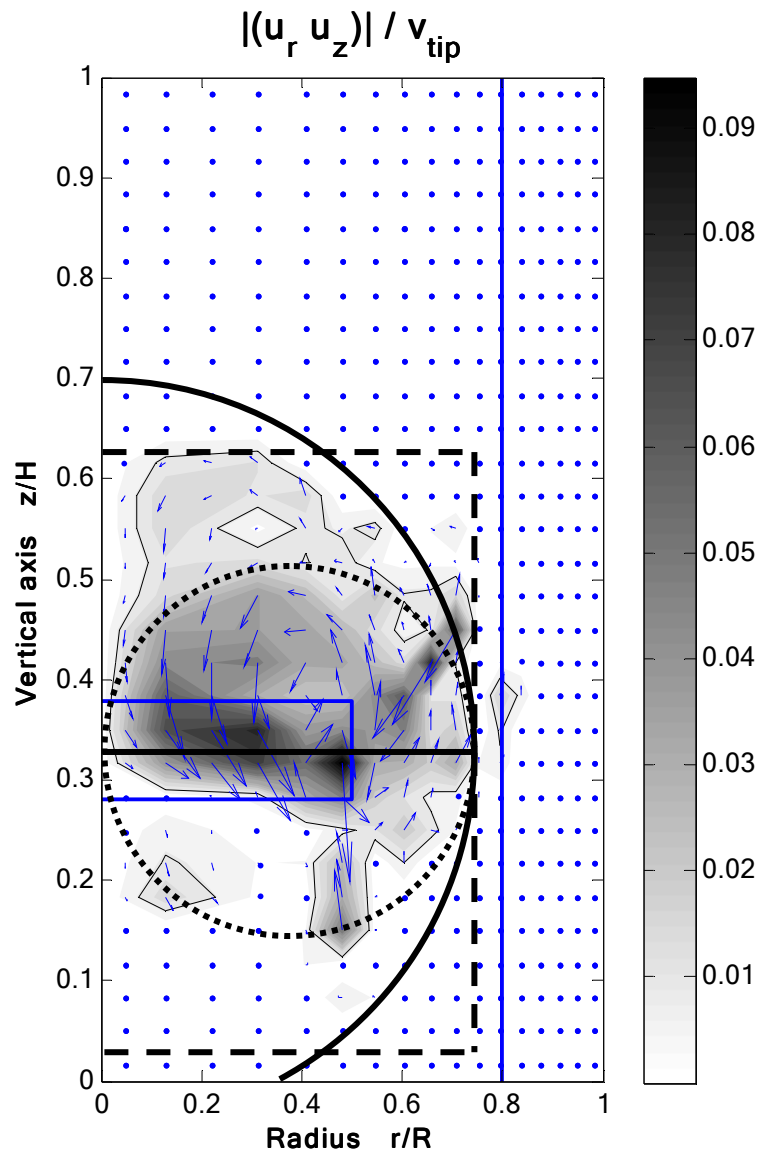
Figure 7.16 Example of cavern prediction fit for one set of results:
Dashed rectangle– Cylindrical, Solid semi-circle – Spherical and Dotted circle – toroidal

Table 7.5 Estimate yield stress values for paper pulp using three cavern models

Impeller Speed	Pumping Direction	τ_y (Pa)		
		Cylindrical	Spherical	Toroidal
80	Down	10.36	23.53	29.96
	Up	10.76	21.41	27.26
100	Down	11.25	25.48	32.45
	Up	9.30	22.07	28.10
120	Down	6.00	20.06	25.54
	Up	7.23	18.61	23.70
150	Down	6.63	21.47	27.33
	Up	7.63	20.07	25.56
	Average	**8.65**	**21.59**	**27.49**

7.6. Conclusions

PEPT was performed on a 3% wt/wt paper pulp fibre suspension being mixed in both the small and large tank, the data extracted made it possible to measure velocities and flow patterns at various impeller speeds. This type of data are unique since it enables the measurement of overall flow patterns in opaque systems similar to the optical techniques for transparent fluids. CARPT can provide similar data obtained through PEPT, but to the authors knowledge this has not been done yet on these types of fluids on the same scale of experiments completed in this chapter. Data was similar for both tank sizes, except for the large tank no secondary loops were generated, possibly due to the different impeller diameter ratio or that the PEPT tracer did not enter them.

Through the application of power measurements it has been postulated that the large tank experiments were all undertaken in the laminar region and thus all the small tank experiments were in the laminar regime due to the estimated lower Reynolds numbers. Through analysis of radial-axial velocity in the impeller discharge plane it has also been found that above a certain impeller speed the degradation towards the cavern boundary is the same. Cavern size and shape were also gleaned from this data showing similar results to cosmetic foundation creams experiments. The radial-axial approach gave much more realistic descriptions of the caverns in the small tank, but for the large tank the tangential approach seemed to give a much better idea of cavern shape and size. This was contributed to the fact that no secondary loops were captured in the large tank. Through the application of the cavern prediction models it was possible to get an estimation of the yield stress of the paper pulp.

CHAPTER 8

CONCLUSIONS AND FUTURE WORK

In depth conclusions for the work undertaken in this thesis can be found at the end of each associated results chapter: this chapter presents the overall conclusions obtained and any future work that is needed to further research.

8.1. Conclusions

The aim of this work was to study the mixing of various rheologically different fluids in a stirred tank in laminar and transitional flow regimes. Due to the rheology and low Reynolds numbers caverns or pseudo-caverns are formed around the impeller, these types of flow structures are detrimental to overall mixing performance. The cavern formation and flow patterns achieved from mixing these types of fluids were examined using experimental methods and CFD simulations. Cavern size and shape were also estimated using mechanistic prediction models.

8.1.1. Experimental

Using an adaptive PLIF technique on a single phase Herschel-Bulkley fluid it was found that mixing inside caverns was shown to be relatively fast near the centre, where high velocities and shear rates occur, but is very slow near the boundary, where the velocities drop to zero.

PEPT was used to obtain the flow field data for two opaque shear thinning cosmetic foundation slurry systems, an opaque shear thickening china clay slurry, and an opaque paper pulp fibre suspension. The extracted flow fields provided a valuable tool for understanding how these fluids mix in a stirred tank, including size and shape of the flow loops, eyes of mixing and dead zones. For the shear thickening material a jet of constant velocity was seen in the discharge stream and extended towards the tank wall. This is an unknown feature of shear thickening materials as this type of data has not been possible to obtain with optical techniques, due to the opaque nature of these types of fluids. The flow patterns and velocities obtained with the other materials are also unique due to their opaqueness. CARPT can provide similar data that can be obtained through PEPT; to the authors knowledge this has not yet been performed on these types of fluids at similar volumetric scales demonstrated in this thesis.

8.1.2. Simulations

CFD simulations were performed to mimic the experiments of the two shear thinning cosmetic foundation cream slurries and the shear thickening slurry. The shear thinning materials was found to give a reasonable prediction of flow patterns. However, at higher impeller speeds the discharge angles were different. Regarding velocities, the comparison was very good for total velocities but the radial and axial components were over predicted.

The shear thickening material simulations showed good predictions at high Reynolds numbers but predicted smaller flow loops at low Reynolds numbers; discharge angles

were also slightly different at all Reynolds numbers. Tangential velocities were predicted well, with the radial and axial velocities poorly predicted. This became worse at higher Reynolds numbers. The constant velocity jet seen in the PEPT experiments were marginally under-predicted in the simulations but were still present.

8.1.3. Caverns

The mixing configurations, impeller types and impeller speeds used to investigate cavern formation were not chosen for the purpose of understanding how to minimise the presence of caverns in practice. The only time when the whole vessel was in motion was at high impeller speeds, these would be impractical for industrial purposes as the power required to reach and sustain these would be too expensive. The configuration was used as it is a standard geometry and thus is quite easy to understand, so when unexpected results were obtained from mixing these complex materials there was enough data available to make sense of the new flow patterns. Also by having the impeller shaft aligned with the vessel axis, the cavern grew in all directions equally.

It was found that the radial-axial approach for defining cavern boundaries were much better than the tangential definition for both PEPT and CFD data for the majority of experiments: the exception to this occurred in the experiment containing the largest tank and the paper pulp: the tangential definition provided better cavern data than the radial-axial approach. This was due to the absence of a secondary flow loop measured during PEPT. The radial-axial approach gives a much more realistic shape of the cavern, showing eyes of mixing and discharges angles.

For the Herschel-Bulkley fluid the CFD cavern data provided a good fit with the adapted PLIF experiments in both size and shape. However at higher Reynolds numbers cavern size was under predicted by CFD. Simulated cavern data for the shear thinning slurries showed reasonable agreement with shape and size for one slurry but was slightly over predicted for the other. Simulated cavern data for the shear thickening slurry predicted both shape and size very well at high Reynolds numbers but under predicted at low Reynolds numbers. The fits of both shear thinning and shear thickening slurries were very good despite the simulation's simplification of a time dependent slurry to a homogenous fluid with a single rheology, meaning that the time dependency had little effect on determining the cavern boundary. Thus CFD can be used to obtain a reasonable approximation cavern size and shape data for these types of fluids, at low Reynolds numbers for shear thinning materials and Reynolds numbers above 70 for shear thickening materials.

All the cavern models predicted the shape quite poorly for all fluids, since caverns are not simple shapes, especially at higher Reynolds numbers. However, cavern size was predicted very well for the Herschel-Bulkley data, using the toroidal model, at low Reynolds numbers; at higher Reynolds numbers the model under predicted cavern size but still gave a much better approximation than the spherical and cylindrical models. For both shear thinning slurries and the shear thickening slurry all cavern models grossly over predicted the cavern size, with the cylindrical model providing the better fits at high Reynolds numbers. By using the cavern prediction models it was possible to get an estimation of the apparent yield stress of the paper pulp fibre suspension by measuring cavern diameters extracted from the PEPT data.

8.2. Future work

PEPT has proven that it can measure the flow of these very rheologically and structurally different opaque fluids in a stirred tank, allowing this technique to be used for numerous other opaque solutions and a multitude of different mixing configurations, such as multiple impellers systems and a variety of different impeller types.

All PEPT experiments undertaken in this thesis were run for half an hour, for future experiments they could be run for a longer period of time to see if the results obtained are the same or if they yield further flow patterns and larger caverns.

Since this work only investigated low Reynolds numbers, the PEPT technique could be used on these materials to further understand how they mix at higher Reynolds numbers, i.e. in the high transitional regime and turbulent flow. This could be used to measure the minimum Reynolds number required for each fluid to reach the tank wall, floor and surface, and thus the impeller speed to cause motion in all regions of the tank.

PEPT analysis of a single phase fluid that has similar rheology to the complex opaque slurry systems could be completed to see if the simplification of a complex multiphase fluid to a single rheology achieves similar flow patterns as this is what the CFD simulations are assuming. To further complete this analysis a transparent single phase fluid with same rheology could be measured using an optical flow technique to discover flow patterns. The two techniques could then be compared.

CFD was able to handle the simulation of all the experiments undertaken despite the fibre suspension, whose rheology is unknown. Even though some of the comparisons with the experimental data were very good, the simulations failed to predict radial and axial velocities very well and some cavern sizes were incorrectly predicted. This means that further refinement of the simulations is needed, such as increased mesh refinement, decrease minimum shear rate constant and better rheological modelling of the slurries. Since all simulations neglected the time dependant nature of both shear thinning and shear thickening slurries, a full transient simulation, mimicking the PEPT experiments including a varying rheology throughout the simulation, should be performed. This will allow a better comparison between experiment and simulation.

It was an initially thought that the mixing inside of caverns was completely chaotic and homogenous. Both experimental techniques and simulated data for all fluids showed that in fact a large degree of heterogeneity was present. It would be interesting to measure the degree of chaotic motion present within these caverns as a function of impeller speed and fluid rheology.

Since the set-up was undesirable for generating flow throughout the entire vessel for these fluids it is suggested to develop new configurations that will do so. It is proposed that using multiple impeller systems with larger impeller diameter may cause motion through the entire vessel, as long as the circulation loops for both impellers interact. Another simpler approach would be using an off-centred impeller, it is thought that since the impeller would be closer to one wall, the flow would be pushed along the walls and floor of the vessel generating larger caverns at lower impeller speeds.

Since every cavern model over predicted cavern sizes for both the shear thinning and shear thickening slurries a refinement of the current models is needed, or a new model should be developed. Also, since all the cavern models could not predict the shape very well, the refined, or new model, should be able to predict a more reasonable cavern shape, such as a pear or kidney shape, and allow comparison with data to be more accurate.

REFERENCES

Adams, L.W., Barigou, M., 2007, CFD analysis of caverns and pseudo-caverns developed during mixing of non-Newtonian fluids, *Chemical Engineering Research and Design,* **85(A5)**, 598-604.

Alvarez-Hernández, M.M., Shinbrot, T., Zalc, J., Muzzio, F.J., 2002, Practical chaotic mixing, *Chemical Engineering Science,* **57**, 3749-3753.

Anandha Rao, M., Brodkey, R.S., 1972, Continuous flow stirred tank turbulence parameters in the impeller stream, *Chemical Engineering Science*, **27**, 137-156.

Amanullah, A., Hjorth, S.A., Nienow, A.W., 1997, Cavern sizes generated in highly shear thinning viscous fluids by SCABA 3SHP1 impellers, *Transactions I.Chem.E.,* **75(C)**, 232-238.

Amanullah, A., Hjorth, S.A., Nienow, A.W., 1998, A new mathematical model to predict cavern diameters in highly shear thinning, power law liquids using axial flow impellers, *Chemical Engineering Science*, **53(3)**, 455-469.

Ansys Europe Ltd, 2005, Ansys CFX Version 10 Manual.

Armenante, P.M., Chou, C.C., 1996, Velocity profiles in a baffled vessel with single or double pitched-blade turbines, *A.I.Ch.E. Journal,* **42(1)**, 42-54.

Ascanio, G., Foucault, S., Tanguy, P.A., 2004, Time-periodic mixing of shear-thinning fluids, *Chemical Engineering Research and Design,* **82(A9)**, 119-1203.

References

Aubin, J., Naude, I., Bertrand, J., Xuereb, C., 2000, Blending of Newtonian and shear-thinning fluids in a tank stirred with a helical screw agitator, *Chemical Engineering Research and Design,* **78(A),** 1105-1114.

Ayel, V., Lottin, O., Peerhossaini, H., 2003, Rheology, flow behaviour and heat transfer of ice slurries: a review of the state of the art, *International Journal of Refrigeration*, **26,** 95-107.

Bakker, R.A., van den Akker, H.E.A., 1994, A computational study of chemical reactors on the basis of micromixing models, *Chemical Engineering Research and Design,* **72(A)**, 733-738.

Bakker, A., Fasano, J.B., 1994, Time dependent, turbulent mixing and chemical reaction in stirred tanks, *A.I.Ch.E. Symposium Series*, **299**, 71-77.

Bakker, R.A., van den Akker, H.E.A., 1996, A Lagrangian description of micromixing in a stirred tank reactor using 1D-micromixing models in a CFD flow field, *Chemical Engineering Science*, **51(11)**, 2643-2648.

Bakker, A., Myers, K.J., Ward, R.W., Lee, C.K., 1996, The laminar and turbulent flow pattern of a pitch blade turbine, *Chemical Engineering Research and Design,* **74(A)**, 485-491.

Bakker, A., Oshinowo, L.M., 2004, Modelling of turbulence in stirred vessels using large eddy simulations, *Chemical Engineering Research and Design*, **82(A9)**, 1169-1178.

Balhoff, M.T., Thompson, K.E., 2004, Modelling the steady flow of yield-stress fluids in packed beds, *A.I.Ch.E. Journal*, **50(12)**, 3034-3048.

References

Barigou, M., 2004, Particle tracking opaque mixing systems: An overview of the capabilities of PET and PEPT, *Chemical Engineering Research and Design*, **82(A9)**, 1258-1267.

Barrue, H., Xuereb, C., Pitiot, P., Falk, L., Bertrand, J., 1999, Comparison of experimental and computational particle trajectories in a stirred vessel, *Chemical Engineering and Technology*, **22**, 511-521.

Bartels, C., Breuer, M., Wechsler, K., Durst, F., 2002, Computational fluid dynamics applications on parallel-vector computers: computations of stirred vessel flows, *Computers and Fluids*, **31**, 69-97.

Bhattacharya, S., Kresta, S.M., 2002, CFD simulations of three-dimensional wall jets in a stirred tank, *The Canadian Journal of Chemical Engineering*, **80**, 695-709.

Bittorf, K.J., Kresta, S.M., 2000, Active volume of mean circulation for stirred tanks agitated with axial impellers, *Chemical Engineering Science*, **55**, 1325-1335.

Bittorf, K.J., Kresta, S.M., 2001, Three-dimensional wall jets: axial flow in a stirred tank, *A.I.Ch.E. Journal,* **47(6)**, 1277-1284.

Brucato, A., Ciofalo, M., Girsafi, F., Micale, G., 1998, Numerical prediction of flow fields in baffled stirred vessels: A comparison of alternative modelling approaches, *Chemical Engineering Science*, **53(21)**, 3653-3684.

Brucato, A., Ciofalo, M., Girsafi, F., Tocco, R., 2000, On the simulation of stirred tank reactors via computational fluid dynamics, *Chemical Engineering Science*, **55**, 291-302.

References

Bugay, S., Escudié, R., Liné, A., 2002, Experimental analysis of hydrodynamics in axially agitated tank, *A.I.Ch.E. Journal,* **48(3)**, 463-475.

Bujalski, W., Nienow, A.W., Chatwin, S., Cooke, M., 1986, The dependency of scale and material thickness of power numbers of different impellers, *International Conference on Mechanical Agitation,* **1**, 37-42.

Bujalski, W., Nienow, A.W., Chatwin, S., Cooke, M., 1987, The dependency on scale of power numbers of Rushton disc turbines, *Chemical Engineering Science*, **42(2)**, 317-326.

Bujalski, W., Jaworski, Z., Nienow, A.W., 2002(a), CFD study of homogenization with dual Rushton turbines – comparison with experimental results, Part II: The multiple reference frame, *Chemical Engineering Research and Design,* **80(A)**, 97-104.

Bujalski, J.M., Jaworski, Z., Bujalski, W., Nienow, A.W., 2002(b), The influence of the addition of position of a tracer on CFD simulated mixing times in a vessel agitated by a Rushton turbine, *Chemical Engineering Research and Design,* **80(A)**, 824-831.

Campola, M., Sbrizzai, F., Soldati, A., 2003, Time-dependent flow structures and lagrangian mixing in a Rushton-impeller baffled-tank reactor, *Chemical Engineering Science*, **58**, 1615-1629.

Chaouuki, J., Larachi, F., Dudukovic, M.P. (Eds), 1997, Non-invasive monitoring of multiphase flows, *Elsevier, Amsterdam.*

Chung, K.H.K., Barigou, M., Simmons, M.J.H., 2007, Reconstruction of 3-D flow field inside miniature stirred vessels using a 2-D PIV technique, *Chemical Engineering Research and Design,* **85(5)**, 560-567.

References

Ciofalo, M., Brucato, A., Grisafi, F., Torraca, N., 1996, Turbulent flow in closed and free-surface unbaffled tanks stirred by radial impellers, *Chemical Engineering Science*, **51(14)**, 3557-3573.

Couerbe, G., Fletcher, D.F., Xuereb, C., Poux, M., 2008, Impact of thixotropy on flow patterns induced in a stirred tank: Numerical and experimental studies, *Chemical Engineering Research and Design*, **86**, 545-553.

Derksen, J., van den Akker, H.E.A., 1999, Large Eddy simulations on the flow driven by a Rushton turbine, *A.I.Ch.E. Journal,* **45(2)**, 209-221.

Derksen, J., 2001, Assessment of large eddy simulations for agitated flows, *Chemical Engineering Research and Design,* **79(A)**, 824-830.

Ducoste, J.J., Clark, M.M., 1999, Turbulence in flocculators: Comparison of measurements and CFD simulations, *A.I.Ch.E. Journal*, **45(2)**, 432-436.

Edwards, M.F., Godfrey, J.C., Kashani, M.M., 1976, Power requirement for the mixing of thixotropic liquids, *Journal of Non-Newtonian Fluid Mechanics,* **1**, 309-322.

Eggels, J.G., 1996, Direct and large-eddy simulations of turbulent flow using the lattice-Boltzmann scheme, *International Journal of Heat and Fluid Flow,* **17**, 307-323.

Ein-Mozaffari, F., Bennington, C.P.J., Dumont, G.A., Buckingham, D., 2007, Measuring flow velocity in pulp suspension mixing using ultrasonic Doppler velocimetry, *Chemical Engineering Research and Design,* **85(A5)**, 591-597.

References

Elson, T.P., Cheesman, D.J., 1986, X-ray studies of cavern sizes and mixing performance with fluids possessing a yield stress, *Chemical Engineering Science*, **41(10)**, 2555-2562.

Elson, T.P., 1990, The growth of caverns formed around rotating impellers during the mxing of a yield stress fluid, *Chemical Engineering Communication,* **96**, 303-319.

Escudié, R., Liné, A., 2003, Experimental analysis of hydrodynamics in a radially agitated tank, *A.I.Ch.E. Journal*, **49(3)**, 585-603.

Escudié, R., Bouyer, D., Liné, A., 2004, Characterization of trailing vortices generated by a Rushton turbine, *A.I.Ch.E., Journal*, **50(1)**, 75-86.

Escudié, R., Liné, A., 2006, Analysis of turbulence anisotropy in a mixing tank, *Chemical Engineering Science,* **61(9)**, 2771-2779.

Fairhurst, P.G., Barigou, M., Fryer, P.J., Pain, J-P., Parker, D.J., 2001, Using positron emission particle tracking (PEPT) to study nearly neutrally buoyant particles in high solid fraction pipe flow, *International Journal of Multiphase Flow*, **27**, 1881-1901.

Fan, X., Parker, D.J., Smith, M.D., 2006(a), Enhancing ^{18}F uptake in a single particle for positron emission particle tracking through modification of solid surface chemistry, *Nuclear Instruments & Methods in Physics Research*, **558(A)**, 542-546.

Fan, X., Parker, D.J., Smith, M.D., 2006(b), Labelling a single particle for positron emission particle tracking using direct activation and ion-exchange techniques, *Nuclear Instruments & Methods in Physics Research*, **562(A)**, 345-350.

References

Fangary, Y.S., Barigou, M., Seville, J.P.K., Parker, D.J., 2000, Fluid trajectories in a stirred vessel of non-Newtonian liquid using positron particle tracking, *Chemical Engineering Science*, **55**, 5969-5979.

Ferziger, J., Peric, M., 1997. *Computational Methods for Fluid Dynamics*, Springer Verlag.

Fishwick, R.P., Winterbottom, J.M., Stitt, E.H., 2003, Explaining mass transfer observations in multiphase stirred reactors: particle-liquid slip velocity measurements using PEPT, *Catalysis Today*, **79-80**, 195-202.

Fountain, G.O., Khakhar, D.V., Mezic, I., Ottino, J.M., 2000, Chaotic mixing in a bounded three-dimensional flow, *Journal of Fluid Mechanics*, **417**, 265-301.

Gabriele, A., Nienow, A.W., Simmons, M.J.H., 2009, Use of angle resolved PIV to estimate local specific energy dissipation rates for up- and down-pumping pitched blade agitators in a stirred tank, *Chemical Engineering Science,* **64(1)**, 126-143.

Galletti, C., Paglianti, A., Yianneskis, M., 2005, Observations on the significance of instabilities turbulence and intermittent motions on the fluid mixing processes in stirred reactors, *Chemical Engineering Science,* **60**, 2317-2331.

Grisky, R.G., Green, R.G., 1971 Flow of dilatant (shear thickening) fluids, *A.I.Ch.E. Journal*, **17(3)**, 725-728.

Guha, D., Ramachandran, P.A., Dudukovic, M.P., Derksen, J.J., 2008, Evaluation of large eddy simulation and euler-euler CFD models for solids flow dynamics in a stirred tank reactor, *AICHE Journal,* **54(3)**, 766-778.

References

Guida, A., Fan, X., Parker, D.J., Niewnow, A.W., Barigou, M., 2009, Positron emission particle tracking in a mechanically agitated solid-liquid suspension of coarse particles, *Chemical Engineering Research and Design*, **87**, 421-429.

Guillard, F., Trägårdh, C., Fuchs, L., 2000, A study of turbulent mixing in a turbine-agitated tank using a fluorescence technique, *Experiments in Fluids*, **28**, 225-235.

Guillard, F., Trägårdh, C., 2003, Mixing in industrial Rushton turbine-agitated reactors under aerated conditions, *Chemical Engineering and Processing,* **42(5)**, 373-386.

Gunkel, A.A., Weber, M.E., 1975, Flow phenomena in stirred tanks, Part I. The impeller stream, *A.I.Ch.E. Journal*, **21(5),** 931-948.

Hall, J.F., Barigou, M., Simmons, M.J.H., Stitt, E.H., 2005, Comparative study of different mixing strategies in small high throughput experimentation reactors, *Chemical Engineering Science*, **60**, 2355-2368.

Hartmann, H., Derksen, J.J., van den Akker, H.E.A., 2004(a), Macroinstability uncovered in a Rushton turbine stirred tank by means of LES, *A.I.Ch.E. Journal,* **50(10)**, 2383-2393.

Hartmann, H., Derksen, J.J., Montavon, C., Pearson, J., Hamill, I.S., van den Akker, H.E.A., 2004(b), Assessment of large eddy and RANS stirred simulations by means of LDA, *Chemical Engineering Science*, **59**, 2419-2432.

Harvey III, A.D., Lee, C.K., Rogers, S.E., 1995, Steady-state modelling and experimental measurement of a baffled impeller stirred tank, *A.I.Ch.E. Journal*, **41(10)**, 2178-2186.

References

Harvey III, A.D., West, D.H., Tufillaro, N.B., 2000, Evaluation of laminar mixing in stirred tanks using a discrete-time particle-mapping procedure, *Chemical Engineering Science*, **55**, 667-684.

Hobbs, D.M., Muzzio, F.J., 1997, The Kenics static mixer: a three-dimensional chaotic flow, *Chemical Engineering Journal,* **67**, 153-166.

Holden, P.J., Wang, M., Mann, R., Dickin, F.J., Edwards, R.B., 1998, Imaging stirred-vessels macromixing using electrical resistance tomography, *A.I.Ch.E. Journal,* **44(4)**, 780-790.

Hui, L.K., Bennington, C.P.J., Dumont, G.A., 2009, Cavern formation in pulp suspensions using side-entering axial-flow impellers, *Chemical Engineering Science*, **64**, 509-519.

Hutchings, B.J., Weetman, R.J., Patel, B.R., 1989, Computation of flow fields in mixing tanks with experimental verification, *A.S.M.E. Winter Annual Meeting.*

Jaworski, Z., Wyszynski, M.L., Moore, I.P.T., Nienow, A.W., 1997, Sliding mesh computational fluid dynamics – a predictive tool in stirred tank design, *Proceedings Institution of Mechanical Engineers, Part E, Journal of Process Mechanical Engineering,* **211(3)**, 149-156.

Jaworski, Z., Bujalski, W., Otomo, N., Nienow, A.W., 2000, CFD study of homogenization with dual Rushton turbines – Comparison with experimental results, Part I: Initial studies, *Chemical Engineering Research and Design*, **78(A)**, 327-333.

Jayanti, S., 2001, Hydrodynamics of jet mixing in vessels, *Chemical Engineering Science*, **56**, 193-210.

References

Jomha, A.I., Edwards, M.F., Woodcock, L.V., 1990, New method for predicting the power requirement for mixing shear thickening suspensions, *Chemical Engineering Science*, **45(2)**, 1389-1396.

Jones, R.M., Harvey III, A.D., Acharya, S., 2001, Two-equation turbulence modelling for impeller stirred tanks, *Journal of Fluids Engineering,* **123(3)**, 640-648.

Kelly, W., Gigas, B., 2003, Using CFD to predict the behaviour of power law fluids near axial-flow impellers operating in the transitional regime, *Chemical Engineering Science*, **58**, 2151-2152.

Khopkar, A.R., Aubin, J., Xuereb, C., Le Sauze, N., Bertrand, J., Ranade, V.V., 2003, Gas-liquid flow generated by a pitched-blade turbine: Particle image velocimetry measurements and computational fluid dynamics simulations, *Industrial and Engineering Chemistry Research*, **42**, 5318-5332.

Kilander, J., Rasmuson, A., 2005, Energy dissipation nad macro instabilities in a stirred square tank investigated using an LE PIV approach and LDA measurements, *Chemical Engineering Science*, **60(24)**, 6844-6856.

Kovács, T., Troedson, M., Wormbs, G., Trägårdh, C., Östergren, K., Innings, F., Lingestrand, A., Strinning, O., 2003, Mixing of Newtonian and non-Newtonian fluids in static mixers under laminar flow conditions: Experiments and simulations, *11ᵗʰ Conference of Mixing*, October 14-17, Bamberg, **P21**, 421-428.

Kukura, J., Arratia, P.C., Szalai, E.S., Bittorf, K.J., Muzzio, 2002, Understanding pharmaceutical flows, *Pharmaceutical Technology*¸ 48-72.

References

La Fontaine, R.F., Shepherd, I.C., 1996, Particle image velocimetry applied to a stirred vessel, *Experimental Thermal and Fluid Science,* **12**, 256-264.

Lamberto, D.J., Alvarez, M.M., Muzzio, F.J., 1999, Experimental and computational investigation of the laminar flow structure in a stirred tank, *Chemical Engineering Science*, **54**, 919-942.

Lamberto, D.J., Alvarez, M.M., Muzzio, F.J., 2001, Computational analysis of regular and chaotic mixing in a stirred tank reactor, *Chemical Engineering Science*, **56**, 4887-4899.

Lee, K.C., Yianneskis, M., 1994(a), Mixing characteristics of a stirred reactor with an axial flow impeller, *I.Chem.E. Symposium Series*, **136.**

Lee, K.C., Yianneskis, M., 1994(b), The extent of periodicitity of the flow in vessels stirred by Rushton impellers, *Industrial Mixing Technology: Chemical and Biological Applications.*

Lee, K.C., Yianneskis, M., 1997, A liquid crystal thermographic technique for the measurement of mixing characteristics in stirred vessels, *Chemical Engineering Research and Design*, **75(A)**, 746-754.

Link, J.M., Deen, N.G., Kuipers, J.A.M., Fan, X., Ingram, A., Parker, D.J., Wood, J., Seville, J.P.K., 2008, PEPT and discrete particle simulation study of spout-fluid bed regimes, *AICHE Journal*, **54(5)**, 1189-1202.

Liu, X., Bao. Y., Li, Z., Gao, Z., Smith, J.M., 2008, Particle image velocimetry study of turbulence characteristics in a vessel agitated by a dual rushton impeller, *Chinese Journal of Chemical Engineering,* **16(5)**, 700-708.

References

Lyungqvist, M., Rasmuson, A., 2001, Numerical simulation of the two-phase flow in an axially stirred vessel, *Chemical Engineering Research and Design*, **79(A)**, 533-546.

Mahmoudi, S.M.S., Yianneskis, M., 1991, The variation of flow pattern and mixing time with impeller spacing in stirred vessels with two Rushton impellers, *7th European Conference on Mixing*. September 18-20, Brugge Belgium.

Mahoust, M., 1991, Concentration fluctuations in a stirred reactor, *Experiments in Fluids,* **11**, 153-160.

Maingonnat, J.F., Muller, L., Leuliet, J.C., 2005, Modelling the build-up of a thixotropic fluid under viscosimetric and mixing conditions, *Journal of Food Engineering*, **3**, 265-272.

Mann, R., Pillai, S.K., El-Hamouz, A.M., Ying, P., Togatorop, A., Edwards, R.B., 1995, Computational fluid mixing for stirred vessels: Progress from seeing to believing, *The Chemical Engineering Journal*¸ **59**, 39-50.

Mavros, P., Xuereb, C., Bertrand, J., 1998, Determination of 3-D flow fields in agitated vessels by laser-doppler velocimetry: Use and interpretation of RMS velocities, *Chemical Engineering Research and Design*, **76(A)**, 223-233.

Mavros, P., Mann, R., Vlaev, S.D., Bertrand, J., 2001, Experimental visualization and CFD simulations of flow patterns induced by a novel energy-saving dual-configuration impeller in stirred vessels, *Chemical Engineering Research and Design*, **79(A)**, 857-866.

Metzner, A.B., Otto, R.E., 1957, Agitation of Non-Newtonian Fluids, *A.I.Ch.E. Journal*, **3,** 1, 3-10.

References

Michelet, S., Kemoun, A., Mallet, J., Mahouast, M., 1997, Space-time velocity correlations in the impeller stream of a Rushton turbine, *Experiments in Fluids,* **23**, 418-426.

Micheletti, M., Baldi, S., Yeoh, S.L., Ducci, A., Papadakis, G., Lee, K.C., Yianneskis, M., 2004, On spatial and temporal variations and estimates of energy dissipation in stirred reactors, *Chemical Engineering Research and Design*, **82(A9)**, 1188-1198.

Montante, G., Lee, K.C., Brucato, A., Yianneskis, M., 2001(a), Numerical simulations of the dependency of flow pattern on impeller clearance in stirred vessels, *Chemical Engineering Science*, **56**, 3751-3770.

Montante, G., Lee, K.C., Brucato, A., Yianneskis, M., 2001(b), Experiments and predictions of the transition of the flow pattern with impeller clearance in stirred tanks, *Computers and Chemical Engineering*, **25**, 729-735.

Montante, G., Magelli, F., 2004, Liquid homogenization characteristics in vessels stirred with multiple Rushton turbines mounted at different spacings, CFD study and comparison with experimental data, *Chemical Engineering Research and Design*, **82(A9)**, 1179-1187.

Montante, G., Moštěk, M., Jahoda, M., Magelli, F., 2005, CFD simulations and experimental validation of homogenisation curves and mixing time in stirred Newtonian and pseudoplastic liquids, *Chemical Engineering Science*, **60**, 2427-2437.

Murthy Shekhar, S., Jayanti, S., 2002, CFD study of power and mixing time for paddle mixing in unbaffled vessels, *Chemical Engineering Research and Design*, **80(A)**, 482-498.

References

Naude, I., Xuereb, C., Bertrand, J., 1998, Direct prediction of the flows induced by a propeller in an agitated vessel using and unstructured mesh, *The Canadian Journal of Chemical Engineering*, **76**, 631-640.

Nere, N.K., Patwardhan, A.W., Joshi, J.B., 2001, Prediction of flow pattern in stirred tanks: New constitutive equation for eddy viscosity, *Industrial and Engineering Chemistry Research,* **40**, 1755-1772.

Nienow, A.W., Elson, T.P., 1988, Aspects of Mixing in Rheologically Complex Fluids, *Chemical Engineering Research and Design,* **66**, 5-15.

Nienow, A.W., 1997, On impeller circulation and mixing effectiveness in the turbulent flow regime, *Chemical Engineering Science,* **52(15)**, 2557-2565.

Nikiforaki, L., Montante, G., Lee, K.C., Yianneskis, M., 2003, On the origin, frequency and magnitude of macro-instabilities of the flows in stirred vessels, *Chemical Engineering Science*, **58**, 2937-2949.

Nishikawa, M., Okamoto, Y., Hashimoto, K., Nagata, S., 1976, Turbulence energy spectra in baffled mixing vessels, *Journal of Chemical Engineering of Japan¸* **9(6),** 489-493.

Norwood, K.W., Metzner, A.B., 1960, Flow patterns and mixing rates in agitated vessels, *A.I.Ch.E. Journal,* **6(3),** 432-437.

Nouri, J.M., Whitelaw, J.H., Yiannseskis, M., 1987, The scaling of the flow field with impeller size and rotational speed in a stirred reactor, *2nd International Conference on Laser Anemometry – Advances and Applications,* 489-500.

References

Osman, J.J., Varley, J., 1999, The use of computational fluid dynamics (CFD) to estimate mixing times in a stirred tank, *I.Chem.E. Symposium Series*, **146**, 15-22.

Pakzad, L., Ein-Mozaffari, F., Chan, P., 2008(a), Using computational fluid dynamics modelling to study the mixing of pseudoplastic fluids with a Scaba 6SRGT impeller, *Chemical Engineering and Processing*, **47**, 2218-2227.

Pakzad, L., Ein-Mozaffari, F., Chan, P., 2008(b), Using electrical resistance tomography and computational fluid dynamics modelling to study the formation of caver in the mixing of pseudoplastic fluids possessing yield stress, *Chemical Engineering Science*, **63**, 2508-2522.

Parker, D.J., Fan, X., 2008, Positron emission particle tracking – Application and labelling techniques, *Particuology*, **6**, 16-23.

Patwardhan, A.W., 2001, Prediction of residence time distribution of stirred reactors, *Industrial and Engineering Chemistry Research*, **40**, 5686-5695.

Pettersson, M., Rasmuson, A.C., 1998, Hydrodynamics of suspensions agitated by pitched-blade turbine, *A.I.Ch.E. Journal,* **44(3)**, 513-527.

Procházka, J., Landau, J., Studies on mixing. XII. Homogenation of miscible liquids in the turbulent region, *Collection of Czechoslov Chemical Communications*, **26**, 2961-2973.

Raghav Rao, K.S.M.S., Joshi, J.B., 1988, Liquid phase mixing in mechanically agitated vessels, *Chemical Engineering Communications,* **74,** 1-25.

References

Rammohan, A.R., Kemoun, A., Al-Dahhan, M.H., Dudukovic, M.P., 2001, A lagrangian description of flows in stirred tanks via computer-automated radioactive particle tracking (CARPT), *Chemical Engineering Science*¸**56**, 2629-2639.

Ranade, V.V., Joshi, J.B., 1989(a), Flow Generated by pitched blade turbines I: Measurements using laser Doppler anemometer, *Chemical Engineering Communication,* **81**, 197-224.

Ranade, V.V., Joshi, J.B., 1989(b), Flow Generated by pitched blade turbines II: Simulation using k-ε model, *Chemical Engineering Communication*, **81**, 225-248.

Ranade, V.V., Bourne, J.R., Joshi, J.B., 1991, Fluid mechanics and blending in agitated tank, *Chemical Engineering Science*, **46(8)**, 1883-1893.

Ranade, V.V., Dommeti, S.M.S., 1996, Computational snapshot of flow generated by axial impellers in baffled stirred vessels, *Chemical Engineering Research and Design*, **74(A)**, 476-484.

Ranade, V.V., 1997, An effiecient computational model for simulating flow in stirred vessels: a case of Rushton turbine, *Chemical Engineering Science*, **52(24)**, 4473-4484.

Ranade, V.V., Perrand, M., Le Sauze, N., Xuereb, C., Bertrand, J., 2001, Trailing vorticies of Rushton turbine: PIV measurements and CFD simulations with snapshot approach, *Chemical Engineering Research and Design*, **79**, 3-12.

Reilly, C.D., Britter, R.E., 1985, Mixing times for passive tracers in stirred tanks, *5th European Conference on Mixing.* Würzburg, Germany. BHRA Fluid Engineering Centre (Cranfield, Bedford), 365-375.

References

Revstedt, J., Fuchs, L., Trägårdh, C., 1998, Large eddy simulations of the turbulent flow in a stirred reactor, *Chemical Engineering Science*, **53(24)**, 4041-4053.

Revstedt, J., Fuchs, L., Kovács, T., Trägårdh, C., 2000, Influence of impeller type on the flow structure in a stirred reactor, *A.I.Ch.E. Journal,* **46(12)**, 2373-2382.

Revstedt, J., Fuchs, L., 2002, Research News, Large eddy simulation of flow in stirred vessels, *Chemical Engineering and Technology*, **25**, 443-446.

Rushton, J.H., Costich, E.W., Everett, H.J., 1950, Power characteristics of mixing impellers Part I and Part II, *Chemical Engineering Progress*, **46(8)**, 395-404.

Ruszkowski, S.W., Muskett, M.J., 1985, Comparative mixing times for stirred tank agitators, *5ʰ European Conference on Mixing*. Würzburg, Germany. BHRA Fluid Engineering Centre (Cranfield, Bedford), 89-103.

Rutherford, K., Mahmoudi, S.M.S., Lee, K.C., Yianneskis, M., 1996, The influence of Rushton impeller blade and disk thickness on the mixing characteristics of stirred vessels, *Chemical Engineering Research and Design*, **74(A)**, 369-378.

Sahu, A.K., Joshi, J.B., 1995, Simulation of flow in stirred vessels with axial flow impellers: effects of various numerical schemes and turbulence model parameters, *Industrial and Engineering Chemistry Research¸* **34**, 626-639.

Sahu, A.K., Kumar, P., Patwardhan, A.W., Joshi, J.B., 1999, CFD modelling and mixing in stirred tanks, *Chemical Engineering Science*, **54**, 2285-2293.

References

Sano, Y., Usui, H., 1985, Interrelations among mixing time, power number and discharge flow rate number in baffled mixing vessels, *Journal of Chemical Engineering of Japan*, **18(1)**, 47-52.

Schäfer, M., Yianneskis, M., Wächter, P., Durst, F., 1998, Trailing vortices around a 45° pitched-blade impeller, *A.I.Ch.E. Journal,* **44(6),** 1233-1246.

Schofield, D.F., 1994, An Application of CFD to intert and reactive tracer mixing in a batch stirred vessel, *A.I.Ch.E. Symposium Series*, **299**, 19-32.

Sheng, J., Meng, H., Fox, R.O., 1998, Validation of CFD simulations of a stirred tank using particle image velocimetry data, *The Canadian Journal of Chemical Engineering¸***76**, 611-625.

Sheng, J., Meng, H., Fox., R.O., 2000, A large eddy PIV method for turbulence dissipation rate estimation, *Chemical Engineering Science*, **55**, 4423-4434.

Solomon, J., Elson, T.P., Nienow, A.W., 1981, Cavern sizes in agitated fluids with a yield stress, *Chemical Engineering Communications*, **11**, 143-164.

Sun, H., Wang, W., Mao, Z., 2002, Numerical simulation of the whole three-dimensional flow in a stirred tank with anisotropic algebraic stress model, *Chinese Journal of Chemical Engineering¸* **10(1),** 15-24.

Szalai, E.S., Arratia, P., Johnson, K., Muzzio, F.J., 2004, Mixing analysis in a tank stirred with Ekato Intermig® impellers, *Chemical Engineering Science*, **59**, 3793-3805.

Tay, M., Tatterson, G.B., 1985, Form and skin drag contributions to power consumption for the pitched-blade turbine, *A.I.Ch.E. Journal,* **31(11),** 1915-1918.

References

Van 't Riet, K., Smith, J.M., 1975, The trailing vortex system produced by Rushton turbine agitators, *Chemical Engineering Science,* **30**, 1093-1105.

Verzicco, R., Iaccarino, G., Fatica, M., Orlandi, P., 2000, Flow in an impeller stirred tank using an immersed boundary method, *Center for Turbulence Research. Annual Research Briefs*, 251-261.

Wechsler, K., Breuer, M., Durst, F., 1999, Steady and unsteady computations of turbulent flows induced by a 4/45° pitched-blade impeller, *Journal of Fluids Engineering, Transactions of the A.S.M.E.,* **121**, 318-329.

Weetman, R.J., Oldshue, J.Y., 1988, Power, flow and shear characteristics of mixing impellers, *6ᵗʰ European Conference on Mixing*. May 24-26. Pavia, Italy.

Wenersson, E.S., Trägårdh, C., 1998, Scaling of turbulence characteristics in a turbine-agitated tank in relation to agitation rate, *Chemical Engineering Journal*, **70**, 37-45.

Wilkens, R.J., Miller, J.D., Plummer, J.R., Dietz, D.C., Myers, K.J., 2005, New techniques for measuring and modelling cavern dimensions in a Bingham plastic fluid, *Chemical Engineering Science*, **60**, 5269-5275.

Wittmer, S., Falk, L., Pitiot, P., Vivier, H., 1998, Characterisation of stirred vessel hydrodynamics by three dimensional trajectography, *The Canadian Journal of Chemical Engineering*, **76**, 600-609.

Wu, H., Patterson, G.K., 1989, Laser-doppler measurements of turbulent-flow parameters in a stirred mixer, *Chemical Engineering Science*, **44(10)**, 2207-2221.

References

Xu, Y., McGrath, G., 1996, CFD predictions of stirred tank flows, *Chemical Engineering Research and Design*, **74(A)**, 471-475.

Yeoh, S.L., Papadakis, G., Yianneskis, M., 2004(a), Numerical simulation of turbulent flow characteristics in a stirred vessel using the LES and RANS approaches with the sliding/deforming mesh methodology, *Chemical Engineering Research and Design*, **82(A7)**, 834-848.

Yeoh, S.L., Papadakis, G., Lee, K.C., Yianneskis, M., 2004(b), Large eddy simulation of turbulent flow in a Rushton impeller stirred reactor with sliding-deforming mesh methodology, *Chemical Engineering and Technology*, **27(3)**, 257-263.

Yeoh, S.L., Papadakis, G., Yianneskis, M., 2005, Determination of mixing time and degree of homogeneity in stirred vessels with large eddy simulation, *Chemical Engineering Science*, **60**, 2293-2302.

Yianneskis, M., Popiolek, Z., Whitelaw, J.H., 1987, An experimental study of the steady and unsteady flow characteristics of stirred reactors, *Journal of Fluid Mechanics,* **175**, 537-555.

Yianneskis, M., 1991, The effect of flow rate and tracer insertion time on mixing times in jet-agitated vessels, *7th European Conference on Mixing*. September 18-20, Brugge Belgium.

Yianneskis, M., Whitelaw, J.H., 1993, On the structure of the trailing vortices around Rushton turbine blades, *Chemical Engineering Research and Design*, **71(A),** 543-550.

Yoon, H.S., Balachandar, S., Ha, M.Y., Kar. K., 2003, Large eddy simulation of flow in a stirred tank, *Transactions of the A.S.M.E.,* **125**, 486-499.

References

Zalc, J.M., Szalai, E.S., Alvarez, M.M., Muzzio, F.J., 2002, Using CFD to understand chaotic mixing in laminar stirred tanks, *A.I.Ch.E. Journal,* **48(10)**, 2124-2134.

Zhou, G., Kresta, S., 1996(a), Impact of tank geometry on the maximum turbulence energy dissipation rate for impellers, *A.I.Ch.E., Journal*, **42(9)**, 2476-2490.

Zhou, G., Kresta, S., 1996(b), Distribution of energy between convective and turbulent flow for three frequently used impellers, *Chemical Engineering Research and Design*, **74(A),** 379-389.

Zipp, R.P., Patterson, G.K., 1998. Experimental measurements and simulation of mixing and chemical reaction in a stirred tank, *Canadian Journal of Chemical Engineering*, **76**, 657-669.